

AD-A021 275

THERMOMECHANICAL ABLATION

George Y. Jumper, Jr.

Air Force Institute of Technology
Wright-Patterson Air Force Base, Ohio

September 1975

DISTRIBUTED BY:

NTIS

National Technical Information Service
U. S. DEPARTMENT OF COMMERCE

①

AD-A021 275

THERMOMECHANICAL ABLATION

068095

by

George Y. Jumper, Jr., B.S., M.S.

Captain

USAF

Approved:

James E. Hitchcock
Chairman

21 Oct. 1975

Gregory J. Hine

21 Oct 1975

Paul J. Tomcik

21 Oct 1975

Carol E. Wright

21 Oct 1975

Accepted:

William L. ...
Dean, School of Engineering

23 Oct 1975


Reproduced by
NATIONAL TECHNICAL
INFORMATION SERVICE
US Department of Commerce
Springfield, VA. 22151

DDC
RECEIVED
FEB 26 1976
A

DISTRIBUTION STATEMENT A
Approved for public release;
Distribution Unlimited

UNCLASSIFIED

SECURITY CLASSIFICATION OF THIS PAGE (When Data Entered)

REPORT DOCUMENTATION PAGE		READ INSTRUCTIONS BEFORE COMPLETING FORM
1. REPORT NUMBER DS/ME/75-1	2. GOVT ACCESSION NO.	3. RECIPIENT'S CATALOG NUMBER
4. TITLE (and Subtitle) THERMOMECHANICAL ABLATION		5. TYPE OF REPORT & PERIOD COVERED PhD Dissertation
7. AUTHOR(s) George Y. Jumper, Jr., Capt, USAF		6. PERFORMING ORG. REPORT NUMBER
9. PERFORMING ORGANIZATION NAME AND ADDRESS Air Force Institute of Technology (AFIT-EN) Wright Patterson AFB, Ohio 45433		8. CONTRACT OR GRANT NUMBER(s)
11. CONTROLLING OFFICE NAME AND ADDRESS Space and Missile Branch, System Support Division Air Force Materials Laboratory (AFML/MXS) Wright Patterson AFB, Ohio 45433		10. PROGRAM ELEMENT, PROJECT, TASK AREA & WORK UNIT NUMBERS 73810265
14. MONITORING AGENCY NAME & ADDRESS (if different from Controlling Office)		12. REPORT DATE Sept 1975
		13. NUMBER OF PAGES 108 191
		15. SECURITY CLASS. (of this report) Unclassified
16. DISTRIBUTION STATEMENT (of this Report) Approved for public release; distribution unlimited		15a. DECLASSIFICATION/DOWNGRADING SCHEDULE
17. DISTRIBUTION STATEMENT (of the abstract entered in Block 20, if different from Report)		
18. SUPPLEMENTARY NOTES Approved for public release; IAW AFR 190-17  Jerry C. Hix, Capt, USAF, Director of Information		
19. KEY WORDS (Continue on reverse side if necessary and identify by block number) Thermomechanical Ablation Ablation Heat and Mass Transfer Carbon Dioxide		
20. ABSTRACT (Continue on reverse side if necessary and identify by block number) In order to investigate the heat and mass transfer aspects of thermomechanical ablation, ablation experiments were performed with models made of pure carbon dioxide (CO ₂) and a glass bead-CO ₂ composite. The experiments were performed in a low subsonic, low turbulence jet at ambient pressure and near 0°C temperature. The model geometry was a hemispherical forebody-cylindrical afterbody with a diameter of 25mm. The stagnation point mass transfer of the pure CO ₂ models was 6.2% less than predicted by equilibrium theory. The distribution		

DD FORM 1473
1 JAN 73

EDITION OF 1 NOV 65 IS OBSOLETE

UNCLASSIFIED

SECURITY CLASSIFICATION OF THIS PAGE (When Data Entered)

UNCLASSIFIED

SECURITY CLASSIFICATION OF THIS PAGE(When Data Entered)

around the hemisphere generally agreed with the predicted laminar heat transfer result of monotonically decreasing heat transfer with distance from the stagnation point. The internal temperature response was approximately 5% higher than the theoretically predicted wall temperature. These results could be correlated by the inclusion of a nonequilibrium sublimation model into the theoretical prediction equations. The required vaporization coefficient was 0.0005. For the composite models, the stagnation point CO₂ mass flux was 23% below the rate of the pure CO₂ models. The mass flux around the hemisphere did not decrease with distance from the stagnation point until beyond the 45 degree position, and the internal temperature was slightly higher than the pure CO₂ models. The composite results could be predicted by reducing the transfer coefficient by 6% and including in the surface model diffusion of the sublimed CO₂ through the wells between the beads, nonequilibrium sublimation, and the consequences of heat transfer through the beads to the subliming surface.

UNCLASSIFIED

SECURITY CLASSIFICATION OF THIS PAGE(When Data Entered)

✓

A

THERMOMECHANICAL ABLATION

DISSERTATION

DS/ME/75-1

George Y. Jumper Jr.
Capt USAF

DDC
26 1976
A

Approved for public release; distribution unlimited

DS/ME/75-1

THERMOMECHANICAL ABLATION

DISSERTATION

Presented to the Faculty of the School of Engineering
of the Air Force Institute of Technology

Air University
in Partial Fulfillment of the
Requirements for the Degree of
Doctor of Philosophy

by

George Y. Jumper, Jr., B.S., M.S.

Capt

USAF

Approved for public release; distribution unlimited

Preface

The work reported in this dissertation could not have been accomplished without the assistance of many people. First, I would like to thank the Chairman of my dissertation committee and advisor, Dr. James E. Hitchcock, for his advice, guidance, and, at times, physical labor in helping me with the experiment and the analysis of the results. The other members of the committee, Dr. Andrew J. Shine and Dr. Harold E. Wright, were also of great assistance in helping acquire the necessary research equipment and guiding the work. The AFIT technicians, Mr. William Baker and Mr. John Flahive, were indispensable in the daily battles with the equipment. Many special items required for this study were made by Mr. Wolfe and his very capable staff at the AFIT Shops. The Aerospace Research Laboratories Energy Conversion Laboratory engineers and technicians were most generous in allowing me to set up Capt Craig Lyon's wind tunnel in their laboratory and assisting me whenever I had a problem. I'd like to thank Dr. Alan Hopkins, AFML, and Mr. Tom Lee, Mr. Henry Taylor, and other members of the UDRI technical staff for sharing their expertise in optical data acquisition and for allowing me to reduce my optical data on their equipment.

This research was sponsored by the Air Force Materials Laboratory, Wright-Patterson AFB, Ohio. I would like to

thank Mr. Gary Denman for his guidance in the selection of this topic and throughout the investigation. I also thank my supervisors, Capt James Gerber and Maj Henry Keck, and the other members of the branch for their help and encouragement.

Finally, I wish to thank my wife, Lexie, and our sons, who understood the necessity of this work and gave me the support I needed to make it a reality.

Contents

	Page
Preface	iii
List of Figures	vii
List of Tables	x
Notation	xi
Abstract	xiv
I. Introduction	1
II. Simplified Ablation Model	4
III. Experiment	15
Subliming Material and Environmental Conditions	15
Ablation Models	19
Experimental Test Facility and Procedures	22
Data Reduction	25
Experimental Conditions and Physical Properties	29
IV. Experimental Results	32
V. Ablation of the Composite Material	37
Improved Ablation Model	38
The Energy Equation	47
Radiation Heat Transfer	47
Sphere Analysis	48
Gas Column Analysis	52
Resistance Network Analysis	54
Enthalpy Increase of the Evolved Solids	56
Enthalpy Increase of the Evolved Gases	56
Internal Heat Conduction	56
The Conservation of Specie Equation	57
Temperature Difference	58
Concentration Attenuation	58
Nonequilibrium Sublimation	60
Computation Scheme	63

Contents

	Page
VI. Comparison of Theoretical and Experimental Results	65
Pure Carbon Dioxide Models	65
Glass Bead-Carbon Dioxide Models	68
Nonequilibrium Model	68
Equilibrium Model	71
Two Phase Flow Effect on Transfer Coefficients	76
Relative Magnitudes of Correction Terms	81
General Applicability of Results	84
VII. Conclusion	88
VIII. Recommended Improvements to the Experiment	91
Bibliography	94
Appendix A	98
Appendix B	102
Vita	174

List of Figures

<u>Figure</u>		<u>Page</u>
1	Thermochemical - Thermomechanical Ablation Process	5
2	Ablation Response of Dry Ice, Ice, and Camphor (Summarized from Ref 11)	16
3	Boundary Layer Edge Velocity Normalized by Free Stream Velocity for a Sphere and a Hemisphere-Cylinder	18
4	Ablation Model Molds and Center Rod with Thermocouple	20
5	Glass Beads (150X)	20
6	System for Producing Ablation Models	21
7	Free Jet and Ablation Model	23
8	Data Photograph of Model, Stopwatch and Reference Scale Taken Early in a Test	24
9	Typical Set of Recession Profiles	26
10	Typical Recession Plots	28
11	CO ₂ Mass Loss--Experimental Data From Pure CO ₂ Models and Theoretical Prediction--All Normalized by Theoretical Stagnation Point Mass Loss	33
12	CO ₂ Mass Loss--Experimental Data From Composite Models and Theoretical Prediction--All Normalized by Theoretical Stagnation Point Mass Loss	34
13	Typical Internal Temperature Record	36
14	Model of Ablating Glass Bead-CO ₂ Surface	38
15	Control Volume for Ablation Model of the Composite Material	39
16	A Sphere Half Emerged from the CO ₂	49

<u>Figure</u>		<u>Page</u>
17	Temperature Profiles in a Sphere	51
18	Idealized Gas Column Geometry	53
19	Resistance Network	55
20	Arbitrary Geometry for Diffusion Analysis . . .	59
21	Effect of Non-Equilibrium Sublimation on Mass Flux and Wall Temperature	62
22	Iterative Scheme to Predict B' and Model Temperatures for Glass Bead - CO ₂ Composite . .	64
23	Equilibrium and Nonequilibrium Predictions Compared to Experimental Results of Pure CO ₂ Models--All Normalized by Equilibrium Theory Stagnation Point Mass Loss Prediction (T = 280K, P = 0.967 atm, α = 0.0005)	66
24	Effect of Well Depth on Stagnation Point Ablation Response of Composite Models with Nonequilibrium Sublimation Model (T = 273K, P = 0.967 atm, α = 0.0005, Side Wall Wells Have Negligible Diffusion Depth)	70
25	Theoretical Mass Flux and Wall Temperature Distribution for Composite With Nonequil- ilibrium Sublimation Model (T = 273K, P = 0.967 atm, α = 0.0005, y = 50 μ m)	72
26	Effect of Well Depth on Stagnation Point Ablation Response of Composite with Equilibrium Sublimation Model (T = 273K, P = 0.967 atm, Side Wall Wells Have Negligible Diffusion Depth)	73
27	Effect of Well Depth on Stagnation Point Ablation Response of Composite With Equilibrium Sublimation Model and Side Wall Well Diffusion Depth Equal to Stagnation Point Depth (T = 273K, P = 0.967 atm)	75
28	Theoretical Mass Flux and Wall Temperature Distribution for Composite With Equilibrium Sublimation Model (T = 273K, P = 0.967 atm, y = 80 μ m)	77

<u>Figure</u>		<u>Page</u>
29	Parametric Combinations of Coefficient of Vaporization, Well Depth, and Transfer Coefficient Which Will Result in the Stagnation Point Mass Flux $0.0288 \text{ kg/m}^2 \cdot \text{s}$ and the Resulting Internal Temperatures ($T = 273\text{K}$, $P = 0.967 \text{ atm}$, Side Wells Have Negligible Diffusion Depth)	79
30	Comparison of Experimental Data and Theoretically Predicted Stagnation Point Mass Flux and Model Temperature as a Function of Heat Transfer Coefficient ($T = 273\text{K}$, $P = 0.967 \text{ atm}$, $\alpha = 0.0005$, $y = 40 \text{ }\mu\text{m}$, Side Wall Wells Have Negligible Diffusion Depth)	82
31	The Effect of Bead Size on Normalized Mass Flux and Wall Temperature	92

List of Tables

<u>Table</u>		<u>Page</u>
I	Comparison of BLIMP and Simple Theory Predictions for an Axisymmetric Stagnation Point	14
II	Range of Experimental Conditions and Model Component Properties	31
III	Summary of Theoretical Predictions for Heat Flux and Energy Gain of a Sphere	52

Notation

<u>* Symbol</u>	<u>Meaning</u>
A(x)	Area; Eq (52)
A	Constant; Eq (20) and (39)
a	Bead radius
B	Constant; Eq (20) and (39)
B'	Mass addition parameter; $\dot{m}/\rho_e u_e C_H$
C_H	Stanton number; Eq (9)
C_{Ho}	Stanton number with no mass addition; Eq (21)
CO ₂	Carbon dioxide
C_p	Specific heat at constant pressure
D	Binary diffusion coefficient
E	Internal energy
F	Ratio of well area to surface area; Eq (73)
H	Total enthalpy; $h + u^2/2$
h	Enthalpy
K	Mass fraction
k	Thermal conductivity
Le	Lewis number; $\rho D C_p / k$
M	Molecular weight
\dot{M}	Total mass flow rate
\dot{m}	Mass flux of subliming specie
P	Pressure
p	Partial pressure
Pr	Prandtl number; $\mu C_p / k$

<u>Symbol</u>	<u>Meaning</u>
\dot{Q}	Total heat flow rate
\dot{q}	Heat flux
R	Universal gas constant
R_i	Resistance of i^{th} component
r	Coordinate in the radial direction
s	Streamwise coordinate
\dot{s}	Ablation recession rate.
Sc	Schmidt number; $\mu/\rho D$
T	Temperature
u	Streamwise velocity
v	Velocity normal to wall
\bar{X}	Correction to energy equation; Eq (48)
x	Length coordinate
y	Distance from wall
α	Absorptivity; Eq (49) or Coefficient of evaporation; Eq (75)
ϵ	Emissivity
θ	Angular coordinate
μ	Dynamic viscosity
σ	Stephan-Boltzmann constant
ρ	Density

Subscripts

BL	Boundary layer
C	Gas column
diff	Diffusion
e	Edge of boundary layer
eq	Equilibrium
GB	Glass bead
i	Specie index, usually 1 = subliming specie, 2 = air
int	To the interior
M	Maximum
o	Minimum
s	Solid at the subliming surface
sub	Sublimation
T	Total
w	Fluid dynamic wall
r	Recovery or adiabatic wall
rad	Radiation
∞	Free stream

Superscript

*	Glass bead, or nonsubliming component
---	---------------------------------------

Abstract

In order to investigate the heat and mass transfer aspects of thermomechanical ablation, ablation experiments were performed with models made of pure carbon dioxide (CO_2) and a glass bead- CO_2 composite. The experiments were performed in a low subsonic, low turbulence jet at ambient pressure and near 0°C temperature. The model geometry was a hemispherical forebody-cylindrical afterbody with a diameter of 25 mm. The stagnation point mass transfer of the pure CO_2 models was 6.2% less than predicted by equilibrium theory. The distribution around the hemisphere generally agreed with the predicted laminar heat transfer result of monotonically decreasing heat transfer with distance from the stagnation point. The internal temperature response was approximately 5% higher than the theoretically predicted wall temperature. These results could be correlated by the inclusion of a nonequilibrium sublimation model into the theoretical prediction equations. The required vaporization coefficient was 0.0005. For the composite models, the stagnation point CO_2 mass flux was 23% below the rate of the pure CO_2 models. The mass flux around the hemisphere did not decrease with distance from the stagnation point until beyond the 45 degree position, and the internal temperature was slightly higher than the pure CO_2 models. The composite results could be predicted by reducing the transfer coefficient by 6% and including in the surface model diffusion of the sublimed CO_2 through the wells between the beads, nonequilibrium sublimation, and the consequences of heat transfer through the beads to the subliming surface.

THERMOMECHANICAL ABLATION

I. Introduction

The reentry of a vehicle into the atmosphere cannot be experimentally duplicated on the ground, nor can the vehicle in flight be instrumented well enough to determine all of the significant phenomena associated with nosetip ablation. This handicaps the analyst's attempt to model an event governed by aerodynamics, heat transfer, and material science. It is, therefore, no surprise that ablation modeling is a difficult task and is often the subject of much dispute.

Through the efforts of many early researchers, the rate of thermochemical ablation can be approximately determined with rather simple relationships which yield surprisingly accurate predictions for some materials. The key to the simple solution is the application of the "Unity Lewis Number" assumption, which implies equal mass and thermal diffusivities, to the surface energy and specie conservation equations. This assumption was applied to the problem by Shvab and Zeldovich (Ref 21 and 26) in the 1940's and received its widest dissemination when presented in its most general form by Lester Lees at the Third AGARD Colloquium on Combustion and Propulsion in 1958 (Ref 12). Lees' results can be found in textbooks such as Dorrance (Ref 3) and are the basis for most of the ablation

prediction procedures used in the United States aerospace industry today. Spalding (Ref 24) employed the unity assumption in a slightly different presentation to yield equally useful results, which received excellent tutorial treatment in W. M. Kays' text (Ref 8). These formulations allow the determination of surface temperature and the ratio of mass transfer rate to heat transfer coefficient when the boundary layer edge conditions and the thermochemistry of the system are specified. Convective heat transfer theory supplies the transfer coefficient which must be corrected for mass addition at the wall (blowing). Kubota (Ref 11) simplified Lees' theory for a binary mixture with no chemical reactions and performed some early low temperature ablation experiments using ice at Mach 5.8.

When experimental data became available for the ablation of graphite, it was noted that the mass loss rates were higher than the amount predicted by thermochemical theory. The hypothesis which best explained the data was that the graphite did not completely transition to the vapor phase, but that solid particles were removed from the surface in a high enthalpy, high shear ablation environment (Ref 10). In fact, Lundell and Dickey were able to photograph a shower of glowing particles downstream of an ablating graphite model (Ref 13). The phenomena is called thermomechanical ablation or erosion and it was estimated that in reentry the ratio of thermomechanical ablation to thermochemical ablation for graphite could exceed one

(Ref 10). As the understanding of turbulent rough wall heat transfer increased, the estimated mechanical loss fraction was revised downward; however, uncertainties exist due to the fact that it has not been possible to directly measure the fraction of solids removed from an ablating graphite surface.

Ablation performance prediction models include a provision for thermomechanical mass loss. The conservation of mass and energy equations for the ablating surface allow solid as well as vapor to convect through the boundary. However, it is assumed that neither the surface nor the boundary layer phenomena are affected by the solid particles (Ref 9 & 16).

The objectives of this research are to perform an ablation experiment in which a controlled amount of solid material is released from an ablating surface, and to improve existing thermomechanical ablation models.

This dissertation contains a derivation of the approximate ablation theory which was used to select solid carbon dioxide (CO_2 or dry ice) from among various candidates for the experiment. The construction and testing of both pure CO_2 and glass bead- CO_2 models are described. Following a presentation of experimental results, improvements in the thermomechanical theory, including the effects of nonequilibrium sublimation, diffusion wells, and microscale heat transfer events, are developed and discussed.

II. Simplified Ablation Model

The primary purpose of this chapter is to present the approximate ablation theory as applied to a simplified model of a subliming surface including thermomechanical ablation. The other analytical relations needed to determine ablation rates are also presented. A prediction of the simplified theory is then compared to that of a more exact solution.

The heat and mass transfer fluxes are shown schematically in Figure 1. The coordinate system is fixed to the solid-gas interface. The system is assumed to have only two components: the subliming substance and the surrounding gas, "air." The system is analyzed at a fixed location of the streamwise coordinate.

The overall mass flux of the system is described by the equation

$$(\rho v)_w + \dot{m}^* = \dot{m}_T \quad (1)$$

where \dot{m}_T is the total mass flux coming to the surface, \dot{m}^* is the mass flux which leaves the surface in the solid phase, and $(\rho v)_w$ is the normal mass flux of the gas phase. If \dot{m}_T is partitioned into the amount which leaves the surface as a solid, \dot{m}^* , and the amount which vaporizes, \dot{m} , the overall mass conservation equation reduces to

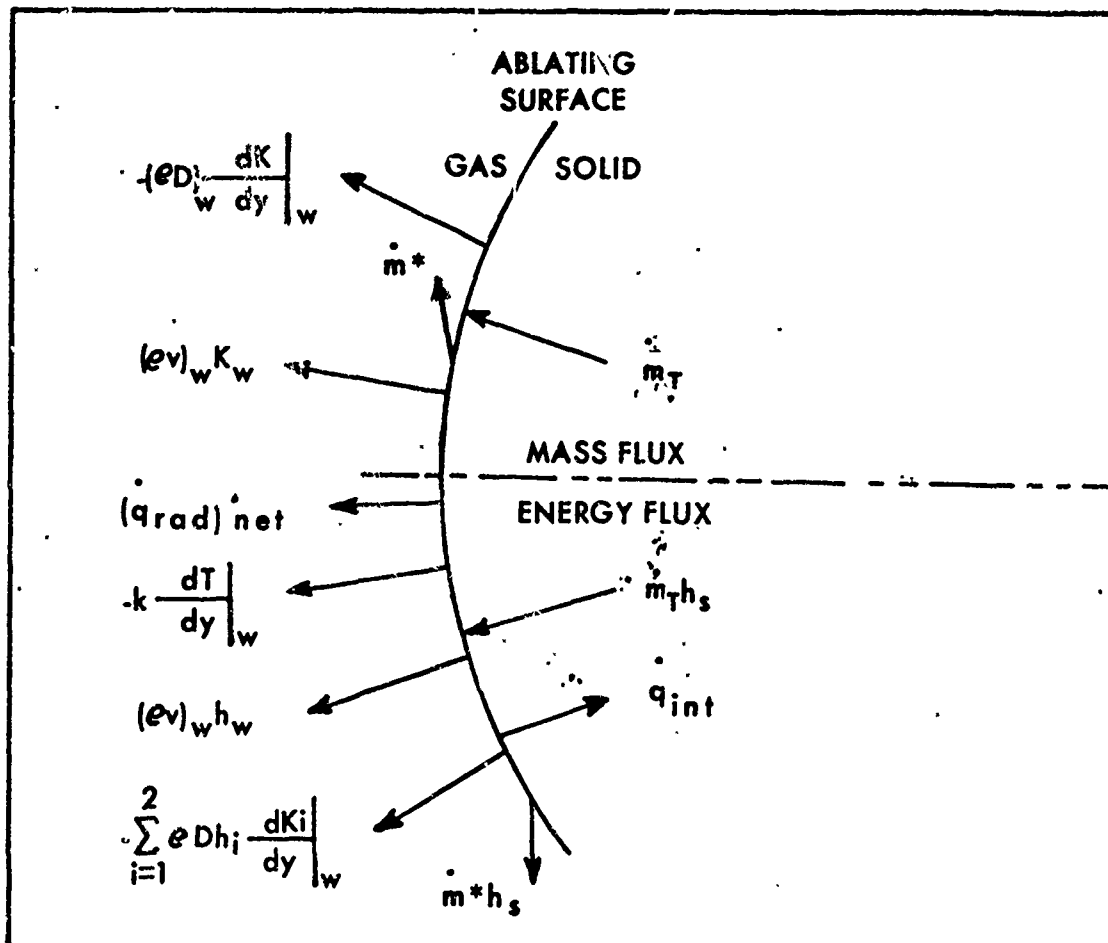


Figure 1. Thermochemical - Thermomechanical Ablation Process

$$(\rho v)_w = \dot{m} \quad (2)$$

The mass flux of the vaporized material is usually partitioned into convected and diffused portions. The convected portion is expressed as the mass fraction of the subliming substance at the wall, K_w , times the normal mass flux of the gas phase at the wall. The expression for the diffused portion is derived from Fick's Law--the diffused flux is proportional to the concentration gradient. Therefore, the conservation of mass equation for the material which vaporizes is

$$(\rho v)_w K_w - (\rho D \frac{\partial K}{\partial y})_w = \dot{m} \quad (3)$$

The equation is further simplified by the substitution of $(\rho v)_w$ from Equation (2) into Equation (3) and by rearrangement.

$$\dot{m} (1 - K_w) = - (\rho D \frac{\partial K}{\partial y})_w \quad (4)$$

The energy flux of the system is described by the equation

$$\begin{aligned} (\dot{q}_{\text{rad}})_{\text{net}} - (k \frac{\partial T}{\partial y})_w - \sum_{i=1}^2 (\rho D h_i \frac{\partial K_i}{\partial y})_w + (\rho v)_w h_w \\ + \dot{m}^* h_s + \dot{q}_{\text{int}} = \dot{m}_T h_s \end{aligned} \quad (5)$$

where the first term is the net flux of heat transferred by radiation, the second term is the classical conductive term, expressed by Fourier's Law applied to the gas phase, the third term is the enthalpy carried by the diffused portion of the gas phase mass flux, and the fourth term is the amount carried by the convected portion. The amount of mass which leaves the surface in the solid phase is assumed to have the same enthalpy as that of the solid coming up to the surface, h_s (Ref 10 & 16). The fifth term is the amount of heat conducted into the interior. Subtracting $\dot{m}^* h_s$ from each side of the equation, the energy equation becomes

$$\begin{aligned} (\dot{q}_{\text{rad}})_{\text{net}} - \left(k \frac{\partial T}{\partial y}\right)_w + \sum_{i=1}^2 (\rho D h_i \frac{\partial K_i}{\partial y})_w \\ + (\rho v)_w h_w + \dot{q}_{\text{int}} = \dot{m} h_s \end{aligned} \quad (6)$$

Thus, by partitioning the total mass flux into the amount which is vaporized and that which is not, the equations for a system with thermomechanical ablation are transformed into the same equations which describe a system with pure thermochemical ablation: Equations (2), (3), (4), and (6). This is an important result in that the development which follows applies to either pure thermochemical ablation or combined thermochemical - thermo-mechanical ablation provided that the term \dot{m} is restricted to that portion of the mass flux which is vaporized at the surface. This result also applies to the more complicated ablation process of graphite (Ref 16), and is the basis of

the thermomechanical ablation experiment of this research. Simply stated, the existing heat and mass transfer theory associated with thermomechanical ablation predicts that the response of the vaporizing material does not depend on the amount of thermomechanical ablation in progress.

To simplify the following development, the radiative heat flux term and the internal heat conduction term are assumed to be negligible relative to the other terms and are eliminated from the analysis. Further simplification of the energy equation results from the assumption that the Lewis number is one. The Lewis number is defined as the ratio of the mass diffusivity to the thermal diffusivity.

$$Le = \frac{D}{k/\rho C_p} \quad (7)$$

The quantity is often close to one for many mixtures of interest. When the Lewis Number equals unity, the heat conduction and the summation of the diffusion enthalpy flux terms of Equation (6) combine into the single term $(\frac{-k}{C_p} \frac{\partial h}{\partial y})_w$. This combination is derived in Chapter V. The energy equation then reduces to

$$\dot{m}(h_w - h_s) = (\frac{k}{C_p} \frac{\partial h}{\partial y})_w \quad (8)$$

At this point it is convenient to replace the term with the derivative by a transfer coefficient times a driving potential. The most convenient coefficient for the

heat and mass transfer problem is the Stanton number, defined by the equation

$$C_H = \frac{\left(\frac{k}{C_p} \frac{\partial h}{\partial y}\right)_w}{\rho_e u_e (h_r - h_w)} \quad (9)$$

where h_r is the recovery enthalpy. Substitution into Equation (8) yields

$$\dot{m}(h_w - h_s) = \rho_e u_e C_H (h_r - h_w) \quad (10)$$

The similarity of Equations (4) and (8) suggests that a transfer coefficient approach might also be useful in Equation (4). In fact, with no chemical reactions, and when the Prandtl and Lewis numbers equal unity, the boundary layer solutions to the concentration and energy equations are similar, which will be shown in Chapter V. With similarity the identical transfer coefficient can be used for mass transfer with the concentration difference replacing enthalpy difference as the driving potential. The Stanton number for mass transfer is

$$C_H = \frac{(\rho D \frac{\partial k}{\partial y})_w}{\rho_e u_e (K_e - K_w)} \quad (11)$$

Substitution of C_H from Equation (11) into Equation (4), with $K_e = 0$, yields

$$\dot{m} = \frac{K_w}{1 - K_w} \rho_e u_e C_H \quad (12)$$

Equation (10) is still somewhat difficult to use since the enthalpy of the gas at the wall is a function of concentration and temperature. For the two species, (1) the subliming substance and (2) "air", the enthalpy at the wall is

$$h_w = K_w h_{1w} + (1-K_w) h_{2w} \quad (13)$$

Substitution of h_w from Equation (13) into (10) yields

$$\begin{aligned} \dot{m} [K_w h_{1w} + (1-K_w) h_{2w} - h_s] = \\ \rho_e u_e C_H [h_r - K_w h_{1w} - (1-K_w) h_{2w}] \end{aligned} \quad (14)$$

Using Equation (12), the terms of Equation (14) can be regrouped such that all terms relating to the enthalpy of the subliming material are on the left and all the terms relating to the enthalpy of the air are on the right.

$$\dot{m} (h_{1w} - h_s) = \rho_e u_e C_H (h_r - h_{2w}) \quad (15)$$

The enthalpy difference on the left is simply the enthalpy of sublimation, Δh_{sub} .

Finally, the nondimensional mass transfer parameter B' is defined by the equation

$$B' = \frac{\dot{m}}{\rho_e u_e C_H} \quad (16)$$

Substitution of B' into Equations (12) and (15) and rearrangement yields

$$B' = \frac{K_w}{1 - K_w} \quad (17)$$

$$B' = \frac{h_r - h_{2w}}{\Delta h_{\text{sub}}} \quad (18)$$

Assuming that the gas at the wall can be modeled as a mixture of ideal gases, Equation (17) can be expressed in terms of the partial pressure of the subliming material.

$$B' = \frac{M_1}{M_2} \frac{P_{1w}/P}{1 - (P_{1w}/P)} \quad (19)$$

Where: M = Molecular weight

P_{1w} = Partial pressure of subliming specie at the wall

P = Mixture pressure

If the vapor of the subliming specie is assumed to be in equilibrium with the solid phase, the partial pressure is the equilibrium vapor pressure which is a function of the wall temperature.

With this system of equations, a unique value of T_w and B' can be determined when h_r , P , and the thermochemistry of the system are specified. The solution of these equations can be obtained graphically by assuming various values of wall temperature and plotting B' from Equations (18) and (19). Ablation response plots are shown in Figure 2. The equilibrium vapor pressure of a material is often correlated in the form

$$\log_{10}(p) = (-0.2185 A/T) + B \quad (20)$$

where p is the vapor pressure in Torr and T is the temperature in degrees Kelvin (e.g. The Handbook of Chemistry and Physics). The Clapeyron equation relates the enthalpy of evaporation or sublimation to the equilibrium vapor pressure--temperature relation. Equation (20) is conveniently arranged so that the constant A is the molal heat of sublimation ($\Delta h_{\text{sub}}/M_1$). Equations (18), (19), and (20) can be solved by an iterative process.

Once B' and T_w have been determined, two corrections must be applied to conventional heat transfer results before mass flux can be determined. First, the Stanton number, which is based on the actual heat transferred to the ablating body, must reflect the reduction in heat transfer due to blowing. Gazley, Gross, and Masson (Ref 5) reported Equation (21), a correlation of theoretical results for the ratio of Stanton number without mass addition to the boundary layer, C_{H_0} , to that with mass addition.

$$\frac{C_{H_0}}{C_H} = 1 + 0.64 \left(\frac{M_2}{M_1}\right)^{1/3} B' \quad (21)$$

The equation compares well with experiment, especially for low B' values.

Second, the results of the simplified heat and mass transfer equations must be corrected for the assumption of unit values for the Lewis and Prandtl numbers. Analysis

and experiment have shown that moderate departures from unity are adequately accounted for by adjustment of the transfer coefficient. Kays (Ref 8) suggests the following Lewis number correction to the heat transfer Stanton number for mass transfer application:

$$\frac{(C_H) \text{ Mass Transfer}}{(C_H) \text{ Heat Transfer}} = (Le)^{2/3} \quad (22)$$

In summary, the mass loss is estimated by the following procedure:

- 1) B' and T_w are determined upon specification of the environmental conditions and the subliming material using a plot or by otherwise solving Equations (18) and (19).
- 2) C_{Ho}/C_H is determined from Equation (21).
- 3) C_{Ho} is determined through conventional heat transfer techniques. Since T_w has been determined, reference temperature methods can be used for properties.
- 4) Finally

$$\dot{m} = (\rho_e c_e C_{Ho})(C_H/C_{Ho})(Le)^{2/3} B' \quad (23)$$

This simple theory provided the information necessary to design a sublimation experiment; however a verification of its accuracy was required before it could be used to evaluate experimental results. The more exact solution was obtained using the Boundary Layer Integral Matrix Procedure (BLIMP) written by Bartlett and Kendall (Ref 2). The BLIMP solution is described in Appendix A. It includes

the mass transfer prediction for the entire hemispherical forebody, and takes into account the individual air species, and unequal diffusion coefficients. A comparison of the simple theory and BLIMP for an axisymmetric stagnation point for the approximate conditions of the experiment performed in this research is shown in Table I. In this case, the unity Lewis number assumption has not only simplified the derivation, but also provided very accurate predictions for the ablation response. The boundary layer is assumed to be laminar.

Table I

Comparison of BLIMP and Simple Theory Predictions for an Axisymmetric Stagnation Point

	<u>BLIMP</u>	<u>APPROXIMATE</u>	<u>DIFFERENCE</u>
T_w (K)	181	172	-5.0%
B'	0.193	0.192	-0.5%
$\rho_e u_e C_{Ho}$ ($\text{kg}/\text{m}^2 \cdot \text{s}$)	0.262	0.268	2.3%
C_{Ho}/C_H	1.094	1.107	0.9%
$\rho_e u_e C_H$ ($\text{kg}/\text{m}^2 \cdot \text{s}$)	0.239	0.242	1.3%
\dot{m} ($\text{kg}/\text{m}^2 \cdot \text{s}$)	0.0461	0.0465	0.9%

III. Experiment

An experiment was performed which provided a direct comparison of ablation with and without solid mass addition to the boundary layer. This chapter contains the rationale used in the selection of a subliming material for the experiment, the method used in the fabrication of the models, a description of the experimental test facility, the experimental procedures, and the methods used in the reduction of the data.

Subliming Material and Environmental Conditions

The initial problem was to find a good combination of subliming material and environmental conditions for the experiment. Kubota's paper (Ref 11) was quite helpful in this regard since it contained graphs of ablation response as a function of environmental conditions for water ice, dry ice, and camphor which are summarized in Figure 2. A low turbulence subsonic free jet was chosen for the experiment because of its ease of operation and low cost. The free jet afforded open access to the model, which facilitated data acquisition. The conditions in the jet were ambient pressure and near 0°C temperature. With this environment, dry ice (solid CO₂) was chosen because it responded with a B' of nearly 0.2, which is high enough to yield sufficient mass transfer for experimental accuracy

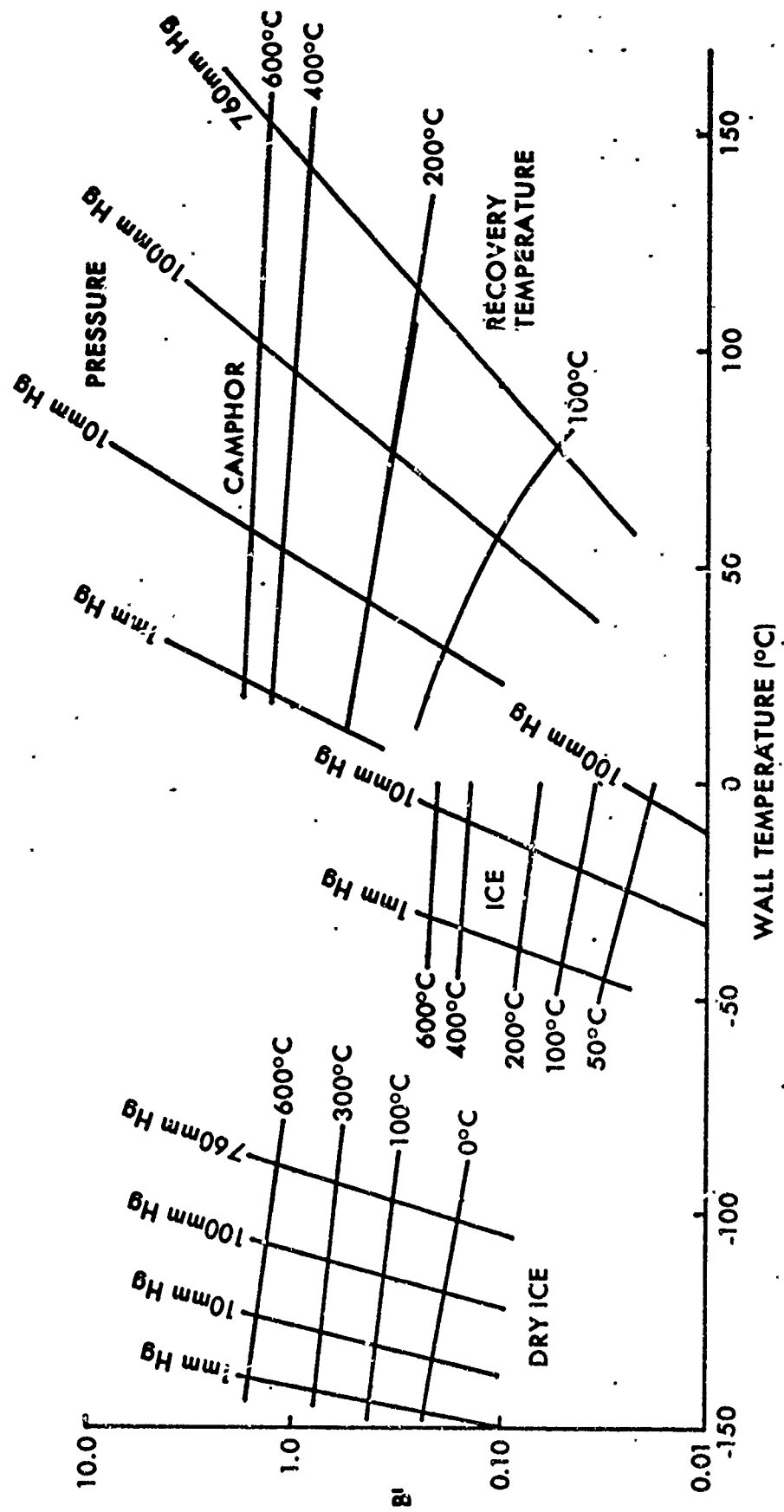


Figure 2. Ablation Response of Dry Ice, Ice, and Camphor (Summarized From Ref 11)

and is within the range of B' values experienced by graphite during reentry.

Axisymmetrical flow over a hemispherical forebody-cylindrical afterbody was chosen over a two-dimensional flow configuration for a more accurate determination of the shape change during the experiment. The potential flow solution for the selected shape is one of the many computed by A.M.O. Smith and Pierce and presented in Reference 22. Their computed velocity distribution merges into that for a sphere near the stagnation point as shown in Figure 3. Therefore, the stagnation point heat transfer coefficient for this geometry is identical to that of a sphere.

The experiment was performed at Mach numbers below 0.1 which further simplified the prediction of the ablation response. The pressure did not significantly vary around the body and the recovery air temperature was essentially constant and equal to the free stream air temperature. With constant environmental conditions, the simple equilibrium theory predicts a constant wall temperature and B' around the body, which further implies a constant ratio of C_H to C_{H_0} . The mass loss is then directly proportional to the heat transfer coefficient around the body as predicted by Equation (23). This conclusion was confirmed by BLIMP in that the predicted variation of wall temperature around the body was only 0.11K (0.065%) and the B' variation was only 0.0015 (0.78%).

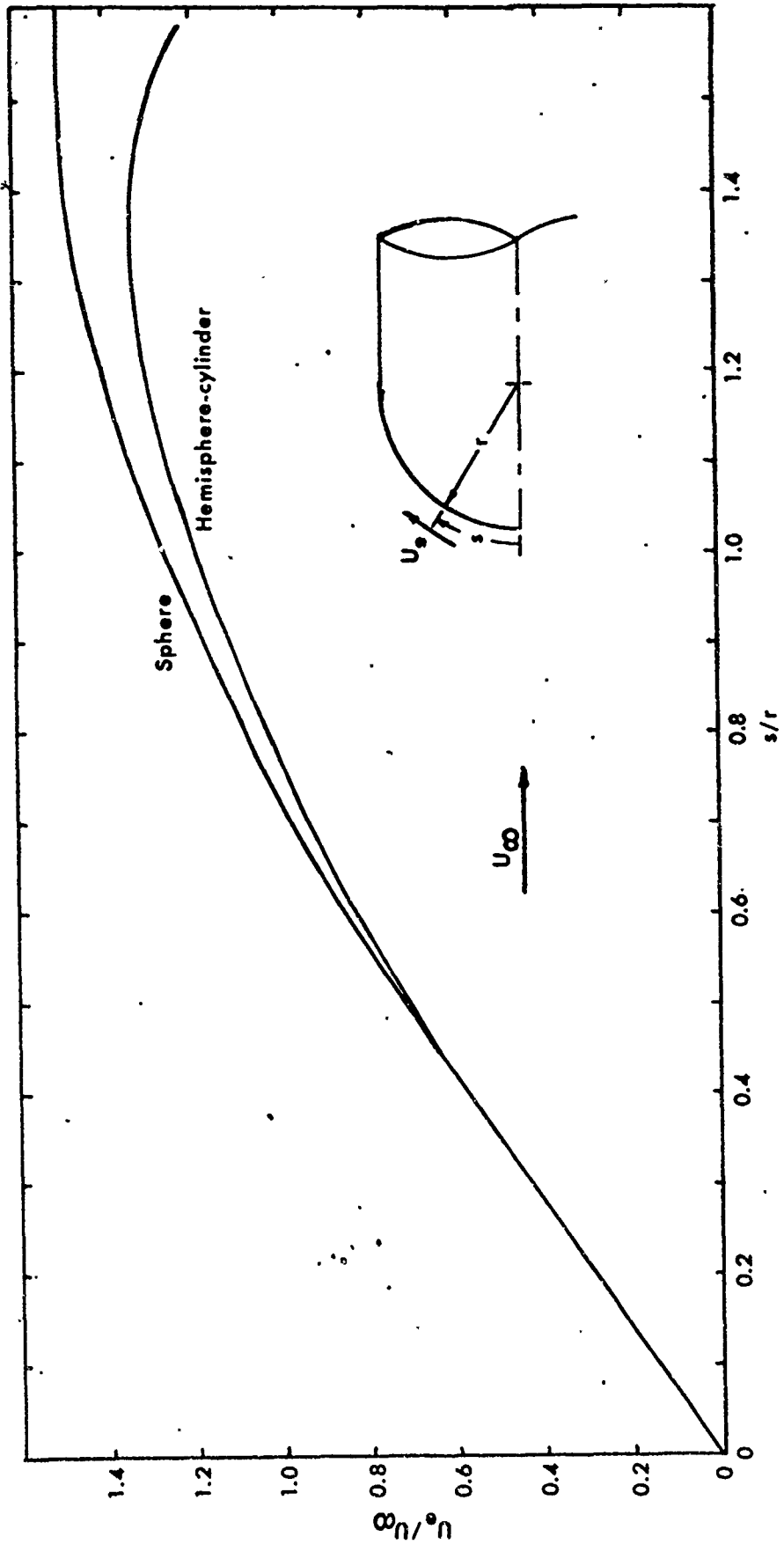


Figure 3. Boundary Layer Edge Velocity Normalized by Free Stream Velocity for a Sphere and a Hemisphere-Cylinder

Ablation Models

The 25 mm diameter models were produced in molds of two designs, which are shown in Figure 4. The first was made from seamless tubing with a welded end plug which had a hemispherical surface machined into it. A second mold was constructed of stainless steel tubing with a hemispherical surface machined into one of the threaded end plugs. The second design was much easier to construct. It facilitated the extraction of the frozen model, since both ends of the tube could be removed and the model pushed out. Both molds had a single entrance port for the introduction of carbon dioxide.

Thermomechanical ablation was simulated by dispersing glass beads in the CO_2 . Since the speculated size of the solid particles removed from ablating graphite was on the order of the stagnation point boundary layer thickness, the boundary layer thickness of this experiment dictated that 120 μm diameter beads be chosen. The beads were screened to improve size uniformity. The bead shape was fairly spherical as shown in the photomicrograph in Figure 5.

The most reliable method of obtaining a uniform dispersion of glass beads in the CO_2 was to fully pack the beads into the mold before introducing the CO_2 . All of the glass bead CO_2 ablation experiments were performed using the fully packed mode of glass bead loading. A plastic rod (also shown in Figure 4) was frozen into the center of each model to serve as a solid attachment point.

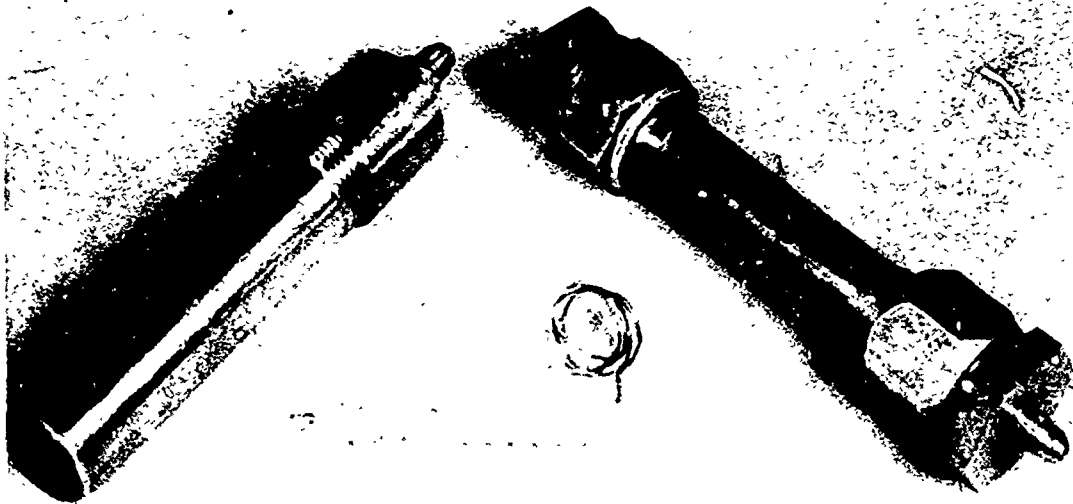


Figure 4. Ablation Model Molds and Center Rod with Thermocouple

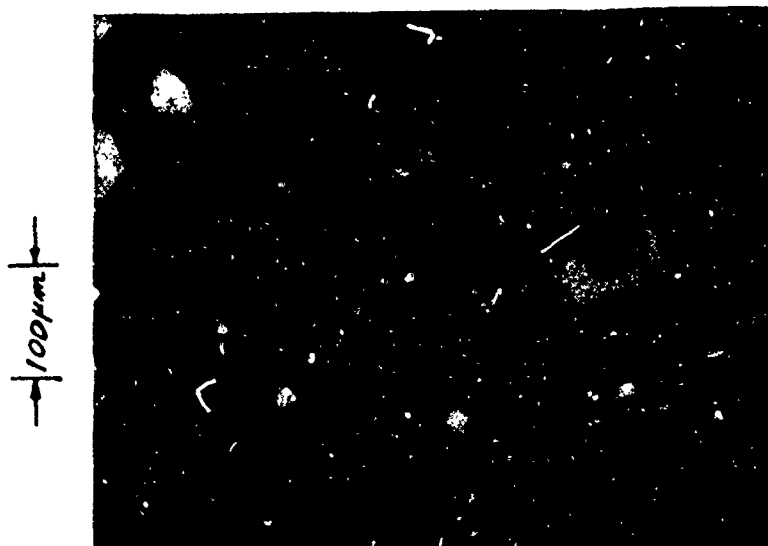


Figure 5. Glass Beads (150X)

The rod had a hole drilled along its axis, so that a thermocouple junction could be placed near the center of the hemispherical nose.

The glass bead and CO₂ composite models were quite sensitive to moisture. If any moisture was present, the beads tended to agglomerate during the experiment, forming a crust on the model surface. The following filling procedure was used to eliminate the moisture. The mold was filled with preheated beads, then maintained at 360 K in an oven for at least one hour. The hot mold was then attached to a system for introducing CO₂ into the mold which is shown in Figure 6.

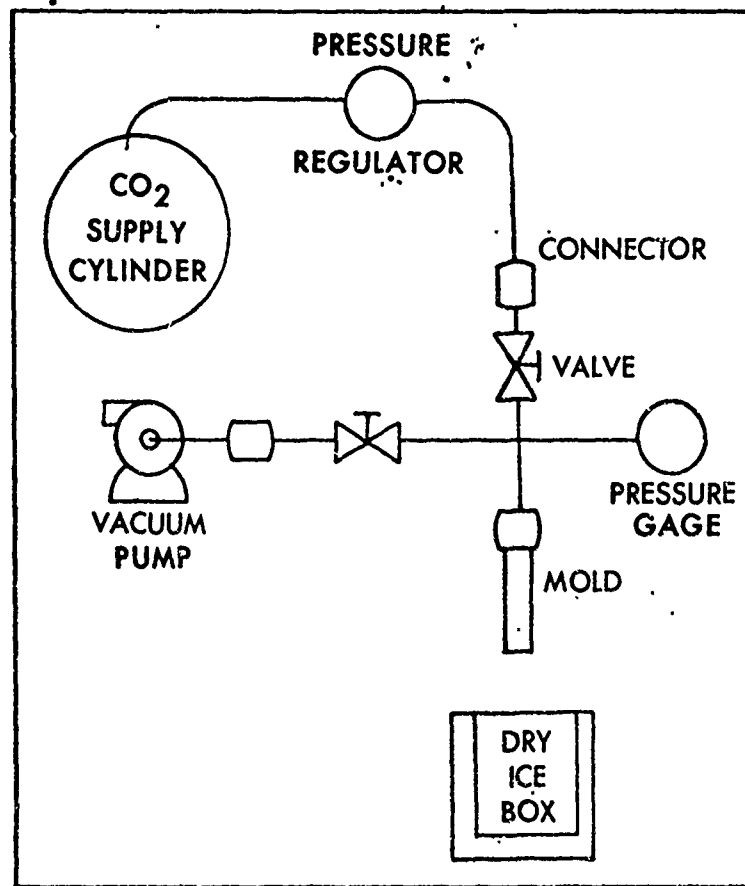


Figure 6. System for Producing Ablation Models

A vacuum pump attached to the fixture maintained a very low pressure in the mold while it was cooling. When cool, the mold was placed in an insulated container and packed with dry ice. The system was then pressurized with CO_2 to approximately 14 atm. The CO_2 pressure was maintained for several hours, typically overnight, then the regulator was closed. Within five hours the pressure in the mold decreased to slightly above atmospheric pressure, as the remaining CO_2 vapor solidified.

Experimental Test Facility and Procedures

A free jet built for an Air Force Institute of Technology aeroacoustic study (Ref 14) supplied dry, very low turbulence air to the models. The jet exit was 102 mm x 76 mm. The model size and placement were consistent with aerodynamic testing standards required to simulate free flight through still air. The jet and model are shown in Figure 7.

Measurements were made of tunnel plenum temperature and pressure, ambient pressure, and the model internal temperature and shape as a function of time. Plenum pressure was measured using a precision manometer. The output of the thermocouple inside of the model was recorded by a continuous strip chart recorder. Model shape as a function of time was obtained from 35 mm photographs of the model with a stop watch and reference scale in the field of view. Typical photographs of pure CO_2 and composite models are shown in Figure 8. The models, positioned in front of

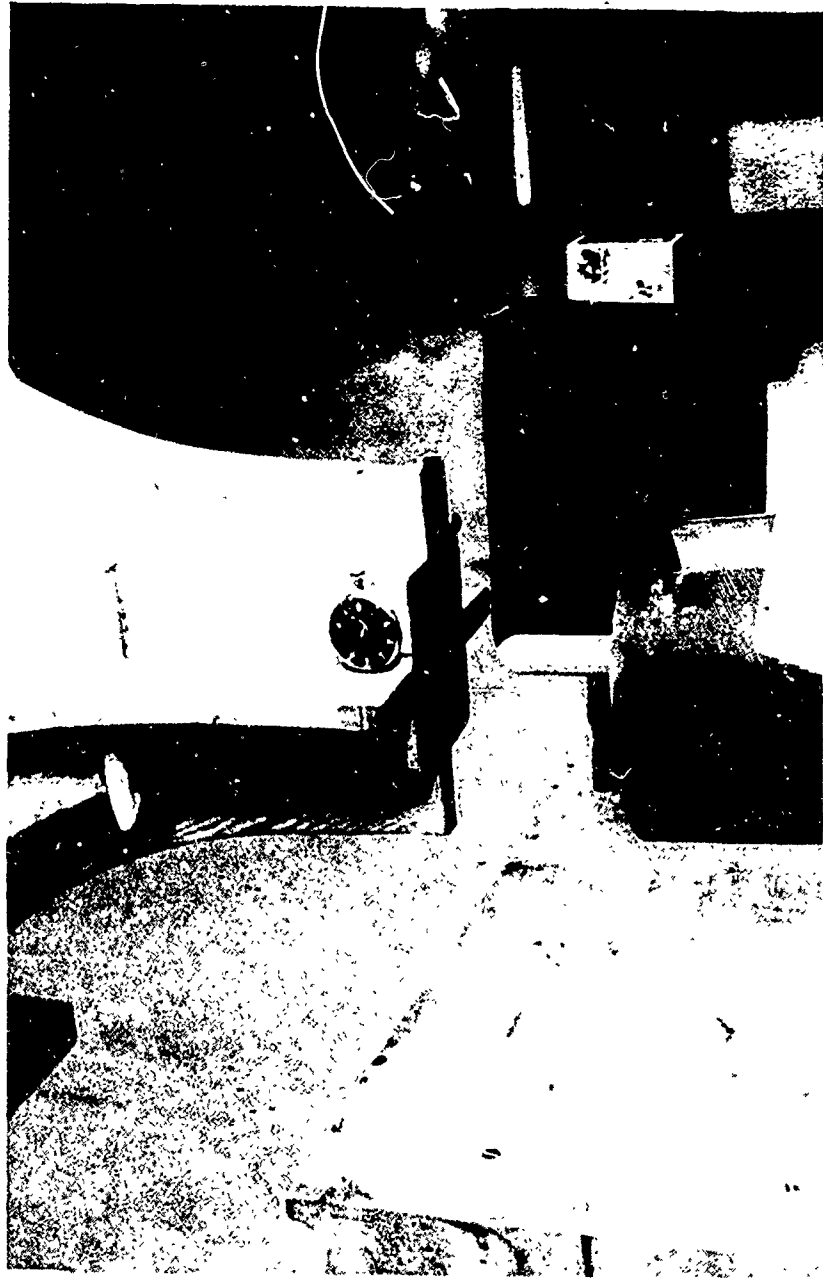


Figure 7. Free Jet and Ablation Model

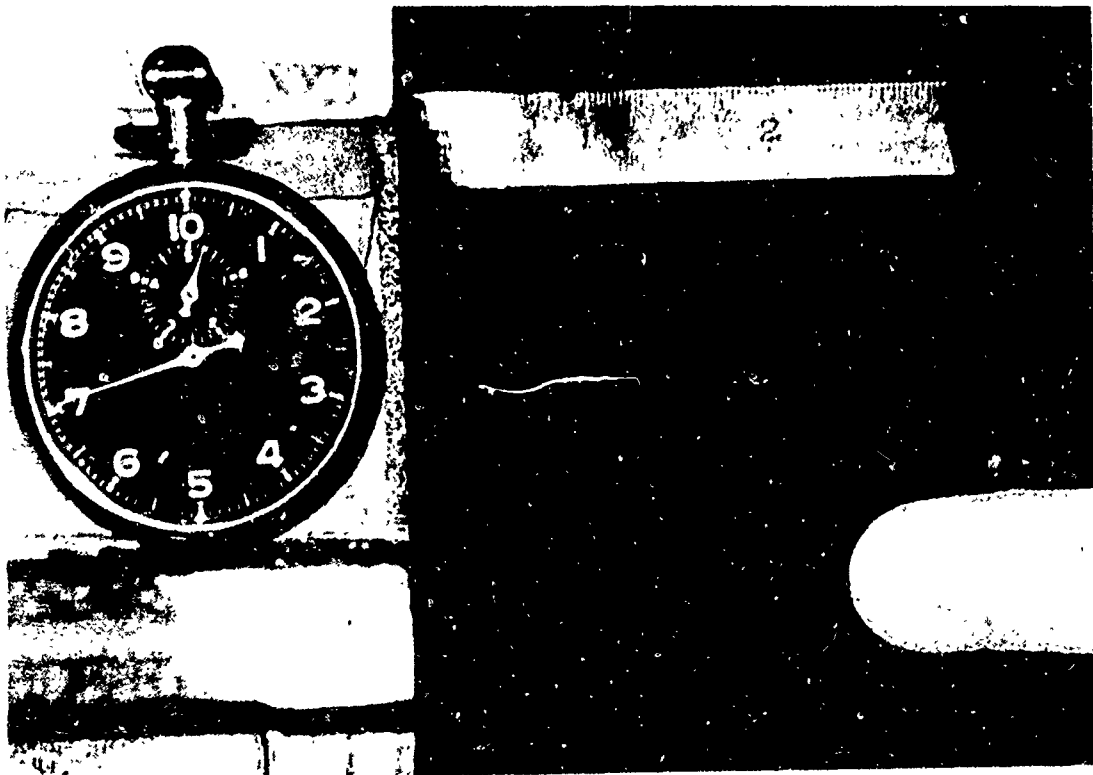
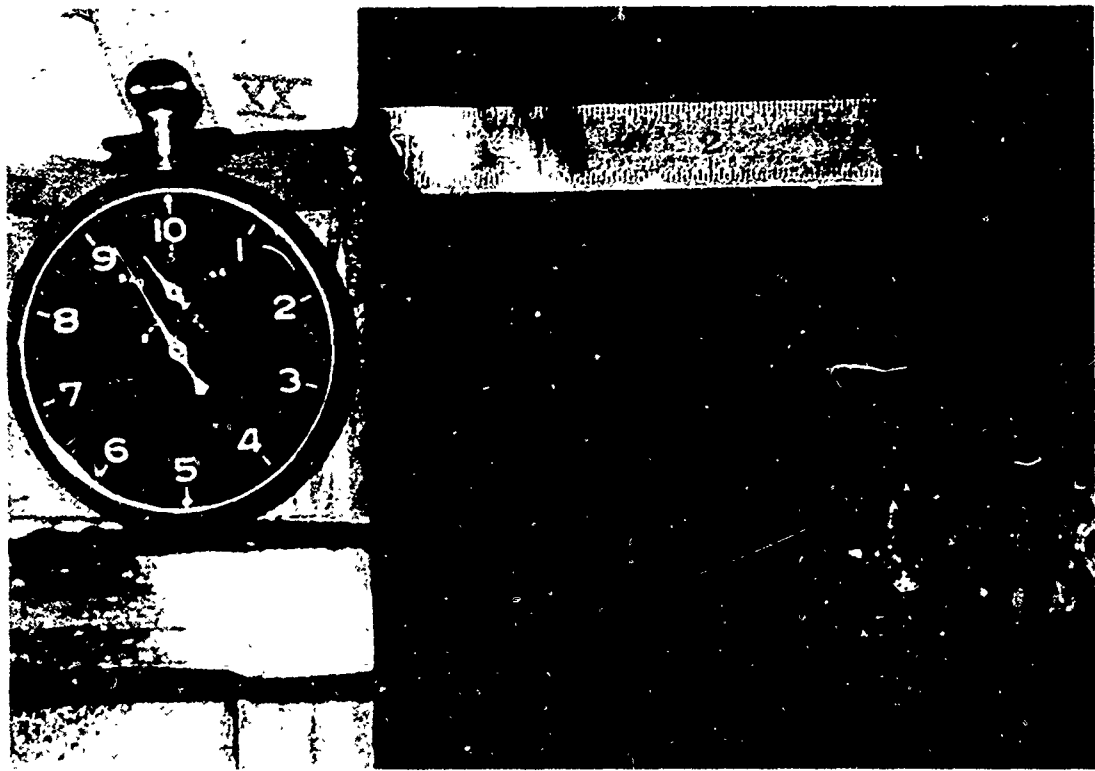


Figure 8. Data Photograph of Model, Stopwatch, and Reference Scale Taken Early in Test. (Top--Pure CO₂, Bottom--Composite)

a flat black background, were front lighted by a strobe flash attached to the camera. The camera was a Mamiya/Sekor 1000 TL with a 270 mm lens. With this system the camera could be positioned about two meters from the model to eliminate parallax.

Air was introduced into the tunnel at the desired flow rate and the ambient conditions were recorded. When tunnel temperature and pressure stabilized, they were recorded. Then the pressure was vented from the mold, the mold was opened, and the model was extracted. The model was attached to the support system while positioned out of the jet and the thermocouple wires were connected to the recorder system. The support was then swung into the jet and locked into position on the jet centerline. Pictures were taken at approximately ten second intervals until the surface receded to the embedded thermocouple.

Data Reduction

All of the data required to determine surface recession rate are contained on the 35 mm film. Each frame was projected onto a light table by a precision film reader and the distance reference and surface profile were traced. A typical set of recession profiles is shown in Figure 9. The complete set of recession profiles is contained in Appendix B.

The conversion of the recession profiles to local recession rates around the hemispherical surface was facilitated by the use of an HP 9820A Calculator with an

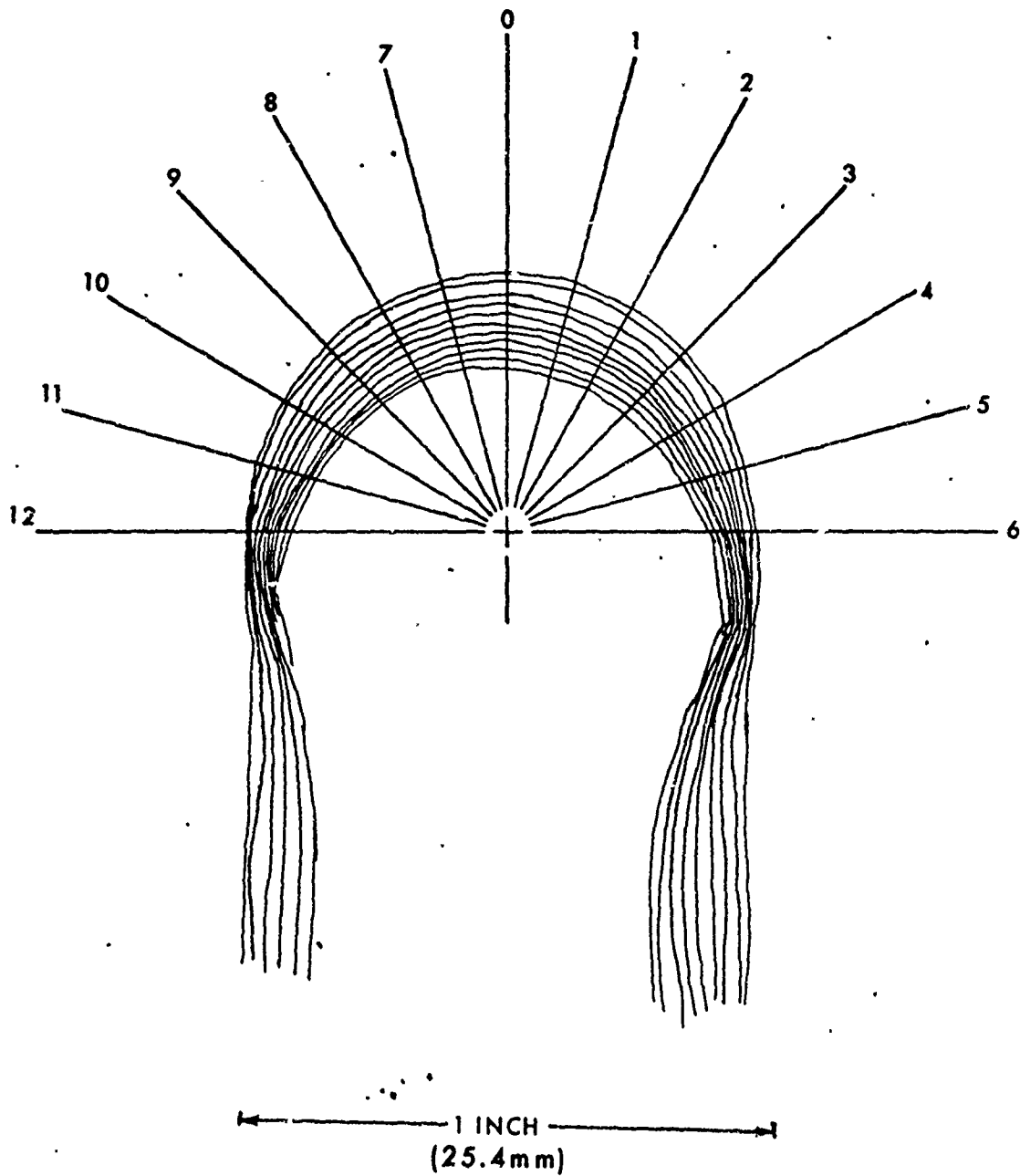


Figure 9. Typical Set of Recession Profiles

input digitizer and an output plotter. Of primary interest was the normal recession of the stagnation region while the surface was still essentially hemispherical. In preparation for the data reduction, the recession profile trace was placed on the digitizer and the center of curvature of the front surface was determined with the aid of an overlay of concentric circles. A protractor was then placed over the recession trace with its axis on the center of curvature and with the center ray (labeled zero) perpendicular to the nozzle exit plane as shown in Figure 9. The radii of the protractor are 15 degrees apart.

After entering the time associated with each profile trace, the recession along each radius was digitized. As each point was digitized, the location was stored, the location and time for that point were plotted, and the point was numbered on the plot. The calculator referenced all distances to the first point digitized and all times to the time associated with the first profile. After each point along the ray was digitized, points were selected to include in a least squares linear curve fit. The equation of the line was then printed and the line was plotted on the recession trace through the range of interest. The recession rate is the slope of the curve. Two typical recession plots are shown in Figure 10. The essentially constant stagnation point recession rate shown in the top plot is a result of the compensating factors of decreasing model diameter and increasing nose bluntness. In the

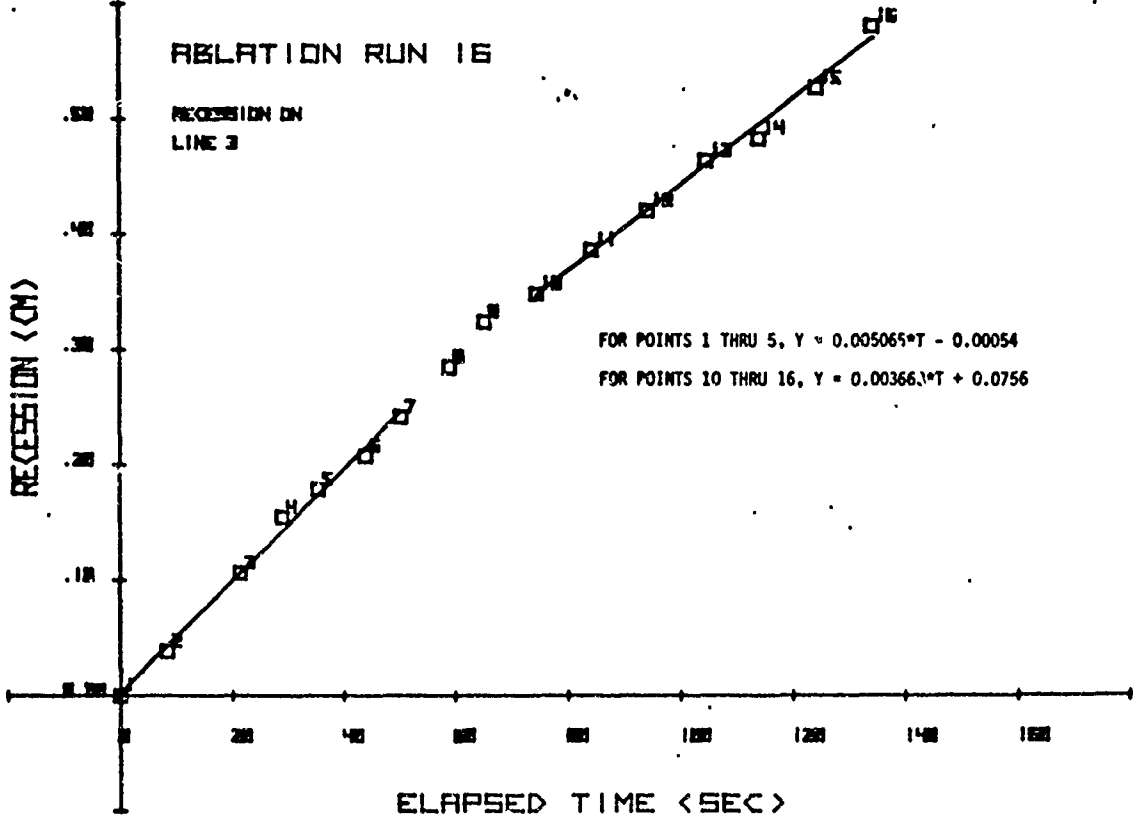
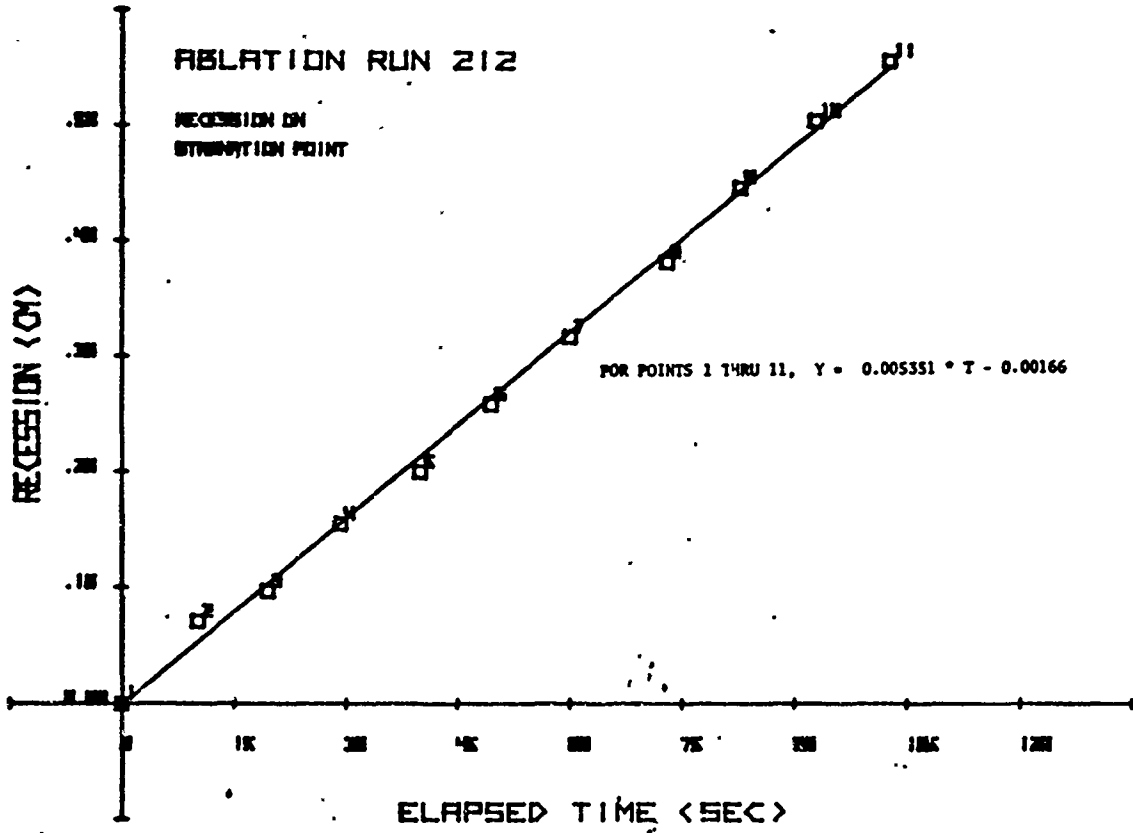


Figure 10. Typical Recession Plots

second plot, the curve indicates an initial rate, associated with the hemispherical shape, which decreases as model shape change decreases the transfer coefficient. All of the recession plots are contained in Appendix B.

The carbon dioxide mass loss rate is related to the normal recession rate, \dot{s} , by the equation $\dot{m}_{CO_2} = \rho_{CO_2} \dot{s}$.

The density of solid CO_2 in the temperature range of interest was determined by Maass to be 1.60 Mg/m^3 (Ref 15). For the glass bead CO_2 mixture, the density of each constituent was determined by measuring the increase in weight of the mold after addition of the glass beads, then after CO_2 solidification. The center rod was not used in the five models especially fabricated for density determination. The density of glass in the mixture was $1.48 \pm 0.02 \text{ Mg/m}^3$ of mixture and the density of the composite was $2.09 \pm 0.03 \text{ Mg/m}^3$. Therefore, the density of the CO_2 was $0.61 \pm 0.05 \text{ Mg/m}^3$ of mixture.

Experimental Conditions and Physical Properties

The range of experimental conditions and physical properties of the experimental materials are listed in Table II. The glass bead- CO_2 composite thermal properties are based on the properties of the constituents. Since the conductivities of the materials are nearly identical, the effective conductivity of the composite is essentially that of the continuous phase, CO_2 , $0.71 \text{ W/m}\cdot\text{K}$ (Ref 7). The

density of the composite was determined to be 2.09 Mg/m^3 . By adding the mass weighted contribution of the specific heat of each material, the specific heat of the composite is determined to be $0.92 \text{ kJ/kg}\cdot\text{K}$. The effective thermal diffusivity of the composite is, therefore, $0.37 \text{ mm}^2/\text{s}$. This result is quite fortuitous, since, with nearly identical thermal conductivity and diffusivity, the pure CO_2 models and the composite models respond essentially the same in both transient and steady state conduction.

Table II

Range of Experimental Conditions
and Model Component Properties

MODEL RADIUS (mm)	10.0 - 12.7		
VELOCITY (m/s)	18.6 - 38.3		
AIR TEMPERATURE (K)	270 - 282		
PRESSURE (atm)	0.957 - 0.980		
REYNOLDS NUMBER Re_R	19,500 - 32,400		
$\rho_e u_e C_H$ (kg/m ² ·s)	0.21 - 0.33		
PRANDTL NUMBER Pr^*	0.735		
LEWIS NUMBER Le^*	0.886		
SCHMIDT NUMBER Sc^*	0.829		
SOLID PROPERTIES AT 170K	<u>CARBON DIOXIDE</u>	<u>GLASS</u>	<u>COMPOSITE</u>
DENSITY (Mg/m ³)	1.60 (15)**	2.7 (4)	2.09
THERMAL CONDUCTIVITY (W/m·K)	0.71 (6)	0.79 (4)	0.71
SPECIFIC HEAT (kJ/kg·K)	1.2 (15)	0.84 (4)	0.92
THERMAL DIFFUSIVITY (mm ² /s)	0.38	0.35	0.37
MASS FRACTION IN COMPOSITE	0.29	0.71	
ENTHALPY OF SUBLIMATION (kJ/kg)	589.1 (6)		
CO ₂ VAPOR PRESSURE	$\log_{10} P$ (atm) = -1352.4/T(K) + 6.9576 †		

* At Eckert's reference temperature (approximately 222K)

** Number in parenthesis is the reference number

† This correlation is based on the enthalpy of sublimation at 170 K and the vapor pressure data reported in Reference 6.

IV. Experimental Results

The mass loss results for the pure CO₂ models are shown in Figure 11. The data have been normalized by the stagnation point mass flux predicted by BLIMP, adjusted to the particular conditions of the experiment by the approximate theory presented in Chapter II. The normalized BLIMP distribution is also shown. Except for the stagnation point value, each data point shown is the average of the values on either side of the stagnation point. The results are in fair agreement with the predicted results; although on the average, the experimental values are less than predicted, -6.5% less at the stagnation point.

The normalized carbon dioxide mass transfer results of the glass bead laden models are shown in Figure 12. The average stagnation point carbon dioxide mass loss rate was 28% less than the amount predicted by the approximate theory, or 23% less than the experimentally observed mass loss rate of the pure carbon dioxide models. The distribution of mass loss around the hemisphere was different from the pure CO₂ results in that the mass loss rate did not decrease until beyond the 45 degree location. The mass loss data for these models also exhibited more scatter, which can be attributed, at least in part, to the variation of the CO₂ mass fraction in the composite models.

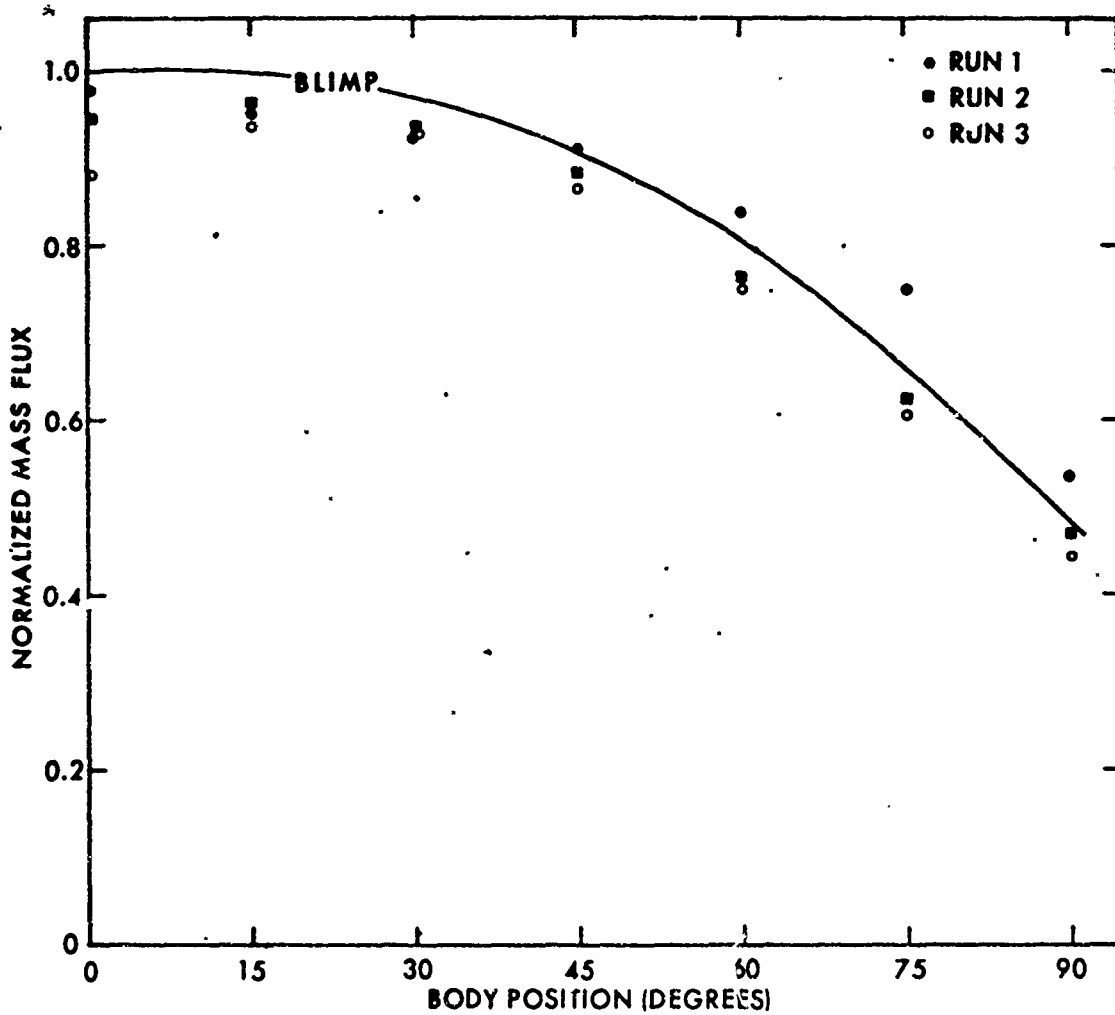


Figure 11. CO₂ Mass Loss--Experimental Data From Pure CO₂ Models and Theoretical Prediction--All Normalized by Theoretical Stagnation Point Mass Loss

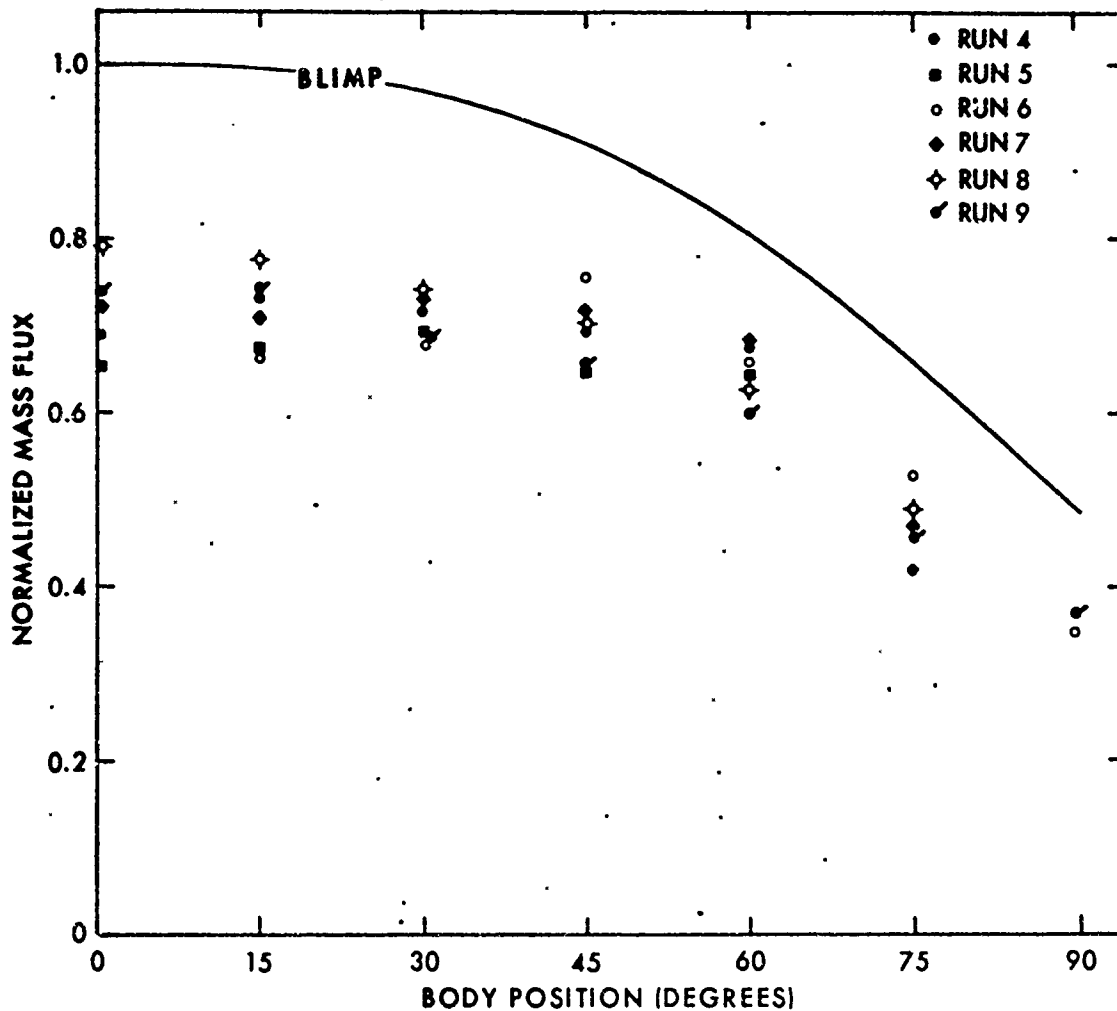


Figure 12. CO₂ Mass Loss--Experimental Data From Composite Models and Theoretical Prediction--All Normalized by Theoretical Stagnation Point Mass Loss

The thermal response, as sensed by the embedded thermocouple, of all models can be divided into three periods. Referring to the labels on the example temperature trace shown in Figure 13, there was a period of decreasing temperature (A to B), a period of approximately constant temperature, referred to as the asymptotic temperature (B to C), and a period of increasing temperature (C to the end of the test). The initial temperature drop is an indication that the temperature of the dry ice packed container in which the mold was placed while the model was solidifying was higher than the equilibrium wall temperature during the convective heat and mass transfer process. The increase in temperature indicates a response to possible thermal gradients near the surface and, upon exposure, the warmth of the air stream.

In a few experiments, the thermocouple data was obviously erroneous, in others, the mass loss data was useless because of flaws in the model, yet the temperature data was acceptable. A table of asymptotic temperatures is included in Appendix B. Of three experiments with pure CO₂, the mean asymptotic value was 179.3 K. Of ten experiments with composite models, the mean asymptotic value was 182.1 K.

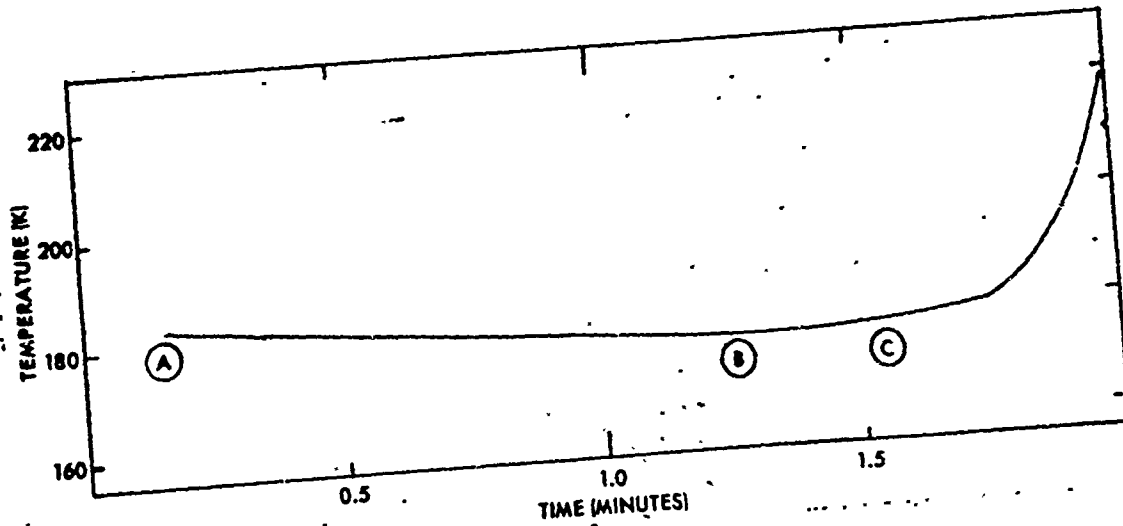


Figure 13. Typical Internal Temperature Record

V. Ablation of the Composite Material

The addition of nonsubliming material to the CO_2 had a significant effect on the observed mass transfer from the model. A change in mass transfer could be attributed to a change in either the transfer coefficient, $\rho_e u_e C_H$, or the driving potential, B' . Had the reduction in mass loss been solely the result of a reduced transfer coefficient, no change in model temperature would be expected. The slightly higher model temperatures associated with the composite material and the high percentage of nonsubliming material dictated that a more thorough analysis of the ablating surface be performed.

Inspection of the enlarged speculated model of the surface shown in Figure 14 suggests items for consideration. First, the wall will most certainly be rough rather than smooth. On a discrete level, the raised glass bead surface probably receives more heat flux than the lower CO_2 surface, especially considering the fact that the CO_2 is outgassing, while the glass is not. The glass beads affect the mass transfer of the CO_2 by constricting the surface area available for sublimation, which causes a higher local mass transfer rate at the subliming surface. The presence of the beads also caused the CO_2 vapor to diffuse through wells between the beads to the boundary layer.

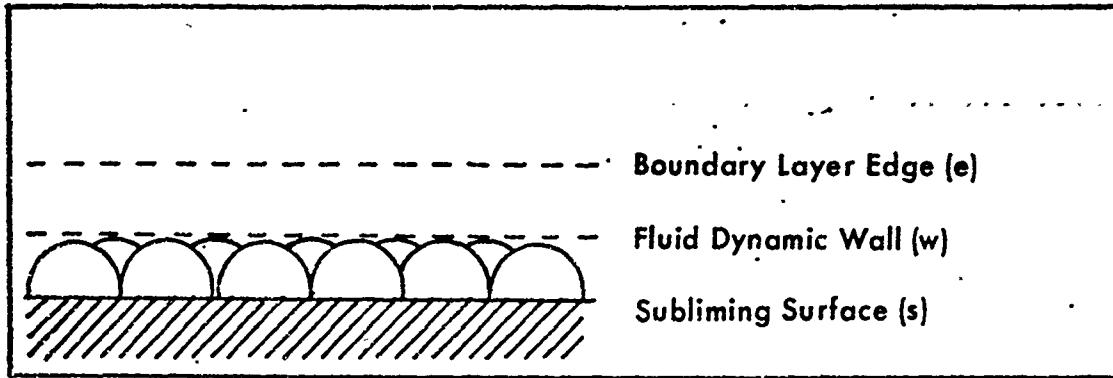


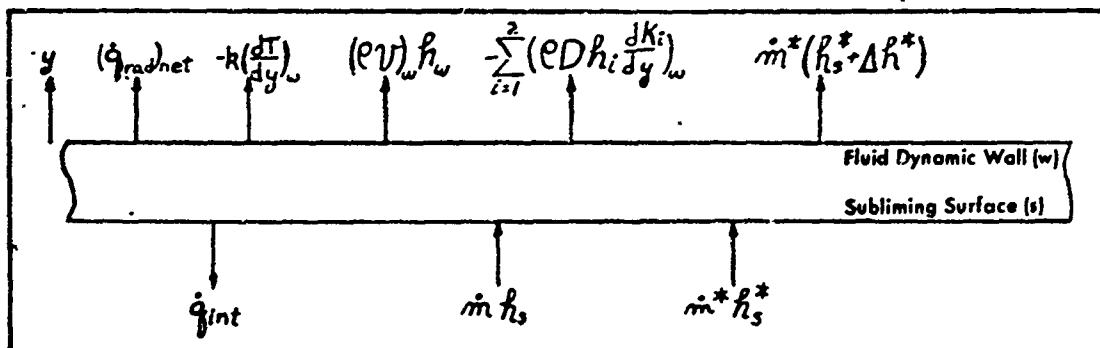
Figure 14. Model of Ablating Glass Bead - CO_2 Surface

In this chapter the heat and mass transfer equations which were presented in simplified form in Chapter II are reexamined with special attention given to the probable microcosm of the glass bead- CO_2 surface. The improved equations are then individually investigated, first the new conservation of energy equation, then the conservation of mass equation. Finally, the computational scheme used to solve the coupled equations is presented.

Improved Ablation Model

To improve the modeling of the ablating surface, the single control surface is replaced by the control volume shown in Figure 15. The top of the control volume is the fluid dynamic wall, which can be roughly identified as the top of the glass bead layer. The bottom of the volume is the subliming surface.

The total solid mass flux entering the control volume is immediately partitioned into that which will sublime, \dot{m} , and that which will not, \dot{m}^* . The expansion of the control



- \dot{q}_{int} = heat conducted into the interior
- $(\dot{q}_{rad})_{net}$ = net radiative heat flux
- K_i = mass fraction of the i^{th} species
- ρ = density of the gas
- v = normal velocity of the gas
- h = enthalpy
- \dot{m} = mass flux of the subliming material
- y = distance above surface
- T = temperature of the gas
- D = binary diffusion coefficient
- k = thermal conductivity of the gas mixture
- \dot{m}^* = glass bead mass flux
- h_s^* = enthalpy of the glass beads at T_s
- Δh^* = increase in enthalpy of beads through control volume

Subscripts:

- s = solid phase immediately below subliming surface
- w = gas phase at fluid dynamic wall
- 1 = subliming specie
- 2 = "air"

Figure 15. Control Volume for Ablation Model of the Composite Material

surface to a control volume does not affect the conservation of overall mass and individual specie equations. Rather than repeat the previous development, the important results are listed.

$$\dot{m} = (\rho v)_w \quad (2)$$

$$\dot{m}(1-K_w) = -(\rho D \frac{\partial K}{\partial y})_w \quad (4)$$

The improved conservation of energy equation contains all of the terms identified in Chapter II, including the radiative heat flux term and the internal heat conduction term, and some additional terms associated with the flux of the glass beads. The energy terms are shown schematically and defined in Figure 15. The energy equation for this system is

$$\begin{aligned} \dot{m}h_s + \dot{m}^*h_s^* &= - \left[(k \frac{\partial T}{\partial y})_w + \sum_{i=1}^2 (\rho D h_i \frac{\partial K}{\partial y})_w \right] \\ + \dot{m}^*(h_s^* + \Delta h^*) &+ (\dot{q}_{rad})_{net} + (\rho v)_w h_w + \dot{q}_{int} \end{aligned} \quad (24)$$

The terms in the bracket may be simplified under the unity Lewis number assumption. Since this is a binary mixture, the diffusion coefficient, D , is the same for both species (Ref 4:450). First the Lewis number, which was defined in Equation (7), is substituted into the bracketed expression.

$$\left(\frac{k}{C_p}\right)_w \left[(C_p \frac{\partial T}{\partial y})_w + Le \sum_{i=1}^2 (h_i \frac{\partial K_i}{\partial y})_w \right] \quad (25)$$

By definition, the specific heat of a nonreacting mixture is

$$C_p = \sum_{i=1}^2 C_{pi} K_i \quad (26)$$

and, from thermodynamic analysis, the specific heat at constant pressure of a specie is

$$C_{pi} = \left(\frac{\partial h_i}{\partial T} \right)_p \quad (27)$$

Substituting these definitions into Equation (25), the expression becomes

$$\left(\frac{k}{C_p} \right)_w \left[\sum_{i=1}^2 K_i \frac{\partial h_i}{\partial T} \frac{\partial T}{\partial y} + Le \sum_{i=1}^2 h_i \frac{\partial K_i}{\partial y} \right]_w \quad (28)$$

Given the general case, that enthalpy is a function of temperature and pressure, the derivative of enthalpy with distance y is

$$\frac{\partial h}{\partial y} = \left(\frac{\partial h}{\partial T} \right)_p \frac{\partial T}{\partial y} + \left(\frac{\partial h}{\partial P} \right)_T \frac{\partial P}{\partial y} \quad (29)$$

The enthalpy of an ideal gas is a function of temperature only, but for any gas the second term is zero since the pressure is assumed to be constant across the boundary layer in the normal direction. Therefore Equation (28) simplifies to

$$\left(\frac{k}{C_p} \right)_w \left[\sum_{i=1}^2 K_i \frac{\partial h_i}{\partial y} + Le \sum_{i=1}^2 h_i \frac{\partial K_i}{\partial y} \right]_w \quad (30)$$

Now, if it is assumed that $Le = 1$, the sum can be expressed as

$$\left(\frac{k}{C_p}\right)_w \sum_{i=1}^2 \left(K_i \frac{\partial h_i}{\partial y} + h_i \frac{\partial K_i}{\partial y}\right)_w \quad (31)$$

Combining the differentials, the term simplifies to

$$\begin{aligned} \left(\frac{k}{C_p}\right)_w \sum_{i=1}^2 \frac{\partial}{\partial y} (K_i h_i)_w &= \left(\frac{k}{C_p}\right)_w \frac{\partial}{\partial y} \left(\sum_{i=1}^2 K_i h_i\right)_w \\ &= \left(\frac{k}{C_p} \frac{\partial h}{\partial y}\right)_w \end{aligned} \quad (32)$$

The combined term is often referred to as the heat conduction term and, as defined in Chapter II, it is expressed as a coefficient times an enthalpy difference

$$\left(\frac{k}{C_p} \frac{\partial h}{\partial y}\right)_w = \rho_e u_e C_H (h_r - h_w) \quad (33)$$

The driving potential is the difference between the recovery enthalpy and the enthalpy of the mixture at the wall. The Stanton number is substituted into Equation (24), and, after rearrangement, the equation becomes

$$\begin{aligned} \rho_e u_e C_H (h_r - h_w) - \dot{m}(h_w - h_s) - \dot{m}^* \Delta h^* \\ = (\dot{q}_{rad})_{net} + \dot{q}_{int} \end{aligned} \quad (34)$$

Further simplification requires a boundary layer similarity result. The steady state conservation of mass equation for a specie in a nonreacting boundary layer is (Ref 12)

$$\rho u \frac{\partial K_i}{\partial s} + \rho v \frac{\partial K_i}{\partial y} = \frac{\partial}{\partial y} \left(\rho D \frac{\partial K_i}{\partial y} \right) \quad (35)$$

where: s = the streamwise coordinate
 u = streamwise velocity

For the same system, the total enthalpy form of the energy equation is

$$\rho u \frac{\partial H}{\partial s} + \rho v \frac{\partial H}{\partial y} = \frac{\partial}{\partial y} \left(\frac{\mu}{Pr} \frac{\partial H}{\partial y} + \frac{\partial}{\partial y} \left[\mu \left(1 - \frac{1}{Pr} \right) \frac{\partial (u^2/2)}{\partial y} \right] \right) + \frac{\partial}{\partial y} \left[\rho D \left(1 - \frac{1}{Le} \right) \sum_i h_i \frac{\partial K_i}{\partial y} \right] \quad (36)$$

$$\text{where: } H = h + \frac{u^2}{2}$$

Assuming that the Prandtl and Lewis numbers both equal one, the last two terms of the energy equation drop out. This assumption implies that the Schmidt number ($Sc = \rho D / \mu$), the ratio of Prandtl number to Lewis number, is also one. Therefore, μ can be substituted for ρD in Equation (35), and the equations become

$$\rho u \frac{\partial K_i}{\partial s} + \rho v \frac{\partial K_i}{\partial y} = \frac{\partial}{\partial y} \left(\mu \frac{\partial K_i}{\partial y} \right) \quad (37)$$

$$\rho u \frac{\partial H}{\partial s} + \rho v \frac{\partial H}{\partial y} = \frac{\partial}{\partial y} \left(\mu \frac{\partial H}{\partial y} \right) \quad (38)$$

One solution for Equation (37) and (38) is

$$K_i = A_i H + B_i \quad (39)$$

where A_i and B_i are constants for a given specie. The constants for the subliming specie are evaluated by applying the following boundary conditions:

At the fluid dynamic wall:

$$K = K_w \quad \text{and} \quad H = H_w = h_w + \cancel{(u^2/2)}_w^0$$

At the boundary layer edge:

$$K = K_e = 0 \quad \text{and} \quad H = H_e$$

Equation (39) then becomes

$$K = \frac{K_w (H_e - H)}{(H_e - h_w)} \quad (40)$$

The derivative of Equation (40) with respect to y , evaluated at the wall is

$$\left(\frac{\partial K}{\partial y}\right)_w = - \frac{K_w}{(H_e - h_w)} \left(\frac{\partial H}{\partial y}\right)_w \quad (41)$$

and since $H = h + u^2/2$, then

$$\left(\frac{\partial H}{\partial y}\right)_w = \left(\frac{\partial h}{\partial y}\right)_w + \cancel{u^2}_w^0 \left(\frac{\partial u}{\partial y}\right)_w \quad (42)$$

Substitution of Equation (42) into (41) yields

$$\left(\frac{\partial K}{\partial y}\right)_w = - \frac{K_w}{H_e - h_w} \left(\frac{\partial h}{\partial y}\right)_w \quad (43)$$

When Equation (43) is substituted into the conservation of specie equation, Equation (4), the result is

$$\dot{m} = \frac{\rho D}{(1-K_w)} \frac{K_w}{(H_e - h_w)} \left(\frac{\partial h}{\partial y}\right)_w \quad (44)$$

The total enthalpy at the edge, H_e , is equal to the recovery enthalpy, h_r , either at the stagnation point, or everywhere if the Prandtl number is one. Application of the unity Lewis number assumption and the definition of the Stanton number finally yields Equation (12)

$$\dot{m} = \left(\frac{K_w}{1-K_w}\right) \rho_e u_e C_H \quad (12)$$

As in Chapter II, the energy equation is now rearranged using the definition of the enthalpy of a mixture and Equation (12) to yield

$$\rho_e u_e C_H (h_r - h_{2w}) - \dot{m}(h_{1w} - h_s) - \dot{m}^* \Delta h^* = (\dot{q}_{\text{rad}})_{\text{net}} + \dot{q}_{\text{int}} \quad (45)$$

Since the fluid dynamic wall temperature, T_w , can be different from the temperature at the subliming surface, T_s , the enthalpy difference ($h_{1w} - h_s$) can be divided into the enthalpy of sublimation at T_s , Δh_{sub} , plus the enthalpy required to raise the temperature of the vapor to T_w , $\Delta h_{w,s}$. When this distinction and the definition of B' are applied to Equation (45), the result is

$$\frac{\dot{m}}{B'} (h_r - h_{2w}) - \dot{m}(\Delta h_{\text{sub}} + \Delta h_{w,s}) - \dot{m}^* \Delta h^* = (\dot{q}_{\text{rad}})_{\text{net}} + \dot{q}_{\text{int}} \quad (46)$$

Solving for B' , Equation (46) becomes

$$B' = \frac{(h_r - h_{2w})}{(\Delta h_{\text{sub}} + \Delta h_{w,s} + \frac{\dot{m}^*}{\dot{m}} \Delta h^* + \frac{(\dot{q}_{\text{rad}})_{\text{net}}}{\dot{m}} + \frac{\dot{q}_{\text{int}}}{\dot{m}})} \quad (47)$$

If each term in the denominator is normalized by Δh_{sub} , the result is

$$B' = \frac{h_r - h_{2w}}{\Delta h_{\text{sub}} (1 + \bar{X})} \quad (48)$$

$$\text{where: } \bar{X} = \sum_{i=1}^4 \bar{X}_i \quad \text{and}$$

$$\bar{X}_1 = \frac{(\dot{q}_{\text{rad}})_{\text{net}}}{\dot{m} \Delta h_{\text{sub}}}; \quad \bar{X}_2 = \frac{\dot{m}^* \Delta h^*}{\dot{m} \Delta h_{\text{sub}}}; \quad \bar{X}_3 = \frac{\Delta h_{w,s}}{\Delta h_{\text{sub}}}; \quad \bar{X}_4 = \frac{\dot{q}_{\text{int}}}{\dot{m} \Delta h_{\text{sub}}}$$

The nondimensional parameter \bar{X} is the sum of the relative contribution of each term which was neglected in Chapter II.

The definition of B' is again applied to the continuity of specie equation which can either be expressed in terms of mass fraction or partial pressure.

$$B' = \frac{K_w}{1 - K_w} \quad (17)$$

$$B' = \frac{M_1}{M_2} \frac{p_{1w}/P}{1 - (p_{1w}/P)} \quad (19)$$

While Equations (17) and (19) are identical to those derived in Chapter II, neither the concentration nor the partial pressure will be assumed to be equilibrium values. The factors which influence the evaluation of the concentration at the wall will be discussed following the modeling of the additional terms of the energy equation.

The Energy Equation

The nondimensional parameter \bar{X} in the energy equation can have either a positive or a negative value. If \bar{X} were zero, Equation (18) of Chapter II would be generated. Each contribution to \bar{X} will be separately evaluated.

Radiation Heat Transfer. \bar{X}_1 is the ratio of net heat transfer by radiative process to the rate of heat absorption due to sublimation. Assuming the surroundings are radiating as a black body at room temperature, the net flux can be approximated by

$$(\dot{q}_{\text{rad}})_{\text{net}} = \epsilon \sigma T_w^4 - \alpha \sigma T_{\text{room}}^4 \quad (49)$$

Further, assuming that the temperature difference is small enough that ϵ and α are approximately equal, the equation simplifies to

$$\frac{(\dot{q}_{\text{rad}})_{\text{net}}}{\dot{m} \Delta h_{\text{sub}}} = \frac{\epsilon \sigma}{\dot{m} \Delta h_{\text{sub}}} (T_w^4 - T_{\text{room}}^4) \quad (50)$$

A pure CO_2 surface and a glass laden CO_2 surface would probably have different ϵ 's, however both are assumed to be unity for this approximation.

The next two contributions to \bar{X} reflect the fact that some energy can be absorbed by the solid and the gas passing through the control volume. The evaluation of these terms requires an estimate of the temperature difference across the control volume. In the development which follows, a sphere is analyzed to determine the temperature rise that is caused by an imposed heat flux, and the increase in energy implied by that temperature rise. Next an analysis is performed to determine the thermal resistance of the gas between the spheres. An analysis of the relative resistances of the sphere, the gas columns, and the boundary layer finally yields an estimate of the temperature drop.

Sphere Analysis. It will be shown that the majority of the heat flux to the model passes through the glass beads. The thermal analysis of the beads requires certain assumptions which cannot be directly verified. It is assumed that the beads are spherical, and that they do not leave the surface until the CO_2 surface has receded to the bead equator. It is further assumed that the thermal response of the sphere is symmetrical about the axis normal to the model surface - temperature is a function of radial position r , and angle θ , Figure 16. While it might be suspected that a transient heat conduction solution would

be required to obtain the thermal response of the sphere, steady state solutions are adequate. Even at the highest mass transfer rate, the surfaces receded at about 0.07 mm/s, traveling one bead depth is about two seconds. The

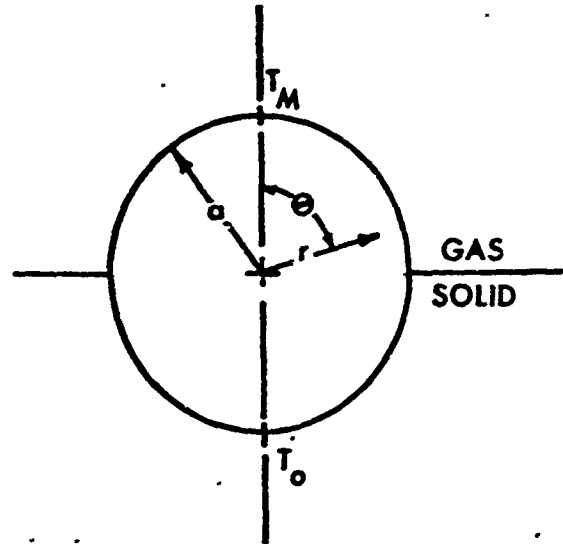


Figure 16. A Sphere Half Emerged From the CO₂

Fourier modulus, defined as the thermal diffusivity times the time divided by the square of the radius, is the nondimensional time scale with which transient fluxes are correlated. By the time the modulus is equal to unity, the transient flux in a sphere is negligible. With the small radius of the glass beads, the modulus becomes greater than one within 0.01 seconds. The steady state heat conduction equation, in spherical coordinates, for the axisymmetrical temperature distribution is (Ref 20:135)

$$2r \frac{\partial T}{\partial r} + r^2 \frac{\partial^2 T}{\partial r^2} + \text{ctn } \theta \frac{\partial T}{\partial \theta} + \frac{\partial^2 T}{\partial \theta^2} = 0 \quad (51)$$

There is an analytical solution to this problem in the form of the Legendre polynomial series. Unfortunately, unless the surface temperature is of a fortuitous distribution, convergence can require a prohibitive number of terms.

While several numerical programs were available which could solve the conduction problem in rectangular form, it was decided that it would be more fruitful to write a relaxation routine to solve the spherical problem directly. The program computed internal temperatures for a specified surface temperature distribution, the heat flux through the sphere, and the amount of energy stored in the sphere above the amount it would have had at a uniform minimum temperature level.

Solutions were obtained for two cases: I) a cosine distribution from a maximum T_M at $\theta = 0$ to the minimum T_0 at $\theta = \pi$, II) a cosine distribution over the top hemisphere and a constant T_0 on the bottom hemisphere. The first case is actually the first Legendre polynomial, which supplied a good test case for the program. The resulting temperature distributions are shown in Figure 17 and the nondimensional heat flux and energy storage are shown in Table III.

These two cases bracket the expected result. If the temperature distribution is symmetrical about the equator, as in Case I, the mean energy stored in the bead is half the amount it would have if it reached a uniform T_M . If the CO_2 maintained the bottom surface at an approximately constant temperature, T_0 , the energy gain is about one fourth the uniform T_M value. The fluxes remained essentially equal. These results were the relations used to estimate the expected temperature difference and the resulting increase in energy because of that difference.

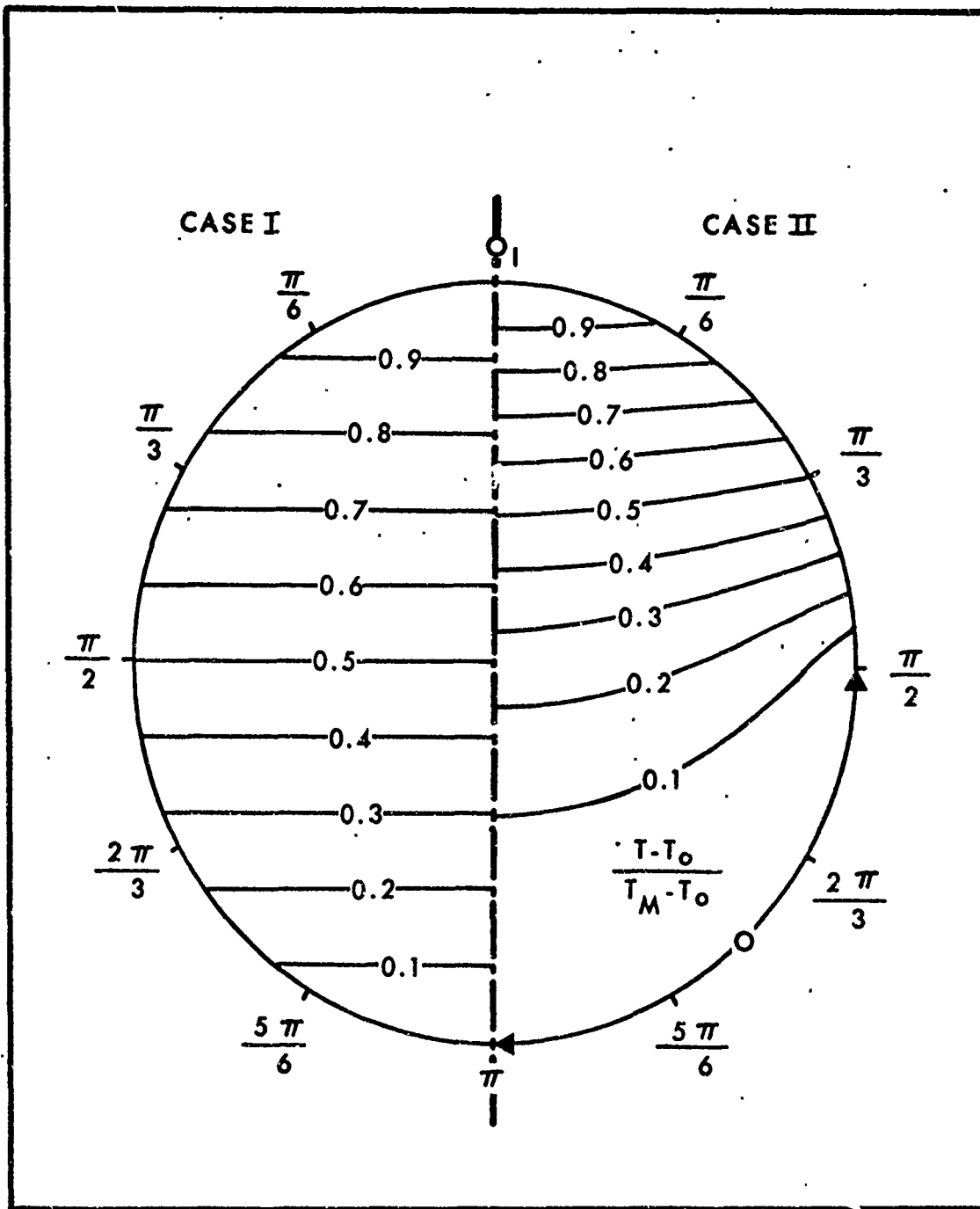


Figure 17. Temperature Profiles in a Sphere

Table III

Summary of Theoretical Predictions for Heat Flux and Energy Gain of a Sphere

CASE	$\frac{Q}{k\pi a(T_M - T_0)}$	$\frac{\Delta E}{\rho C_p (4/3)\pi a^3 (T_M - T_0)}$
I	0.5	0.5
II	0.5	0.24

Gas Column Analysis. In order to estimate the heat flux through the bead, the thermal resistance of a gas column must be estimated. For analysis, assume the idealized geometry of three spheres half exposed from the surface as shown in Figure 18. The column of interest begins as a triangle at the top of the beads with an area of $\sqrt{3} a^2$ and bottoms in the shaded region which has an area $\frac{2\sqrt{3} - \pi}{2} a^2$. The area at any intermediate plane x is

$$A(x) = \frac{\pi}{2} \left[\frac{(2\sqrt{3} - \pi)a^2}{\pi} + x^2 \right] \quad (52)$$

Assuming no heat flow out of the gas column to the glass walls, a quasi-one dimensional expression for the heat transferred through any plane is

$$\dot{Q} = -k \frac{dT}{dx} A(x) \quad (53)$$

The solution of this equation with the boundary conditions that the temperature at the top of the column is T_M and at the bottom is T_0 is

$$T_M - T_0 = \frac{2\dot{Q}}{k\pi a} \sqrt{\frac{\pi}{2\sqrt{3}-\pi}} \tan^{-1} \sqrt{\frac{\pi}{2\sqrt{3}-\pi}} \quad (54)$$

Evaluating the constants and rearranging the equation yields

$$\frac{\dot{Q}}{\pi k a (T_M - T_0)} = 0.127 \quad (55)$$

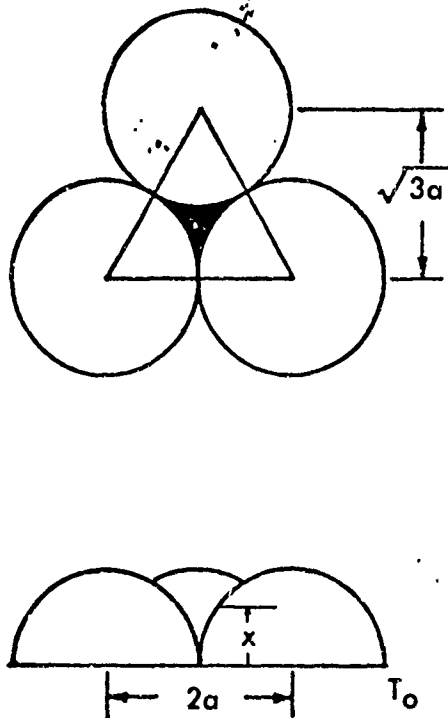


Figure 18. Idealized Gas Column Geometry

Resistance Network Analysis. Finally a network can be constructed to represent the system. A "unit cell" of surface consists of one glass bead and two gas columns with a total cross sectional area of $2\sqrt{3}a^2$. The network is shown in Figure 19. The heat flux through the boundary layer is

$$\dot{Q}_{BL} = \rho_e u_e C_H C_p (T_e - T_w) A \quad (56)$$

Therefore, the thermal resistance is

$$R_{BL} = \frac{\Delta T}{\dot{Q}_{BL}} = \frac{1}{\rho_e u_e C_H C_p 2\sqrt{3} a^2} \quad (57)$$

For the glass bead, using the results of the sphere analysis

$$\dot{Q}_{GB} = 1/2 \pi k_{GB} a (T_w - T_s) \quad (58)$$

Therefore

$$R_{GB} = \frac{2}{\pi k_{GB} a} \quad (59)$$

For two gas columns

$$\dot{Q}_c = 2 \pi k_{GAS} a (T_w - T_s) (0.127) \quad (60)$$

Therefore

$$R_c = \frac{4}{\pi k_{GAS} a} \quad (61)$$

The overall resistance of the network is

$$R = R_{BL} + \frac{R_{GB} R_c}{R_{GB} + R_c}$$

The resistance of the glass bead is about two orders of magnitude less than either the boundary layer or the air columns; therefore, the overall resistance to heat flux is essentially the boundary layer resistance.

Since the temperature difference imposed on the columns and the bead is the same

$$T_w - T_s = \dot{Q}_{GB} R_{GB} = \dot{Q}_C R_C \quad (63)$$

The ratio of the heat fluxes is

$$\frac{\dot{Q}_{GB}}{\dot{Q}_C} = \frac{R_C}{R_{GB}} \quad (64)$$

Considering the order of magnitude of the resistances, essentially all of the flux is through the beads. The flux through the bead is, then, approximately equal to the flux through the boundary layer; therefore

$$\dot{Q}_{BL} = \frac{\Delta T_{BL}}{R_{BL}} = \frac{\Delta T_{GB}}{R_{GB}} \quad (65)$$

Equation (65) is the important relation for estimation of the temperature difference between the fluid dynamic

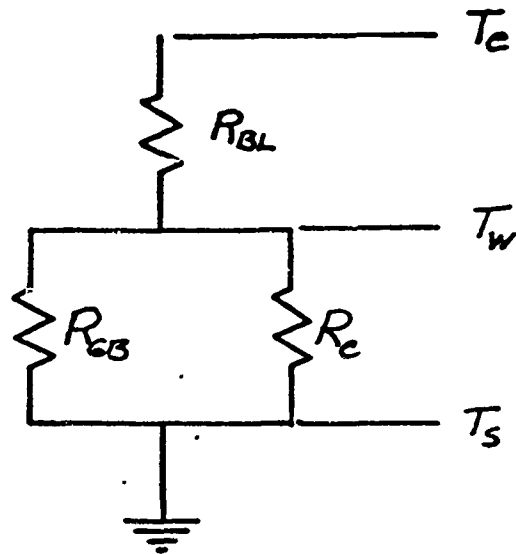


Figure 19. Resistance Network

wall and the subliming surface, which is assumed to be ΔT_{GB} .

Enthalpy Increase of the Evolved Solids. The enthalpy increase, Δh^* , corresponds to the energy increase per unit mass as predicted by the glass bead analysis.

$$\Delta h^* = \frac{\Delta E}{\rho (4/3 \pi a^3)} \quad (66)$$

It is assumed that the actual value of this quantity is bracketed by the predictions for Case I and Case II shown in Table III. If the average of the two cases is used, then \bar{X}_2 is

$$\frac{\dot{m}^* \Delta h^*}{\dot{m} \Delta h_{\text{sub}}} = \frac{(\frac{\dot{m}^*}{\dot{m}})(0.37) C \Delta T}{\Delta h_{\text{sub}}} \quad (67)$$

Enthalpy Increase of the Evolved Gases. \bar{X}_3 is the ratio of the heat absorption rate of the gas while increasing in temperature from T_s to T_w , to the heat absorption rate due to sublimation, which is

$$\frac{\Delta h_{w,s}}{\Delta h_{\text{sub}}} = \frac{C_p (T_s - T_w)}{\Delta h_{\text{sub}}} \quad (68)$$

Internal Heat Conduction. \bar{X}_4 is the ratio of the internal heat flux to the heat absorption rate due to sublimation. This term is composed of a transient rate as the model cools and a steady state rate if any temperature differences persist. The transient heat flux can be

estimated with standard techniques and will be discussed in the next chapter. A mechanism will be described later whereby the front of the model could be maintained at a different temperature than the sides. Assuming that the front of the model responds to this in a way similar to a sphere with a cosine temperature distribution on one hemisphere and a constant temperature on the other (Case II), the results of the glass bead analysis can be applied. The predicted heat flux at the high temperature point is

$$\frac{\dot{q}_r}{k\Delta T} = 0.8 \quad (69)$$

Therefore

$$\frac{\dot{q}_{int}}{\dot{m} \Delta h_{sub}} = \frac{(0.8) k (T_s - T_{int})}{r \dot{m} \Delta h_{sub}} \quad (70)$$

The Conservation of Specie Equation

The result of the more thorough analysis showed that Equation (17) of Chapter II also applies to the ablation of the composite material. In this case, the concentration of CO_2 at the fluid dynamic wall is not necessarily that determined by phase equilibrium at the wall temperature. Three phenomena could cause the concentration to be otherwise. The first is the possibility that the sublimation temperature is different from the wall temperature, the second is that the concentration could be attenuated between the subliming surface and the fluid dynamic wall,

and finally, because of the mass transfer, the vapor pressure of the CO_2 at the subliming surface could be something less than the equilibrium value.

Temperature Difference. The possibility of a difference between the fluid dynamic wall temperature, T_w , and sublimation temperature, T_s , must be accounted for in the simultaneous solution of the mass and energy conservation equations. It is the fluid dynamic wall temperature which is required to determine energy transfer; the sublimation temperature controls the mass transfer. In the simultaneous solution, the temperature difference is assumed to be the difference across the glass beads, and is computed using Equation (65).

Concentration Attenuation. If the columns of gas between the glass beads were essentially stagnant with respect to the boundary layer flow, the only mass flux would be normal to the surface. This can be most reasonably imagined at or very near the stagnation point where velocities parallel to the wall are quite low. The result of this situation is a diffusion well effect which causes attenuation of concentration levels (Ref 4:452). Given the arbitrary well geometry shown in Figure 20, the quasi-one dimensional equation for the flow rate of a specie is

$$A(x) \left[K_i(\rho v) - \rho D \frac{dK_i}{dx} \right] = \dot{M}_i \quad (71)$$

If the area is constant, the resulting concentration distribution is

$$\frac{1-K_w}{1-K_s} = \exp\left(\frac{\rho v}{\rho D} y\right) \quad (72)$$

Furthermore, if a surface were completely covered with one dimensional wells of infinitesimal wall thickness, then the mass flux in the well (ρv) would also be the fluid dynamic wall flux, \dot{m} . Given walls of finite thickness, the one dimensional analysis could be used with an adjustment to the mass flux by the ratio of well area to surface area, F.

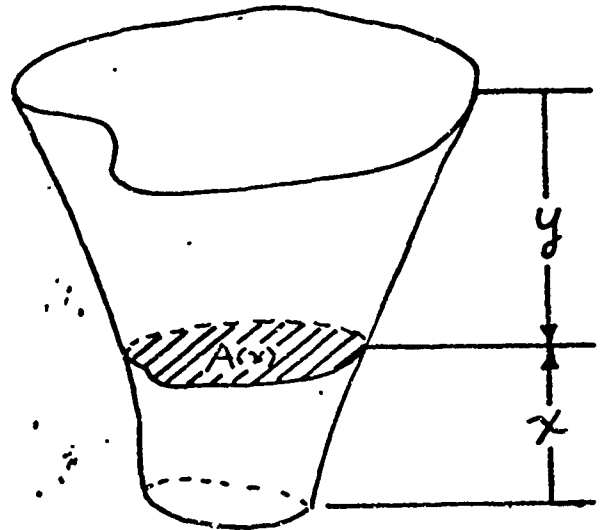


Figure 20. Arbitrary Geometry for Diffusion Analysis

$$(\rho v) = \dot{m}/F \quad (73)$$

An improved approximation for the glass bead simulation is to perform a quasi-one dimensional analysis using the idealized gas column geometry shown in Figure 18. The concentration attenuation for a well depth y , no greater than a , is

$$\frac{1-K_w}{1-K_s} = \exp\left[\frac{(\rho v)_w}{\rho D} \frac{2\sqrt{3} a}{\pi} \sqrt{\frac{\pi}{2\sqrt{3}-\pi}} \left(\tan^{-1} \sqrt{\frac{\pi}{2\sqrt{3}-\pi}} - \tan^{-1} \left(\frac{a-y}{a}\right) \sqrt{\frac{\pi}{2\sqrt{3}-\pi}}\right)\right] \quad (74)$$

where $(\rho v)_w = \dot{m}$, the mass flux at the top of the well

Nonequilibrium Sublimation. The pure CO₂ models exhibited the traits of a system experiencing nonequilibrium sublimation, which are a mass loss rate lower than the analytical prediction of an equilibrium model and a wall temperature higher than the prediction (Ref 1). The definition of the equilibrium vapor pressure is that pressure which exists in a closed space over a liquid or solid with no net mass transfer through the phase interface and with no other substances present. Since the ablation environment is quite different, nonequilibrium effects are possible. This effect has been investigated by many authors. The direct result of nonequilibrium vaporization is a decrease in partial pressure below the equilibrium value. For nonequilibrium vaporization (Ref 18 and 23)

$$(P_{eq.} - P)_s = \frac{\dot{m} s}{\alpha} \sqrt{2\pi RT/M} \quad (75)$$

where: α = The coefficient of vaporization

R = The universal gas constant

M = Molecular weight

and s indicates the phase interface

The coupled effect of the inclusion of nonequilibrium vaporization in the heat and mass transfer equations for ablation of pure CO_2 in air is shown in Figure 21. The effect is negligible at low mass flux levels, but as the ratio of mass flux to coefficient of vaporization reaches a threshold value of $10 \text{ kg/m}^2 \cdot \text{s}$, the effect becomes quite dramatic.

Application of the nonequilibrium vaporization equation to the glass bead - CO_2 model requires a correction to the mass flux term. The glass beads block the surface area available for vaporization; therefore, continuity of mass requires an increase in the mass flux at the phase boundary which aggravates the nonequilibrium condition. Again, using the glass bead surface model shown in Figure 18, the CO_2 mass flux at the subliming surface required to sustain the mass flux \dot{m} at the fluid dynamic wall is

$$\dot{m}_s = \dot{m} \frac{2\sqrt{3}}{2\sqrt{3} - 2(y/a) + (y/a)^2} \quad (76)$$

Substituting \dot{m}_s into the nonequilibrium equation, the model for the glass bead CO_2 surface is

$$(P_{\text{eq}} - P)_s = \left(\frac{\dot{m}}{\alpha}\right) \frac{2\sqrt{6RT_s M_1}}{2\sqrt{3} - 2(y/a) + (y/a)^2} \quad (77)$$

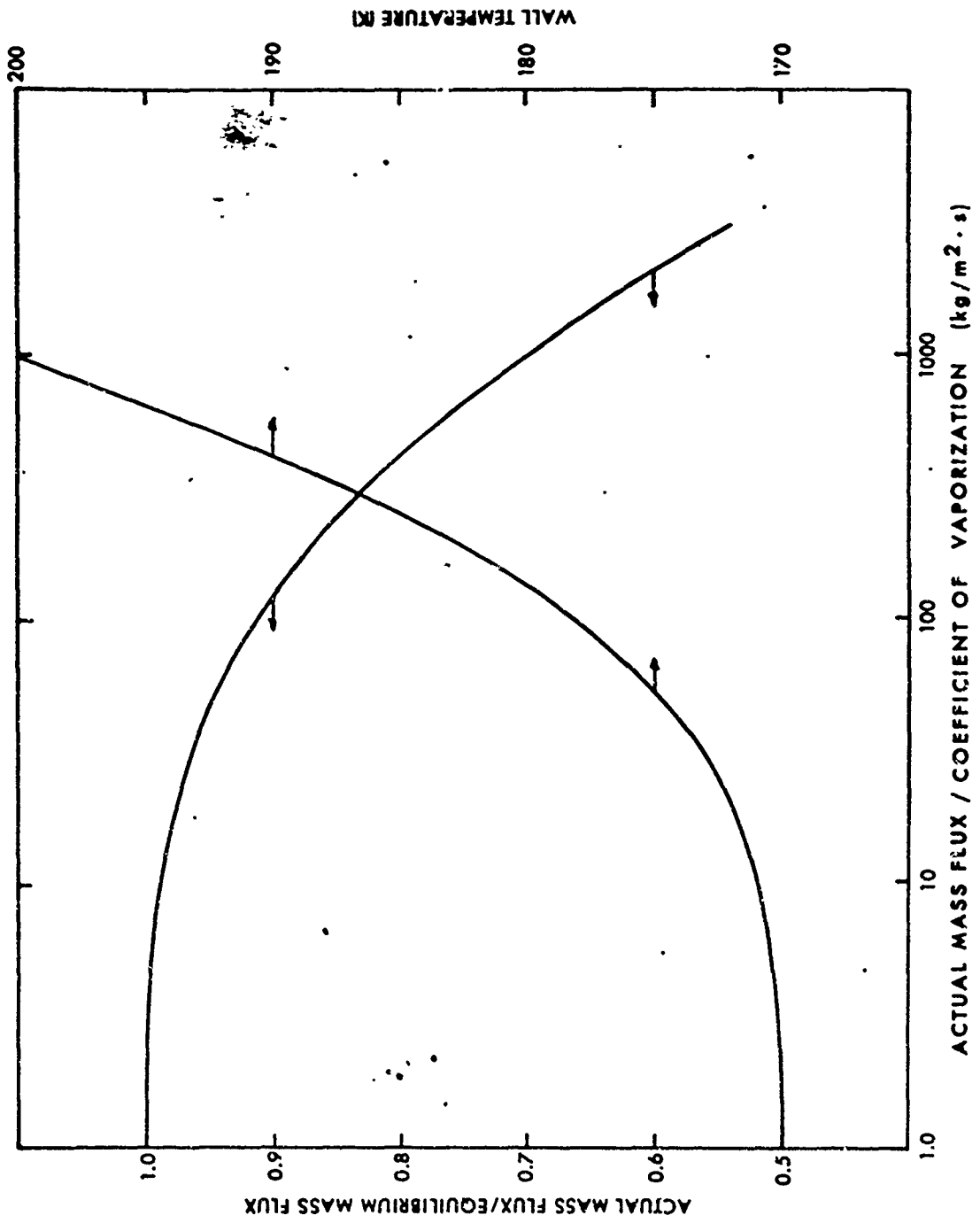


Figure 21. Effect of Nonequilibrium Sublimation on Mass Flux and Wall Temperature

Computation Scheme

The improved B' equations must be solved simultaneously to determine the overall effect on the CO₂ mass loss.

A B' prediction program was written to include the discussed effects and is shown schematically in Figure 22. The system is no longer independent of the heat transfer coefficient, so $\rho_e u_e C_H$ must be supplied as input. The inclusion of nonequilibrium sublimation necessitates the input of a first estimate for the temperature at the subliming surface.

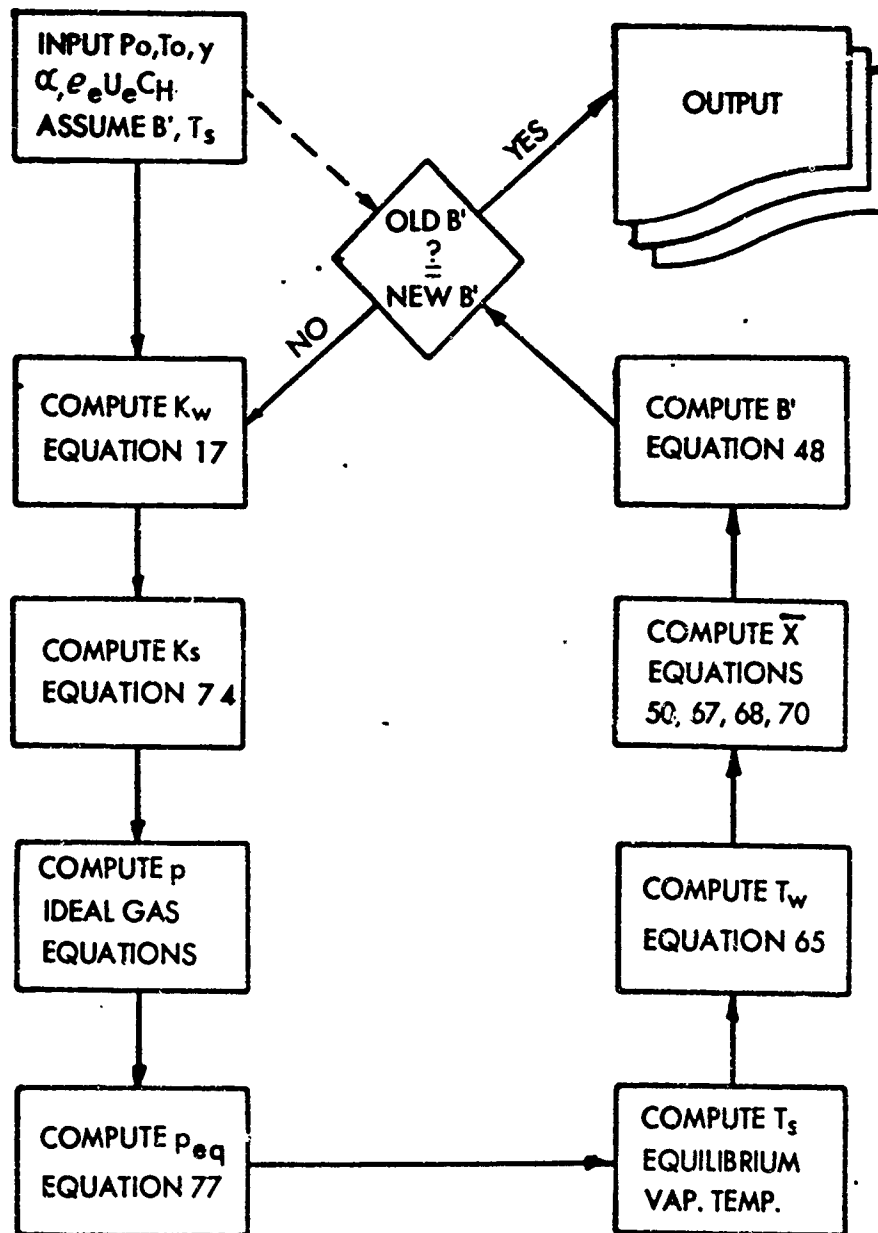


Figure 22. Iterative Scheme to Predict B' and Model Temperatures For Glass Bead - CO_2 Composite

VI. Comparison of Theoretical and Experimental Results

While it would be desirable to subject the models to a broad range of heat transfer conditions, the actual range was quite narrow. Excluding Run 4, the average value of stagnation point $\rho_e u_e C_H$ for both pure CO_2 and composite experiments was $0.227 \pm 0.021 \text{ kg/m}^2 \cdot \text{s}$. This stagnation point mean value and the BLIMP distribution around the hemispherical nose, scaled to the mean stagnation value, became the base line for the theoretical results which follow. Before attempting to predict the composite response, the pure CO_2 prediction model is examined. The base line environmental conditions for the pure CO_2 results were $P = 0.976 \text{ atm}$ and $T_{\text{air}} = 280\text{K}$, the average for those runs.

Pure Carbon Dioxide Models

Two corrections to the simple theory which could affect the ablation performance of the pure CO_2 models are nonequilibrium sublimation and radiant heat flux. When these phenomena, Equations (50) and (75), were added to the simplified ablation equations presented in Chapter II, a coefficient of vaporization equal to 0.0005 brought the theoretically predicted mass loss into closest agreement with the experimental mass loss data and improved the temperature agreement as shown in Figure 23. Since more confidence was placed on the mass loss data, the

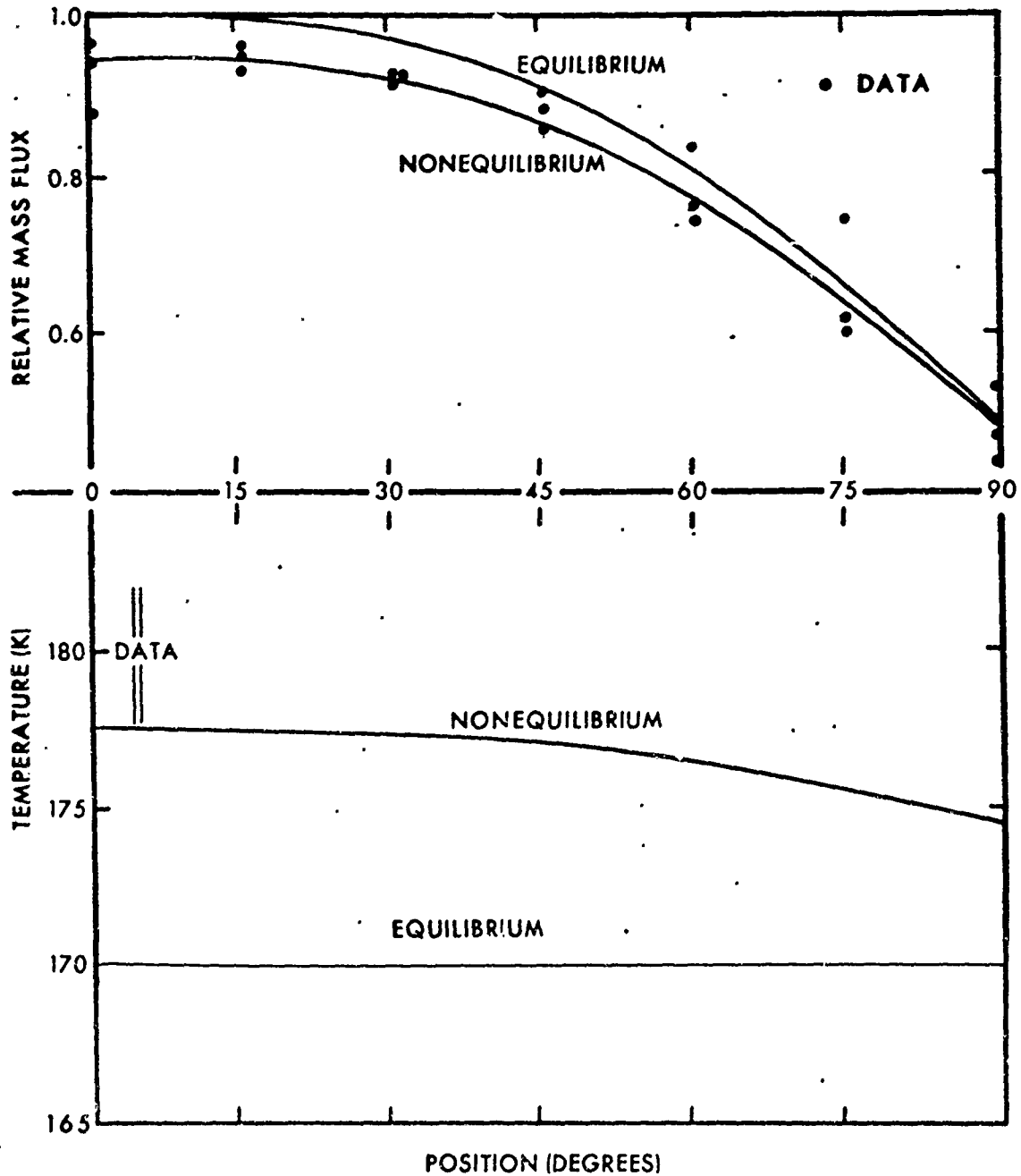


Figure 23. Equilibrium and Nonequilibrium Predictions Compared to Experimental Results of Pure CO₂ Models--All Normalized by Equilibrium Theory Stagnation Point Mass Loss Prediction (T = 280K, P = 0.967 atm, α = 0.0005)

vaporization coefficient was chosen to fit the mass loss data rather than the temperature data, which would have resulted in a coefficient of 0.0003. The effect of the nonequilibrium sublimation is to reduce the partial pressure of the CO_2 at the surface. Referring to the conservation of species equation

$$B' = \frac{M_1}{M_2} \frac{p_{1w}/P}{1 - (p_{1w}/P)} \quad (19)$$

a reduced partial pressure results in a reduced B' . In order to then satisfy the energy equation

$$B' = \frac{h_r - h_{2w}}{\Delta h_{\text{sub}} (1 + \bar{X})} \quad (48)$$

there must be an increase in wall temperature. The radiation term is only a 1.5% correction and hardly affected the solution.

The evaporation coefficients of most materials are not known. Scala (Ref 18) lists several of the known coefficients which vary from approximately one for water ice to 10^{-6} for red phosphorus. It is also known that the value of the coefficient reduces with a decrease in temperature (Ref 9). While a value of 0.0005 is lower than most known values, it does not appear to be out of the question. There are not many other reported CO_2 mass loss experiments to examine. Spalding and Christie (Ref 25) report experimental results which were 13 to 20 percent below their

theoretical predictions; however, the mass loss rates were sufficiently low that nonequilibrium effects could only improve their agreement by less than two percent.

As a result of these corrections, the predicted B' and T_w are no longer constant around the body. The variable wall temperature gives rise to steady state heat transfer through the nosetip; therefore, internal heat conduction should have also been listed as a potential correction term. However, the slight temperature difference for the pure CO_2 models is too small to significantly affect the solution.

Glass Bead - Carbon Dioxide Models

Nonequilibrium Model. Using the iterative scheme outlined in Figure 22, ablation predictions were obtained for the glass bead- CO_2 models using the base line heat transfer distributions and average environmental conditions of $P = 0.967$ atm and $T_{air} = 273K$. Parametric solutions in terms of stagnation point diffusion well depth were obtained using the previously deduced value of 0.0005 for the coefficient of vaporization. In the case of the composite models, the temperature variation around the body is significant and a consistent method is required to determine the internal heat flux. As discussed in Chapter V, the side wall temperature, assumed equal to the temperature of the subliming surface at the 90 degree location, is used in conjunction with the Case II spherical conduction

solution to approximate the internal conduction term, Equation (70). The special input conditions for the solution at the 90 degree location were the convective heat flux from the BLIMP distribution, negligible internal heat transfer as predicted by the Case II solution, and a diffusion well depth which could be different from that specified for the stagnation point. The average geometrical well depth is probably the same around the body and was assumed to be so for the calculation of mass flux at the subliming surface in Equation (77). Yet, the depth for diffusion purposes probably decreases as increased boundary layer velocities promote circulation between the beads. In order to bracket this effect, the following distributions were examined:

- 1) $y_{diff} = y$ (A constant around the hemisphere)
- 2) $y_{diff} = y (\cos \theta)$
- 3) $y_{diff} = y \left(\frac{u_{e \max} - u_e}{u_{e \max}} \right)$ (See Figure 3)

For each case, a geometrical well depth, y , was assumed, the ablation solution for the 90 degree location was obtained, and T_s for that location was specified as the internal temperature for the ablation solutions around the body.

The stagnation point solutions are shown in the B' versus T plot, Figure 24, for Cases 2 or 3 which had a negligible well depth at the 90 degree location. If the

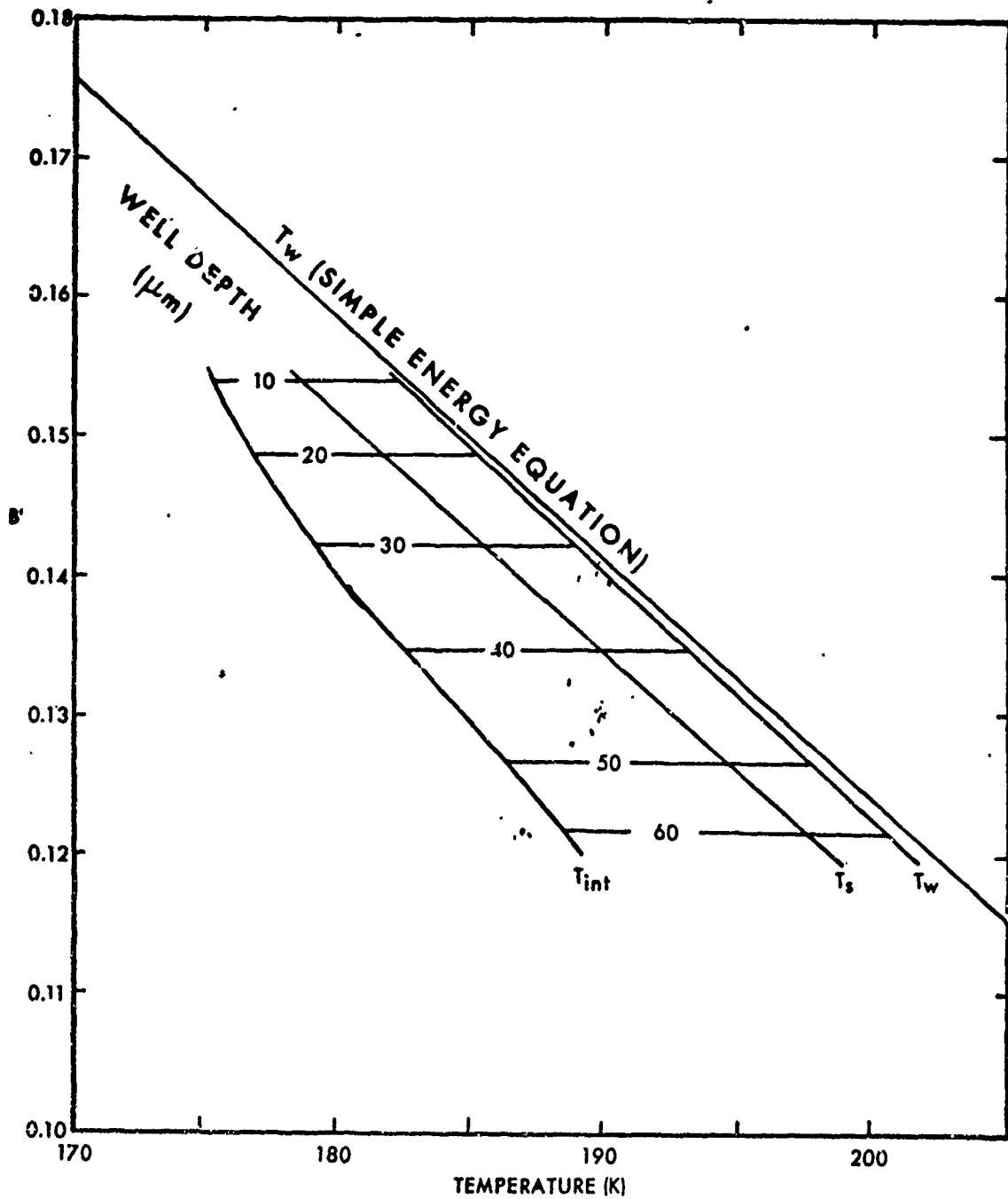


Figure 24. Effect of Well Depth on Stagnation Point Ablation Response of Composite Models with Nonequilibrium Sublimation Model. ($T = 273\text{K}$, $P = 0.967 \text{ atm}$, $\alpha = 0.0005$, Side Wall Wells Have Negligible Diffusion Depth)

entire stagnation point mass flux decrease is attributed to a decrease in B' , the required B' value is 0.126, which is obtained with an average geometrical well depth of 50 μm . The effect of this depth on mass loss and temperature around the nose is shown in Figure 25. This model is quite insensitive to the way in which diffusion well depth is varied about the body. The mass loss distribution is reasonably well described by these models; however, the predicted internal temperature of 186K for the zero side wall cases is higher than the observed average asymptotic value of 182K.

Equilibrium Model. Since the deduced value of the vaporization coefficient could not be substantiated in the literature, an equilibrium sublimation model was also investigated. The nonequilibrium effect can be easily nullified by specifying a value of one for the coefficient of vaporization. In this case the assumption is made that the aerodynamic prediction of heat and mass transfer for this shape is 6.5% high for both the pure CO_2 and the composite which brings the base line stagnation point mass flux down to 0.212 $\text{kg/m}^2 \cdot \text{s}$. The average experimental mass flux is 23% below the new base line, which is equivalent to a reduction of B' to 0.135.

The ablation response as a function of well depth for the cases with negligible side wall diffusion depth are shown in Figure 26. In order to reduce B' to 0.135, a well depth of 80 μm is required, which is in excess of the bead

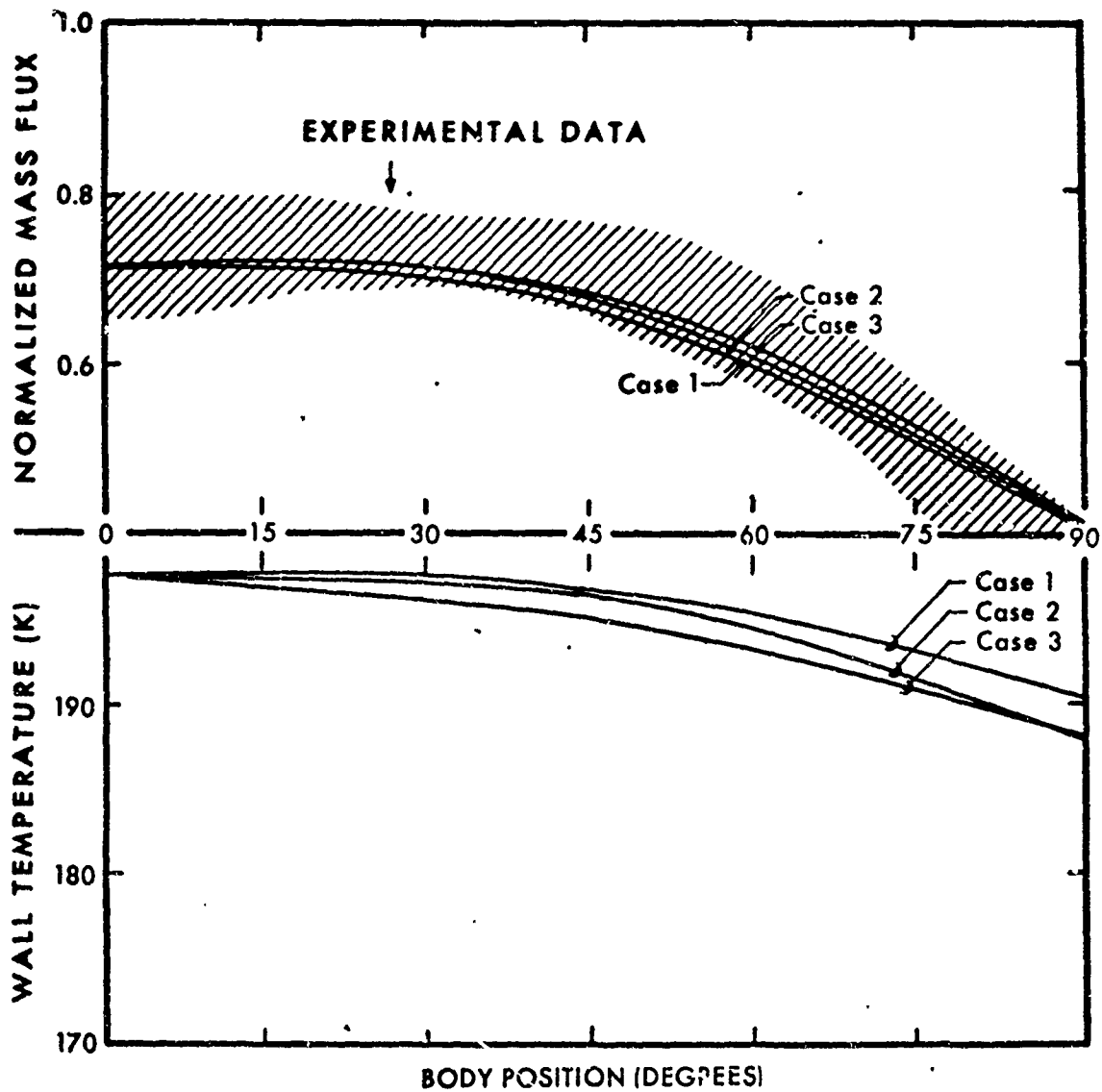


Figure 25. Theoretical Mass Flux and Wall Temperature Distribution for Composite With Nonequilibrium Sublimation Model ($T = 273\text{K}$, $P = 0.967 \text{ atm}$, $\alpha = 0.0005$, $y = 50 \mu\text{m}$)

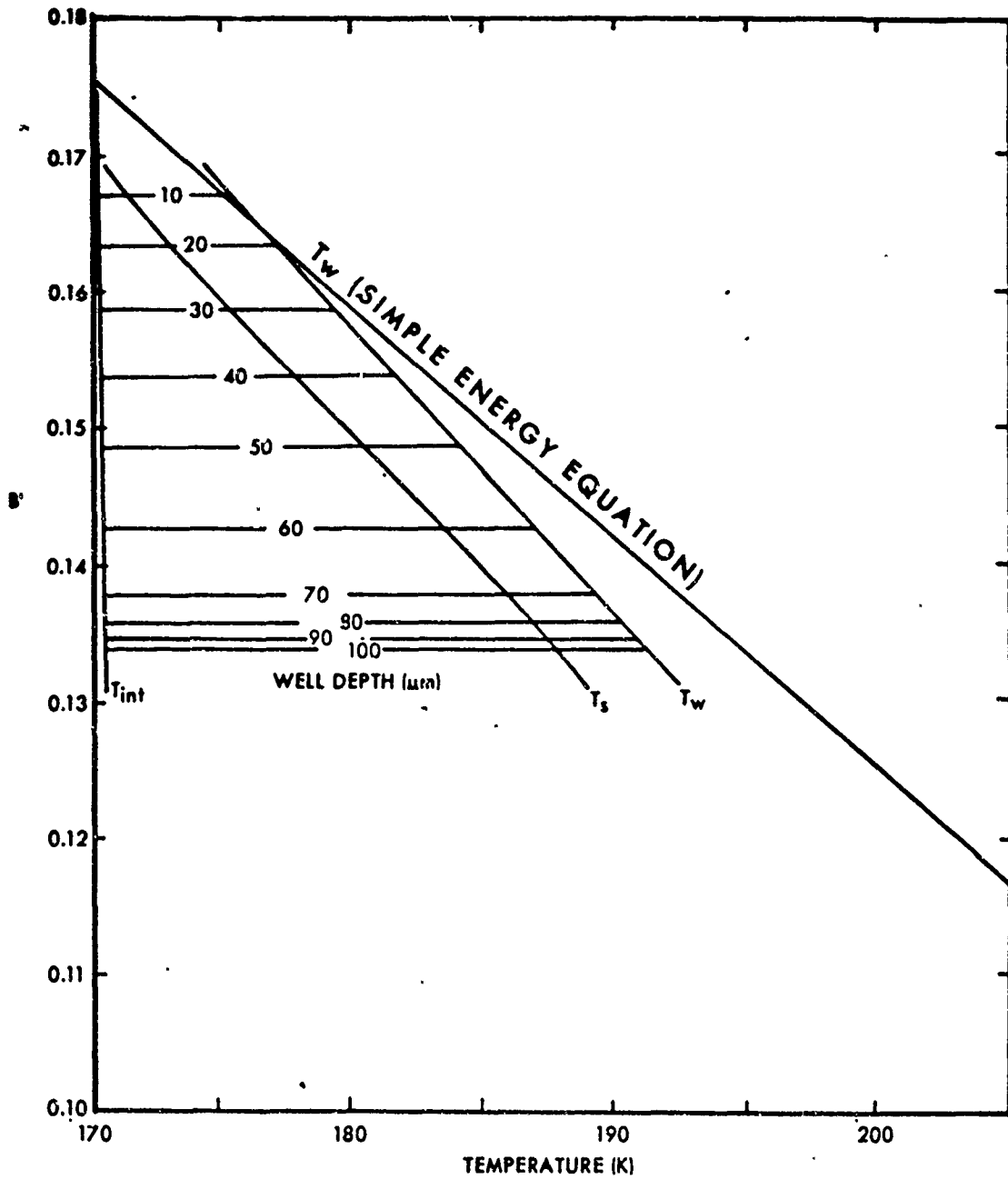


Figure 26. Effect of Well Depth on Stagnation Point Ablation Response of Composite with Equilibrium Sublimation Model ($T = 273\text{K}$, $P = 0.967 \text{ atm}$, Side Wall Wells Have Negligible Diffusion Depth)

radius of 60 μm . The quasi-one dimensional solution for the concentration attenuation probably under predicts the actual two dimensional axisymmetrical process, so an "effective well depth" of 80 μm could have physical significance.

It was possible to reduce the B' to 0.135 for the case of constant well depth; however, an effective depth of almost three times the bead radius was required. Referring to Figure 26, the success of the zero side wall well depth assumption in reducing B' was a strong function of the internal heat conduction promoted by the low side wall temperature. The parameter \bar{X} is the measure of divergence of the solution from the simple ablation theory energy equation which is also plotted; a positive \bar{X} results in a solution below the line, negative \bar{X} solutions are above. With a side well as deep as the stagnation point well, the internal temperature rises with well depth at about the same rate as the stagnation point sublimation temperature, thereby keeping the internal heat conduction contribution to \bar{X} low as shown by the proximity of wall temperature to the energy line in Figure 27.

Another interesting feature of the model is also exhibited in Figure 27; increasing well depth has a limit in its ability to decrease B' . This figure was generated by increasing well depth up to 60 μm using Equation (74), then adding a multiplicative factor to the exponent, keeping the 60 μm value constant in the trigonometric

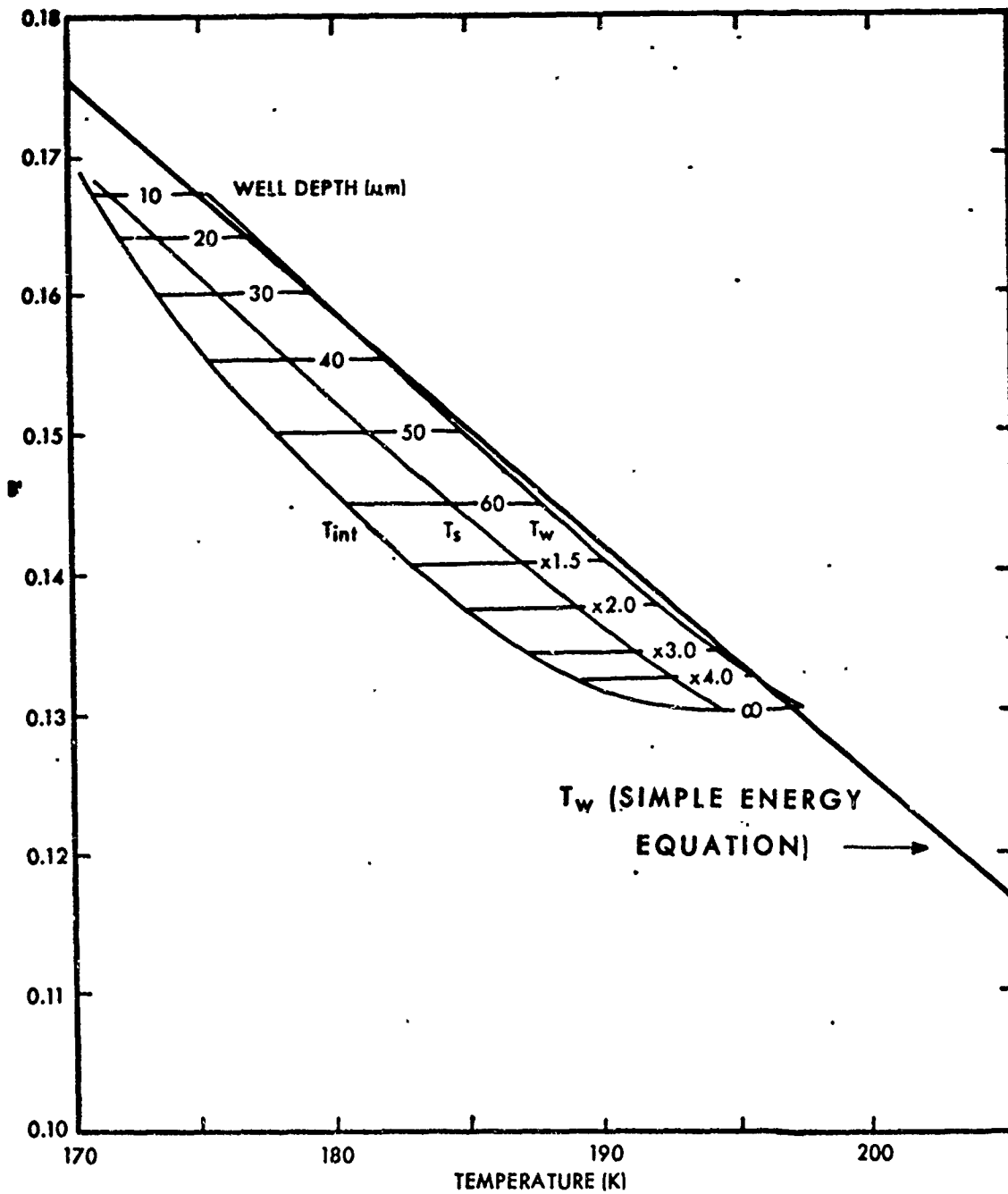


Figure 27. Effect of Well Depth on Stagnation Point Ablation Response of Composite With Equilibrium Sublimation Model and Side Wall Well Diffusion Depth Equal to Stagnation Point Depth
 ($T = 273\text{K}$, $P = 0.967 \text{ atm}$)

expression. Hence, effective well depths in excess of 60 μm were generated and indicated by the factor on the chart. The value $\times 1.5$ can be interpreted as a well with an effective depth 1.5 times that of the ideal 60 μm depth. When the combination of mass flux and well depth reaches a sufficiently high value, the concentration of CO_2 at the bottom of the well reaches 100%. The stagnation point wells saturate before the side wall wells since side wall mass flux is lower. Increasing depth no longer affects the stagnation point wells, but finally saturates the side wall wells which reach the same temperature as the stagnation point sublimation surface-the carbon dioxide surface temperature in equilibrium with carbon dioxide vapor with a partial pressure equal to the ambient pressure.

The mass flux and wall temperature predicted for the zero side wall well depth cases are shown in Figure 28. In these solutions there is a significant dependence on the manner in which well depth is varied. The predicted mass flux for the case of well depth as a function of edge velocity actually increases with distance from the stagnation point to about the 45 degree position, which was observed in some of the experiments.

Two Phase Flow Effect on Transfer Coefficients. The previous results were computed assuming that the boundary layer heat and mass transfer coefficients were unaffected by the presence of the glass beads. Reduced mass flux can

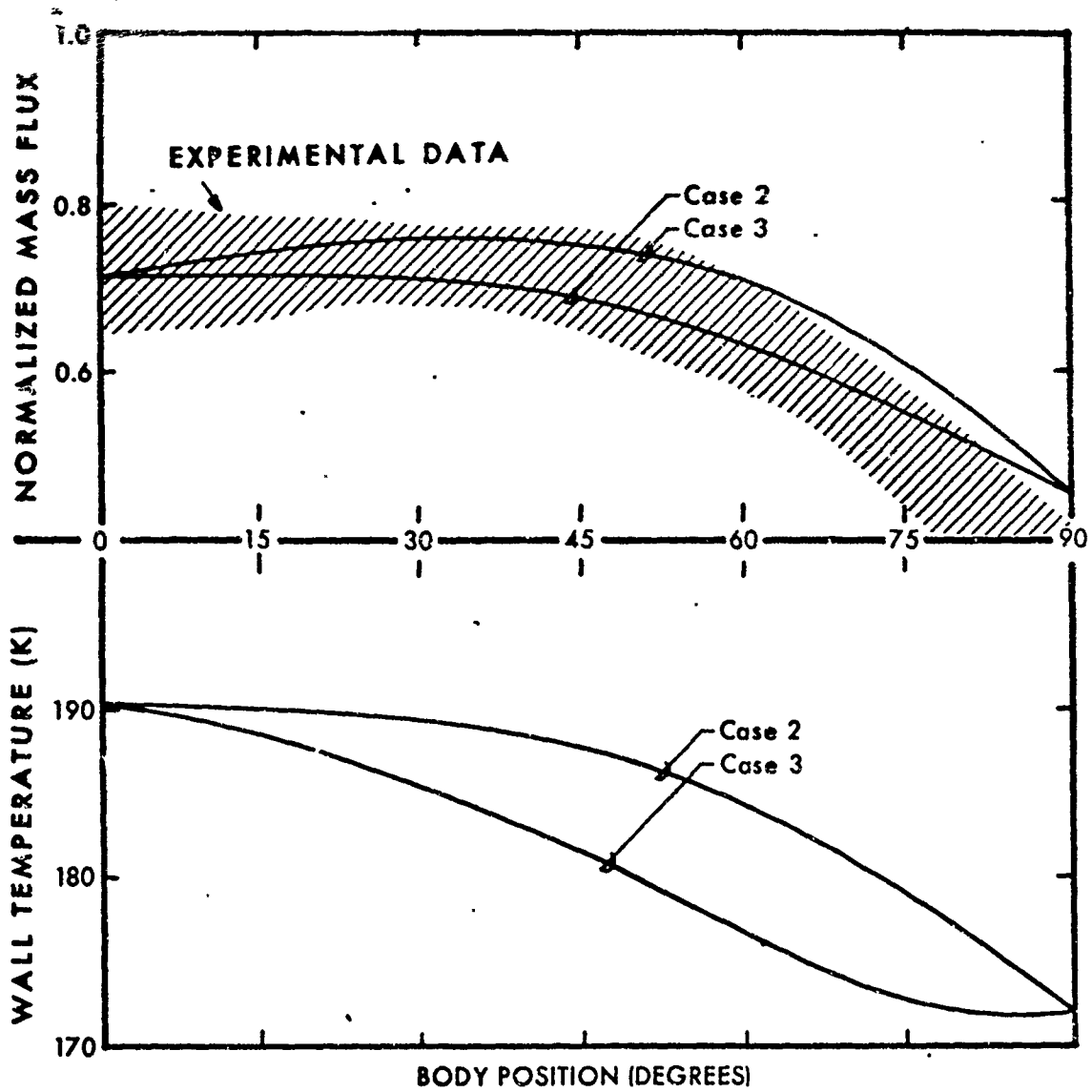


Figure 28. Theoretical Mass Flux and Wall Temperature Distribution for Composite With Equilibrium Sublimation Model ($T = 273\text{K}$, $P = 0.967 \text{ atm}$, $y = 80 \mu\text{m}$)

also be the result of a drop in transfer coefficient or a combination of changes in both B' and $\rho_e u_e C_H$. A parametric study was performed of the combinations of $\rho_e u_e C_H$, well depth, and coefficient of vaporization which would yield a mass flux of $0.0288 \text{ kg/m}^2 \cdot \text{s}$, which is equal to a 28% reduction of the simple theory mass flux prediction at the base line condition. The more probable zero side wall diffusion depth models were used. The results are shown in Figure 29; also shown are the predicted internal temperatures associated with the parametric combinations. It is evident from this figure that the knowledge of internal temperature and either well depth or coefficient of vaporization is sufficient to determine the combination of $\rho_e u_e C_H$ and B' responsible for the reduced mass flux.

The most consistent explanation of the experimental results was obtained by using the average recorded minimum temperature, 182K, as the internal temperature and the previously deduced value of coefficient of vaporization, 0.0005. The intersection of these values on Figure 29 occurs near the $40 \mu\text{m}$ well depth curve and corresponds to a transfer coefficient of $0.213 \text{ kg/m}^2 \cdot \text{s}$. The average well depth, which is two thirds of the bead radius, seems reasonable. The slight reduction in transfer coefficient is not altogether unexpected since the beads must be accelerated at the expense of boundary layer gas momentum which thickens the boundary layer. With higher velocities and, consequently, higher Reynolds numbers, the effect on

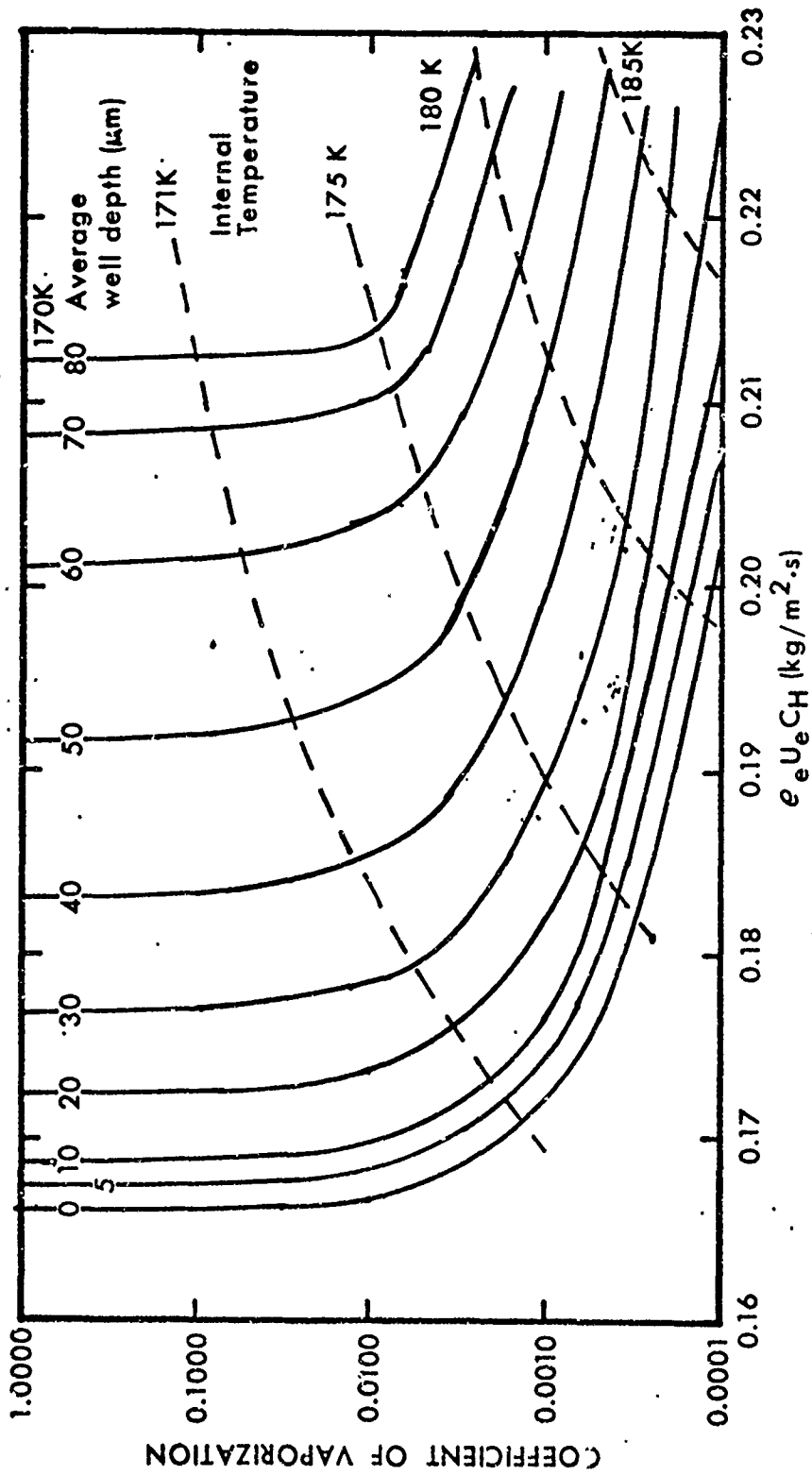


Figure 29. Parametric Combinations of Coefficient of Vaporization, Well Depth, and Transfer Coefficient Which Will Result in the Stagnation Point Mass Flux 0.0288 kg/m².s and the Resulting Internal Temperatures (T = 273K, P = 0.967 atm, Side Wells have Negligible Diffusion Depth)

transfer coefficient could be reversed. The disturbances caused by the solid particles and the rough wall would be expected to cause boundary layer transition to turbulent flow at a lower than usual Reynolds number, which would be accompanied by the increased heat transfer associated with turbulent flow (Ref 19:509). Prior to transition, the rough wall has little effect on the laminar transfer coefficients (Ref 19:580).

It should be recognized that the single embedded thermocouple does not provide the important temperature variations in time and space required to definitely specify the internal temperature; yet the fact that the recorded temperature remained for a significant period at or very near the asymptotic value suggests that the indicated minimum temperature is a good estimate of the internal temperature for the theoretical model. Future experimentation could revise the value for the coefficient of vaporization; although, as shown in Figure 29, greater values would require deeper and, therefore, more unreasonable well depths. In fact this theoretical model predicts that values of coefficient of vaporization greater than about 0.0015 are not admissible with a 182K internal temperature.

The optimum analytical model to correlate the data of this experiment is that the glass beads caused a 6% reduction in the stagnation point boundary layer transfer coefficient and a 23% drop in B' due to the presence of beads at the surface. The effect of this model on mass

flux and temperature is compared to the experimental data in Figure 30 as a function of the single phase flow transfer coefficient. This plot is based on the assumption that the two phase flow effect has caused a constant 6% reduction in transfer coefficient, which is probably a good assumption over the narrow range of the experiment. Further experimentation is required to improve the functional relationship with transfer coefficient.

Relative Magnitudes of Correction Terms

The actual value of each correction varied with the particular case chosen; however certain trends were evident. Two of the contributions to \bar{X} , the increase in enthalpy of the glass beads and the evolved gas from T_s to T_w , were always quite negligible compared to the heat absorbed by sublimation. Typically they were only one percent each for the base line solutions. The relative radiation flux term was a negative two percent effect at the base line condition, and internal conduction at the stagnation point varied from one percent to nearly four percent for the equilibrium solutions which had the lowest side wall temperatures. Since the radiation term has the opposite sign from the other contributions, the net correction to the energy equation was never very significant. This is graphically illustrated in Figures 24, 26, and 27 by the fact that the predicted wall temperature is quite close to the reference line plot of the simple energy equation.

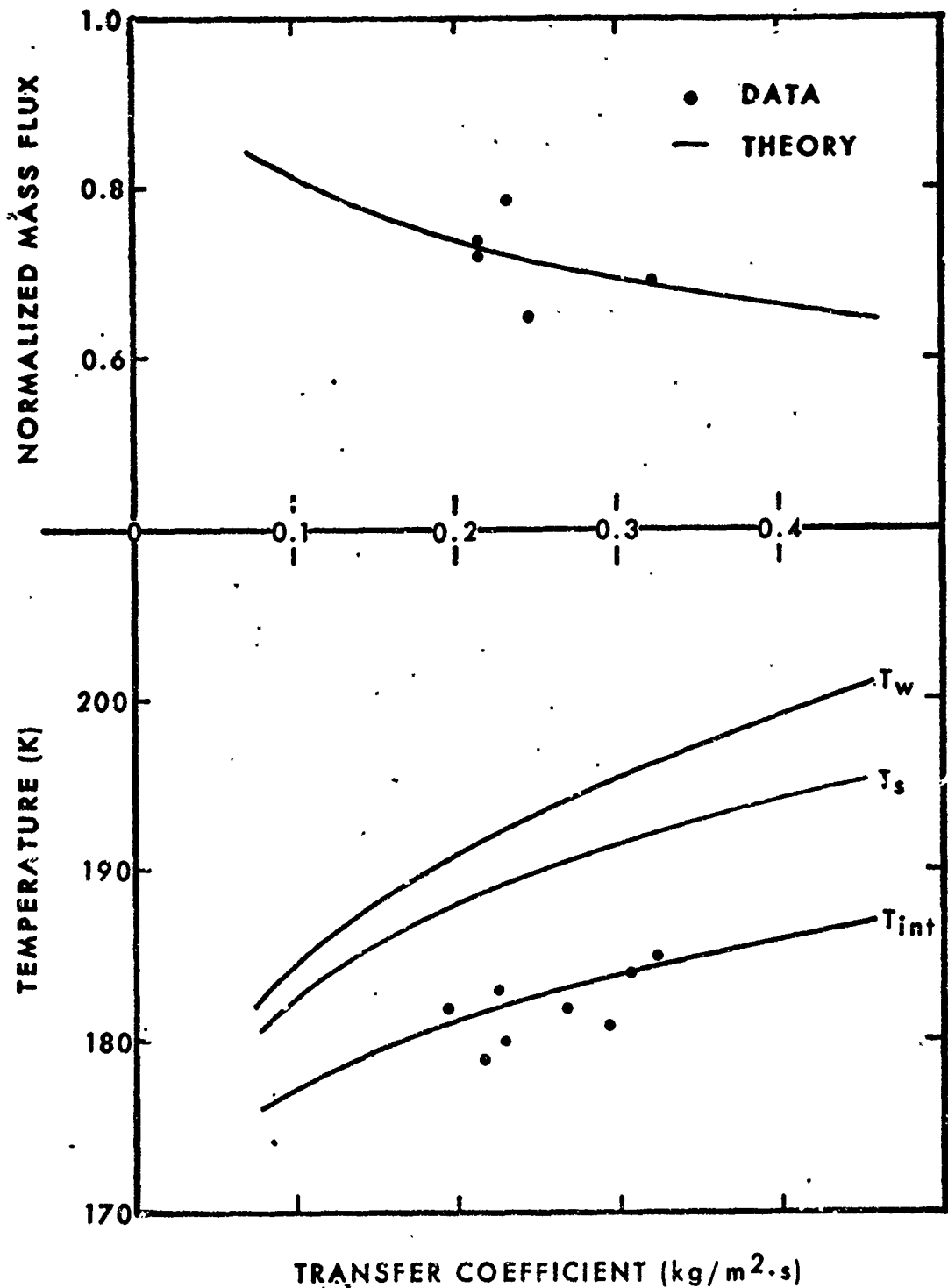


Figure 30. Comparison of Experimental Data and Theoretically Predicted Stagnation Point Mass Flux and Model Temperature as a Function of Heat Transfer Coefficient ($T = 273K$, $P = 0.967 \text{ atm}$, $\alpha = 0.0005$, $y = 40 \mu\text{m}$, Side Wall Wells Have Negligible Diffusion Depth)

The transient conduction was estimated using the solutions presented in Schneider (Ref 20:246). While heat and mass transfer processes actually begin when the model is removed from the mold, an upper bound for the transient conduction can be established if it is assumed that the model temperature is initially uniform at the measured internal temperature at the time of model insertion (Figure 13-A) and subjected to an instantaneous change in surface temperature to the asymptotic temperature (Figure 13-B). Since the area of interest is the hemispherical nosetip, the solution for a sphere is used. The thermal conductivity and diffusivity of both pure CO₂ and the composite are approximately equal; therefore the internal heat flux for all models is approximately the same. The result of this analysis was that the transient heat flux is initially very high and can remain a significant contribution to the energy equation for approximately thirty seconds. The heat flux is toward the surface, a negative contribution to \bar{X} , and consequently causes a higher mass flux. The initial assumptions for this analysis must have been too conservative since no general trend of high initial mass transfer rates was observed. The heat and mass transfer generated in the free convection portion of the experiment must have established the internal temperature gradient well enough that the transient effects were negligible. Therefore, transient heat conduction was not included in the improved modeling of this experiment.

The most significant effects were caused by alterations in the application of the simple conservation of species equation. Because of the diffusion wells, the concentration of CO_2 was attenuated 69% from the subliming surface to the fluid dynamic wall at the stagnation point for the nonequilibrium solution. The deeper wells required for the equilibrium solutions caused an attenuation of more than 75%. The nonequilibrium sublimation effect, which caused a 0.12 atm reduction in CO_2 partial pressure for the pure CO_2 predictions, was amplified to an 0.73 atm reduction because of the higher local mass flux due to the blockage of surface area by the glass beads. The two phenomena, diffusion well attenuation and nonequilibrium sublimation, have the similar net effect in that they cause a reduction of the available CO_2 concentration at the wall for a given surface temperature. This reduces the potential B' in accordance with Equation (17) or (19), which results in a higher wall temperature to satisfy the energy equation. The difference in temperature from the subliming surface to the fluid dynamic wall was only about three degrees. While this had a negligible effect on the energy equation, it decreased the convective heat flux to the surface by about three percent, reducing the energy available for sublimation and, hence, the B' .

General Applicability of Results

This research is the first investigation of thermo-mechanical ablation in which a known amount of solid

material was introduced into the boundary layer of an ablating body. The solid addition resulted in significant departures from pure thermochemical ablation performance. The causes of the different response have been identified. It is the purpose of this section to discuss those phenomena which have applicability to the ablation performance of actual reentry vehicle materials or more general applicability.

The commonly used assumption that the thermomechanically removed material departs the surface with the same enthalpy as the material coming up to the ablating surface was shown to be not always true, but probably a good approximation. The mechanically removed mass fraction in the simulation was very high, 0.71, which would tend to amplify this effect. Yet, in spite of the definite temperature increase of the beads, when properly normalized, the increase in solid enthalpy contributed only a 1% correction to the energy equation.

The possibility of two phase flow effects on the boundary layer transfer coefficients has general applicability. For the conditions of the experiment, a 6% reduction in transfer coefficient was realized. This is generally less than the precision of current ablation test data, or accuracy of prediction capability, but must be considered as ablation prediction and testing techniques improve. The utilization of the techniques of this experiment to investigate two phase boundary layer phenomena in

general has promise. The data reduction and analytical techniques required to determine the effects on transfer coefficient have been developed in this research.

The concentration attenuation through the diffusion wells; which had a large influence on this experiment, probably also affects the ablation performance of graphites and composite materials. Real materials are not perfectly homogeneous; as ablation progresses the surfaces roughen and lower density matrix areas recede faster than higher density grains or re-inforcements (Ref. 9 and 17). Micro-cracking increases indepth porosity and some indepth sublimation occurs (Ref 9). The glass bead simulation produced diffusion wells which were easily modeled because of the nonsubliming walls; yet every ablating rough wall, especially in the vicinity of the stagnation point, has regions which are not realizing the full benefit of the convective currents of the boundary layer. Therefore, the diffusion well effect is probably present, to some degree, whenever ablation occurs.

Of general interest is the result that CO_2 exhibits a rather strong nonequilibrium effect. Since no reference to this could be found in the literature, this should be independently verified. Embedding nonsubliming particles in a subliming substance is a unique method of amplifying nonequilibrium effects by blocking the area available for mass transfer. Unfortunately, since the question of nonequilibrium sublimation of graphite is of current

interest,* there is no known substance which can perform the same function at the temperatures of ablating graphite (greater than 3500K). Currently, graphite specimens are being arc jet tested over a large range of transfer coefficient to determine the departure from equilibrium predictions. The surface roughness of ablating graphite probably tends to alleviate the nonequilibrium effect since roughness increases the surface area available for mass transfer.

* AFML Contract F33615-74-C-5094 with the Acurex Corporation

VII. Conclusion

The heat and mass transfer effects of thermomechanical ablation were investigated by simulating this phenomena with embedded glass bead spheres in solid carbon dioxide (CO_2) ablation models. Composite and pure CO_2 models, which were approximately 25 mm diameter hemispherical forebodies with cylindrical afterbodies, were ablated in a low speed jet at approximately ambient pressure and 0°C conditions. The pure CO_2 models performed generally in the manner predicted by simple equilibrium ablation theory and laminar heat transfer results; however, the stagnation point mass flux was 6.2% lower than that predicted and the temperature was slightly higher. These anomalies can be explained as a nonequilibrium sublimation effect, with a coefficient of vaporization of 0.0005 yielding the best fit of the experimental data. The effect of the glass bead addition was threefold: (1) The CO_2 mass flux was reduced by 23% at the stagnation point, which was 28% below the simple ablation theory prediction. (2) The CO_2 mass flux around the hemisphere did not monotonically decrease with distance from the stagnation point, but remained constant or increased slightly with distance from the stagnation point to beyond the 45 degree location before decreasing. (3) The internal temperature was increased approximately 3K.

A reduction in analytically predicted mass flux can be accomplished by reducing either the transfer coefficient, $\rho_e u_e C_H$, or the potential for mass transfer, B' . An analysis was performed which considered the possibility of a reduced transfer coefficient and modeled those phenomena which could change the predicted B' , which is generally accompanied by a change in model temperature. The modeled effects were nonequilibrium sublimation, radiative heat transfer, internal heat conduction, concentration attenuation through the diffusion wells caused by the protrusion of the densely packed glass beads through the CO_2 surface, and the consequences of heat flux through the glass beads to the subliming surface. The average diffusion well depth was left as a free parameter in the analysis.

The most consistent explanation of the data was that in the ablation of the composite models there was a 6% reduction in the boundary layer transfer coefficient due to two-phase flow effects and a 23% reduction in the B' . The reduction in B' was primarily the result of reduced available CO_2 at the fluid dynamic wall due to the combined effects of (1) concentration attenuation through diffusion wells with an average depth of $2/3$ of the radius of the glass beads, and (2) reduced surface area available for sublimation which amplified the nonequilibrium sublimation effect. Some reduction in mass flux was due to the insulating effect of the glass beads which maintained a 3K degree drop in temperature between the fluid dynamic wall and the

subliming surface, and the predicted steady state internal heat flux from the stagnation point to the side walls. Radiative heat flux, transient internal conduction, and reduced heat flux to the CO_2 due to the increase in glass bead temperature at the surface were relatively insignificant.

This research yielded aspects of the ablation process which are applicable to reentry vehicle materials. The diffusion well effect is probably present, to some degree, for any ablating material. Two phase flow effects on the boundary layer transfer coefficients should be considered whenever a large fraction of solid material enters the boundary layer. The commonly used assumption that the solids depart the surface with the same enthalpy as the material coming up to the surface has been shown to be a good approximation.

VIII. Recommended Improvements to the Experiment

Further experimentation is recommended to confirm the value used for the coefficient of vaporization, improve the estimate of internal temperature, and further investigate the two phase flow boundary layer phenomena.

An independent estimate of the coefficient of vaporization should be made using existing physical chemistry procedures such as the Knudson Cell Experiment. In lieu of that, the problem can be indirectly addressed by performing the ablation experiment with smaller beads. The result of bead radius on B' , as predicted by equilibrium and non-equilibrium models, is shown in Figure 31. The equilibrium model predicts a gradual trend toward the simple ablation model prediction as bead radius and, hence, well depth decrease. The nonequilibrium solution predicts only a slight change in B' and T_w since the percentage of surface area blocked by the beads is not a function of bead size; therefore, the nonequilibrium effect remains constant even though the diffusion well depth is reduced.

Improved temperature measuring capability is strongly recommended in any future experiments. An increased number of quick response thermocouples precisely positioned with protection from the influence of the center rod would resolve questions of actual internal temperature and internal temperature gradients influencing either transient

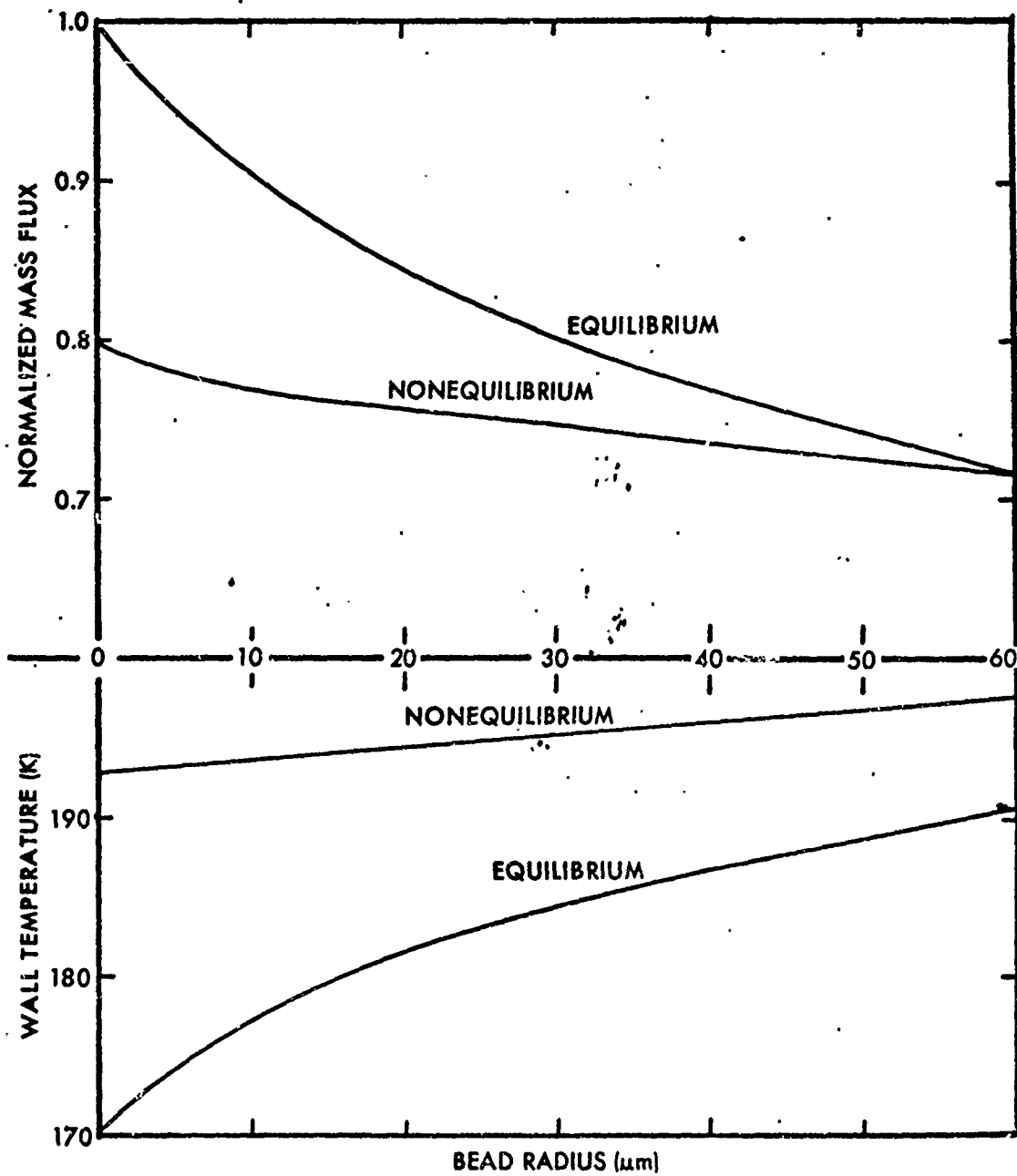


Figure 31. The Effect of Bead Size on Normalized Mass Flux and Wall Temperature

or steady heat conduction.

The possibility of reduced boundary layer transfer coefficients due to two-phase flow effects could be further investigated using beads of varying density. Reduced bead material density would certainly reduce the two phase flow effect on the boundary layer; yet the net effect on predicted B' and internal temperature would be negligible since this would only affect the solution through the corrections to the energy equation which were quite insignificant.

Bibliography

1. Baker, R. L. "Graphite Ablation Chemistry Non-equilibrium Effects." AIAA Paper No. 75-735 presented at AIAA 10th Thermophysics Conference, Denver, Colorado, May 1975.
2. Bartlett, E. P. and R. M. Kendall. An Analysis of the Coupled Chemically Reacting Boundary Layer and Charring Ablator. Part 3. Non-Similar Solution of the Multicomponent Laminar Boundary Layer by an Integral Matrix Method. NASA-CR-1026, June 1963. (Issued by originator as Aerotherm Report No. 66-7, Part III.)
3. Dorrance, W. H. Viscous Hypersonic Flow. New York: McGraw-Hill Book Company, Inc. 1962.
4. Eckert, E. R. G. and R. M. Drake, Jr. Heat and Mass Transfer. New York: McGraw-Hill Book Company, Inc. 1959. p 493ff.
5. Gazley, C., J. Gross, and D. J. Masson. "Mass Transfer Cooling in High-Velocity Flight." Third Symposium on High-Speed Aerodynamics and Structures. San Diego, California, Vol 1, 1958, pp 295-347.
6. Giaque, W. F. and C. J. Egan. "Carbon Dioxide, The heat capacity and vapor pressure of the solid. The heat of sublimation. Thermodynamic and spectroscopic values of the entropy." J. Chem. Physics, 5, 1937, pp 45-54.
7. Gotoh, K. "Thermal Conductivity of Two-Phase Heterogeneous Substances." Int. J. Heat and Mass Transfer, 14, 1971. p 645.
8. Kays, W. M. Convective Heat and Mass Transfer. New York: McGraw-Hill Book Company, Inc. 1966.
9. Kratsch, K. M., R. B. Dirling, Jr., and C. E. Swain. Erosion Mechanisms and Improvement of Graphite Materials. AFML-TR-70-307, Vol IV. May 1973.
10. Kratsch, K. M., M. R. Martinez, F. I. Clayton, R. B. Greene, and J. E. Wuerer. "Graphite Ablation in High Pressure Environments." AIAA Paper No. 68-1153, Dec 1968.

11. Kubota, T. "Ablation With Ice Model at $M = 5.8$." ARS Journal, Dec 1960, p 1164-1169.
12. Lees, L. "Convective Heat Transfer with Mass Addition and Chemical Reactions." Combustion and Propulsion, Third AGARD Colloquium, Mar 1958, Palermo, Sicily, New York: Pergamon Press.
13. Lundell, J. H. and R. R. Dickey. "Graphite Ablation at High Temperatures." AIAA J., II, 3, 1973. p 216.
14. Lyon, C. A. The Design and Construction of a Low Turbulence, Quiet, Free Jet Wind Tunnel. Air Force Institute of Technology Thesis. GAM/AE/73-3, 1973.
15. Maass, O. and W. H. Barnes. "Some Thermal Constants of Solid and Liquid Carbon Dioxide." Proc. Roy. Soc. A111, 1926. p 224-44.
16. Rindall, R. A. An Evaluation of Design Analysis Techniques for High Performance Ballistic Vehicle Graphite Tips, Appendix D. Thermochemical and Thermomechanical Ablation. AFML-TR-69-73, Vol IV, Jan 1970.
17. Ross, E. M. The Carbon-Carbon Assessment Program. AFML-TR-74-39, Sep 1974.
18. Scala, S. M. and G. L. Vidale. "Vaporization Processes in the Hypersonic Laminar Boundary Layer." Int. J. Heat and Mass Transfer, 1, 1960. p 4-22.
19. Schlichting, H. Boundary Layer Theory. New York: McGraw-Hill Book Company, Inc. 6th ed., 1968.
20. Schneider, P. J. Conductive Heat Transfer. Reading, Massachusetts: Addison-Wesley Publishing Company, Inc., 1955.
21. Shvab, V. A. "Relation Between the Temperature and Velocity Fields of the Flame of a Gas Burner." Sbornik Issledovani Professor Gorenia Naturalnogo Topliva. Gas. Energ. M. L., 1948.
22. Smith, A. M. O. and J. Pierce. Exact Solution of the Newmann Problem. Calculation of non-circulatory plane and axially symmetric flows about or within arbitrary boundaries. Douglas Report No. ES 26988, Apr 1958.
23. Spalding, D. B. "The Prediction of Mass Transfer Rates When Equilibrium Does Not Prevail at the Phase Interface." Int. J. Heat and Mass Transfer, 2, 1961. pp 283-313.

24. Spalding, D. B. "A Standard Formulation of the Steady Convective Mass Transfer Problem." Int. J. Heat and Mass Transfer, 1, 1960. pp 192-207.
25. Spalding, D. B. and F. A. Christie. "Solid Carbon Dioxide Sublimation at an Axisymmetric Stagnation Point." Int. J. Heat and Mass Transfer, 8, 1965. pp 511-514.
26. Zeldovich, Y. B. "On the Theory of Combustion of Initially Unmixed Systems." Zhurnal Teck. Fiz., 19, 10, 1944. pp 1199-1210. (Translated as NACA Technical Memorandum No. 1296, Jun 1950)

APPENDICES

APPENDIX A

BLIMP

The Boundary Layer Integral Matrix Procedure (BLIMP) was written by Bartlett and Kendall (Ref 2). This code can compute a boundary layer along an ablating body including the nonsimilar terms for a general chemical system and incorporates approximate formulations for mixture transport properties, including unequal mass diffusion and thermal diffusion coefficients for all species. A laminar flow solution was obtained up to the hemisphere-cylinder tangent using the velocity distribution shown in Figure 3. BLIMP was run in the mode which uses a complete surface mass and energy balance for wall boundary conditions with the "quasi-steady" assumption that $\dot{q}_{int} = \dot{m} (h_s - h_o)$, where \dot{q}_{int} is the heat conduction into the interior, and h_o is the enthalpy associated with the asymptotic interior temperature. In order to insure that the BLIMP prediction would be comparable to the approximate theory, the interior temperature assigned to the CO_2 for BLIMP was wall temperature predicted by the approximate theory. The "air" for BLIMP was a mixture of oxygen and nitrogen. The input environmental conditions were: $P = 0.976$ atm, $T = 273K$, velocity = 30.5 m/s, and nose radius = 10 mm.

BLIMP solves the boundary layer equations directly including the mass addition at the wall, so the unblown heat transfer coefficient and blowing correction are not normally determined. For purposes of comparison, BLIMP was run a second time with no mass addition at the wall and in the fixed wall temperature mode using the temperature computed with mass addition. The comparison for the stagnation point is shown in Table I in the body of the dissertation. The predicted heat transfer coefficient around the hemisphere is shown in Figure A-1. The predicted concentration profiles across the stagnation point boundary layer are shown in Figure A-2.

After the BLIMP run, it was discovered that the input CO_2 vapor pressure-temperature equilibrium correlation was not very accurate in the temperature regime of interest for the experiment. Since the primary purpose of the BLIMP was the verification of the simple theory and the prediction of the relative distribution of heat and mass flux around the hemisphere, it was not necessary to perform a computation with the improved correlation.

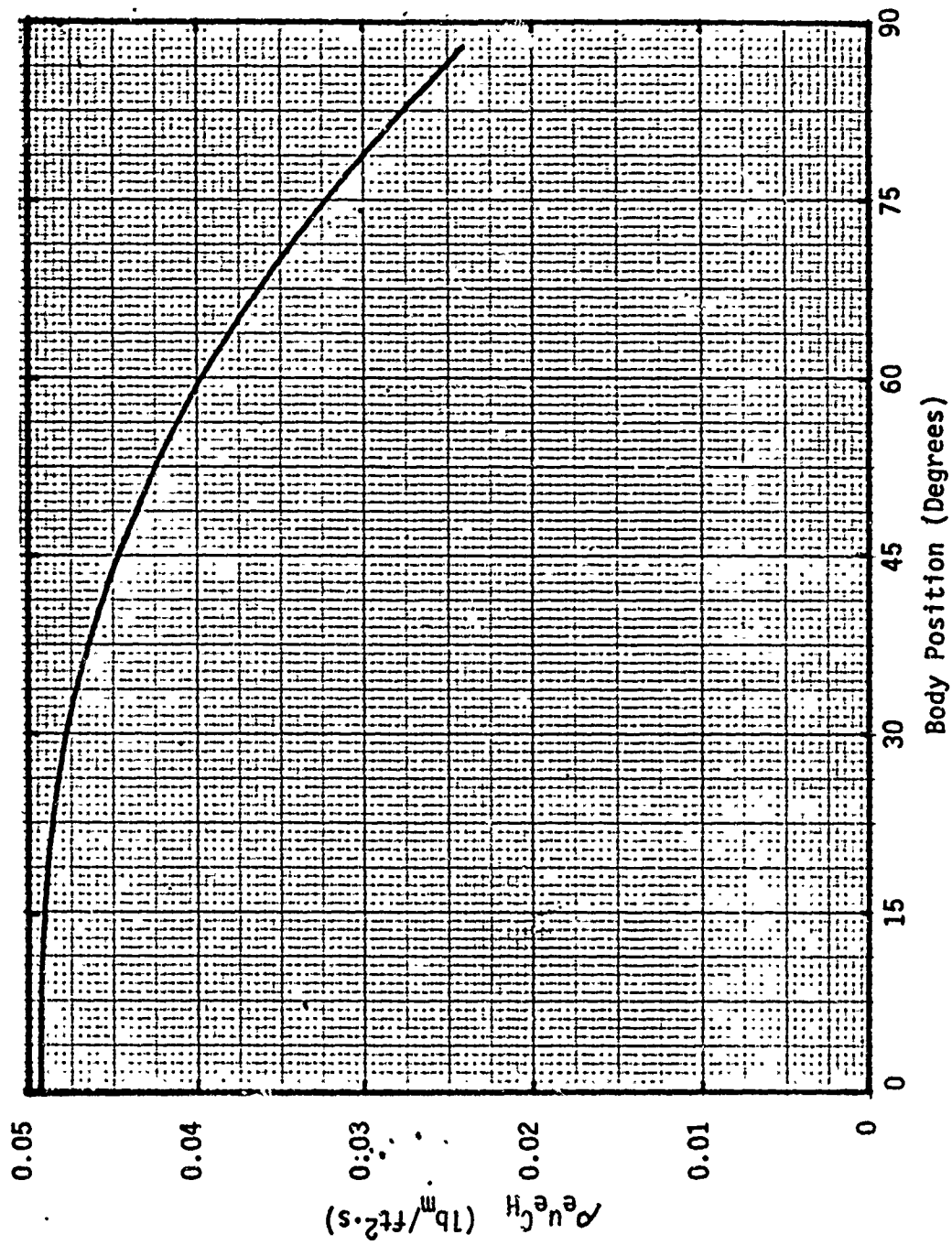


Figure A-1. Heat Transfer Distribution Predicted by BLIMP

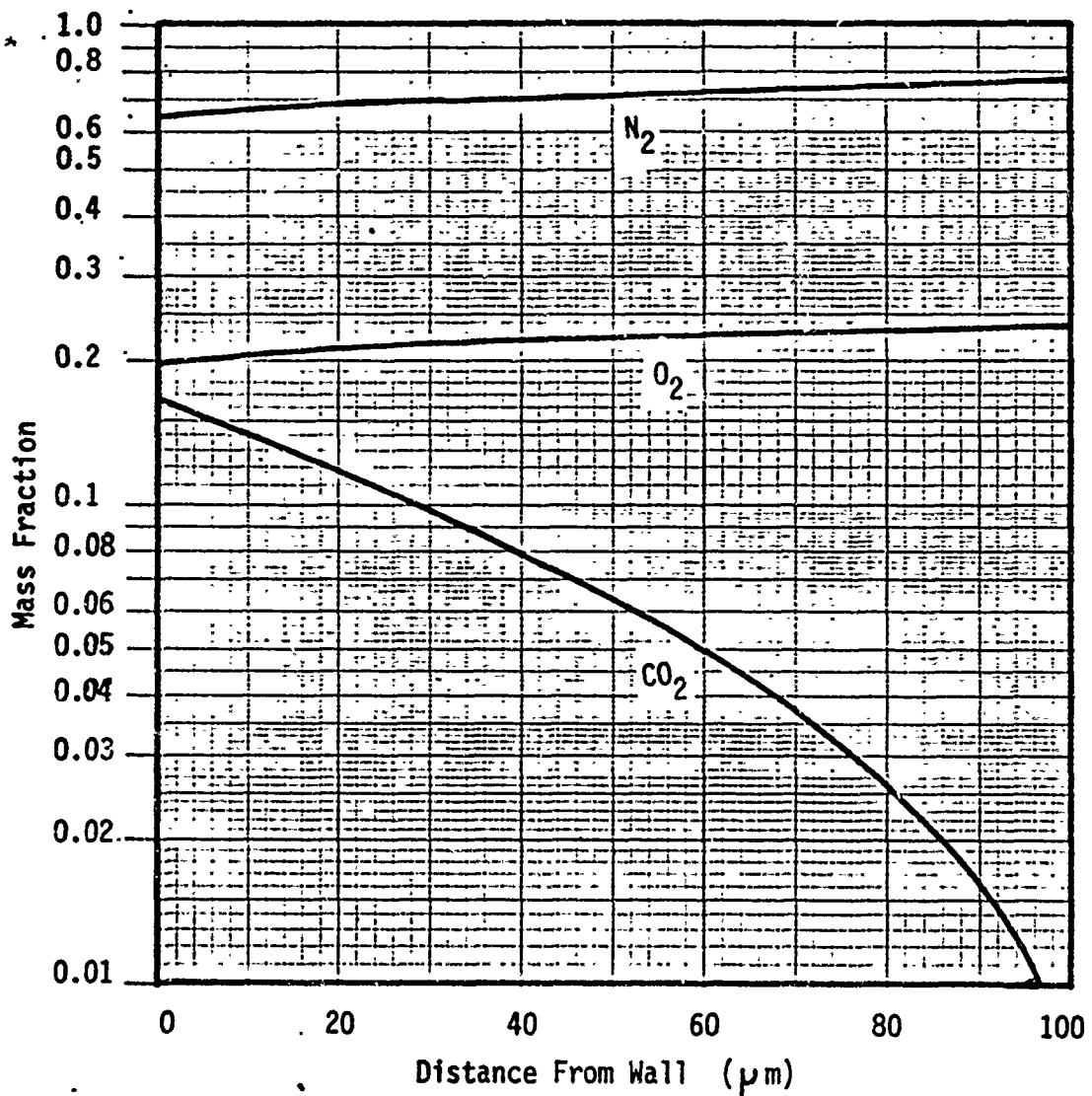


Figure A-2. Concentration Profiles Through the Stagnation Point Boundary Layer

APPENDIX B

	Page
B' versus Wall Temperature for CO ₂ in Air with Experimental Conditions Shown	103
Experimental Asymptotic Temperature Values	104
Summary of Reduced Data for Stagnation Point Mass Flux Prediction	105
Run 1	106
Run 2	114
Run 3	122
Run 4	130
Run 5	138
Run 6	145
Run 7	152
Run 8	159
Run 9	166

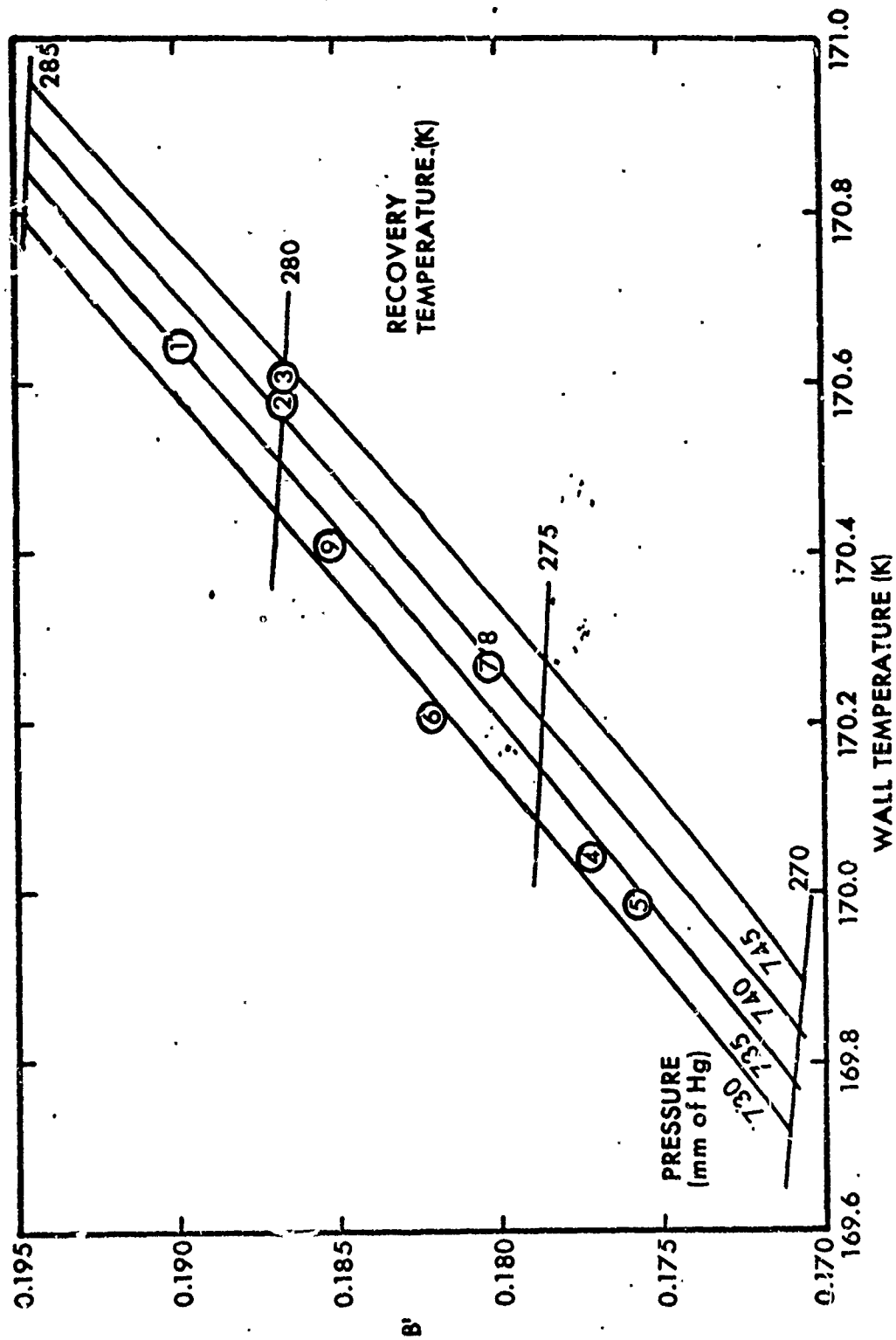


Figure B-1. B' versus Wall Temperature for CO_2 in Air with Experimental Conditions Shown

Experimental Asymptotic Temperature Values

Run		$\rho_{e^i e^c H}$ (kg/m ² .s)	Temperature (K)
New	Old		
Pure CO ₂ Data			
1	1	0.209	177
3	3	0.225	182
-	20	0.254	179
Composite Data			
-	7	0.292	181
-	10	0.267	182
4	11	0.324	185
5	12	0.248	182
-	15	0.225	183
6	16	0.224	183
-	18	0.194	182
-	19	0.307	184
9	22	0.217	179

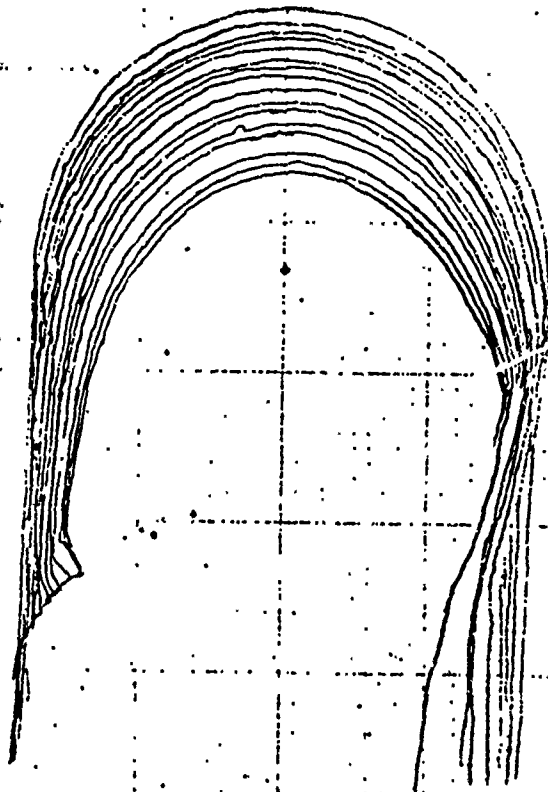
Summary of Reduced Data for Stagnation Point Mass Flux Prediction

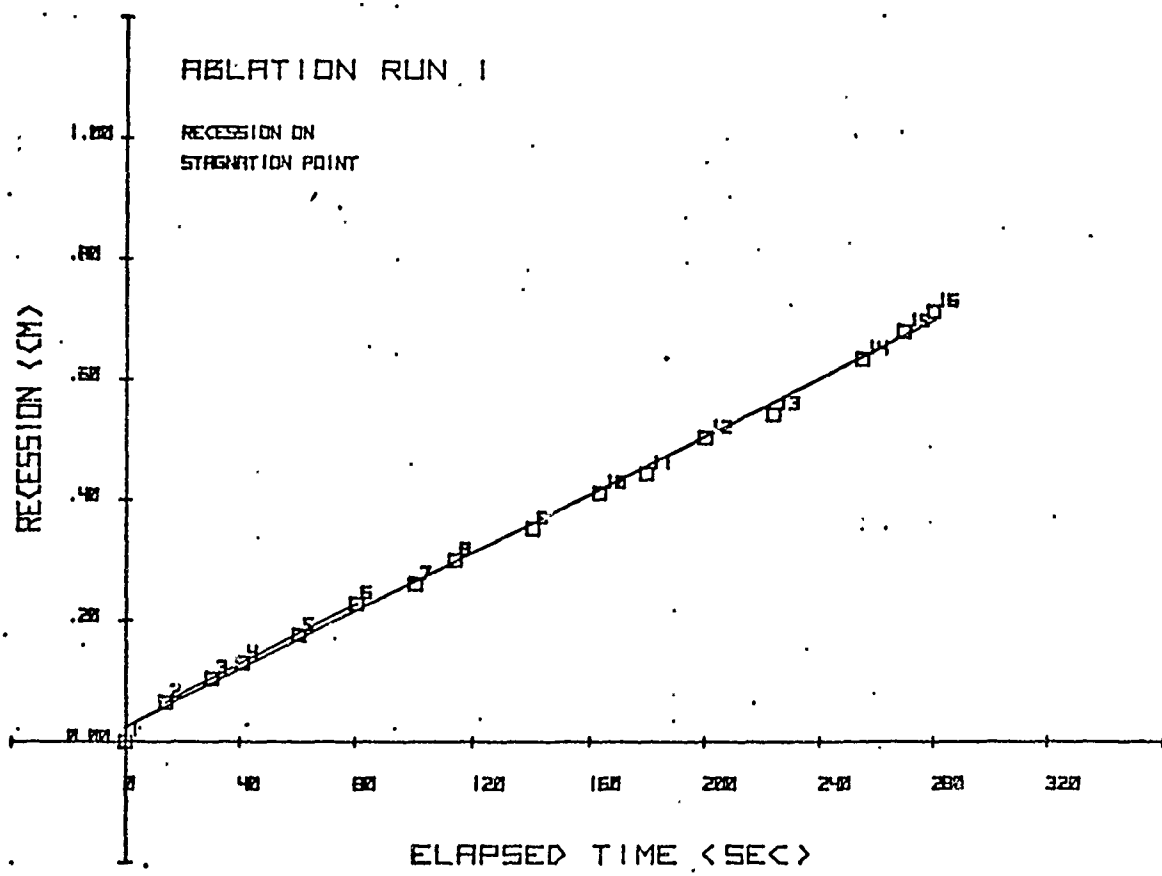
RUN	TEMPERATURE	PRESSURE	VELOCITY	RADIUS	REYNOLDS NO.	ρu_c	B'	T	STAG PT. m
	K	atm	m/s	mm		$\frac{e}{m^2 \cdot s}$		K	$\frac{kg}{m^2 \cdot s}$
1	282	0.970	20.0	11.6	23,700	0.209	0.190	170.6	0.0401
2	280	0.980	29.4	12.3	37,900	0.250	0.187	170.6	0.0465
3	280	0.977	24.3	12.3	31,100	0.225	0.187	170.6	0.0424
4	274	0.964	38.3	9.5	38,500	0.324	0.177	170.0	0.0575
5	273	0.964	28.0	11.9	35,600	0.248	0.176	170.0	0.0435
6	277	0.957	24.6	12.4	31,700	0.224	0.182	170.2	0.0411
7	276	0.972	21.4	11.8	26,700	0.216	0.180	170.3	0.0392
8	276	0.972	21.3	10.2	23,000	0.232	0.180	170.3	0.0421
9	279	0.964	18.6	10.1	19,500	0.217	0.185	170.4	0.0405

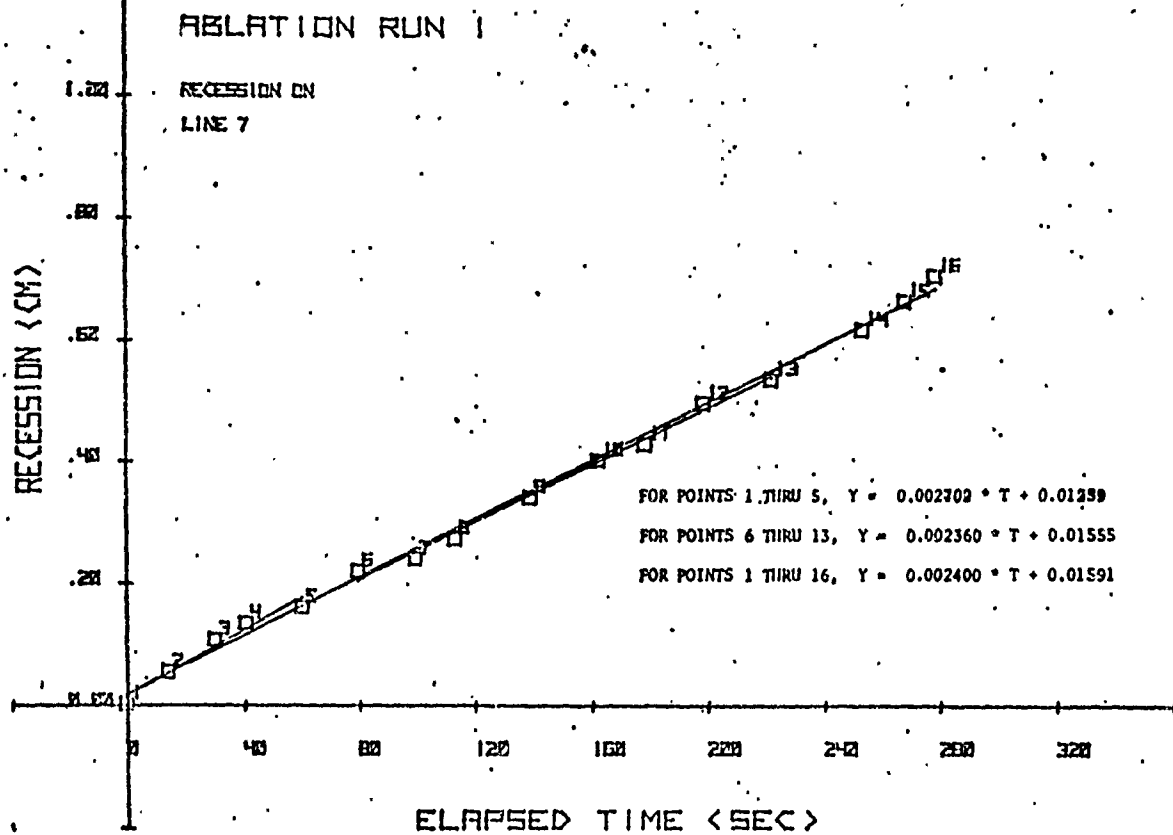
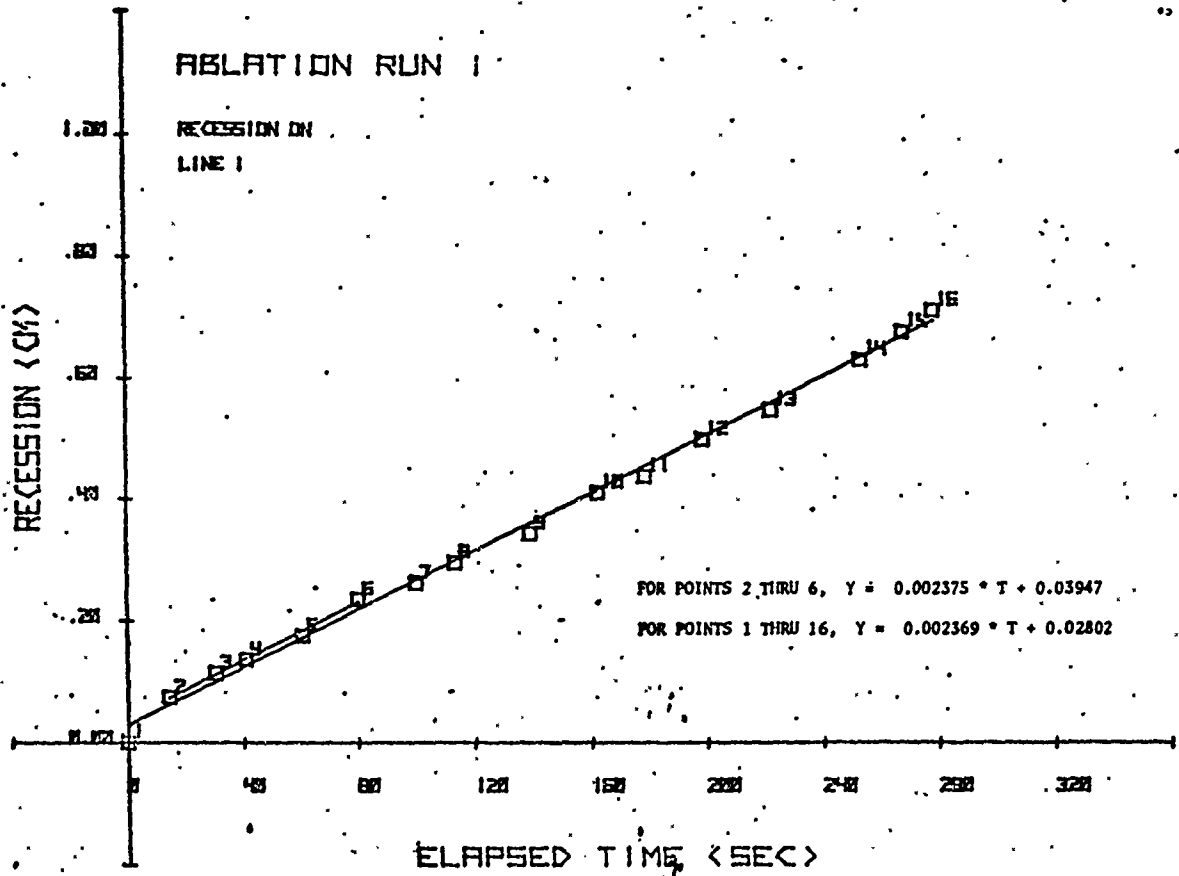
Run 1

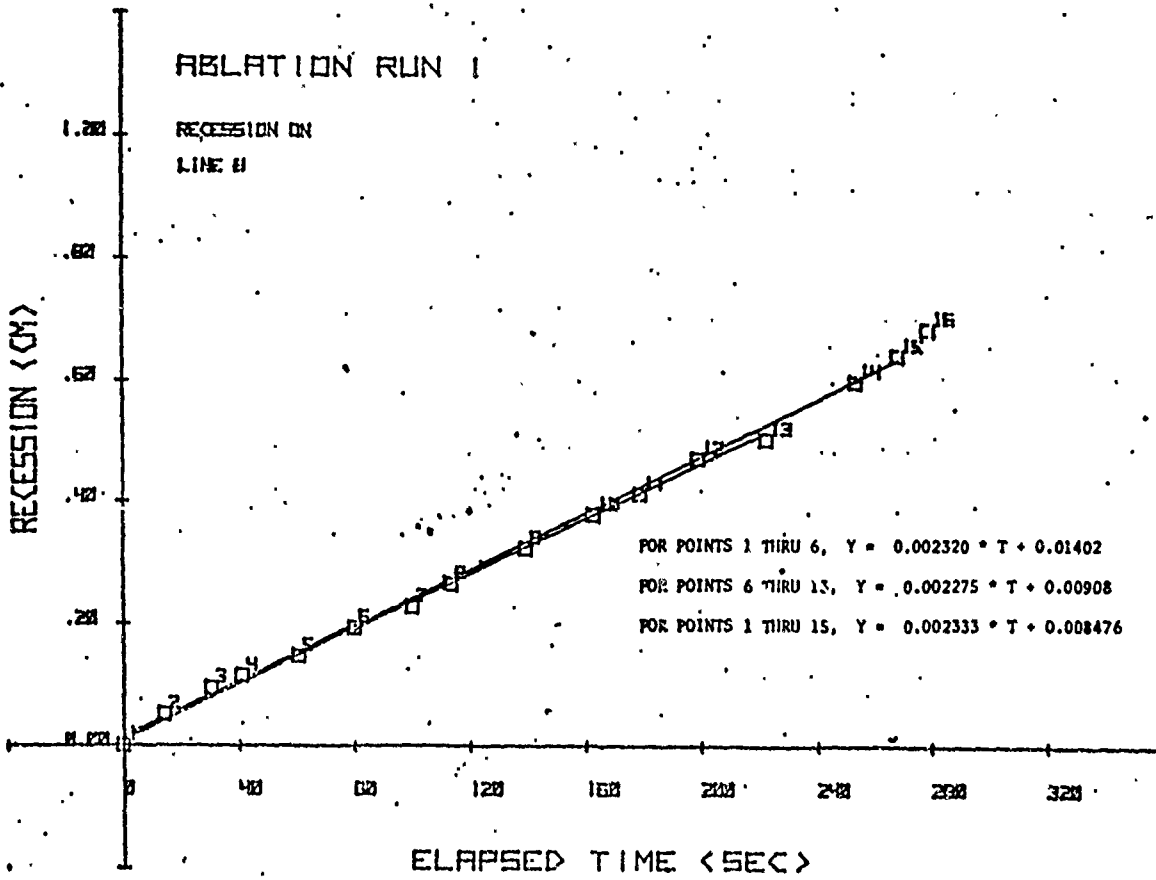
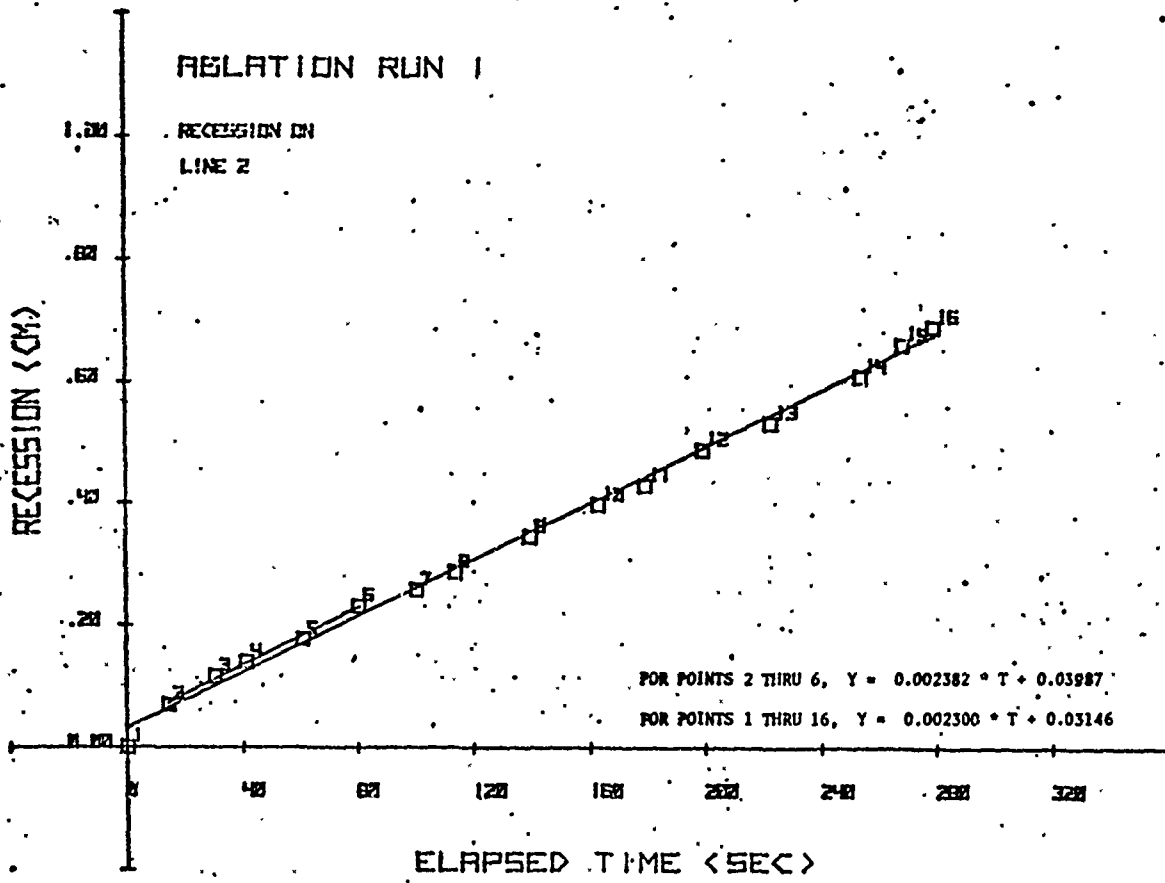
Simple Theory Stagnation Point Mass Flux: $0.00401 \text{ g/cm}^2 \cdot \text{s}$

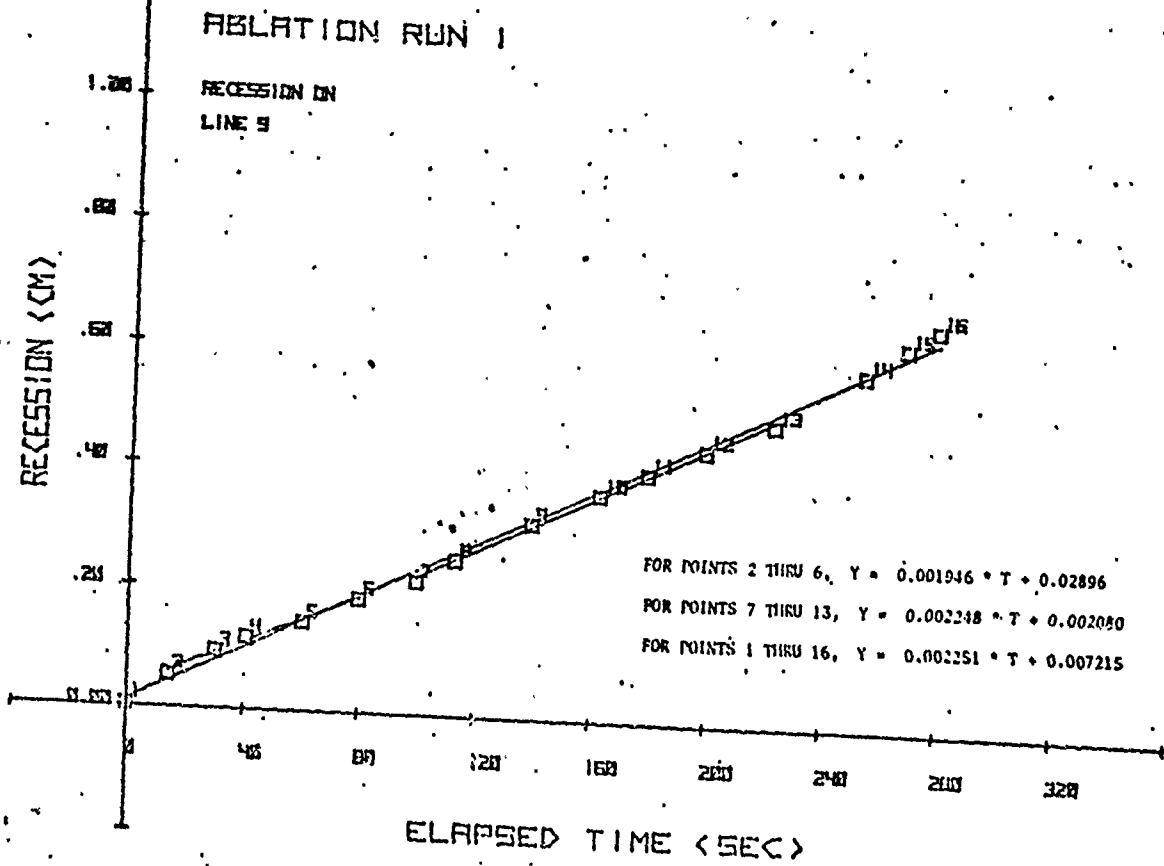
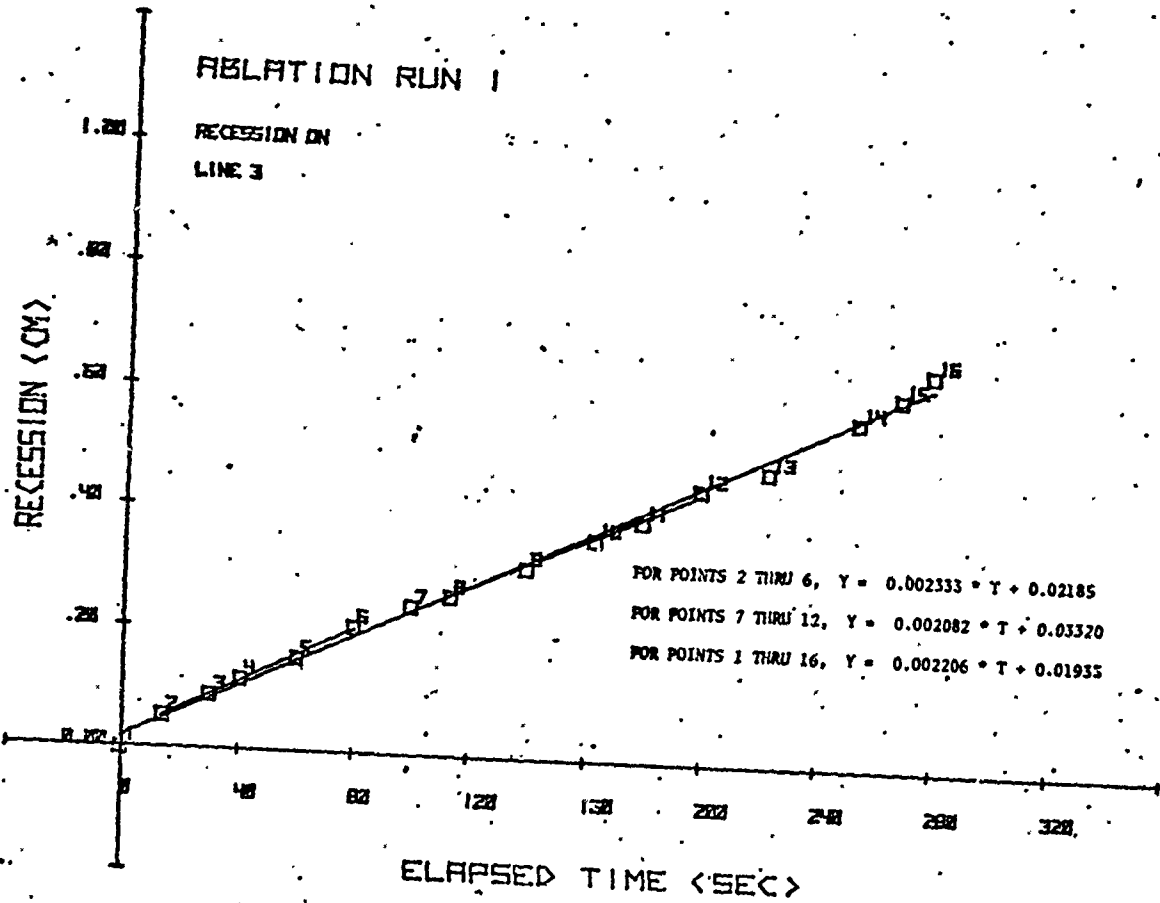
Position	Recession Rate $\text{cm/s (} \times 10^3 \text{)}$	Mass Flux $\text{g/cm}^2 \cdot \text{s (} \times 10^3 \text{)}$	Normalized
Stag Pt	2.450	3.92	0.978
15 right	2.375	3.80	0.948
15 left	2.399	3.84	0.957
30 right	2.382	3.81	0.950
30 left	2.319	3.71	0.925
45 right	2.333	3.73	0.930
45 left	2.251	3.60	0.898
60 right	2.107	3.37	0.940
60 left	2.104	3.37	0.840
75 right	1.892	3.03	0.757
75 left	1.871	2.99	0.746
90 right	1.407	2.25	0.561
90 left	1.268	2.03	0.506

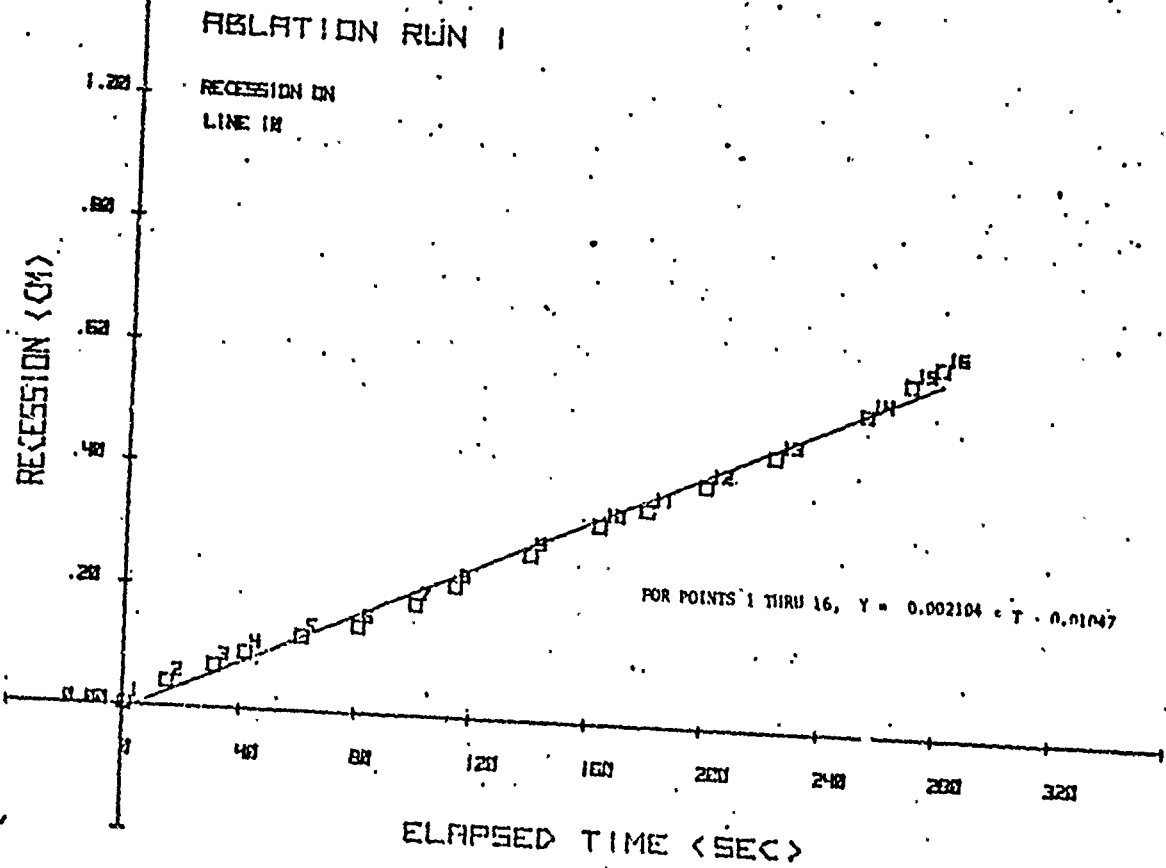
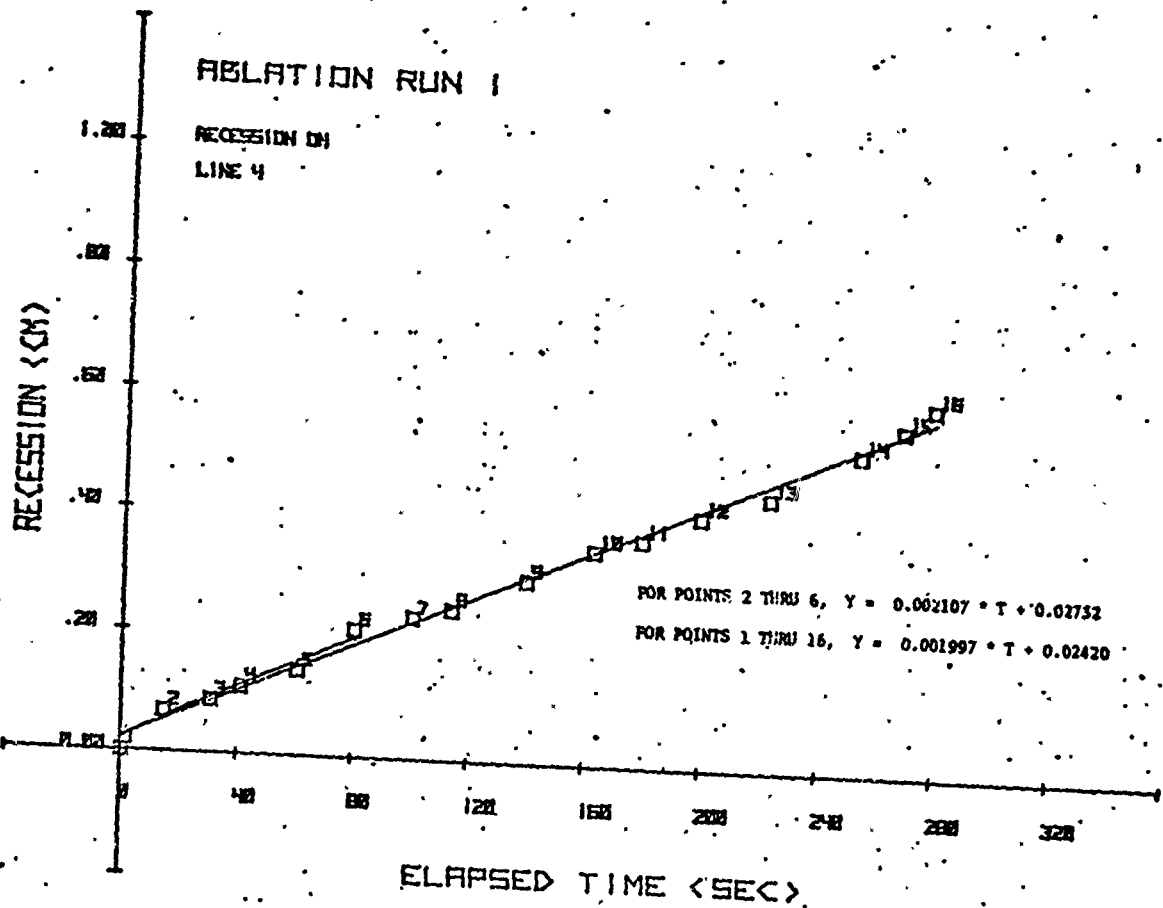


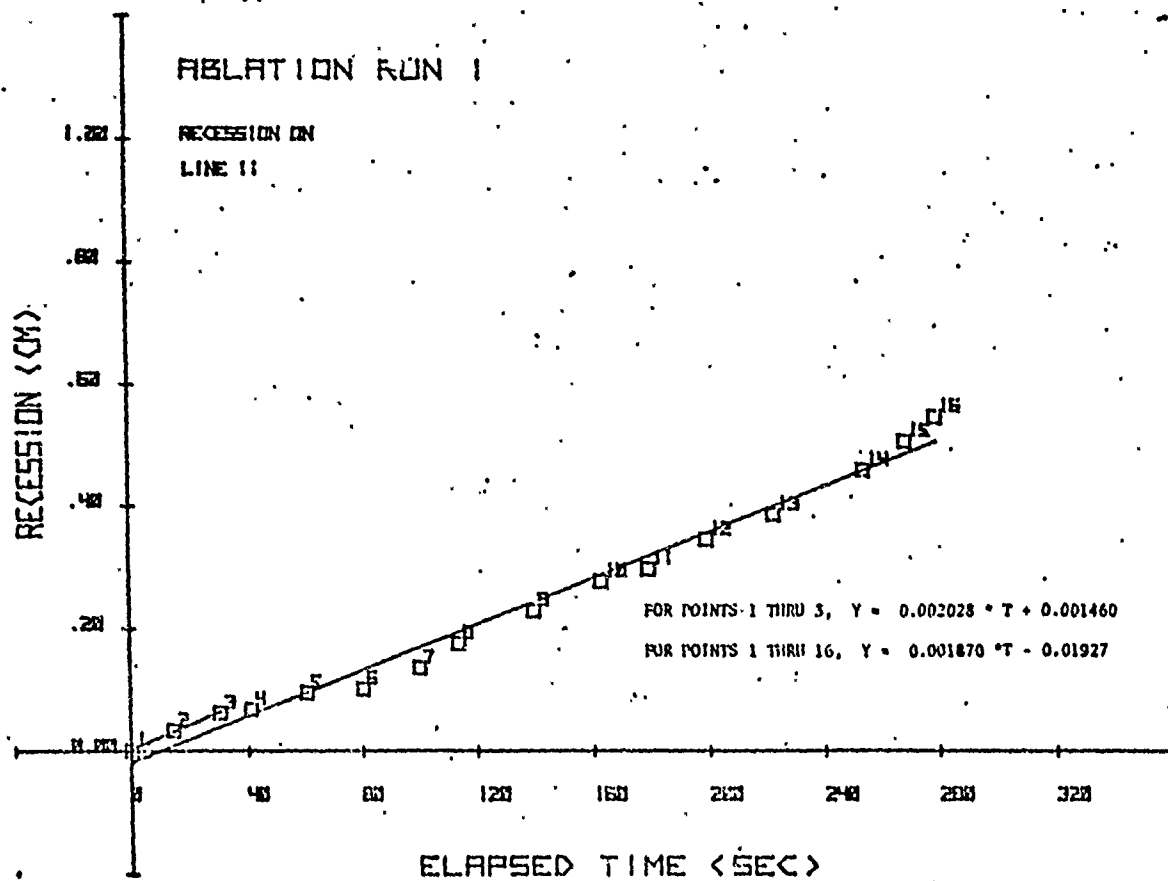
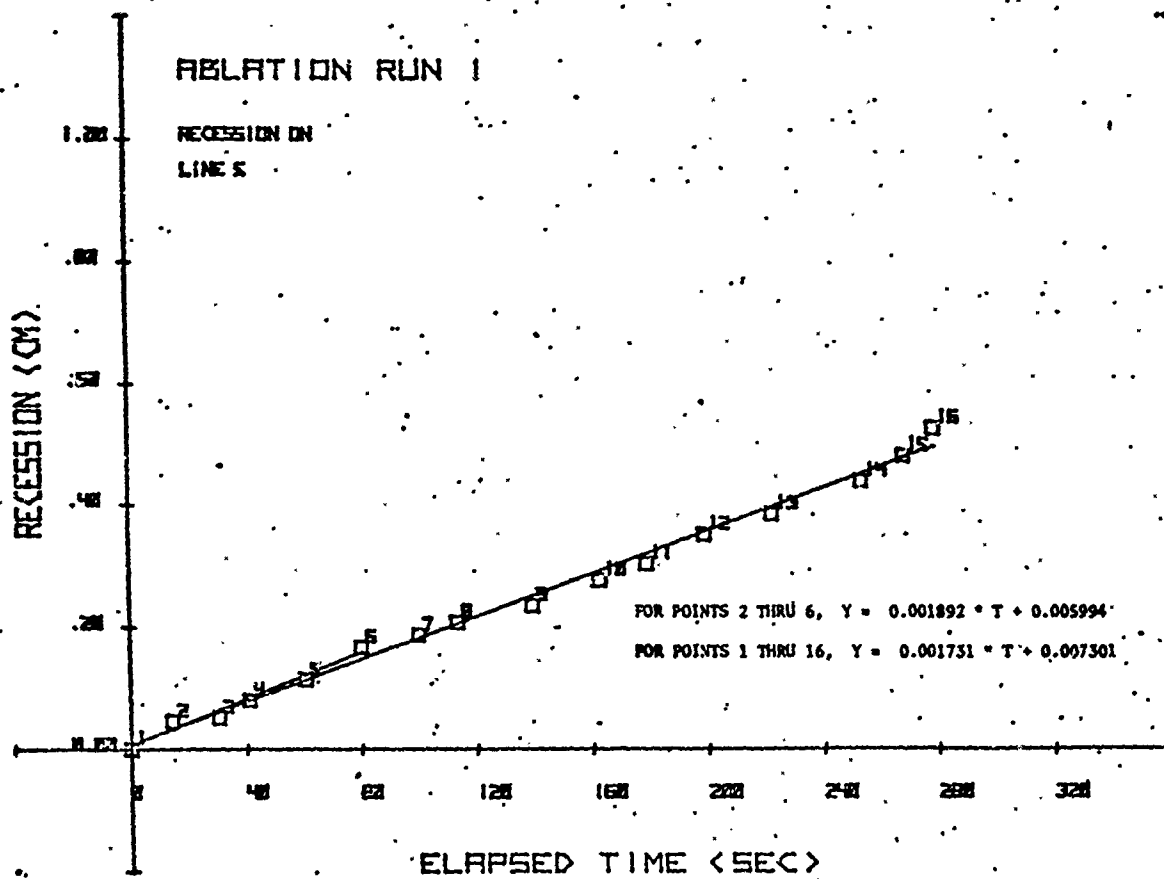


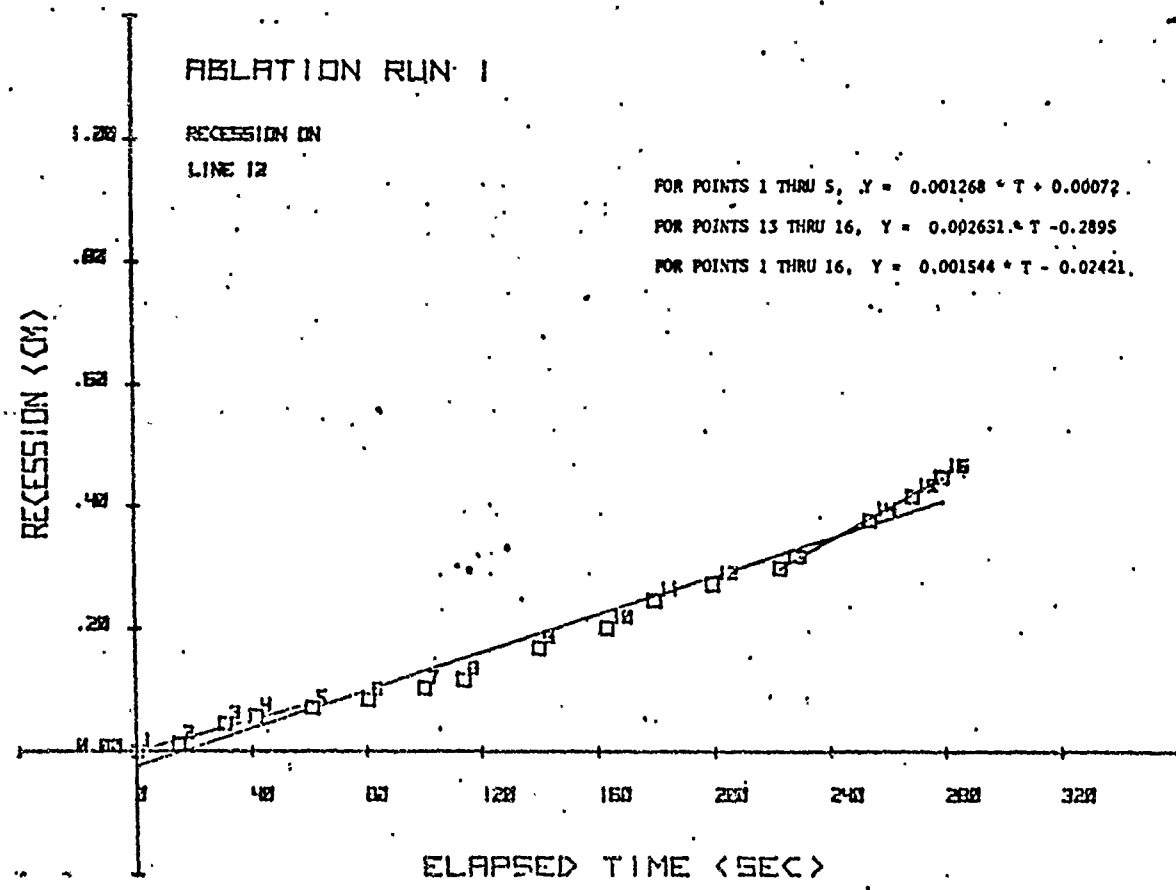
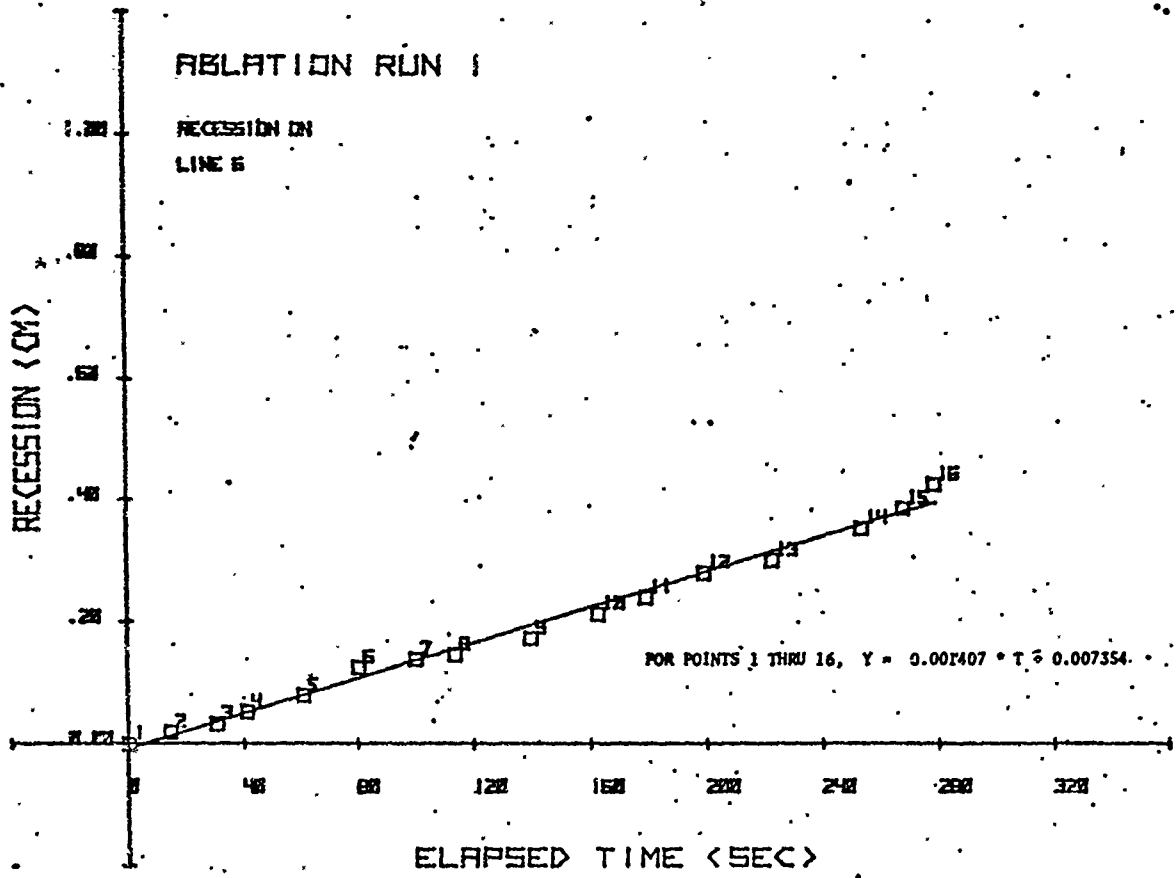








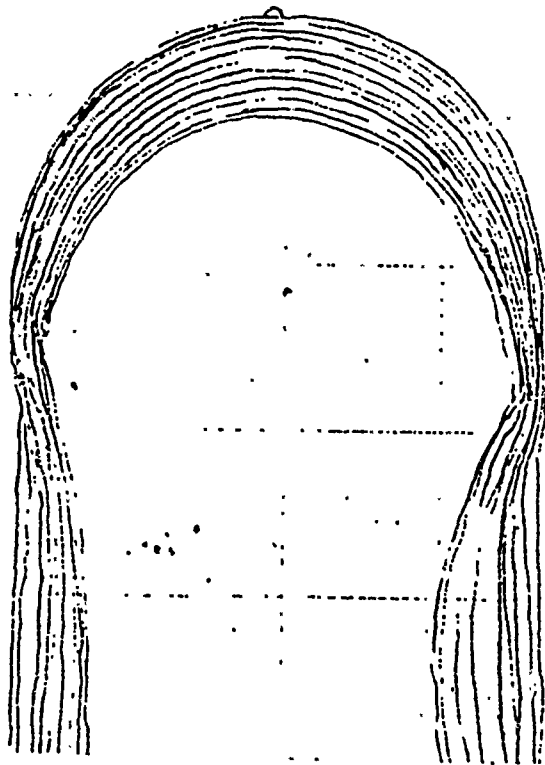


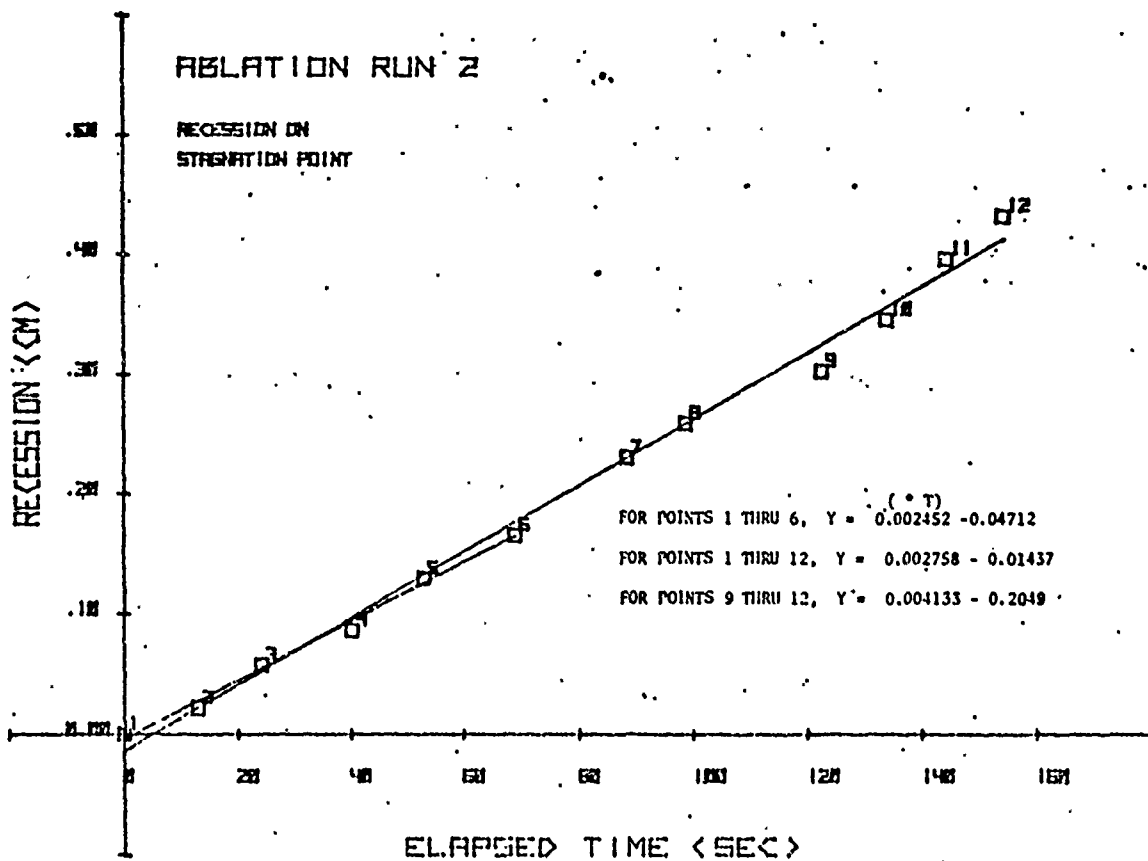


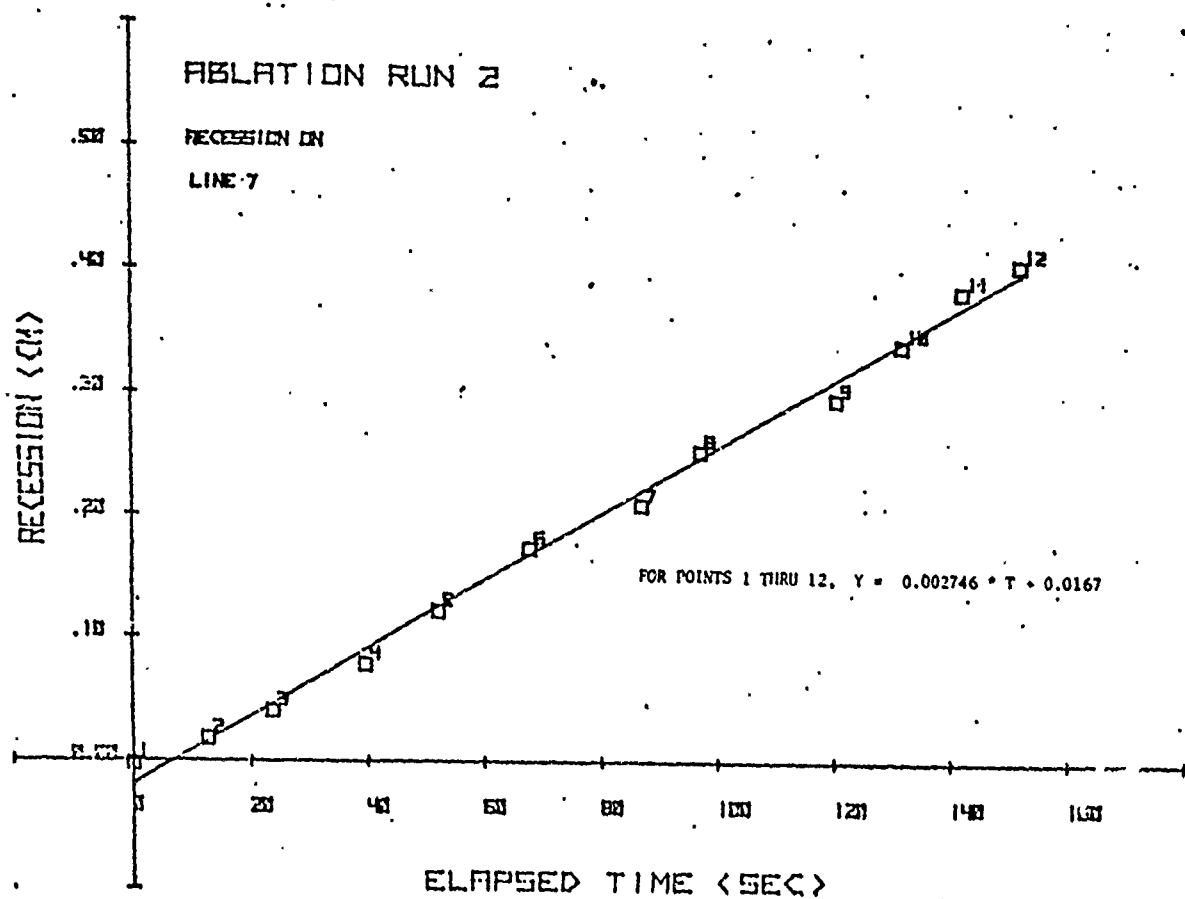
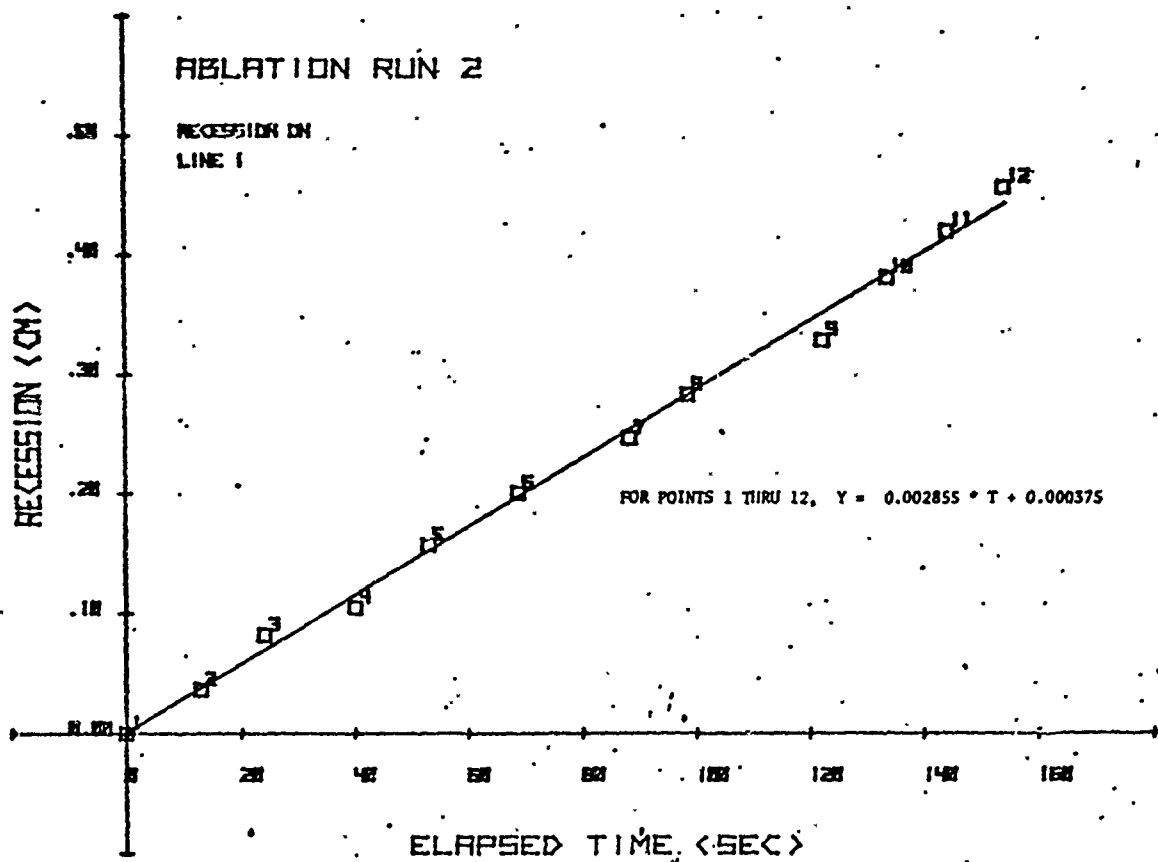
Run 2

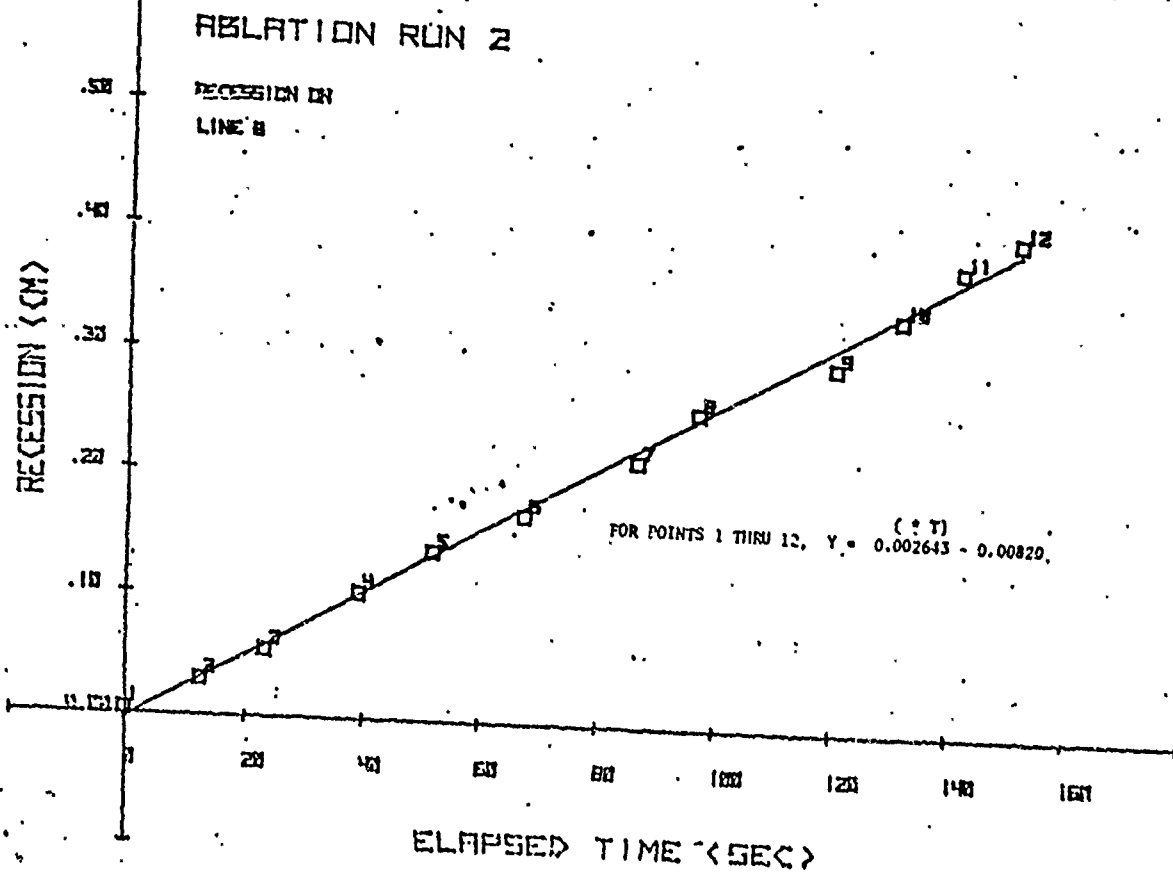
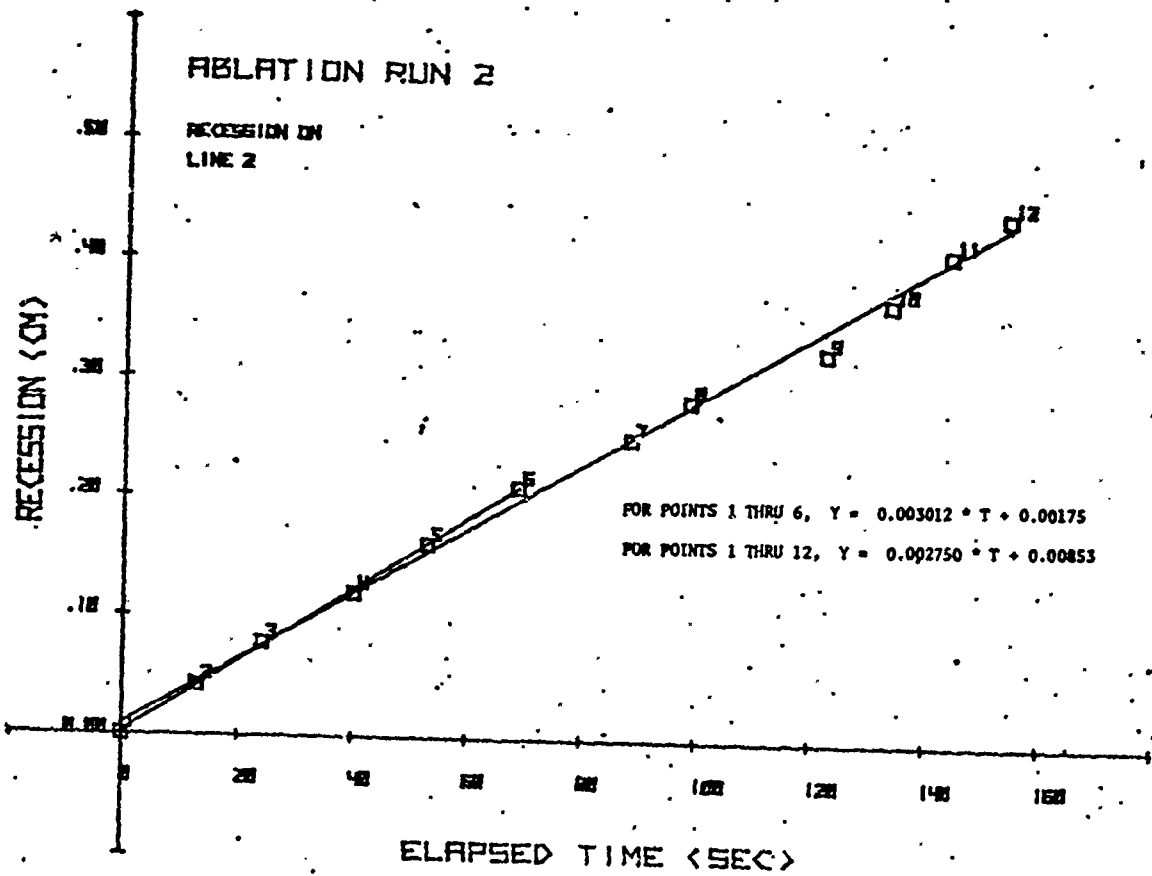
Simple Theory Stagnation Point Mass Flux: $0.00465 \text{ g/cm}^2 \cdot \text{s}$

<u>Position</u>	<u>Recession Rate</u> <u>cm/s ($\times 10^3$)</u>	<u>Mass Flux</u> <u>g/cm²·s ($\times 10^3$)</u>	<u>Normalized</u>
Stag Pt	2.76	4.41	0.948
15 right	2.86	4.57	0.982
15 left	2.75	4.39	0.944
30 right	2.75	4.40	0.946
30 left	2.64	4.23	0.910
45 right	2.61	4.18	0.899
45 left	2.53	4.04	0.869
60 right	2.23	3.56	0.766
60 left	2.21	3.53	0.759
75 right	1.84	2.94	0.632
75 left	1.80	2.89	0.622
90 right	1.38	2.21	0.475
90 left	----	-----	-----



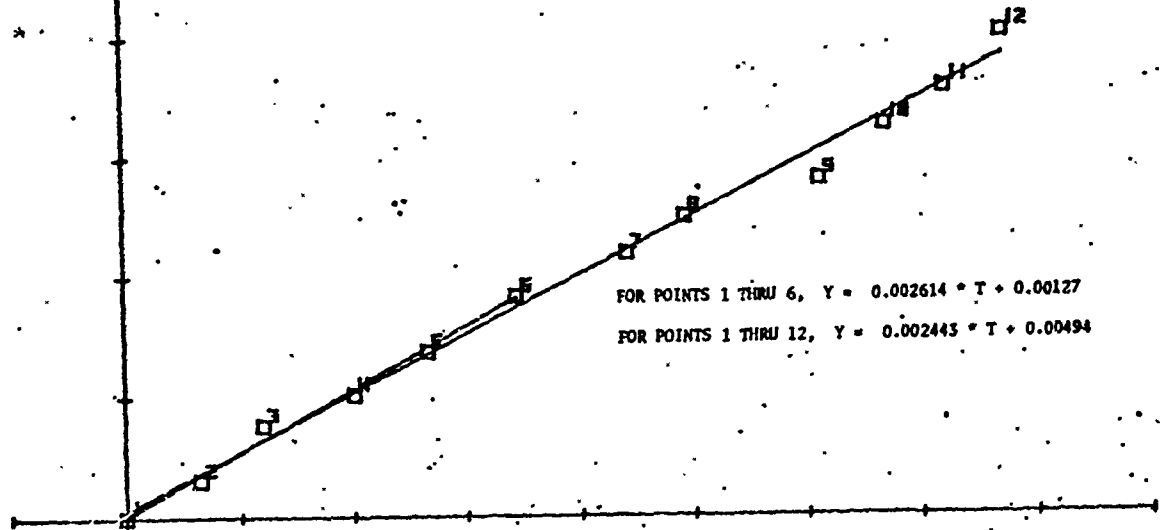






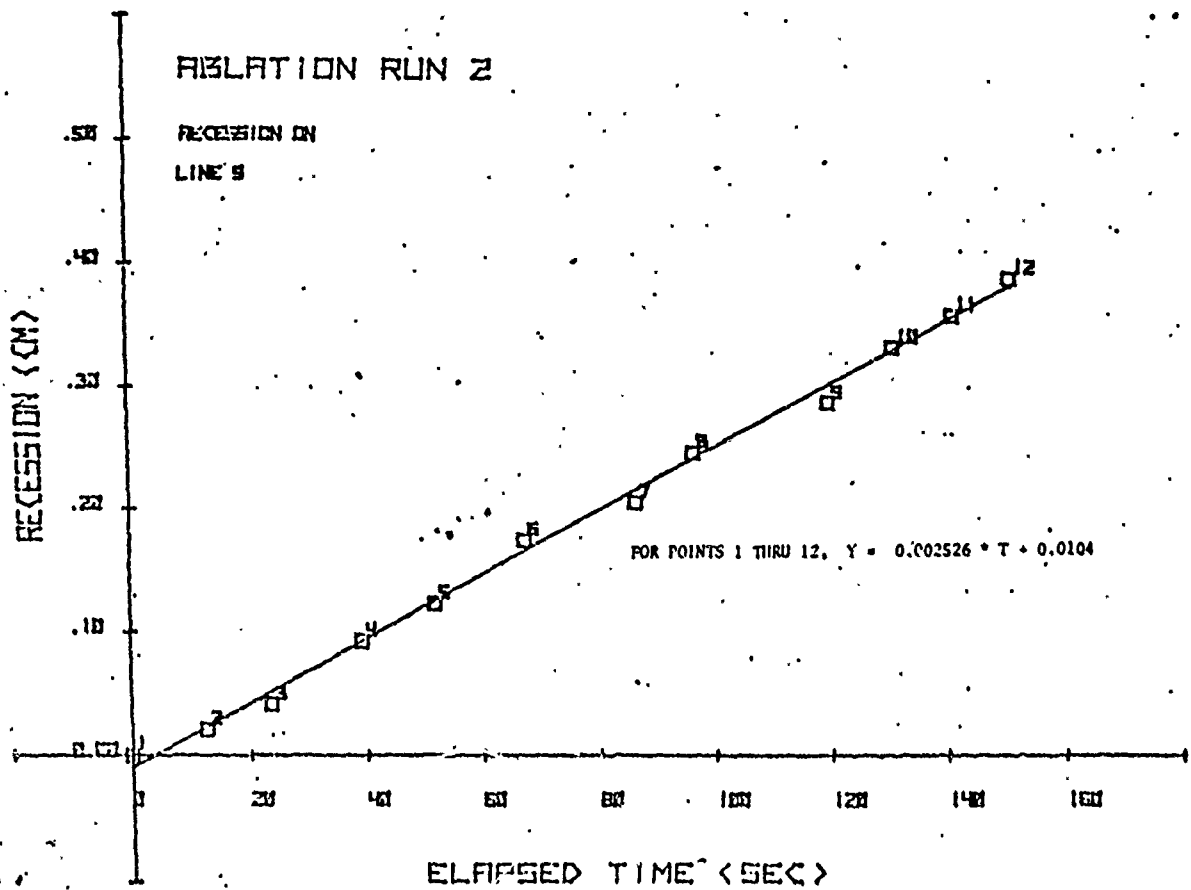
ABLATION RUN 2.00

RECESSION ON
LINE 3



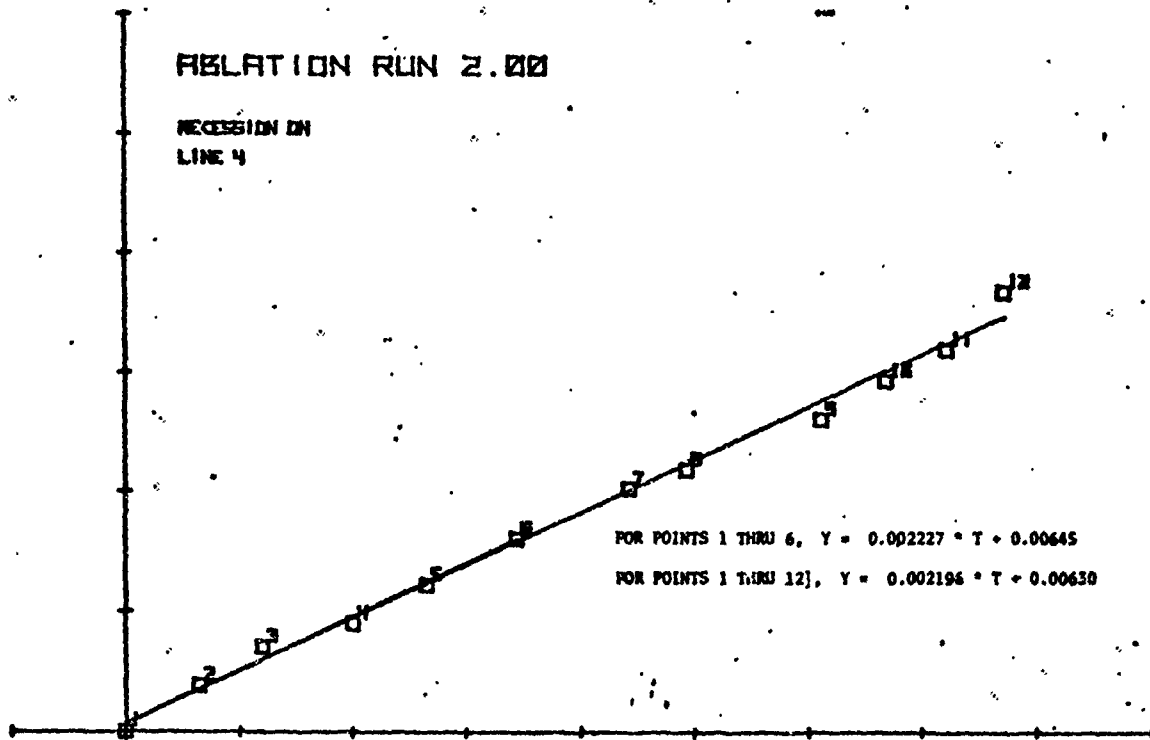
ABLATION RUN 2

RECESSION ON
LINE 9



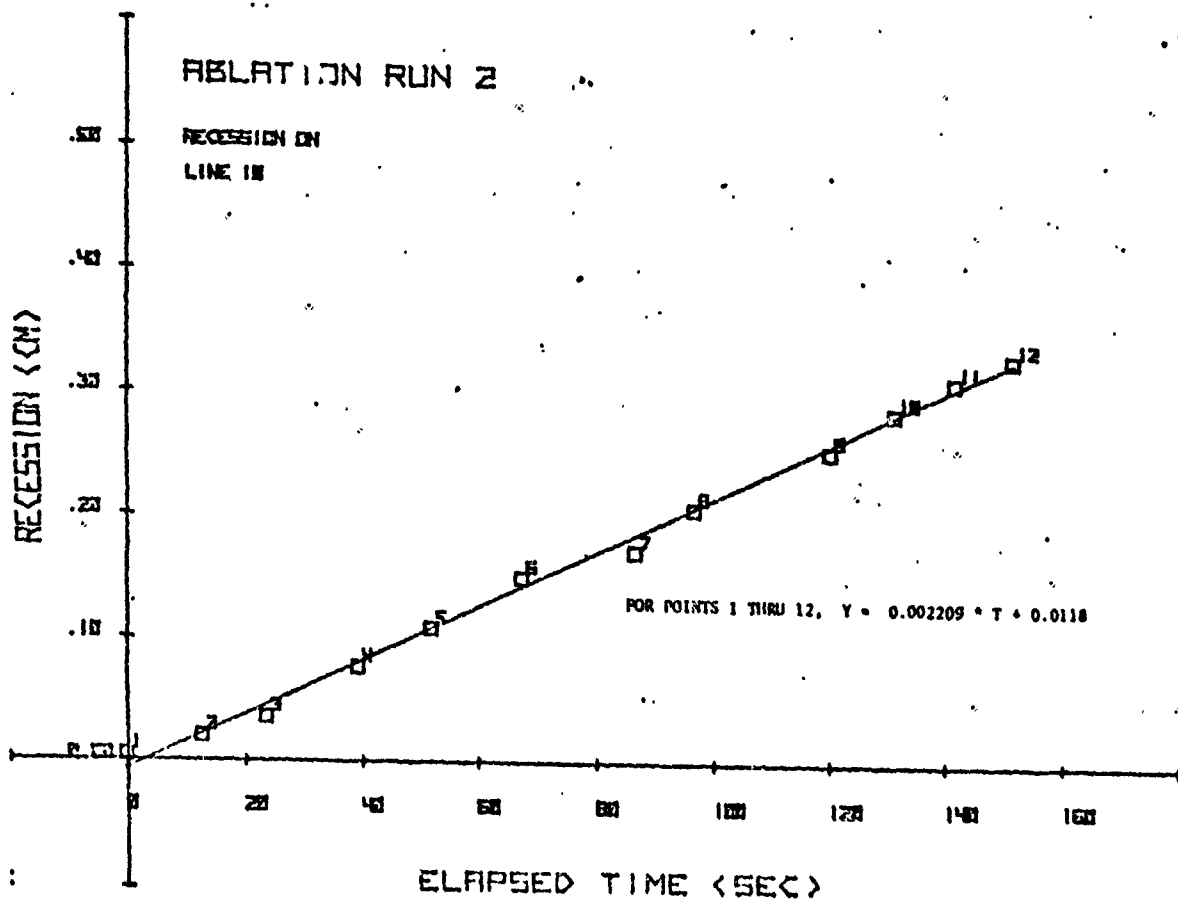
ABLATION RUN 2.00

RECESSION ON
LINE 4



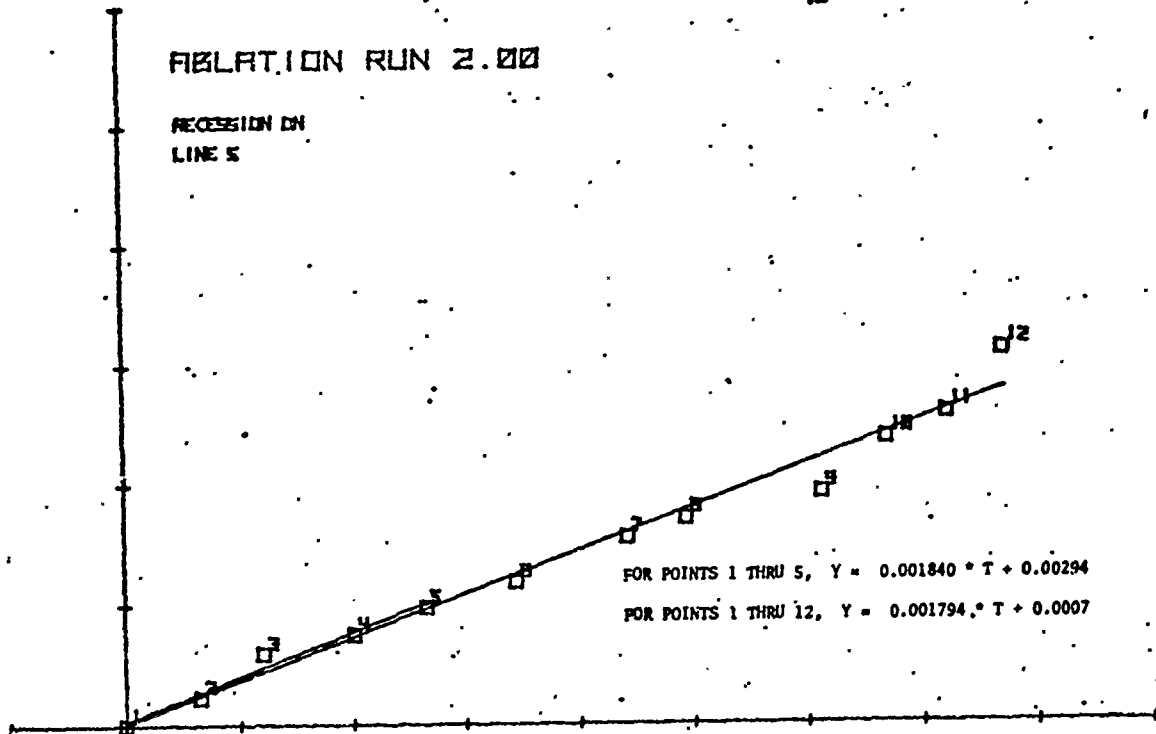
ABLATION RUN 2

RECESSION ON
LINE 18



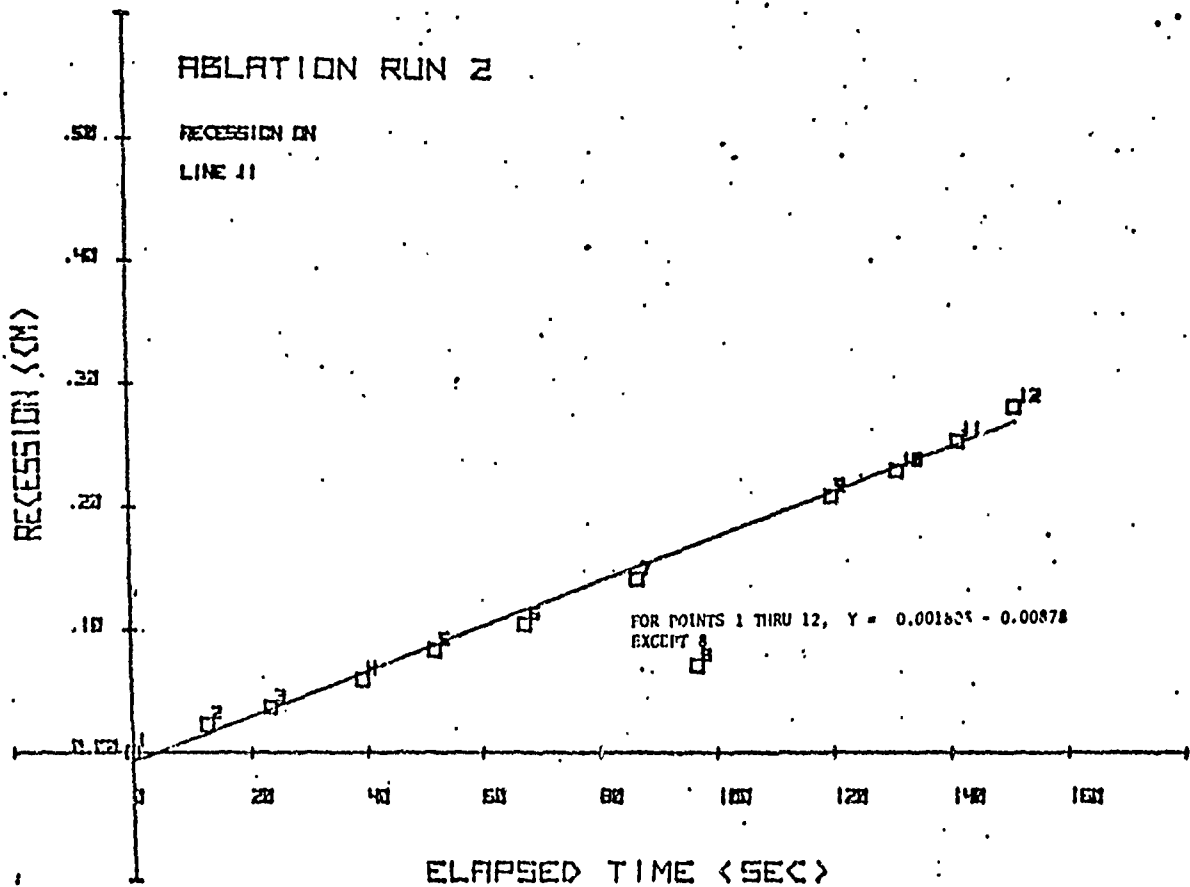
ABLATION RUN 2.00

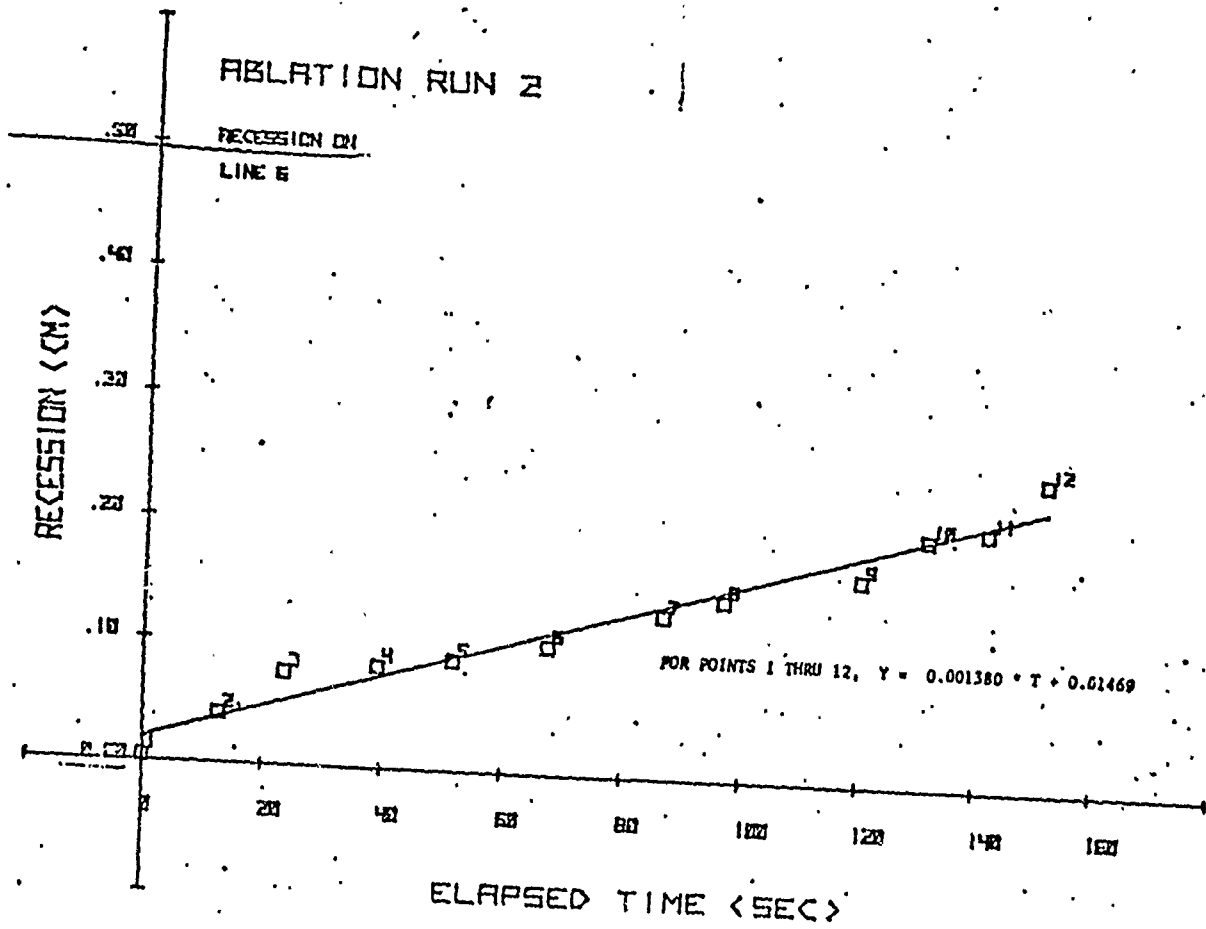
RECESSION ON
LINE 5



ABLATION RUN 2

RECESSION ON
LINE 11

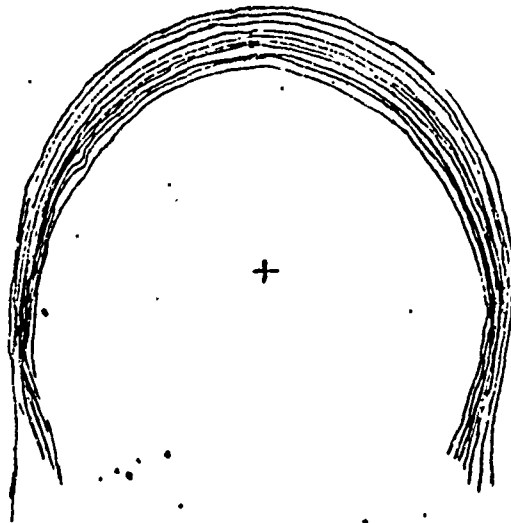


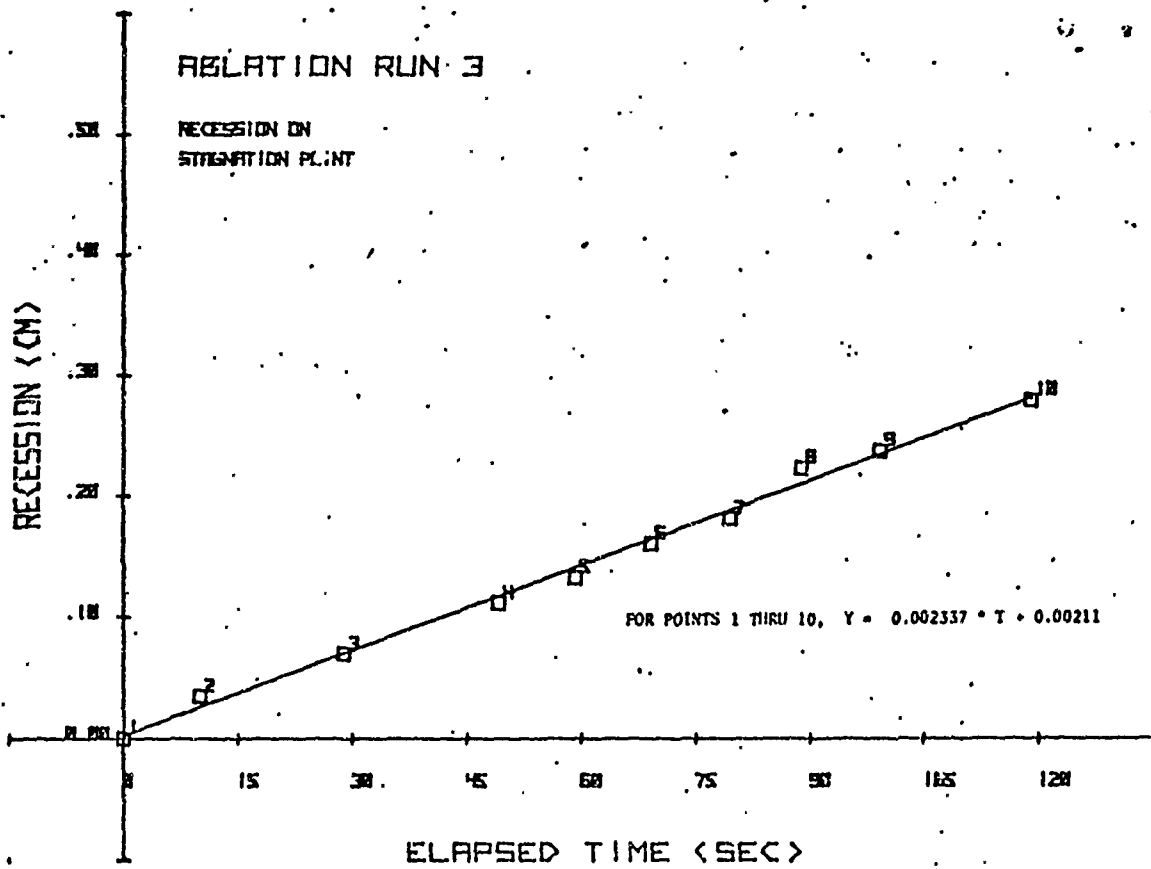


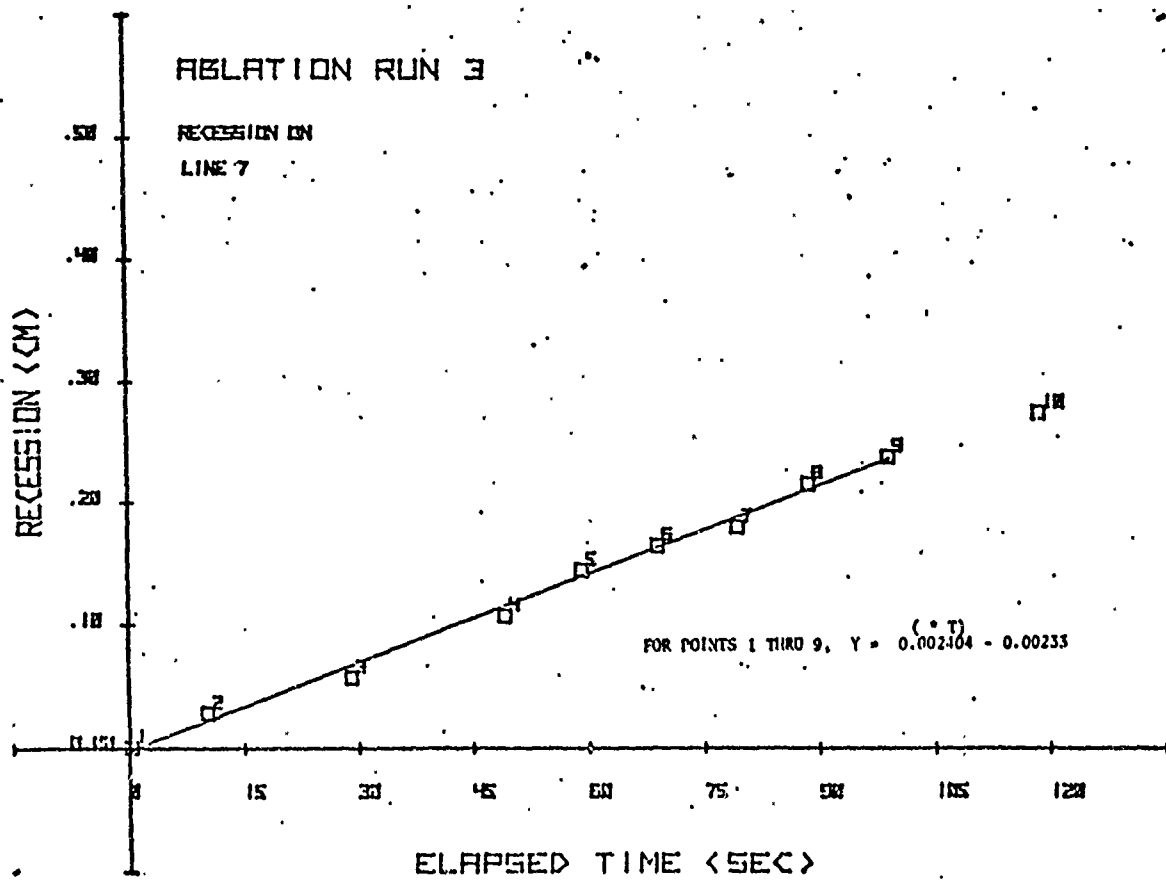
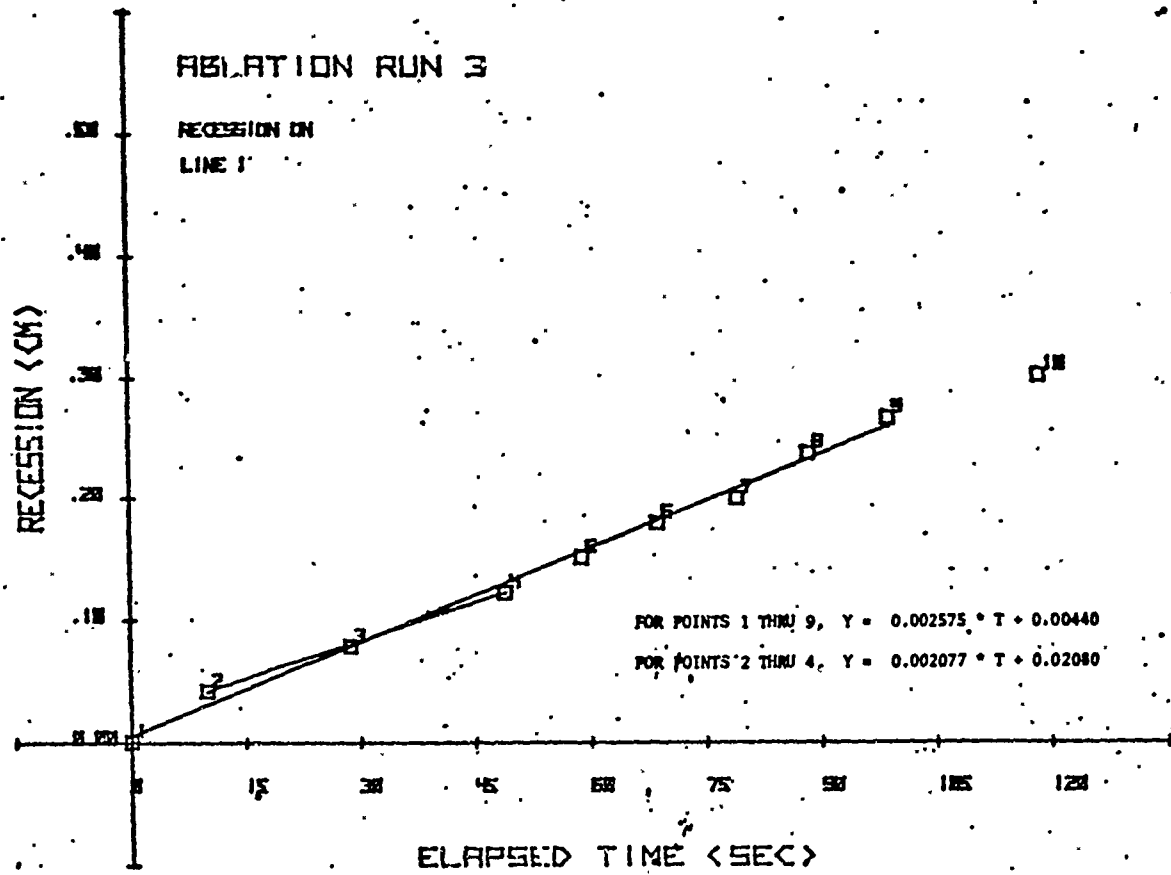
Run 3

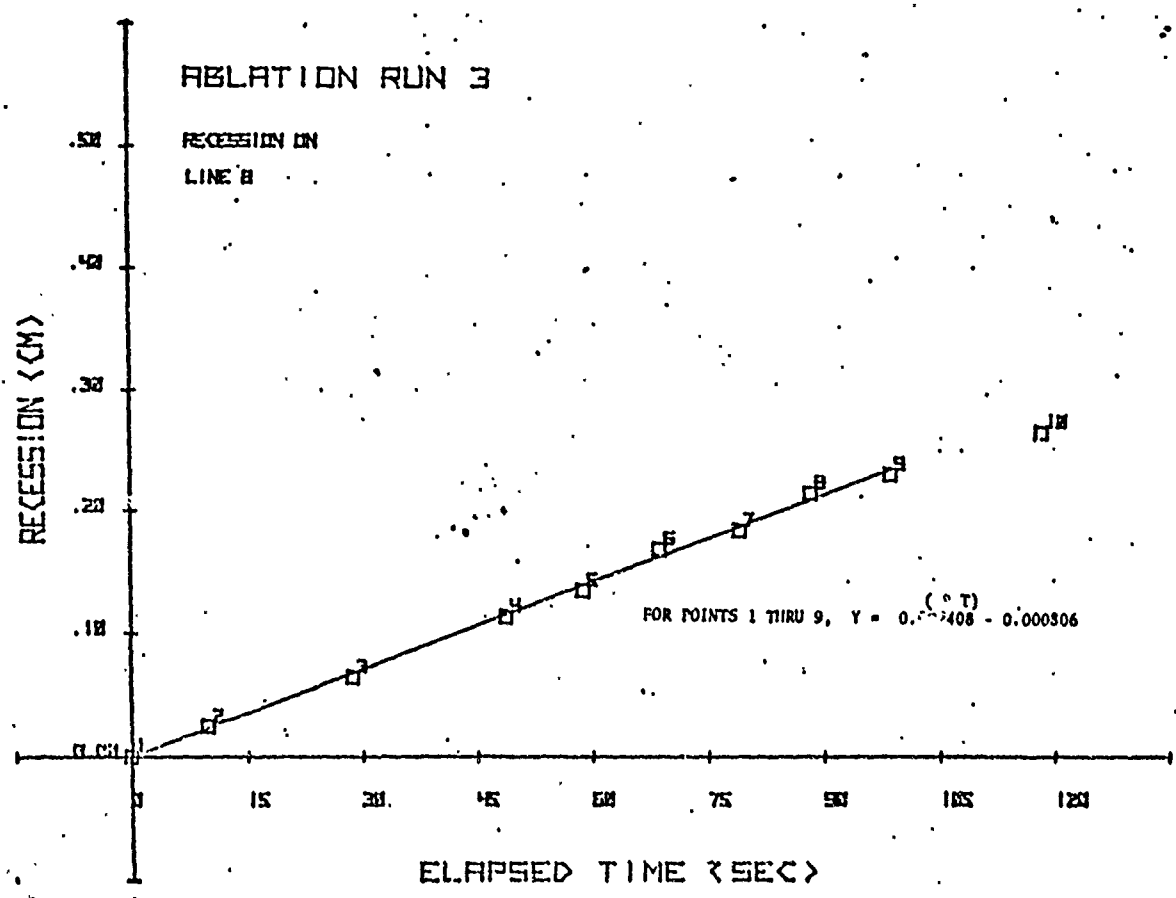
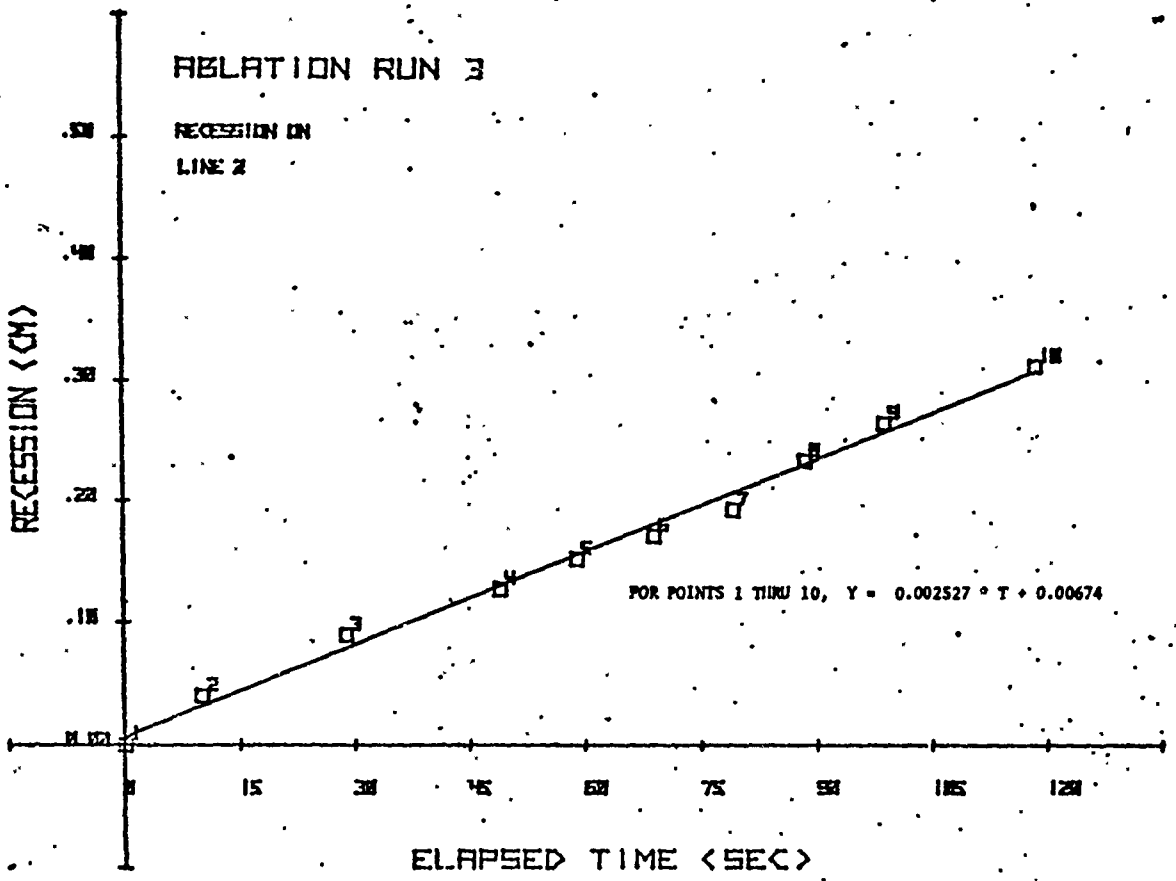
Simple Theory Stagnation Point Mass Flux: $0.00424 \text{ g/cm}^2 \cdot \text{s}$

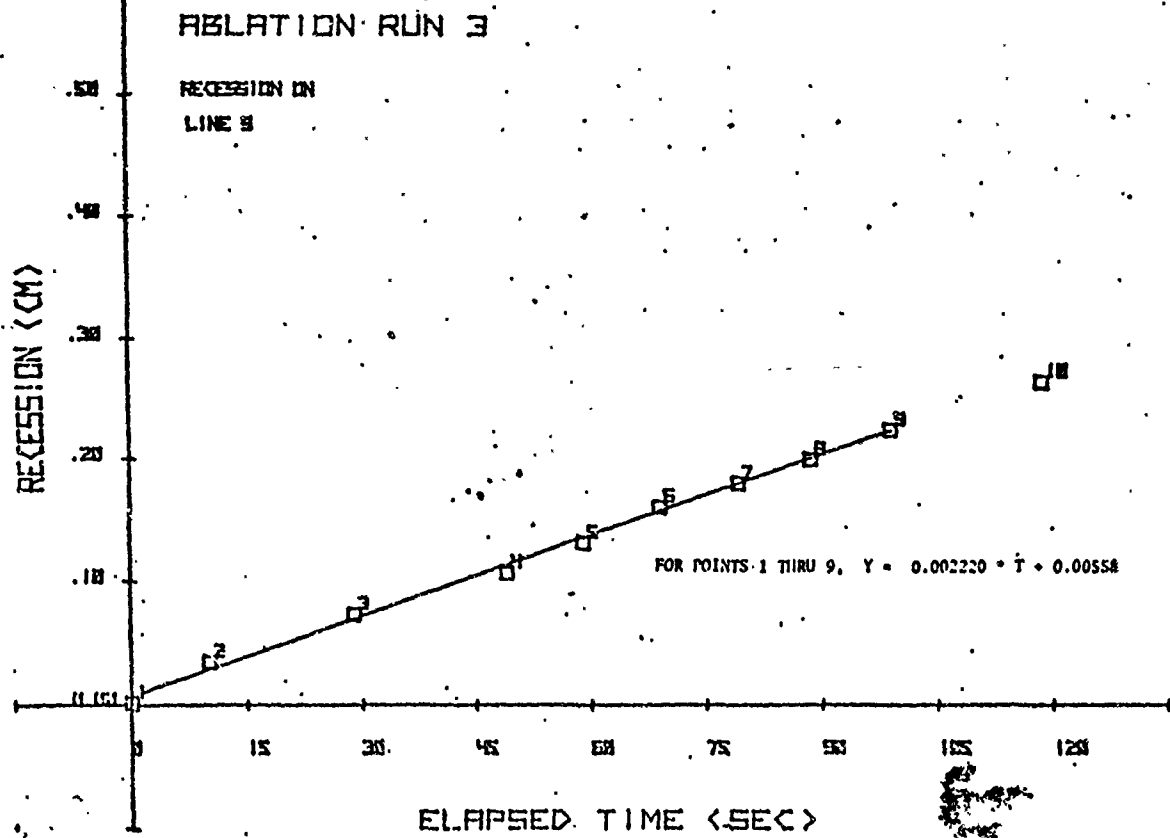
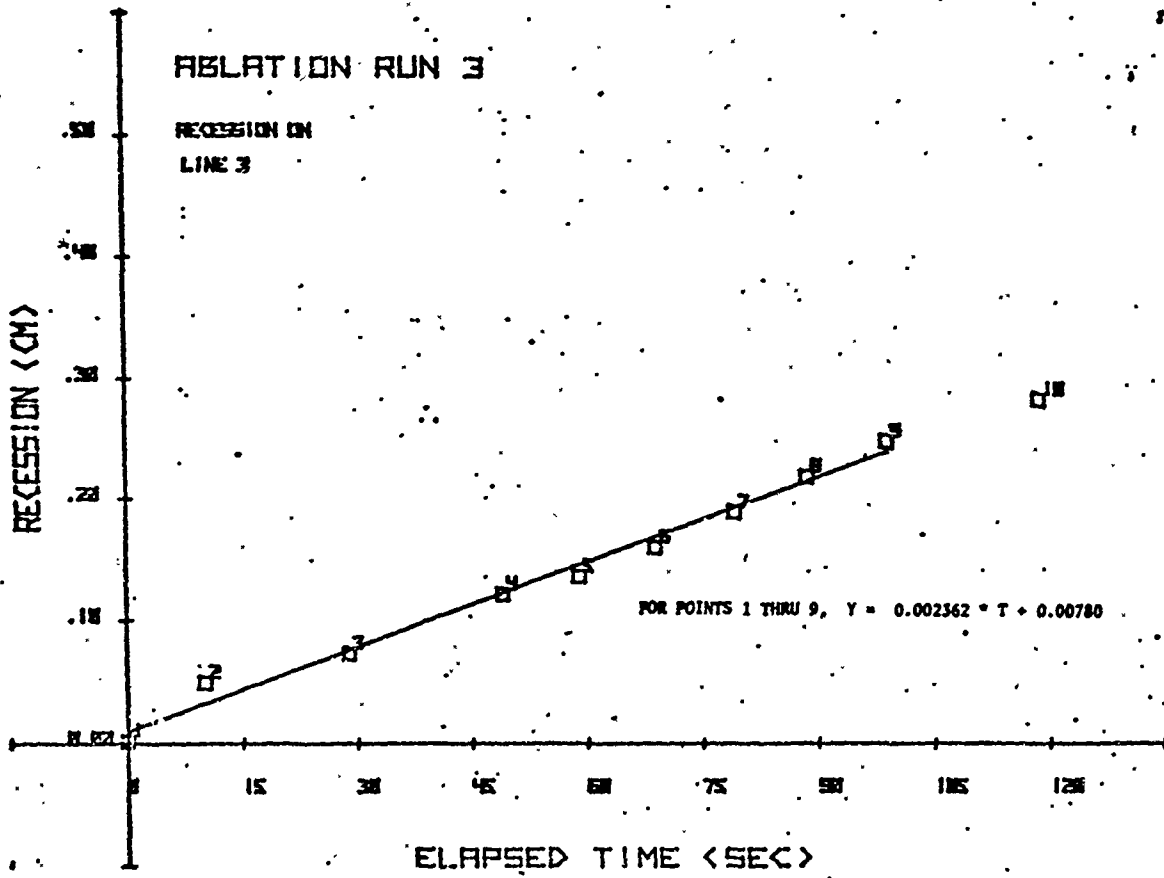
Position	Recession Rate cm/s ($\times 10^3$)	Mass Flux g/cm ² ·s ($\times 10^3$)	Normalized
Stag Pt	2.34	3.71	0.882
15 right	2.58	4.13	0.974
15 left	2.40	3.84	0.906
30 right	2.53	4.05	0.955
30 left	2.41	3.86	0.910
45 right	2.36	3.78	0.892
45 left	2.22	3.55	0.837
60 right	2.05	3.28	0.774
60 left	1.95	3.12	0.736
75 right	1.71	2.74	0.646
75 left	1.53	2.45	0.578
90 right	1.25	2.00	0.472
90 left	1.13	1.80	0.425

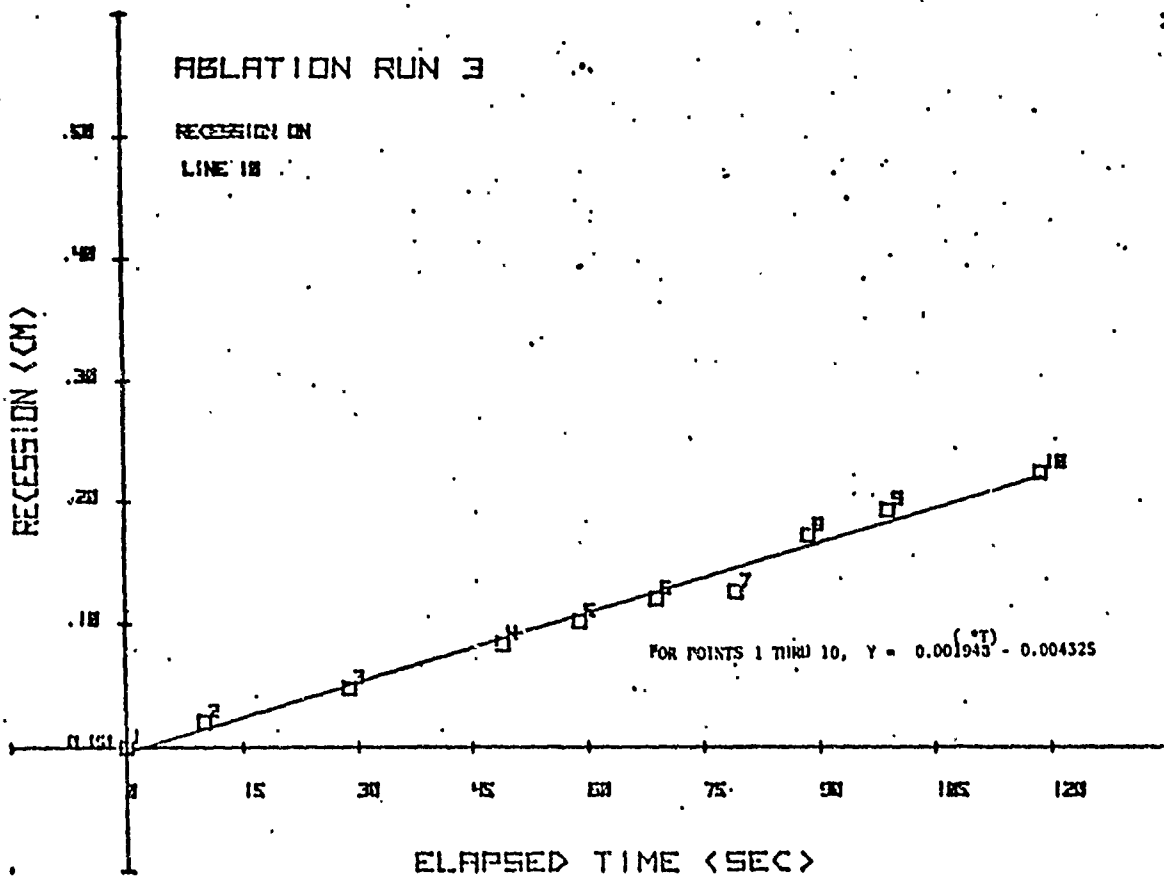
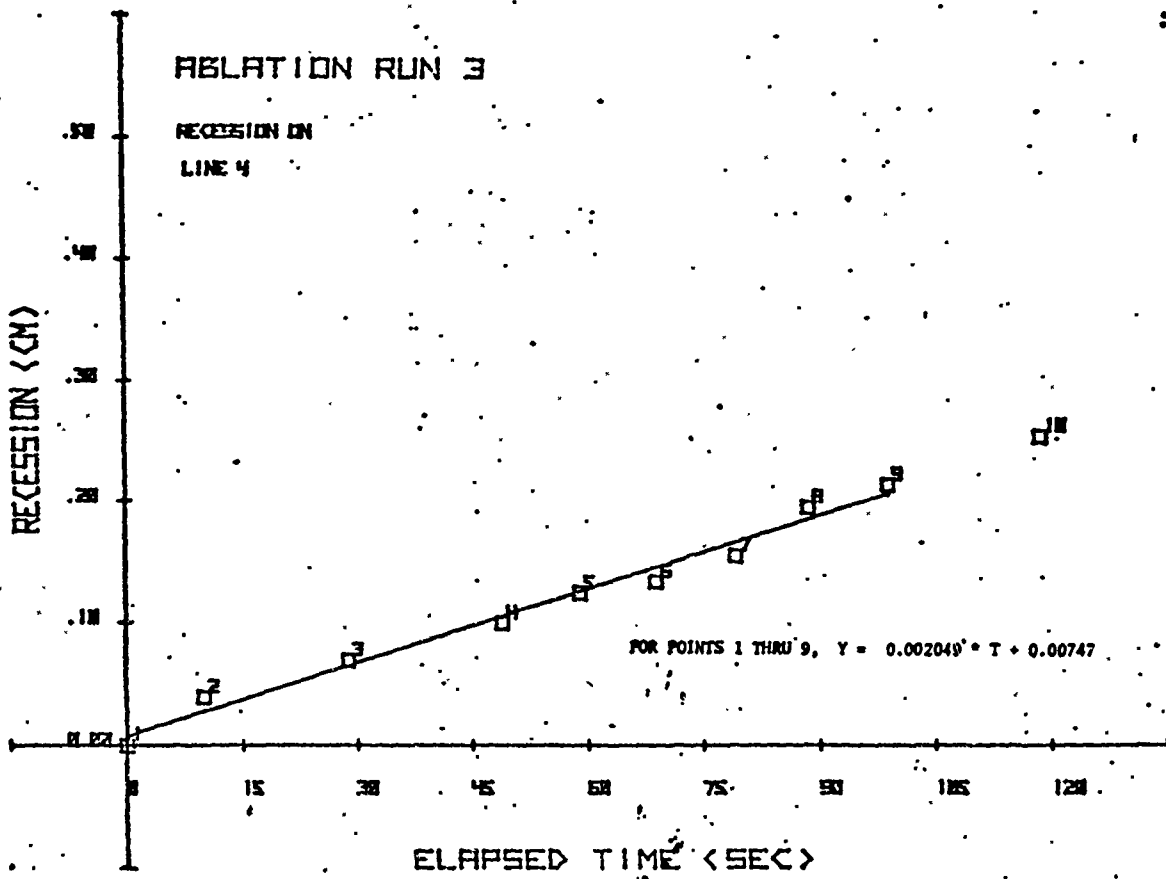


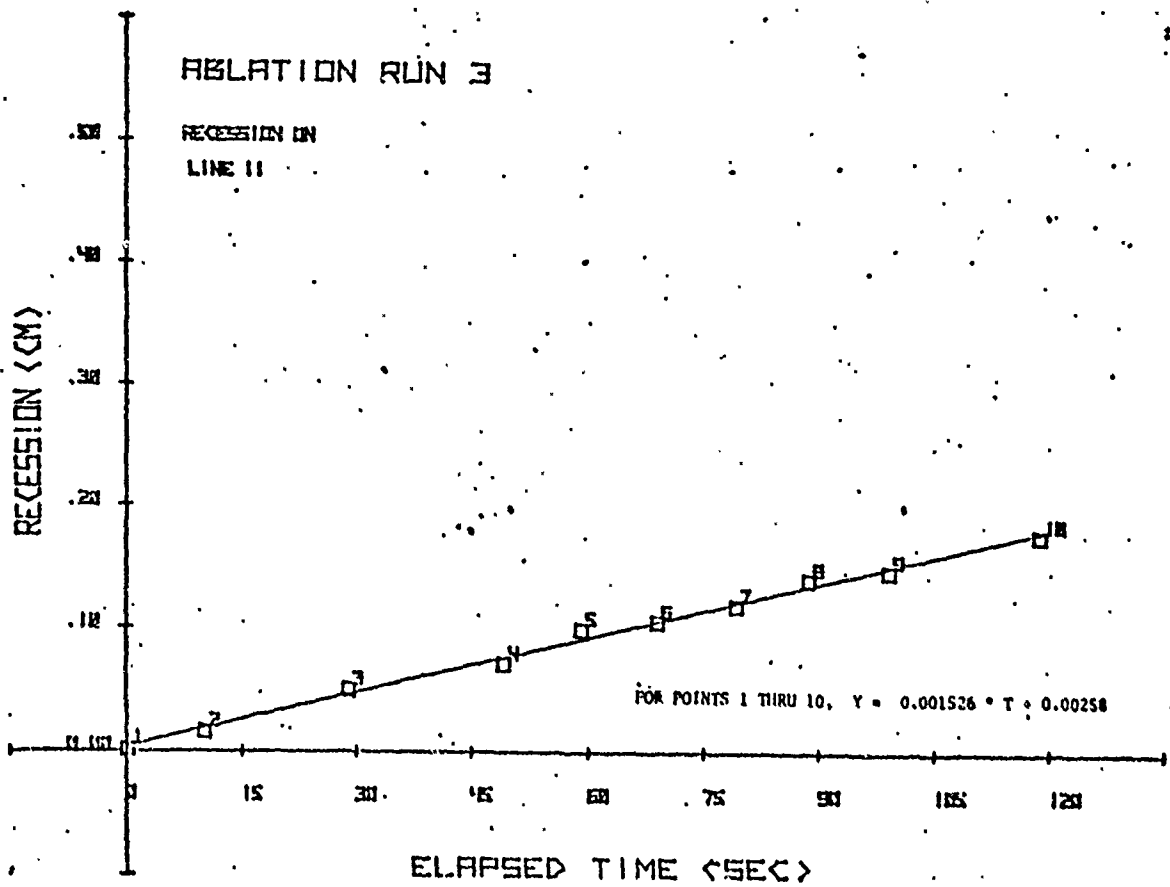
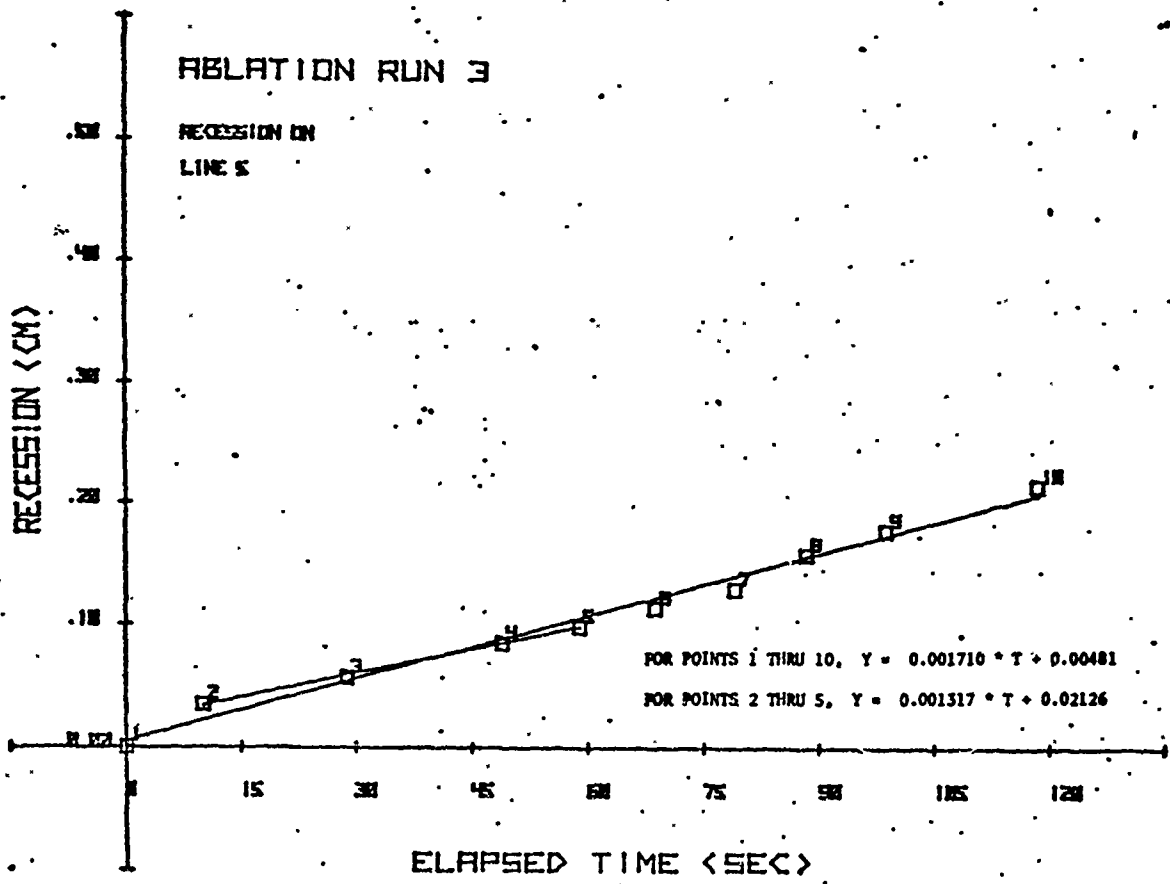


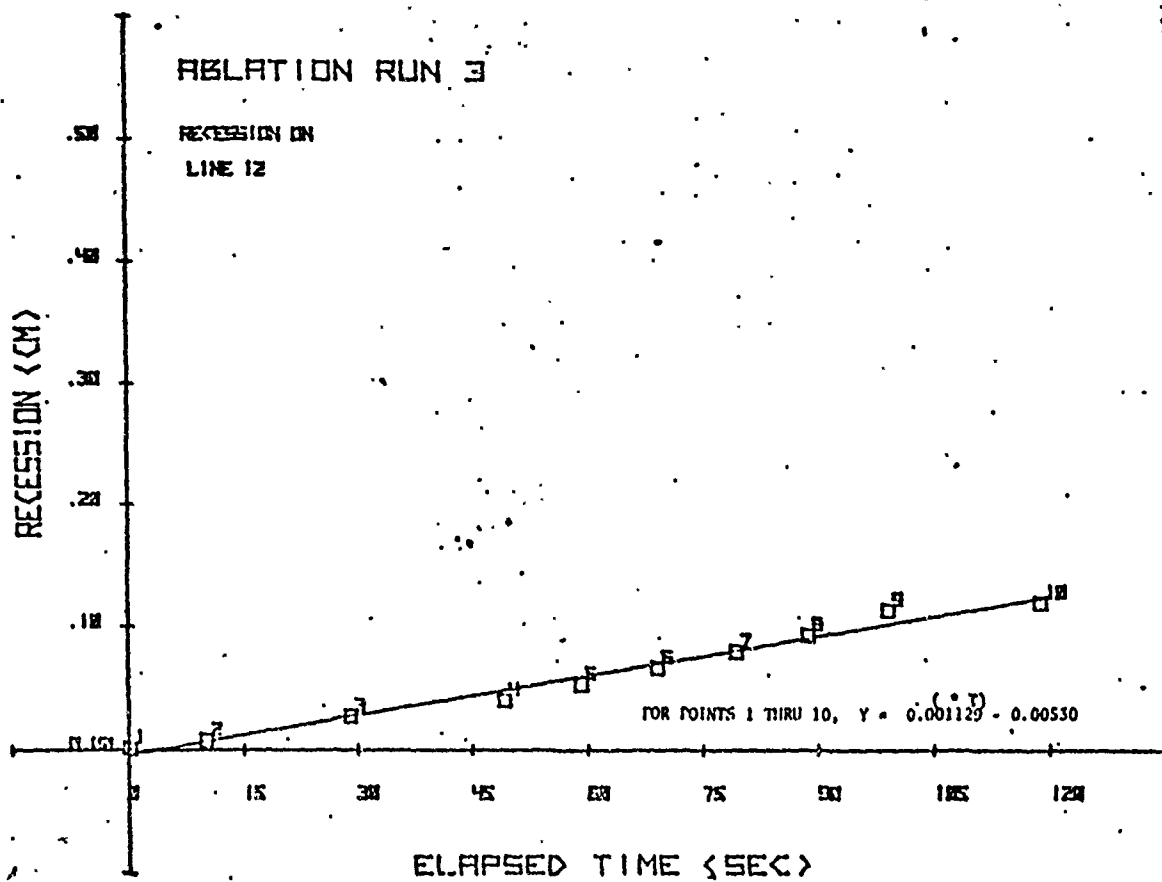
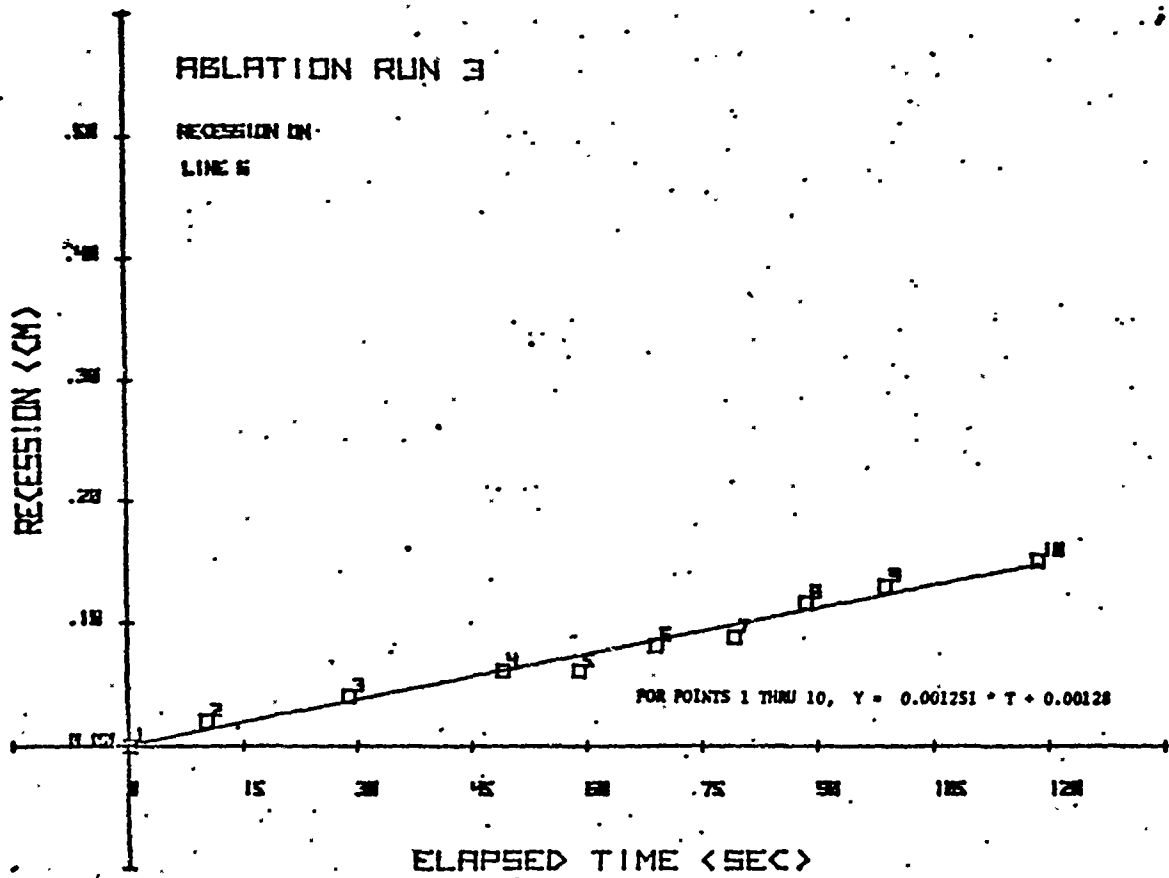








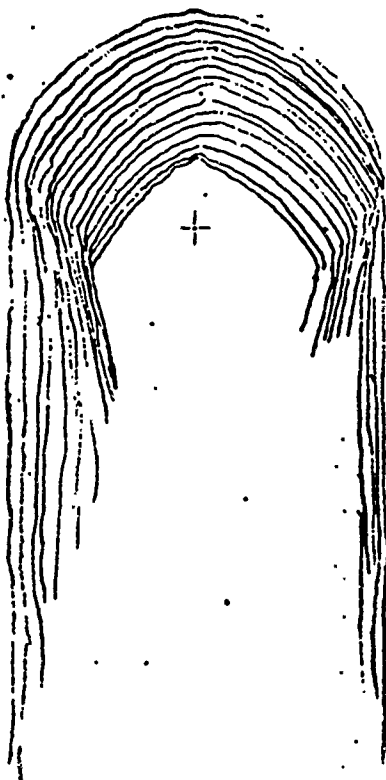


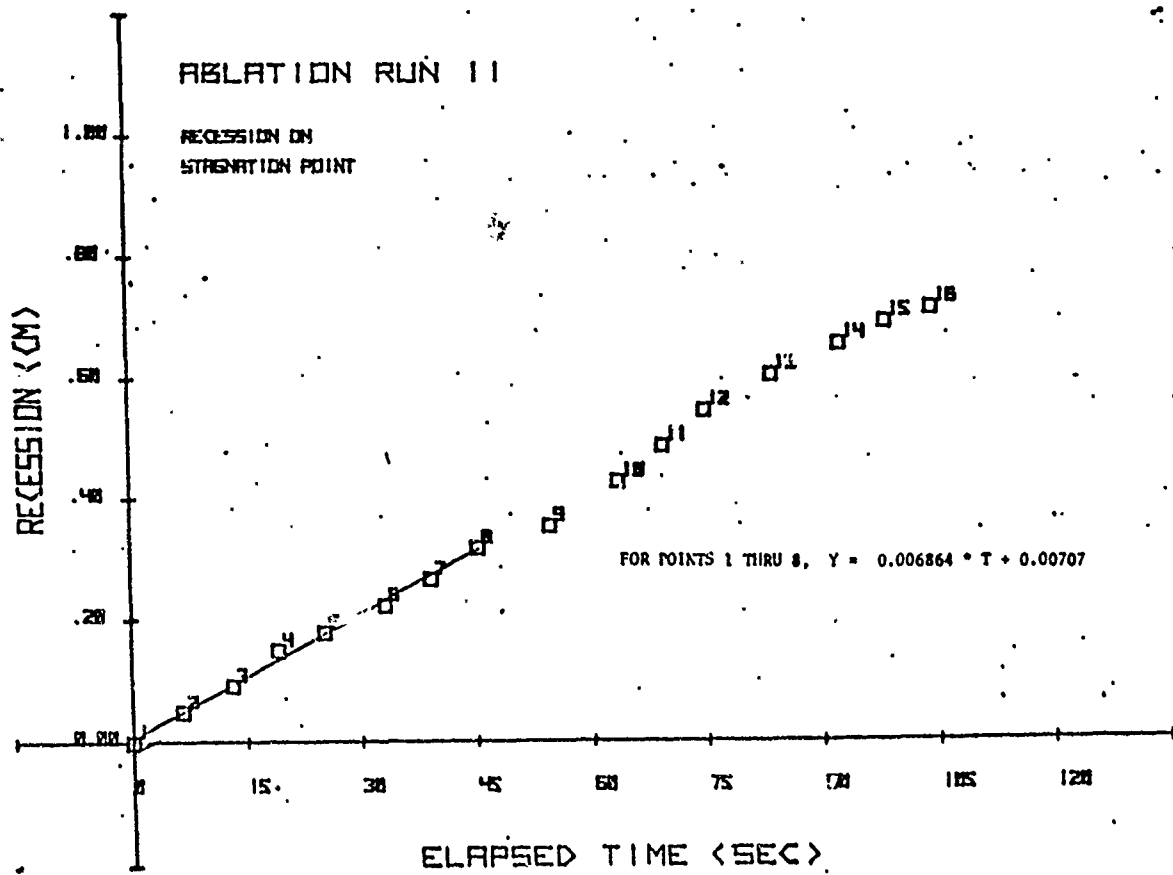


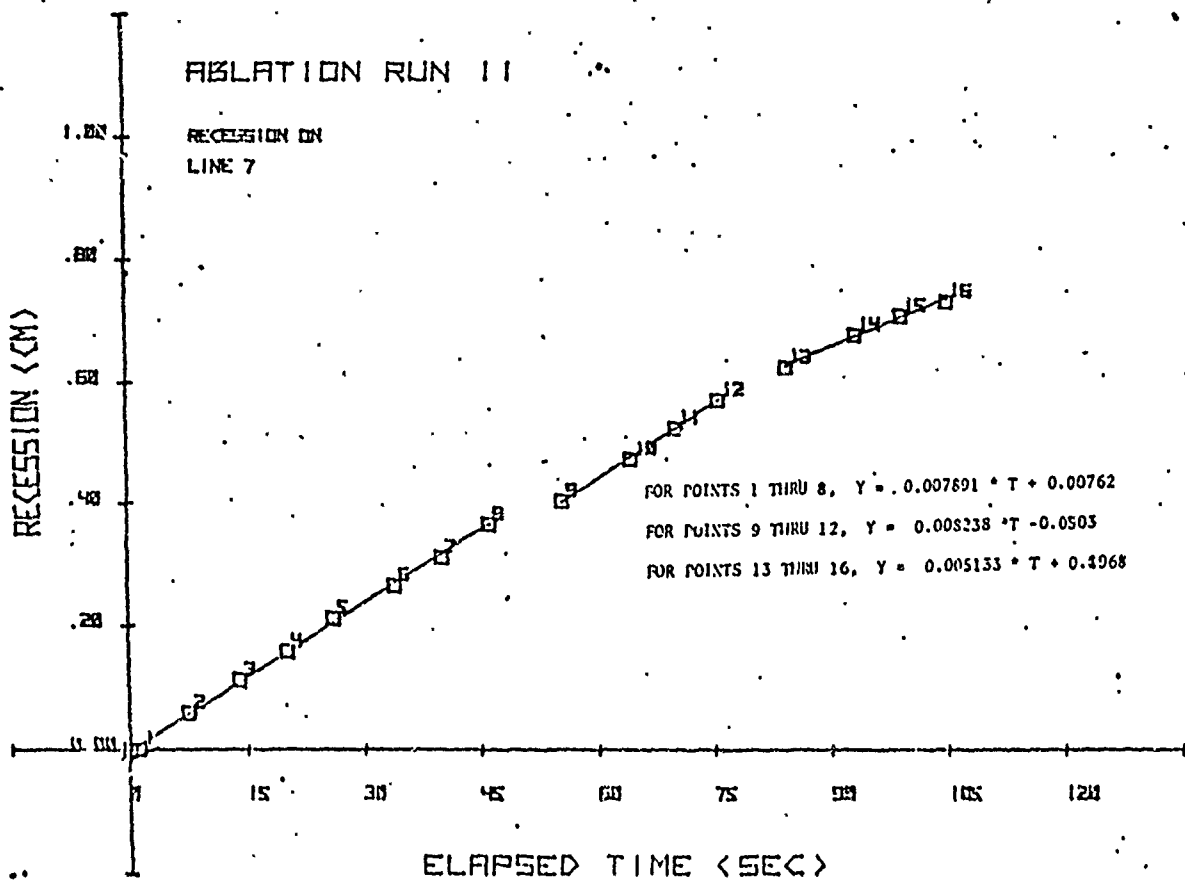
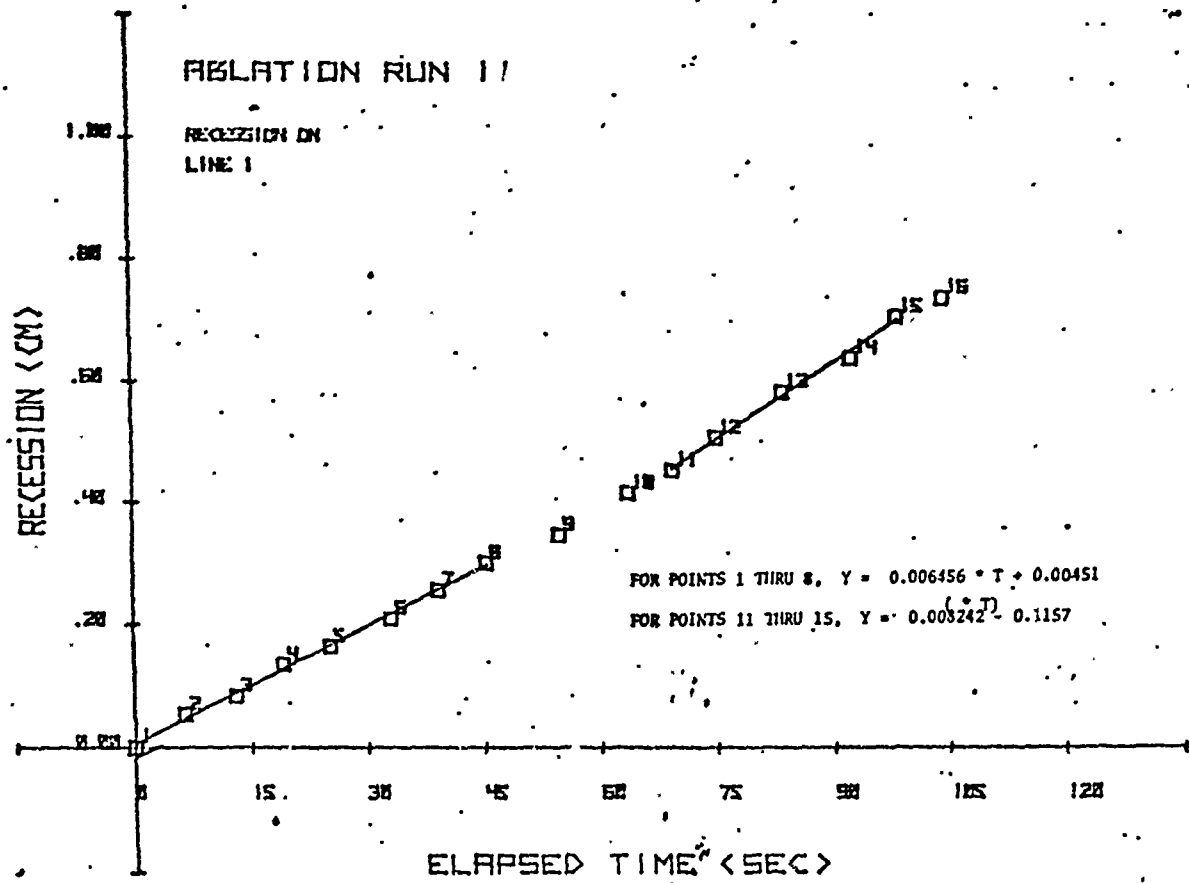
Run 4 (Also Identified as Run 11)

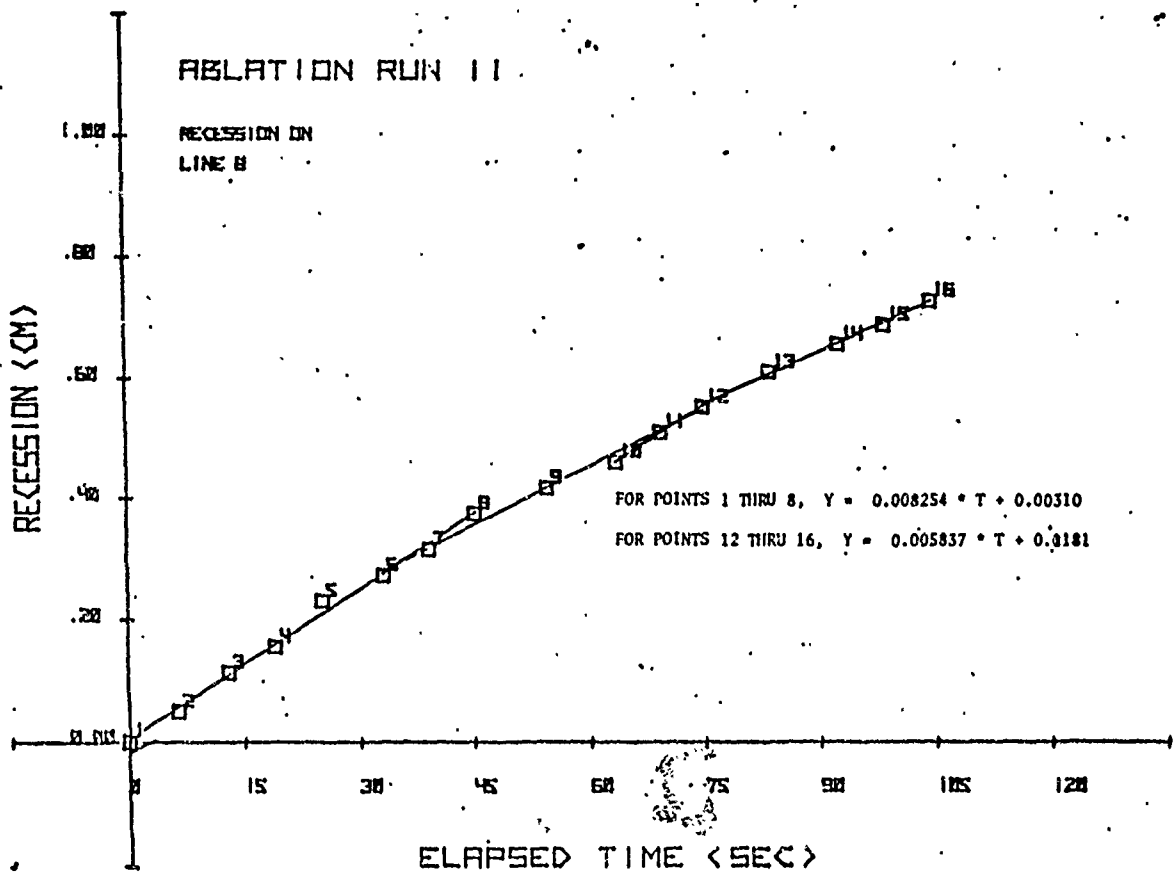
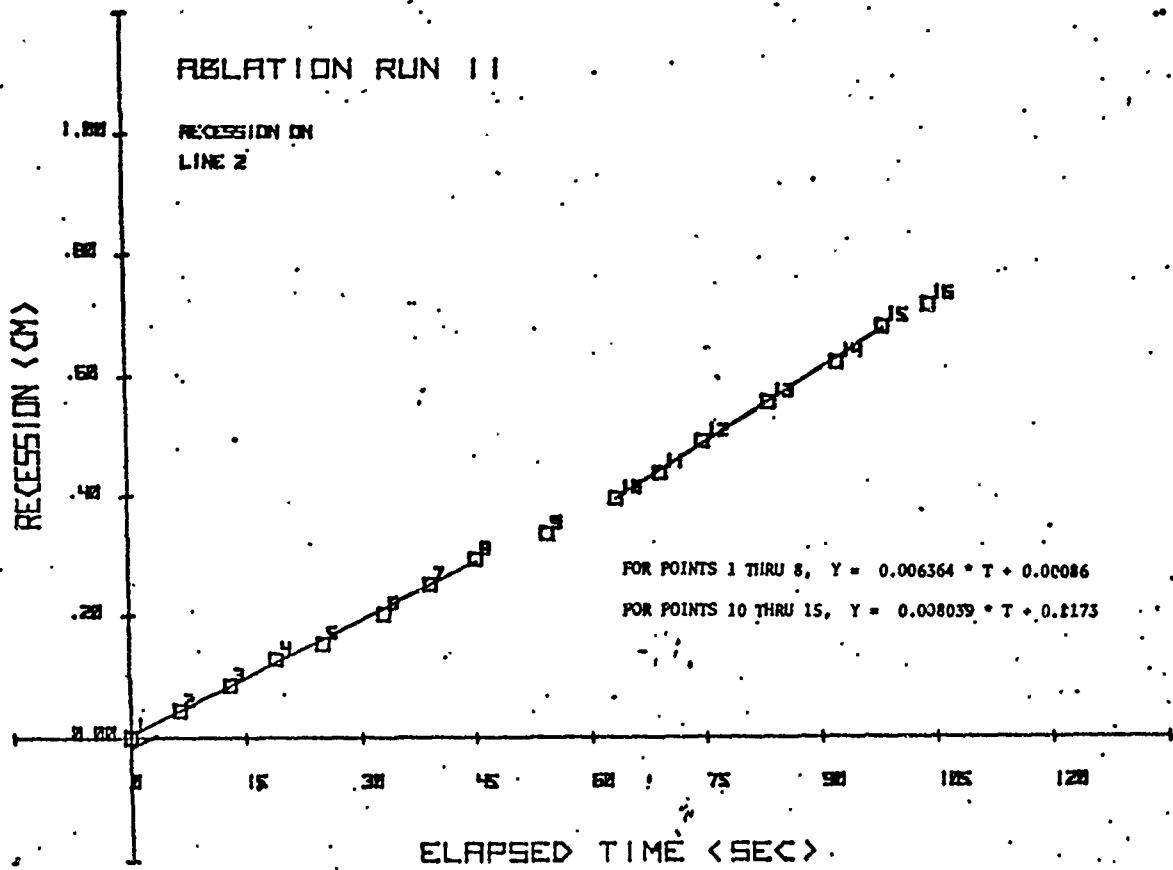
Simple Theory Stagnation Point Mass Flux: $0.00575 \text{ g/cm}^2 \cdot \text{s}$

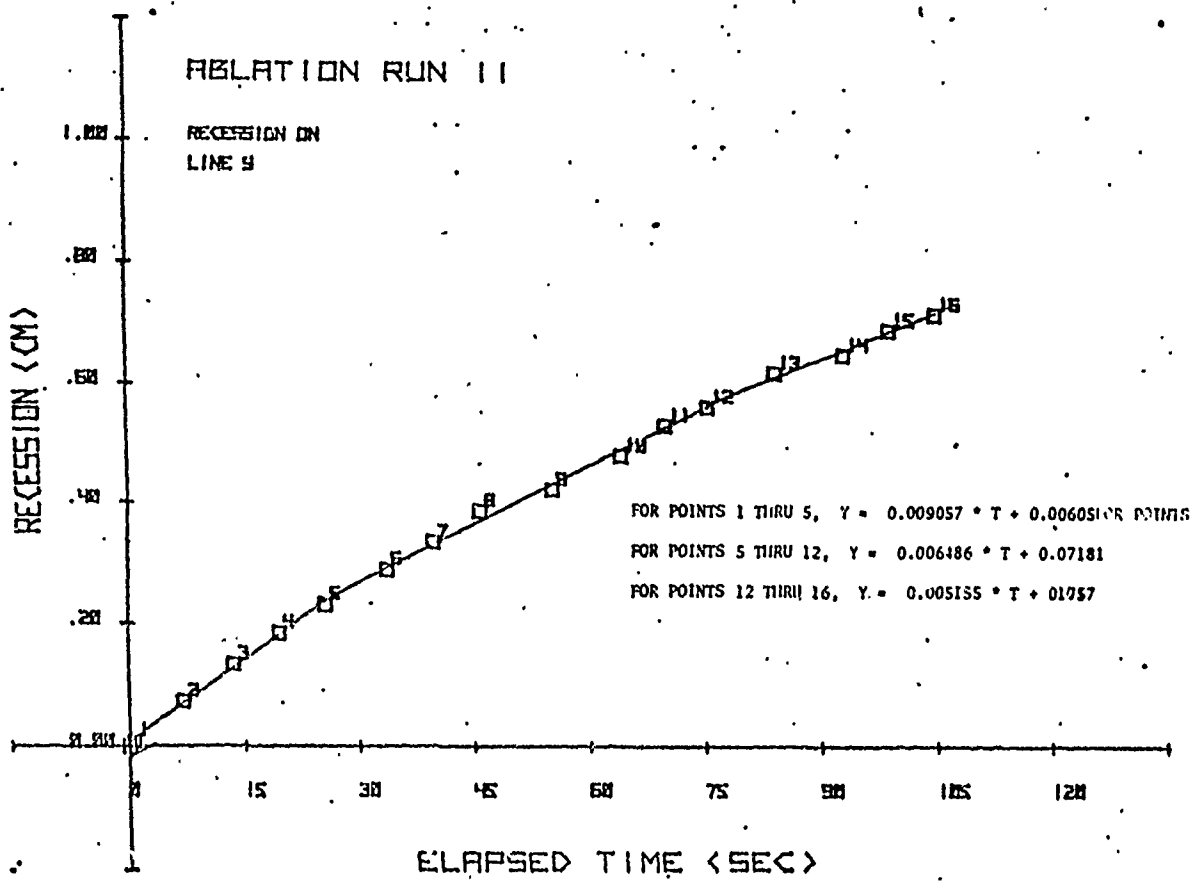
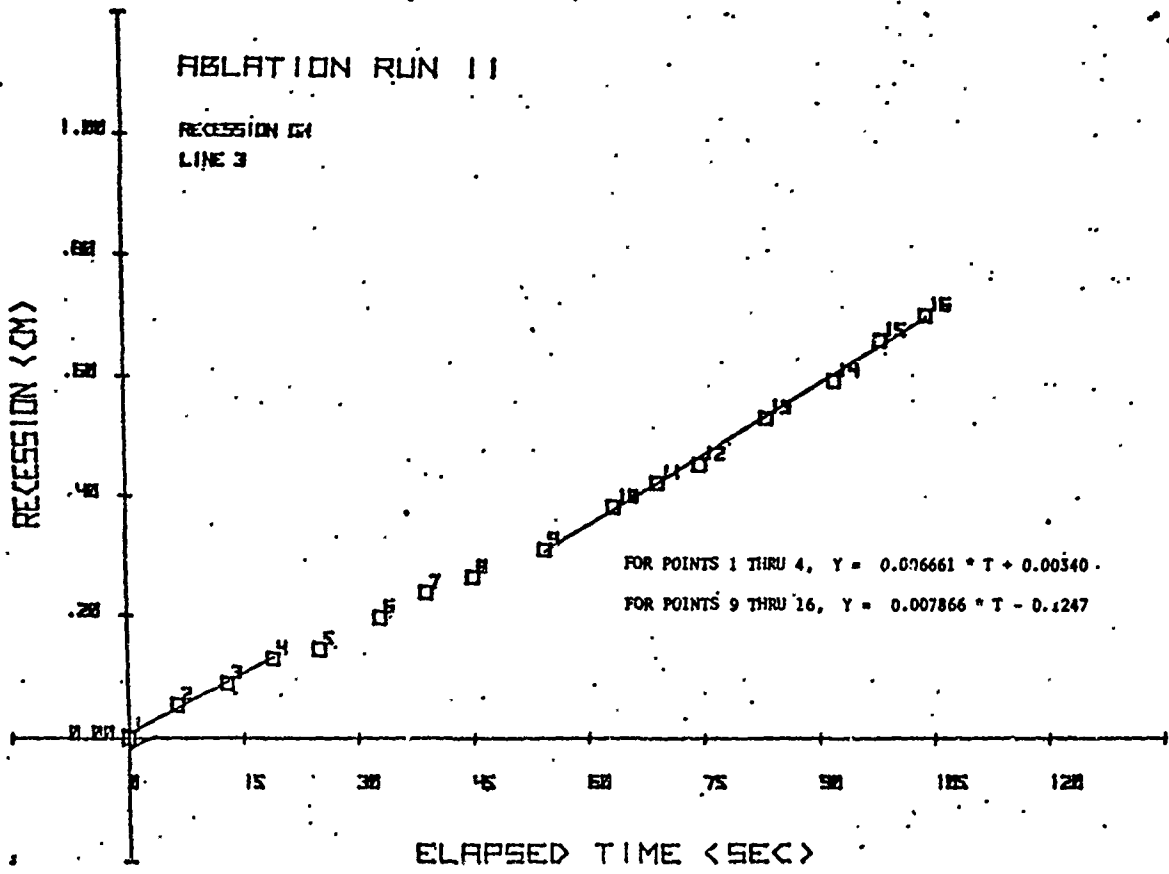
Position	Recession Rate $\text{cm/s (} \times 10^3 \text{)}$	Mass Flux $\text{g/cm}^2 \cdot \text{s (} \times 10^3 \text{)}$	Normalized
Stag Pt	6.49	3.96	0.689
15 right	7.21	4.40	0.765
15 left	6.57	4.01	0.697
30 right	7.08	4.32	0.751
30 left	6.39	3.90	0.678
45 right	6.89	4.20	0.730
45 left	6.13	3.74	0.650
60 right	6.30	3.84	0.669
60 left	-----	-----	-----
75 right	3.90	2.38	0.414
75 left	-----	-----	-----
90 right	-----	-----	-----
90 left	-----	-----	-----

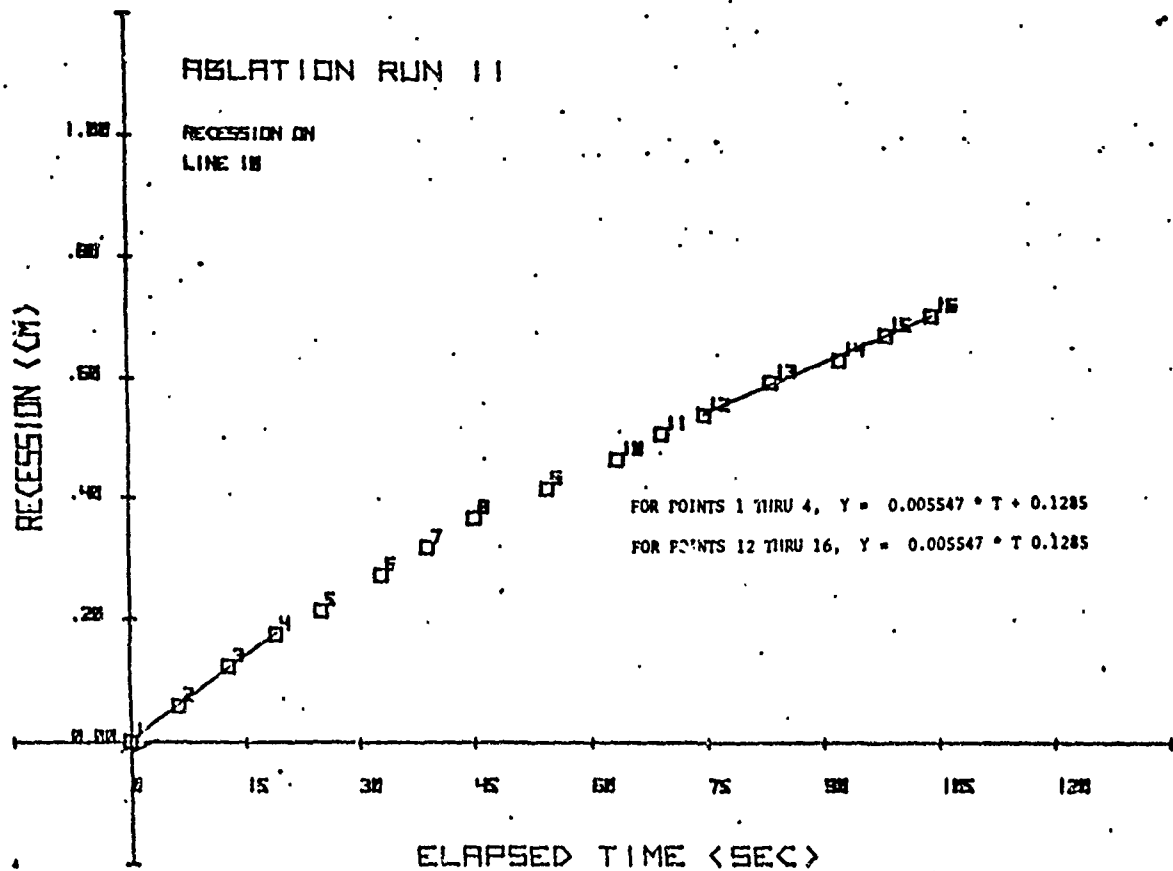
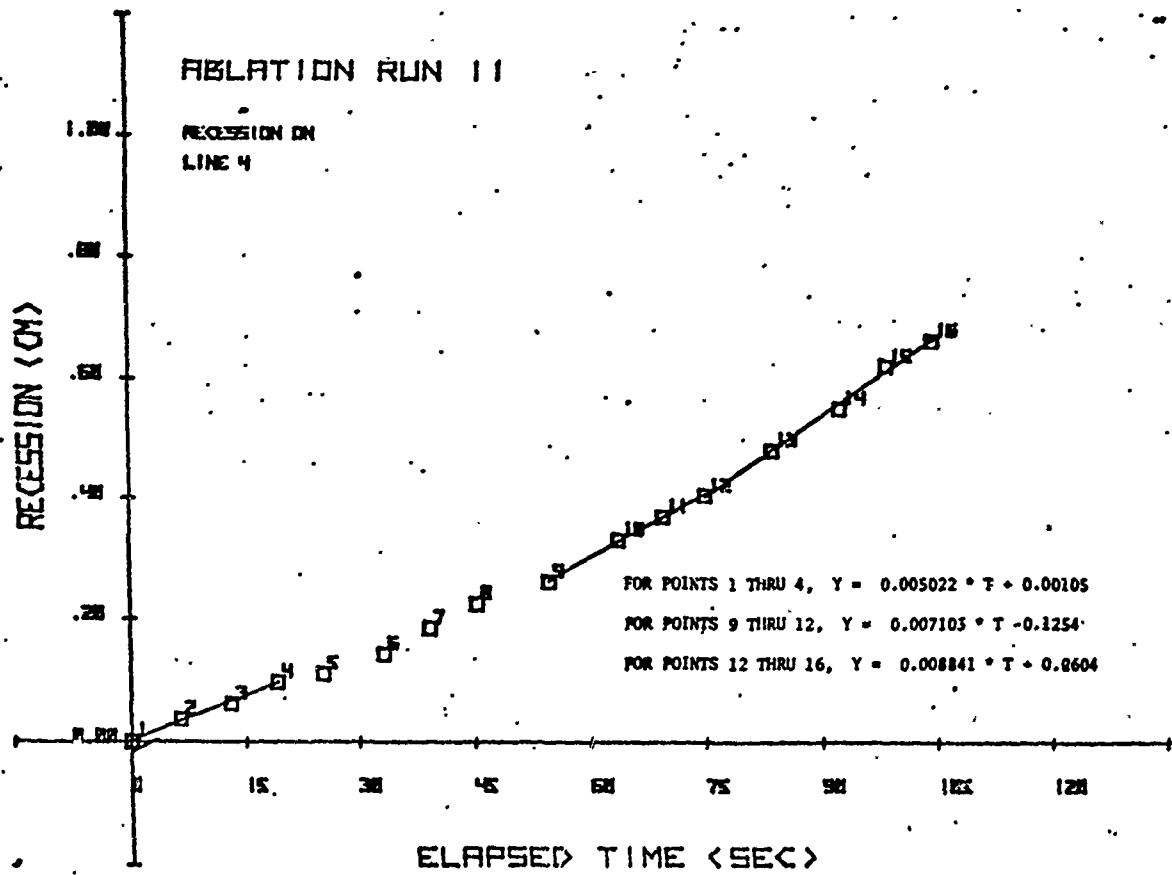


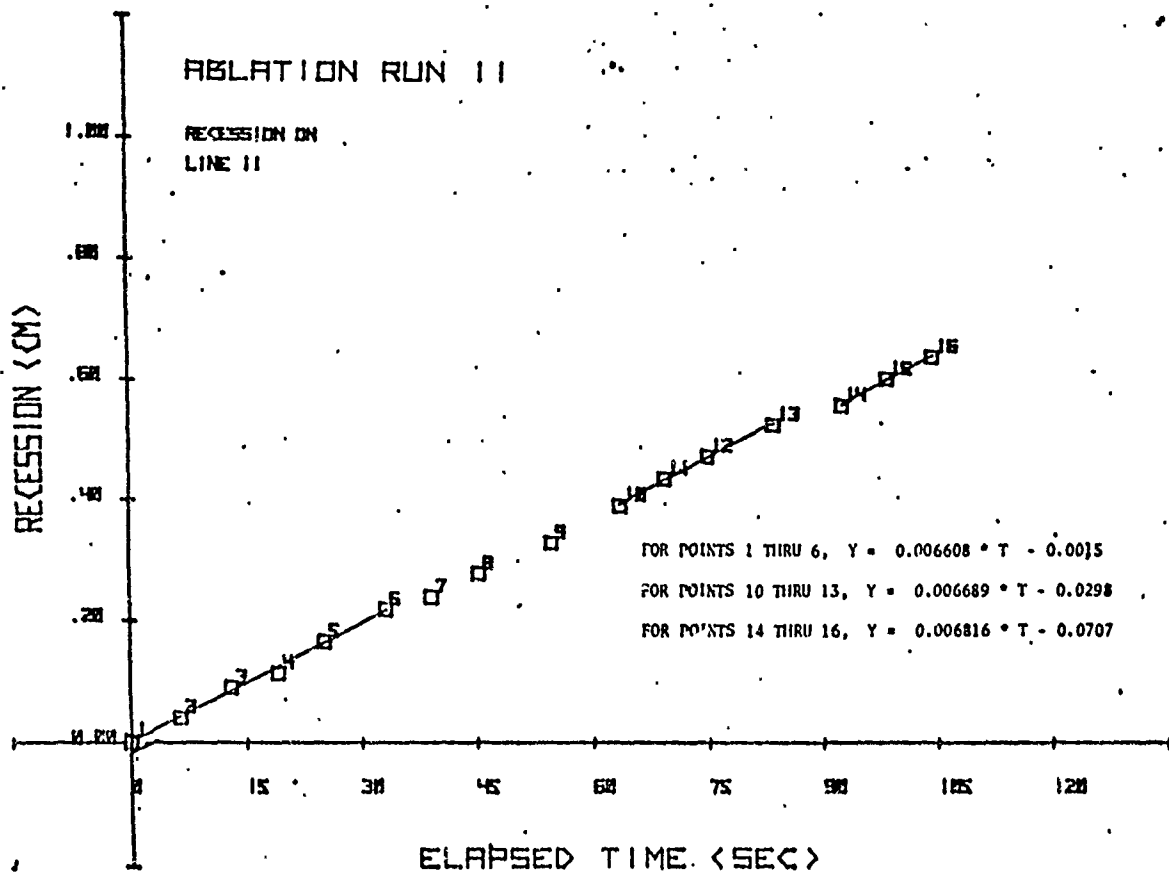


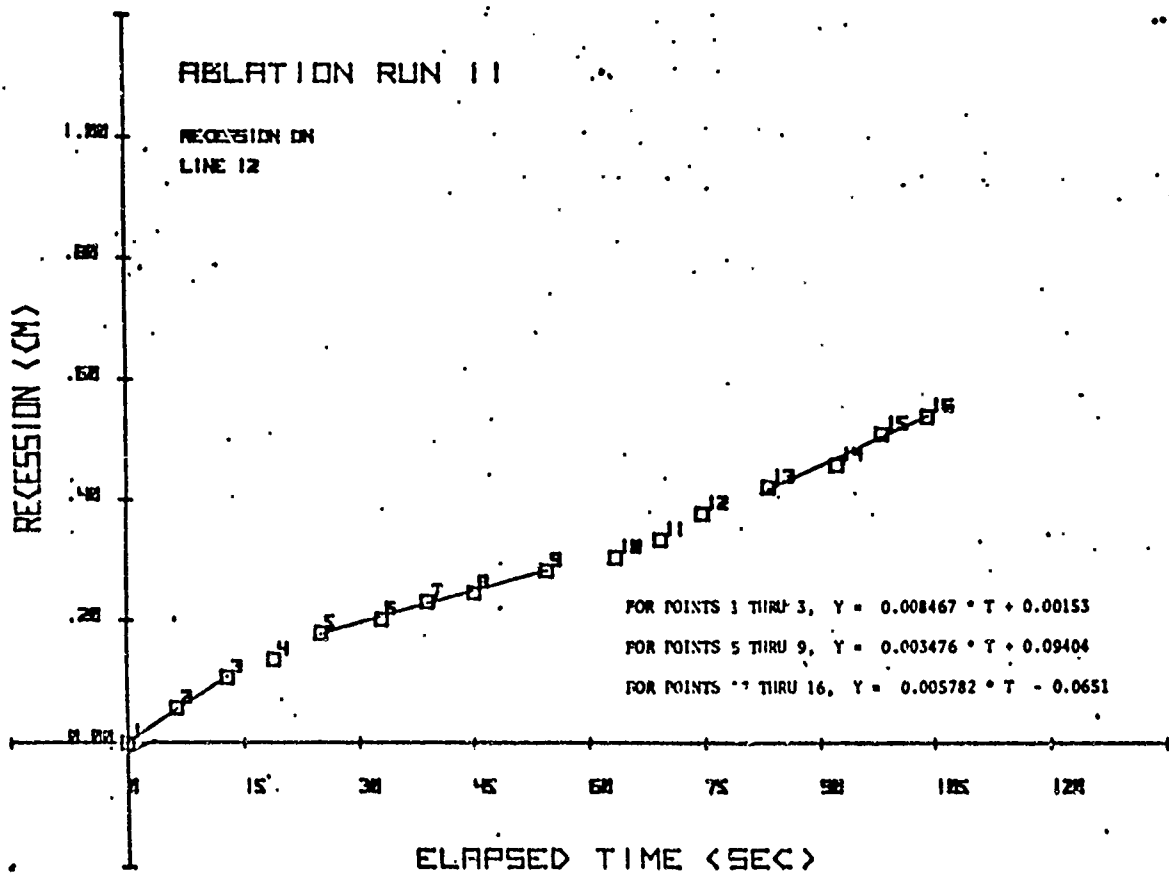








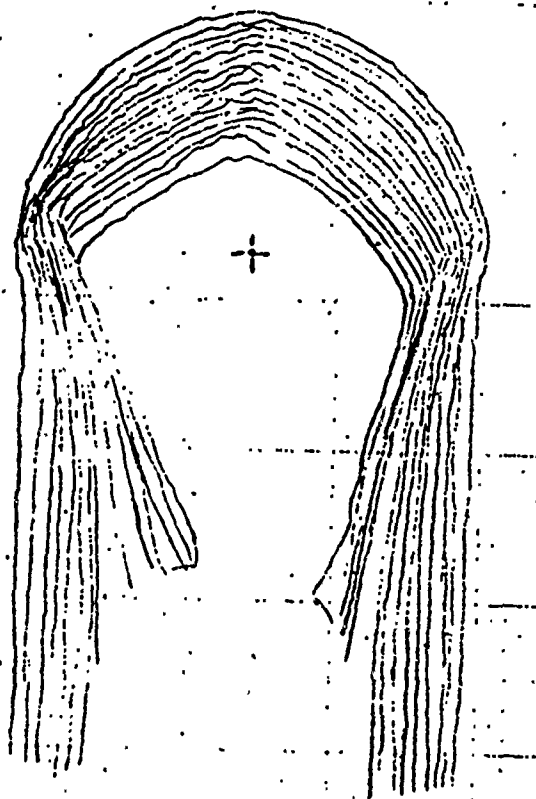


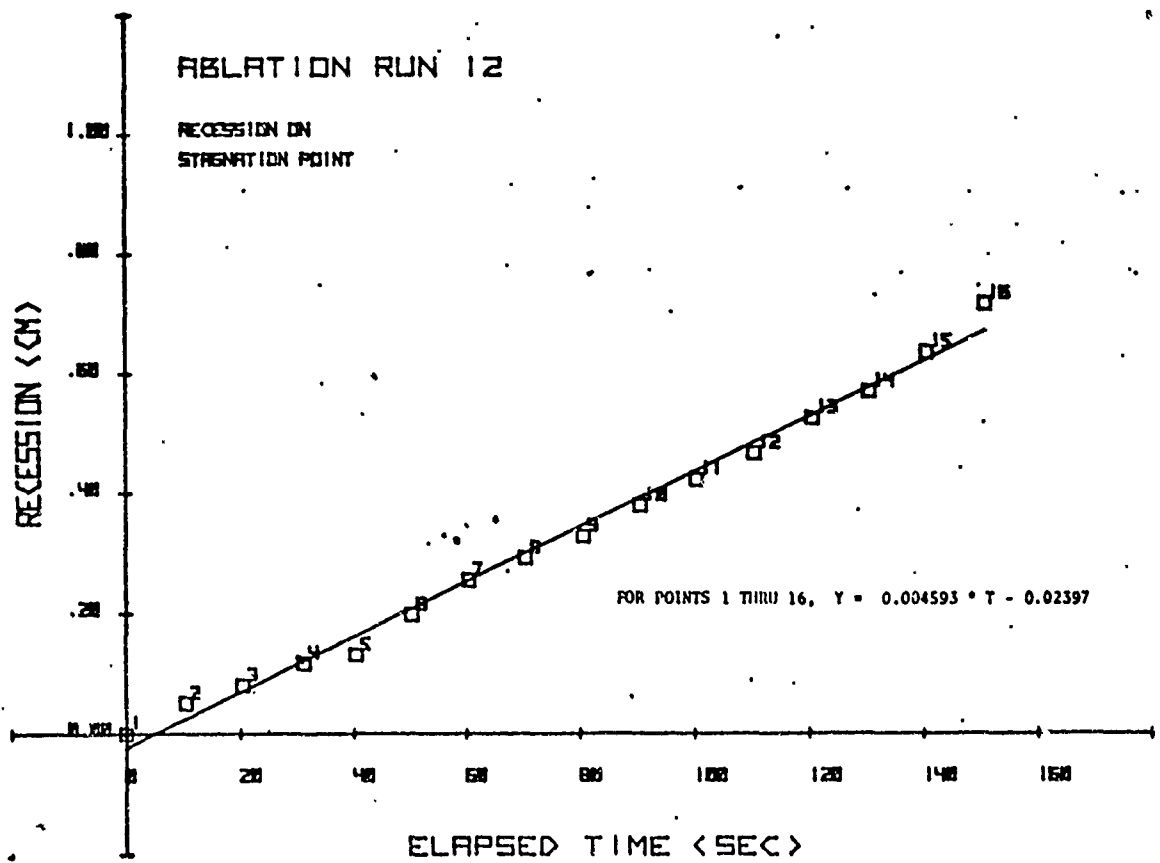


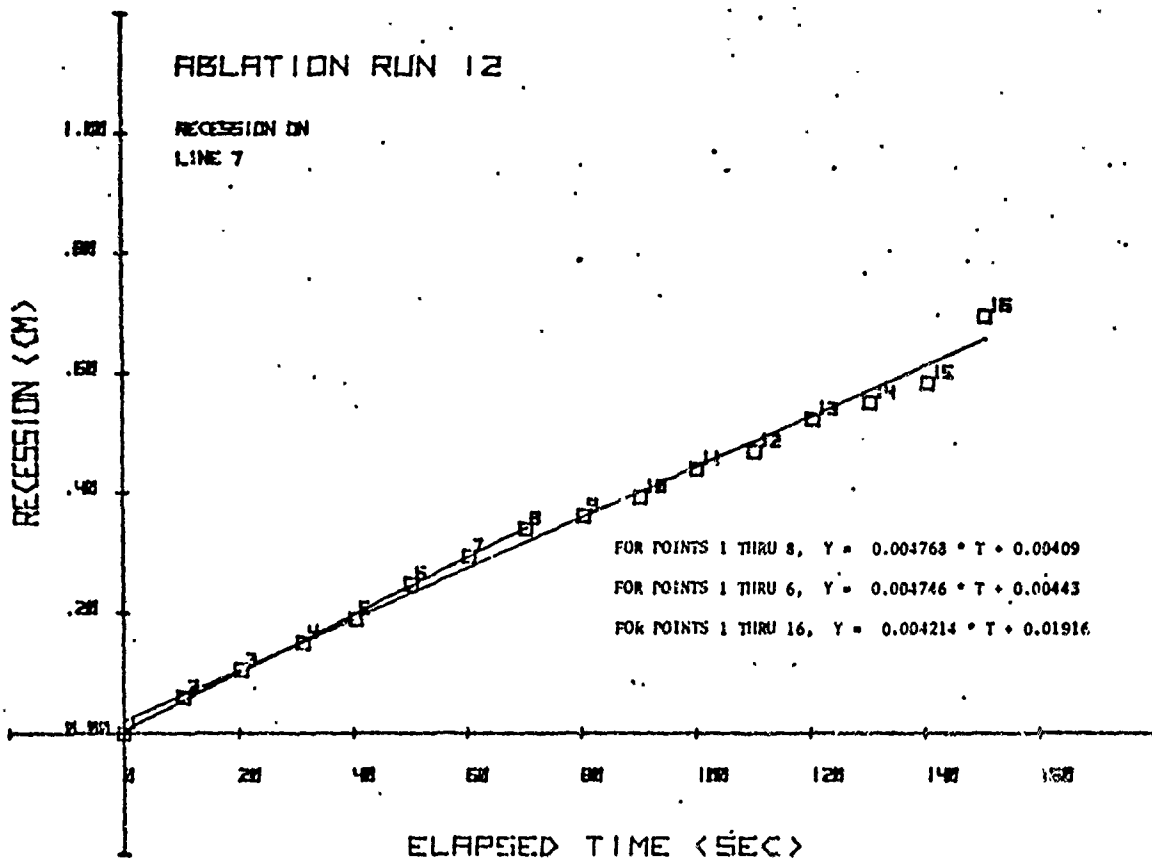
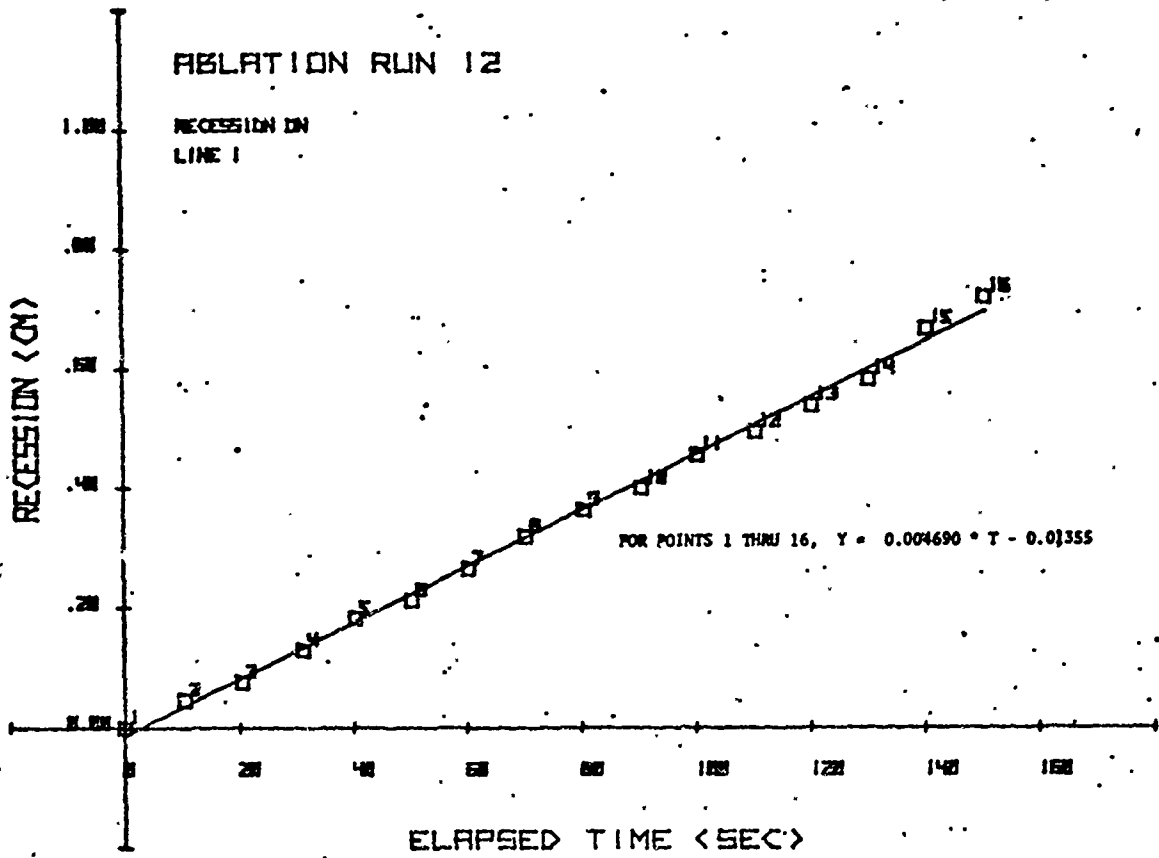
Run 5 (also Identified as Run 12)

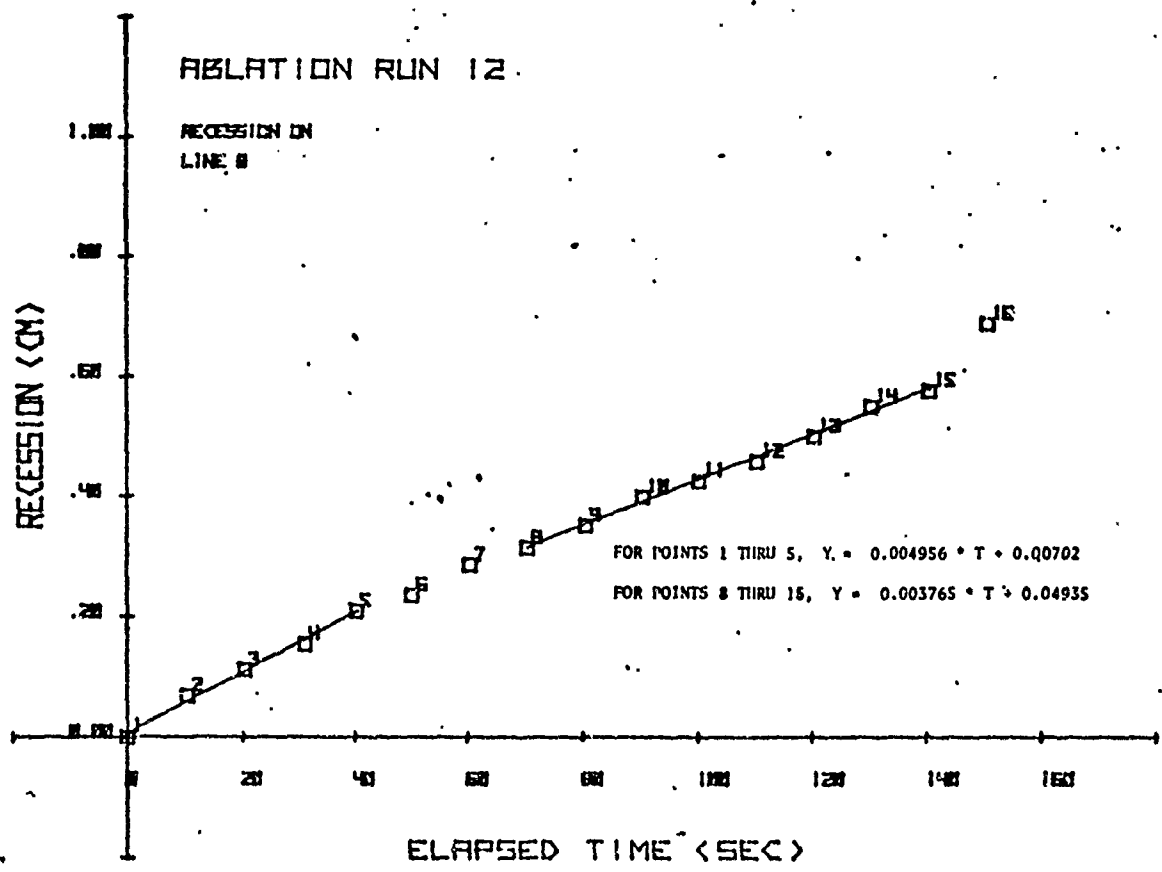
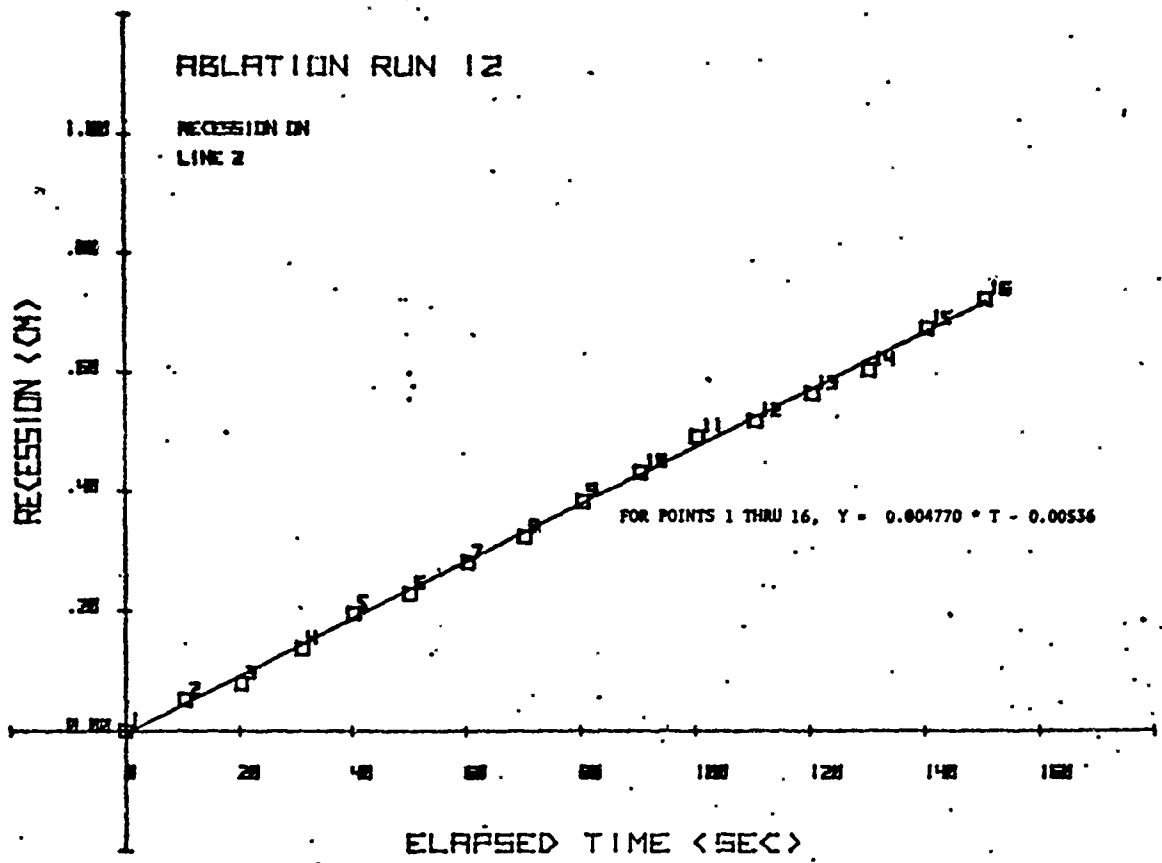
Simple Theory Stagnation Point Mass Flux: $0.00435 \text{ g/cm}^2 \cdot \text{s}$

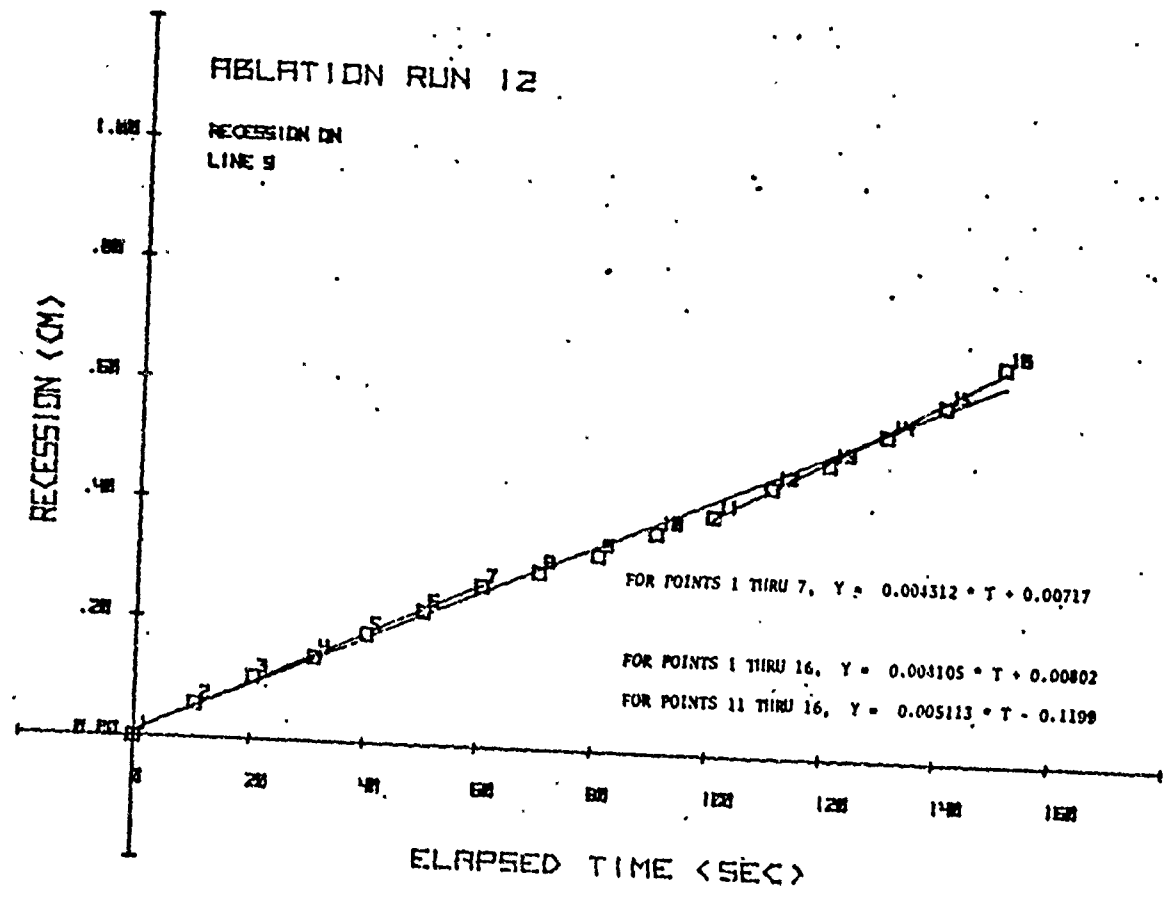
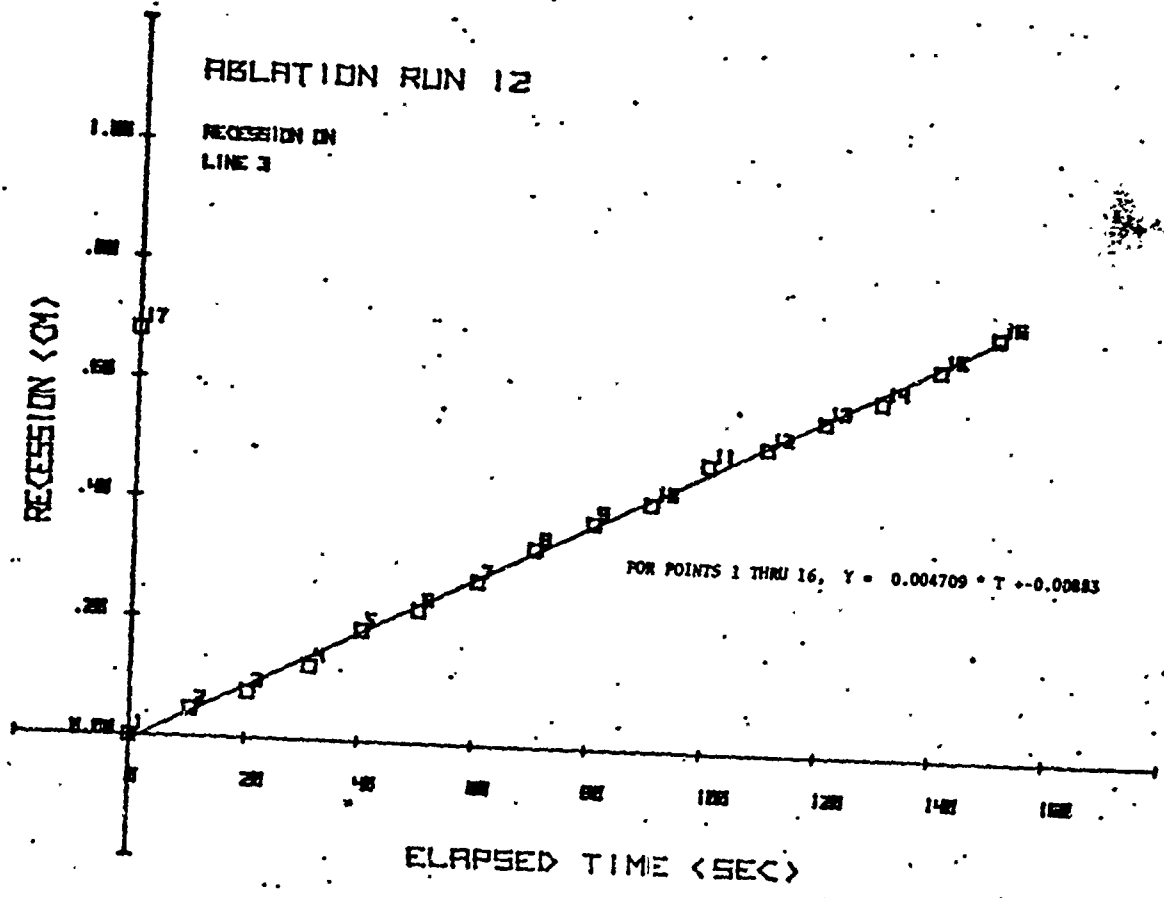
Position	Recession Rate $\text{cm/s} (\times 10^3)$	Mass Flux $\text{g/cm}^2 \cdot \text{s} (\times 10^3)$	Normalized
Stag Pt	4.59	2.85	0.655
15 right	4.69	2.91	0.669
15 left	4.75	2.94	0.676
30 right	4.77	2.96	0.680
30 left	4.96	3.07	0.705
45 right	4.71	2.92	0.671
45 left	4.31	2.67	0.614
60 right	4.49	2.79	0.641
60 left	----	----	----
75 right	4.94	3.06	0.703
75 left	----	----	----
90 right	----	----	----
90 left	----	----	----

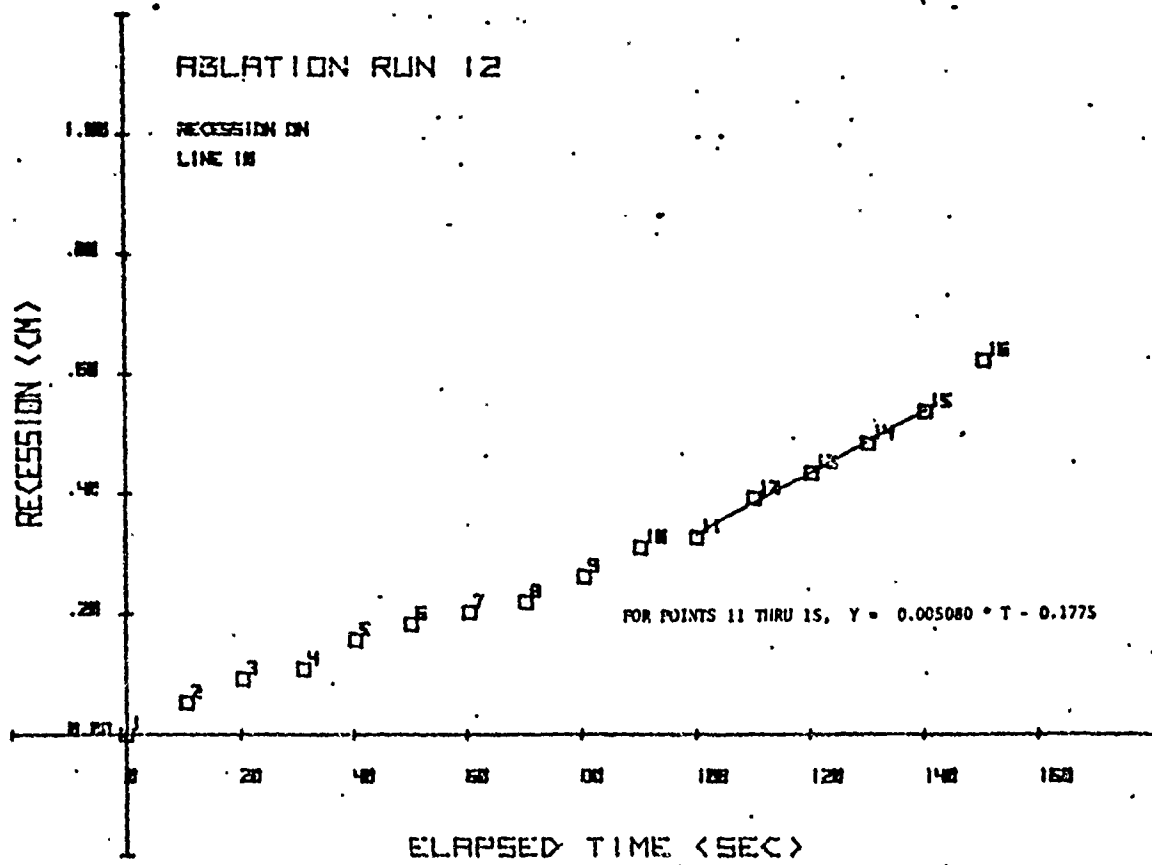
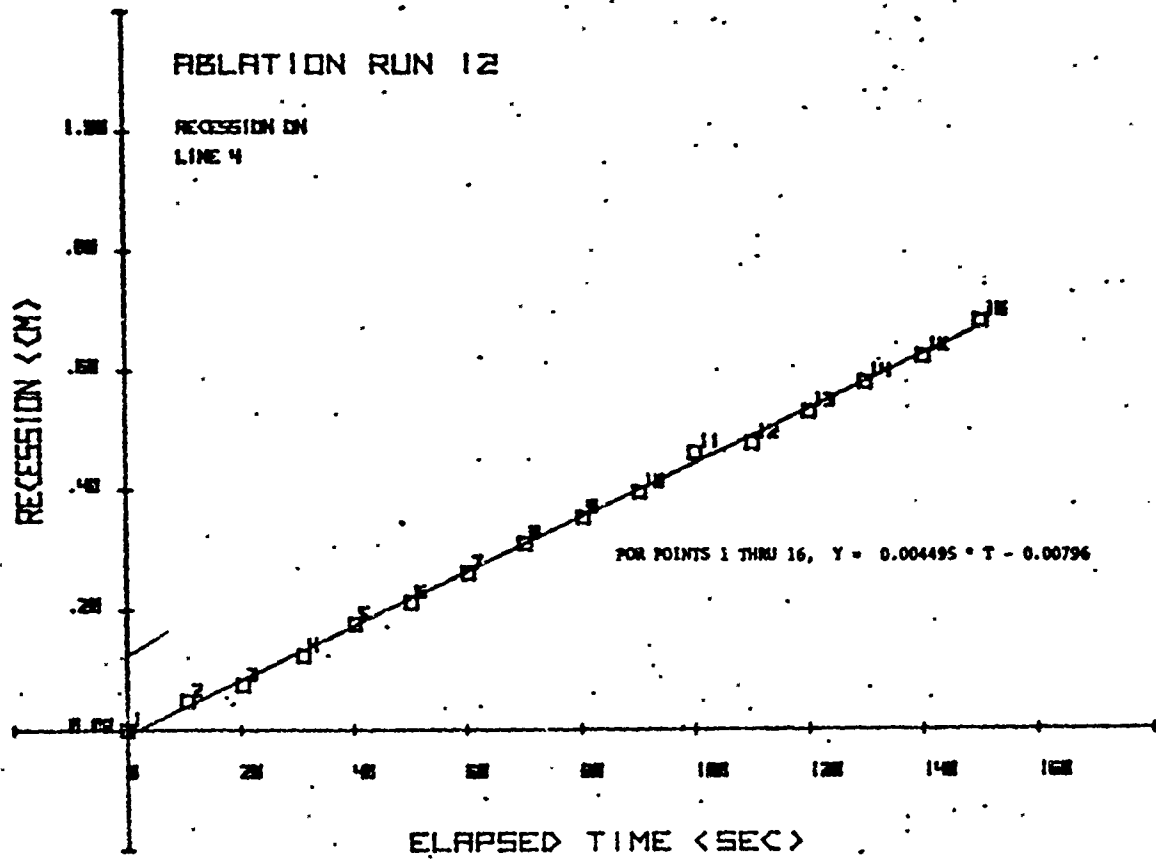


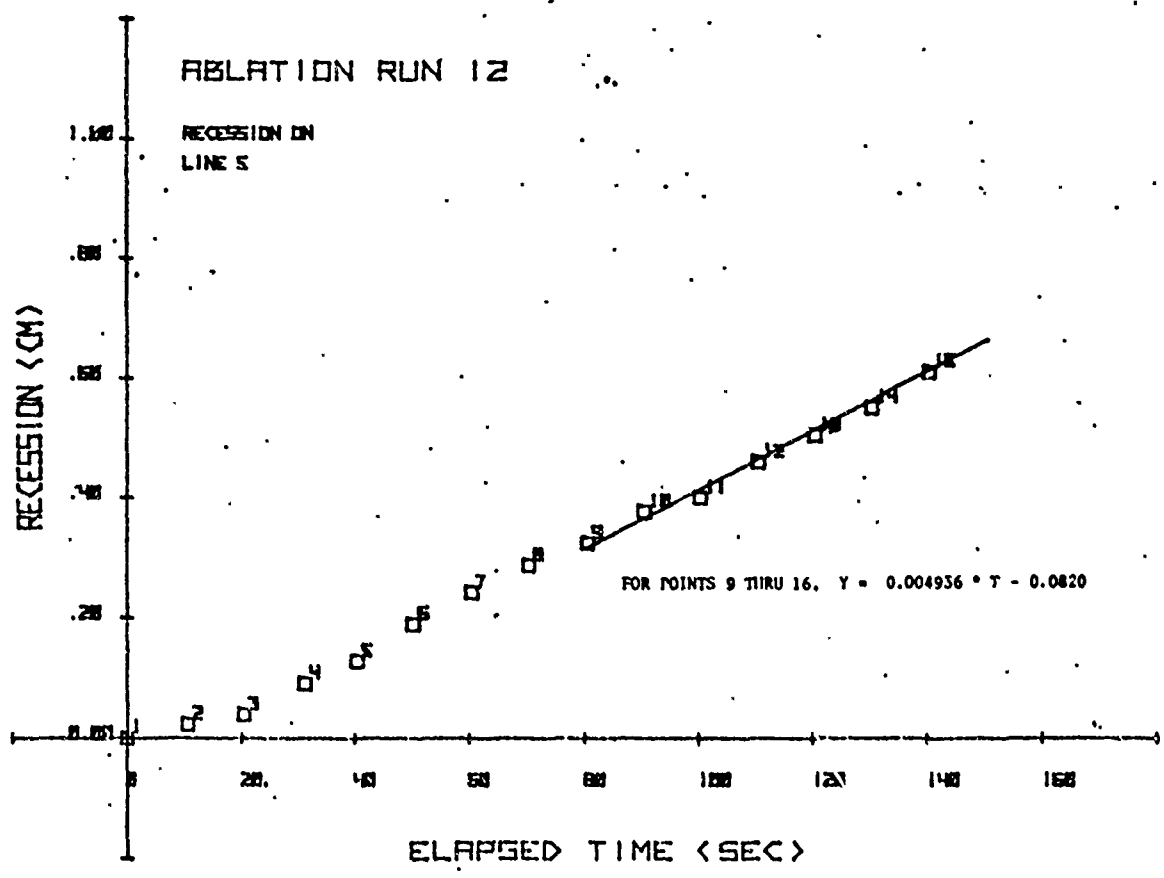








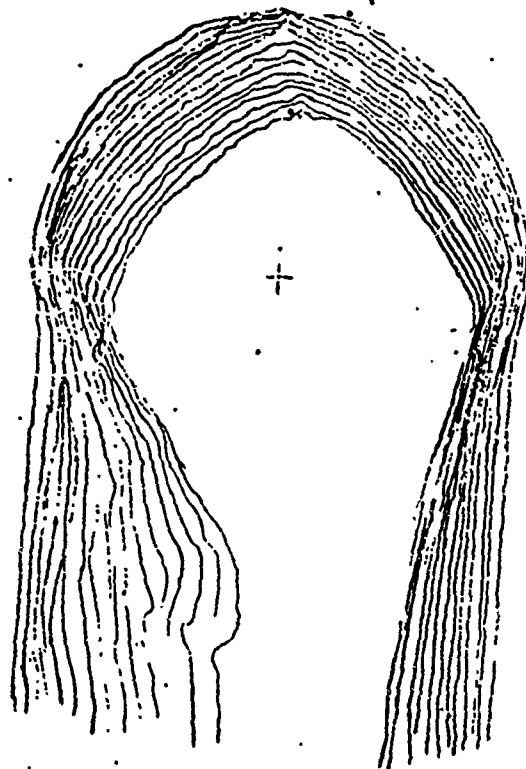


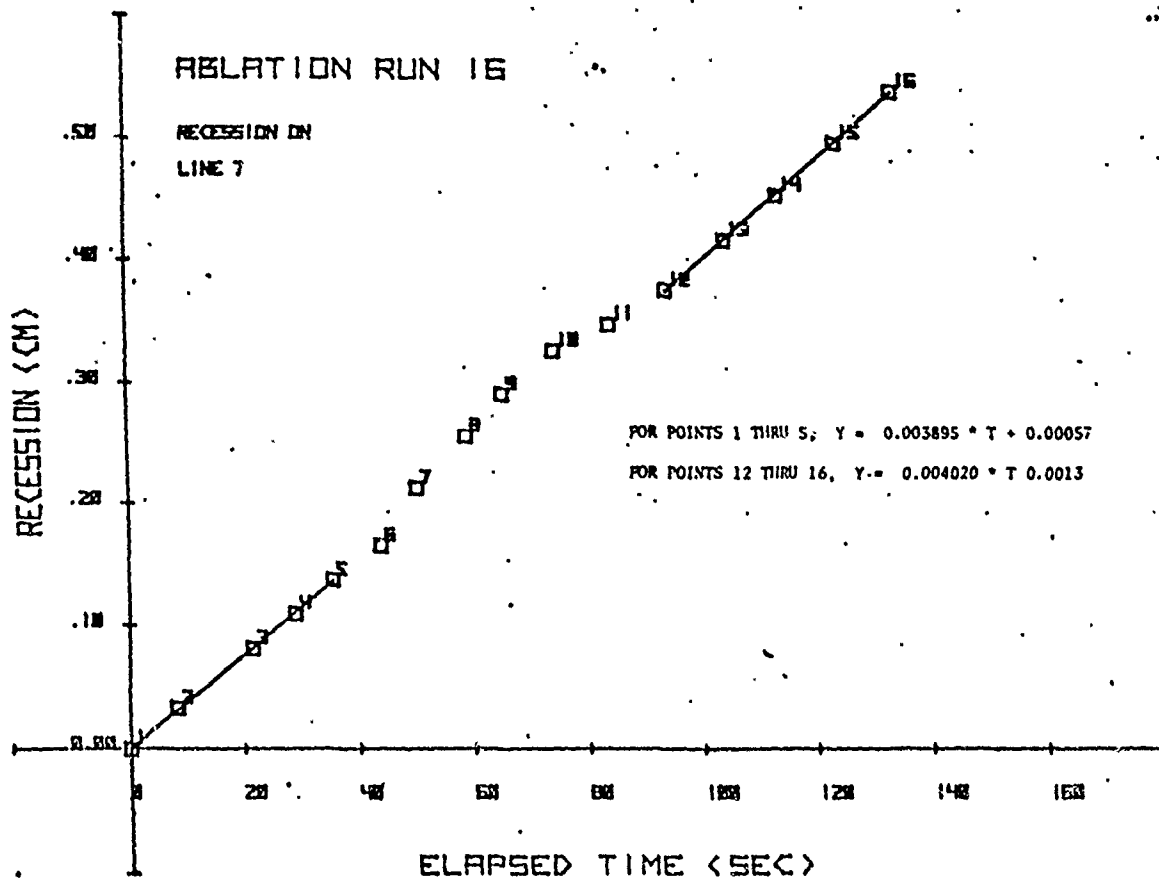
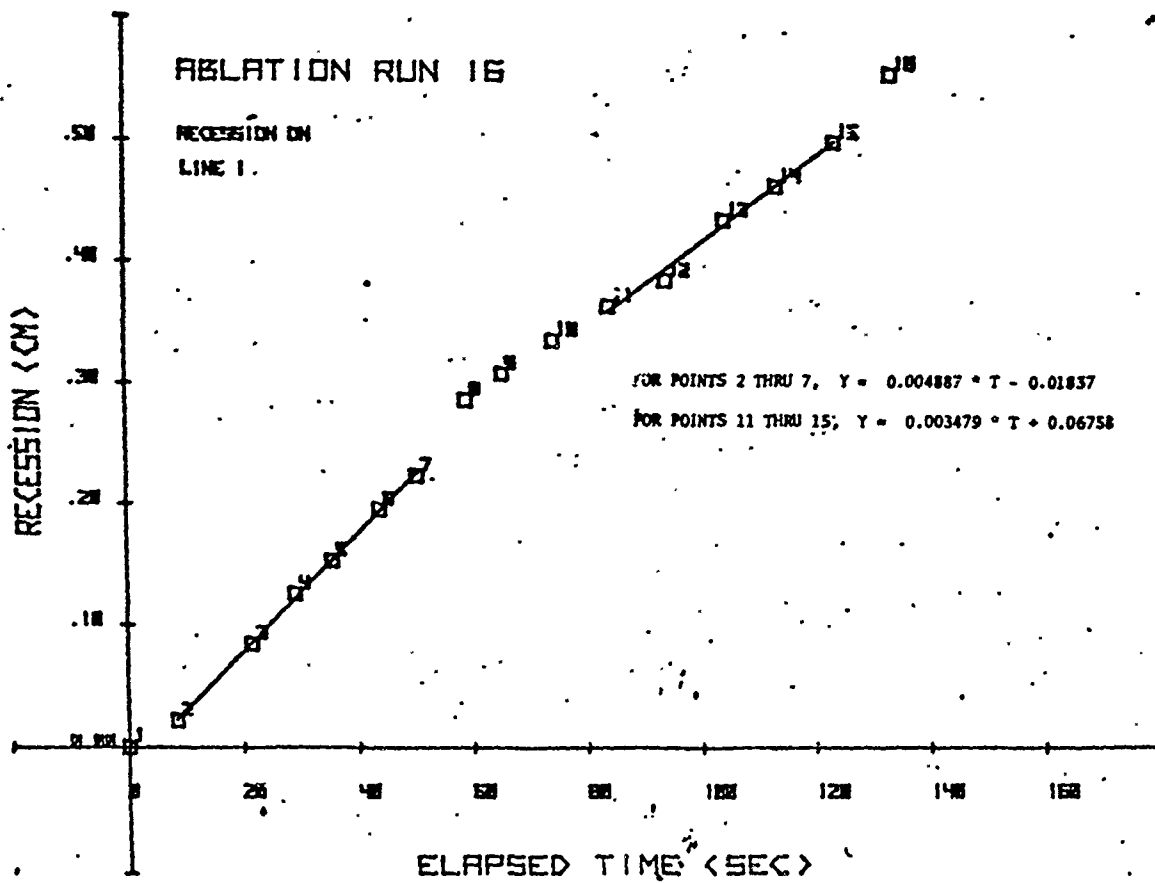


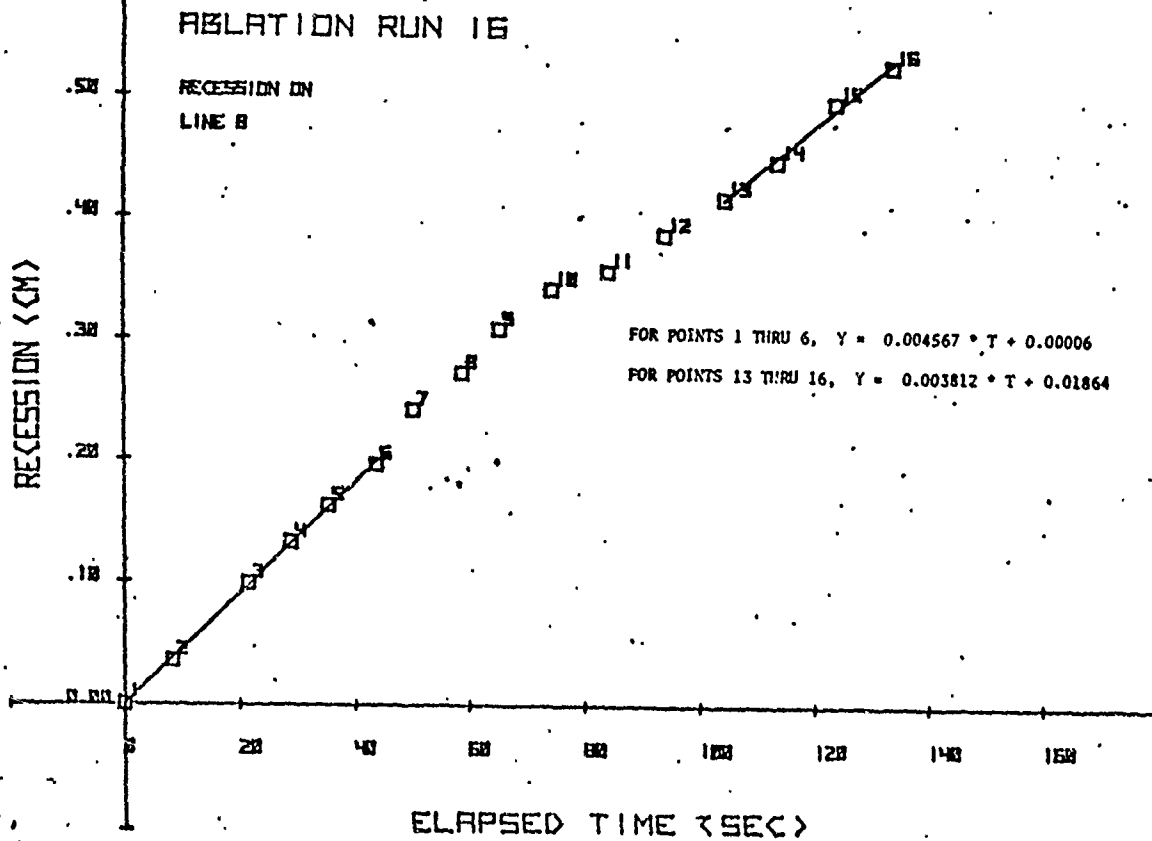
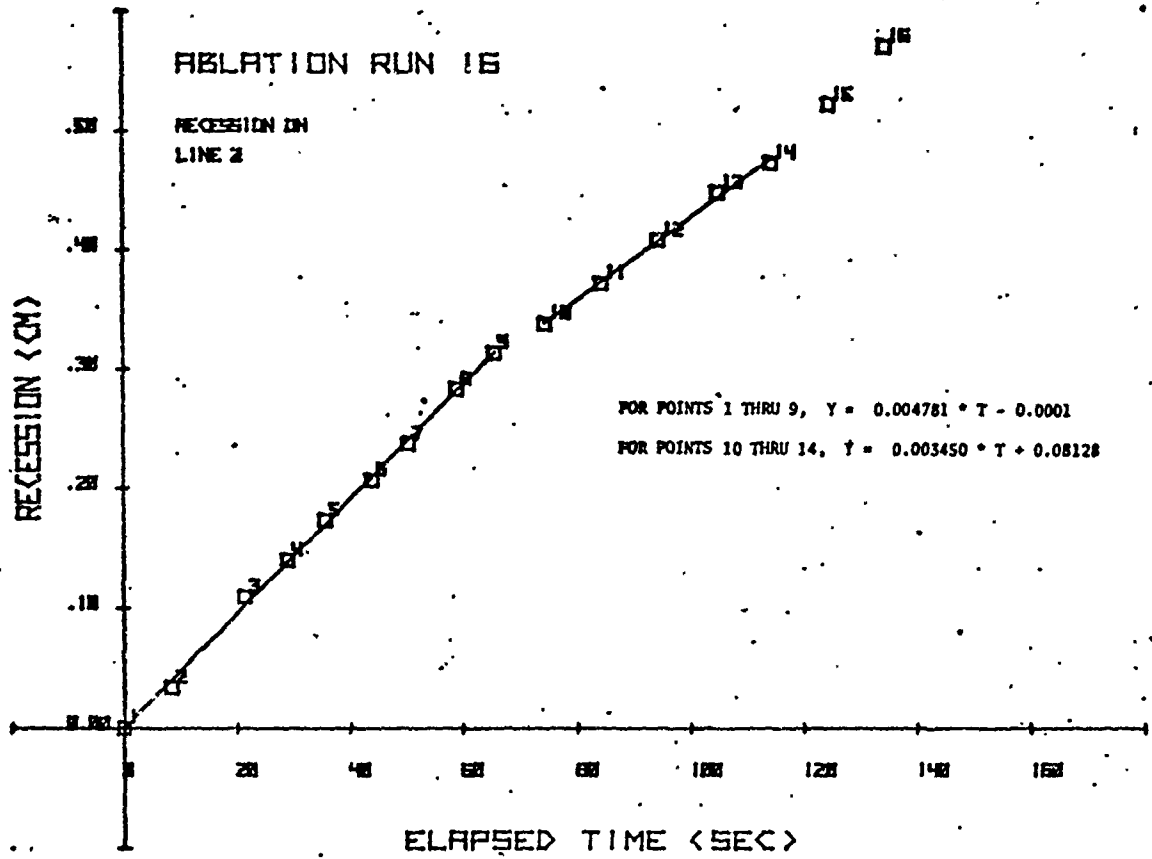
Run 6 (Also Identified as Run 16)

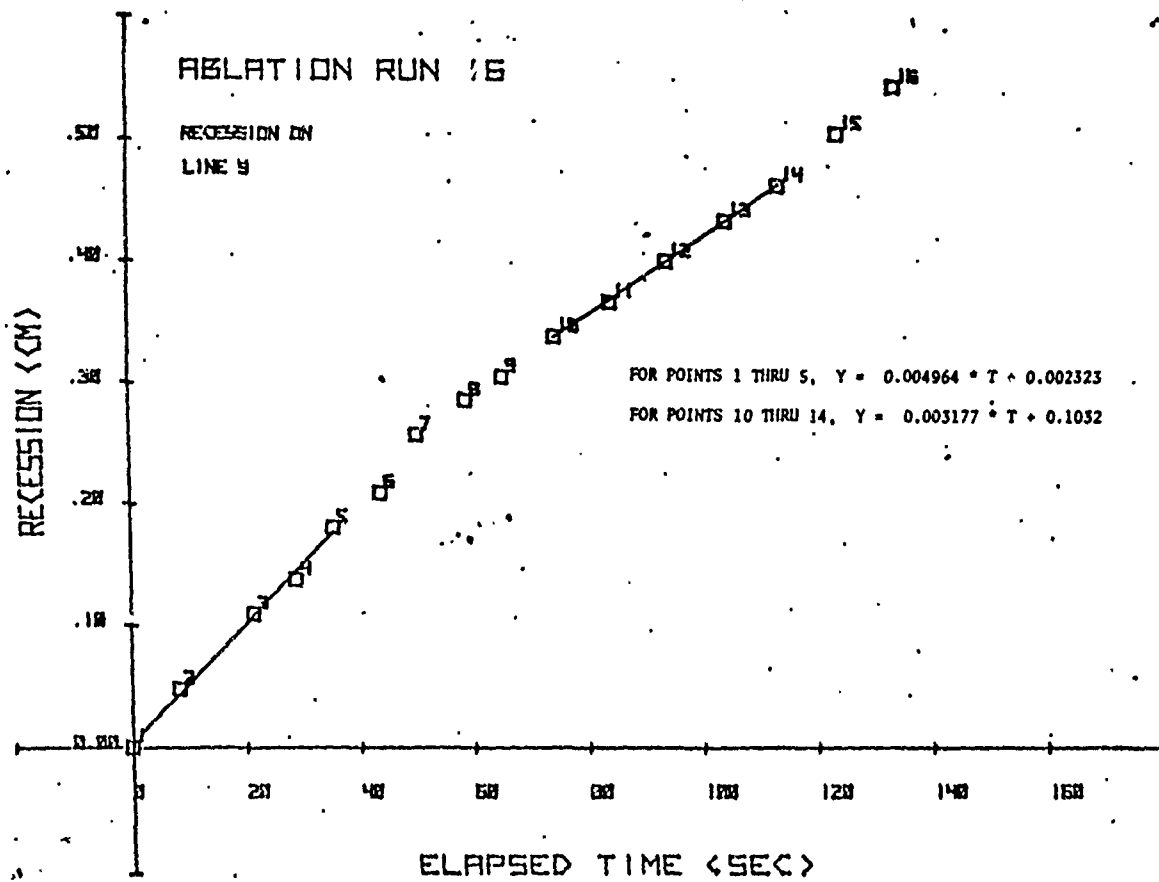
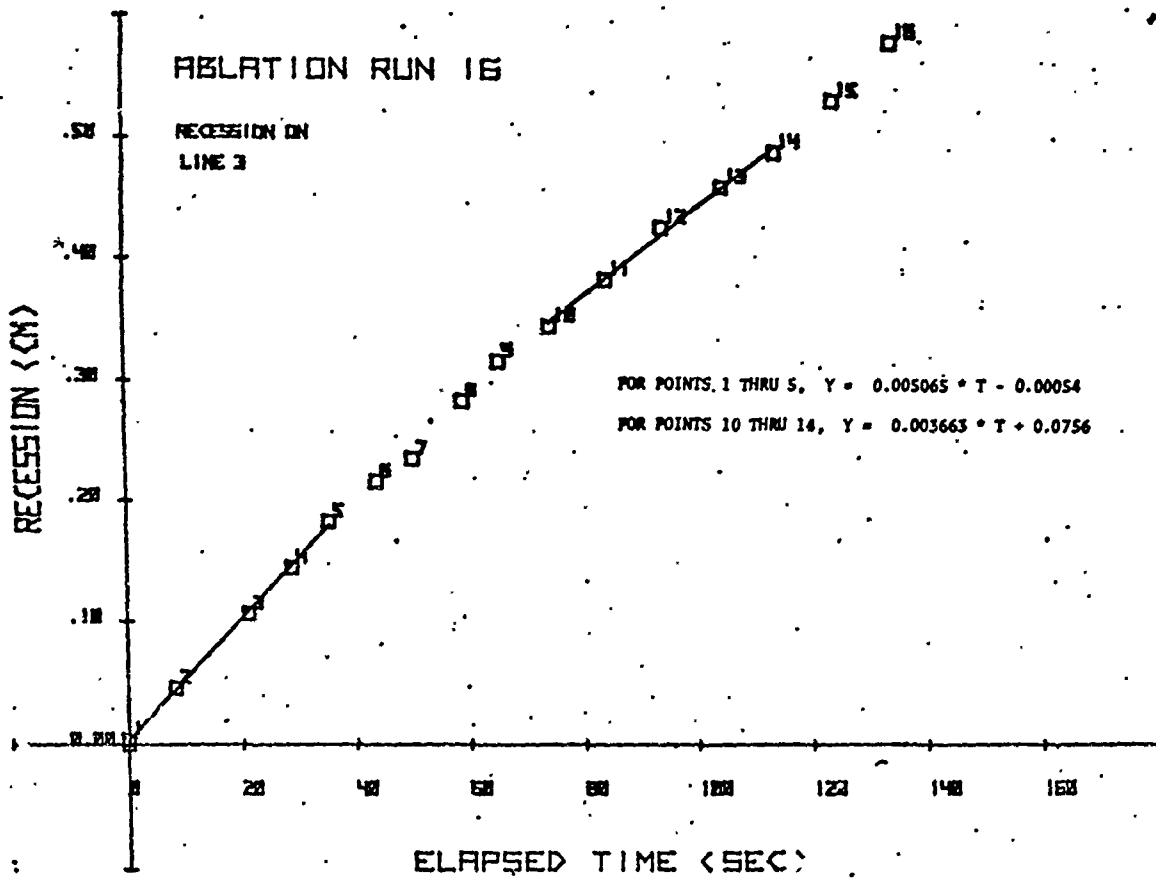
Simple Theory Stagnation Point Mass Flux: $0.00411 \text{ g/cm}^2 \cdot \text{s}$

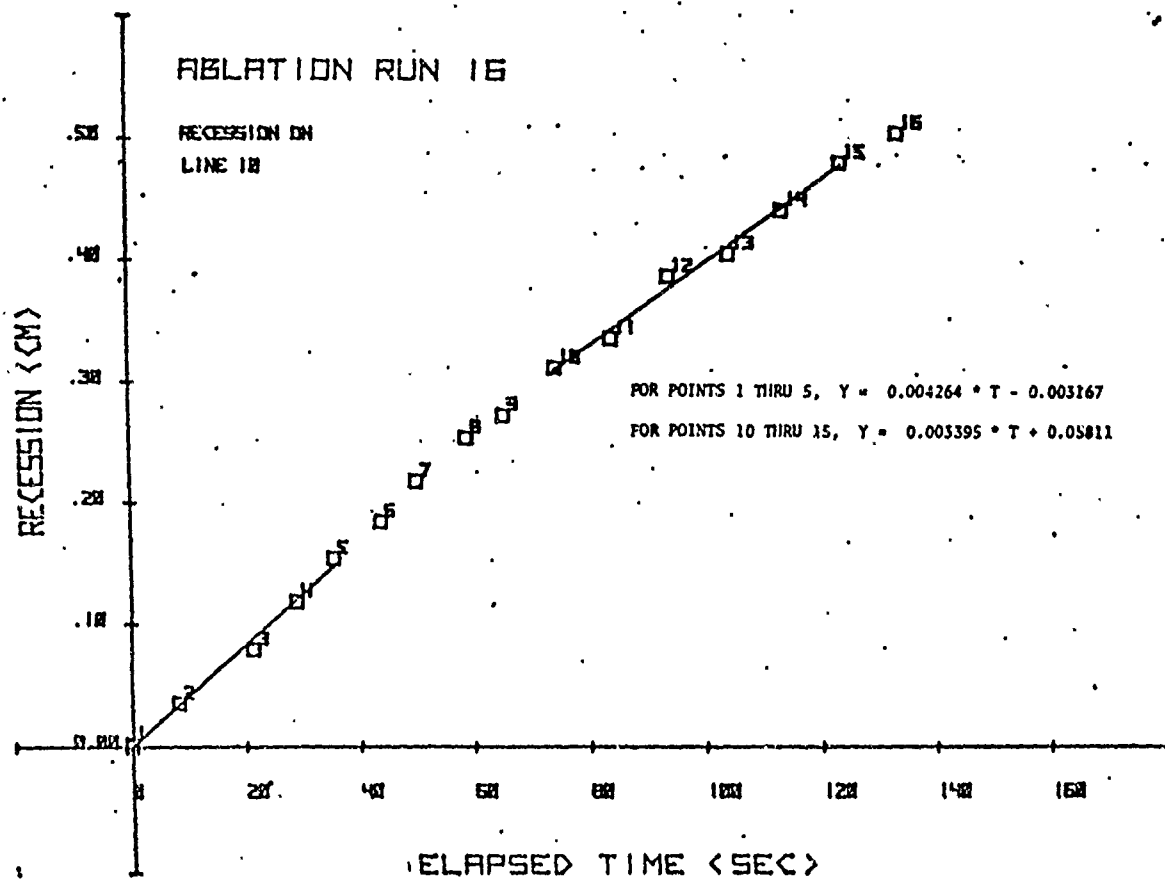
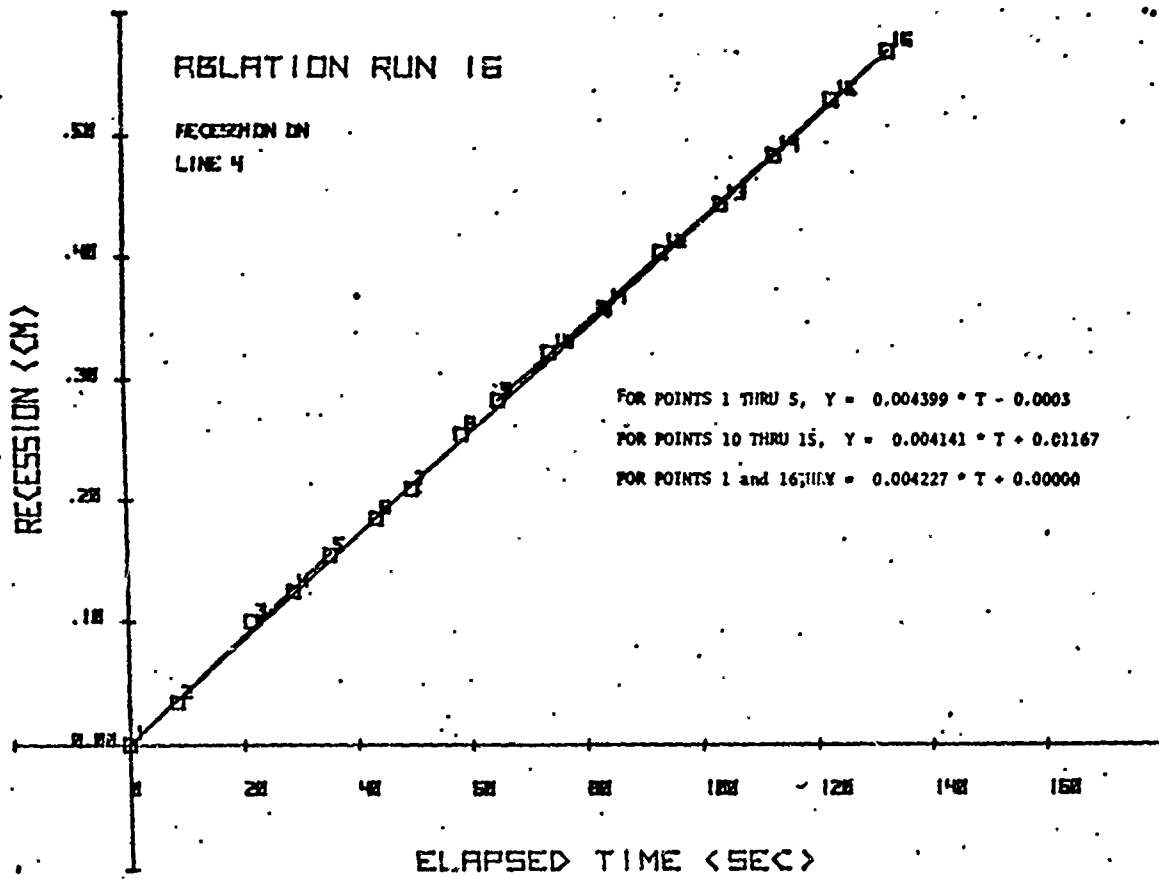
Position	Recession Rate $\text{cm/s (} \times 10^3 \text{)}$	Mass Flux $\text{g/cm}^2 \cdot \text{s (} \times 10^3 \text{)}$	Normalized
Stag Pt	-----	-----	-----
15 right	4.96	3.03	0.737
15 left	3.96	2.42	0.589
30 right	4.85	2.96	0.720
30 left	4.64	2.83	0.689
45 right	5.14	3.14	0.764
45 left	5.06	3.08	0.749
60 right	4.49	2.73	0.664
60 left	4.33	2.64	0.642
75 right	3.59	2.19	0.533
75 left	3.46	2.11	0.513
90 right	2.56	1.56	0.380
90 left	2.03	1.24	0.302

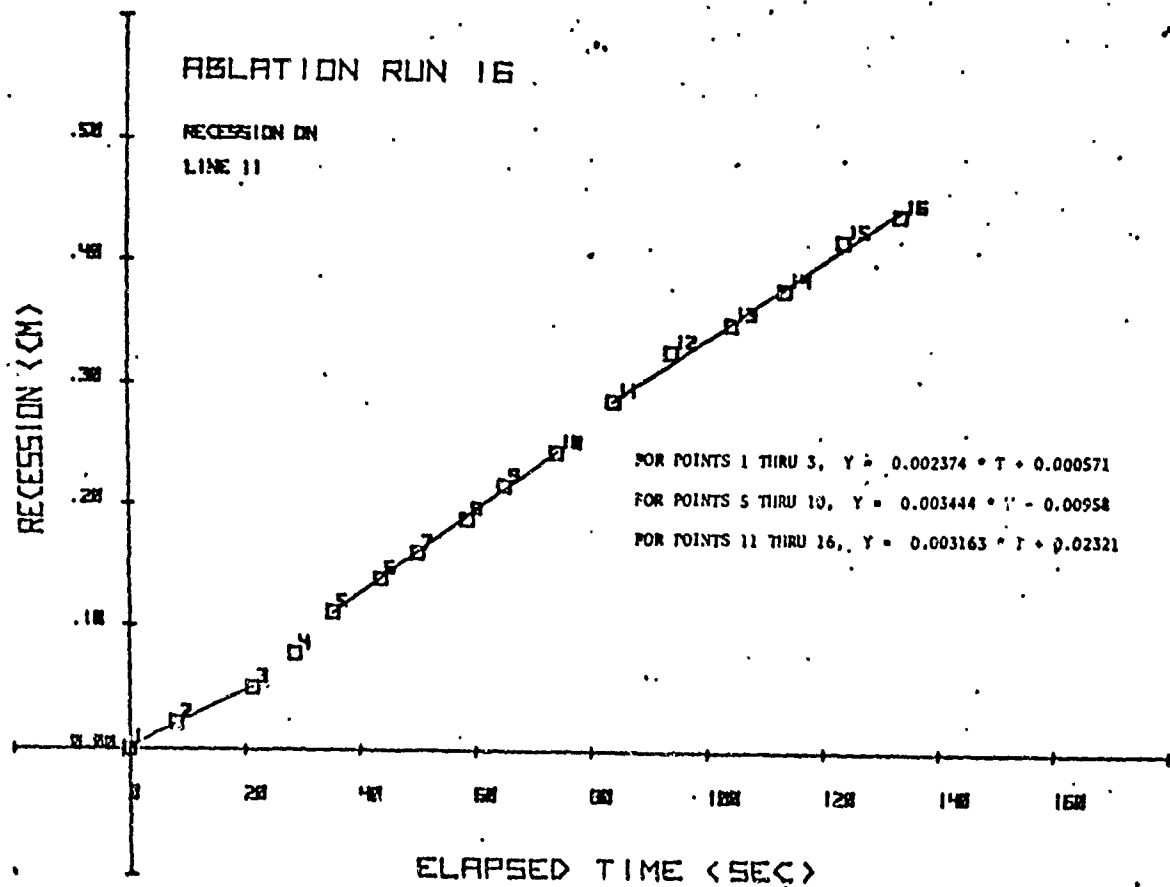
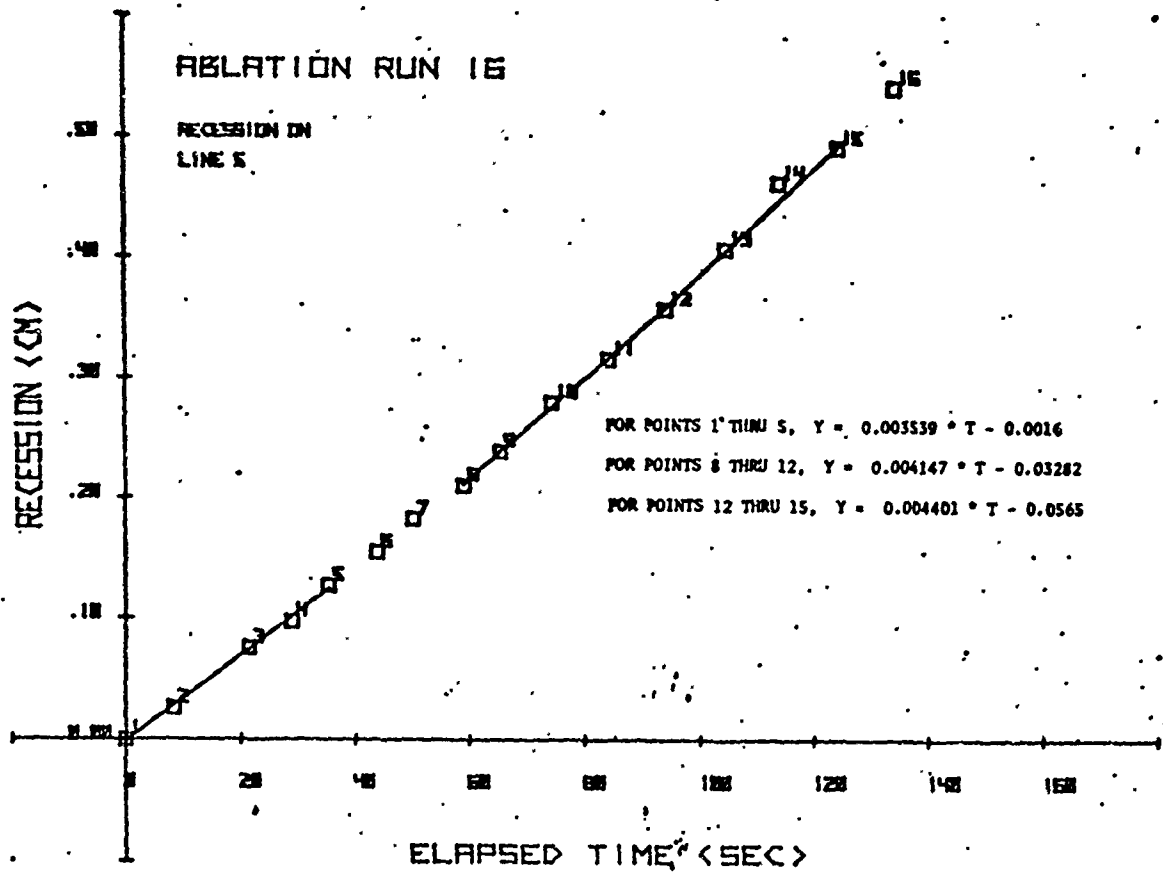


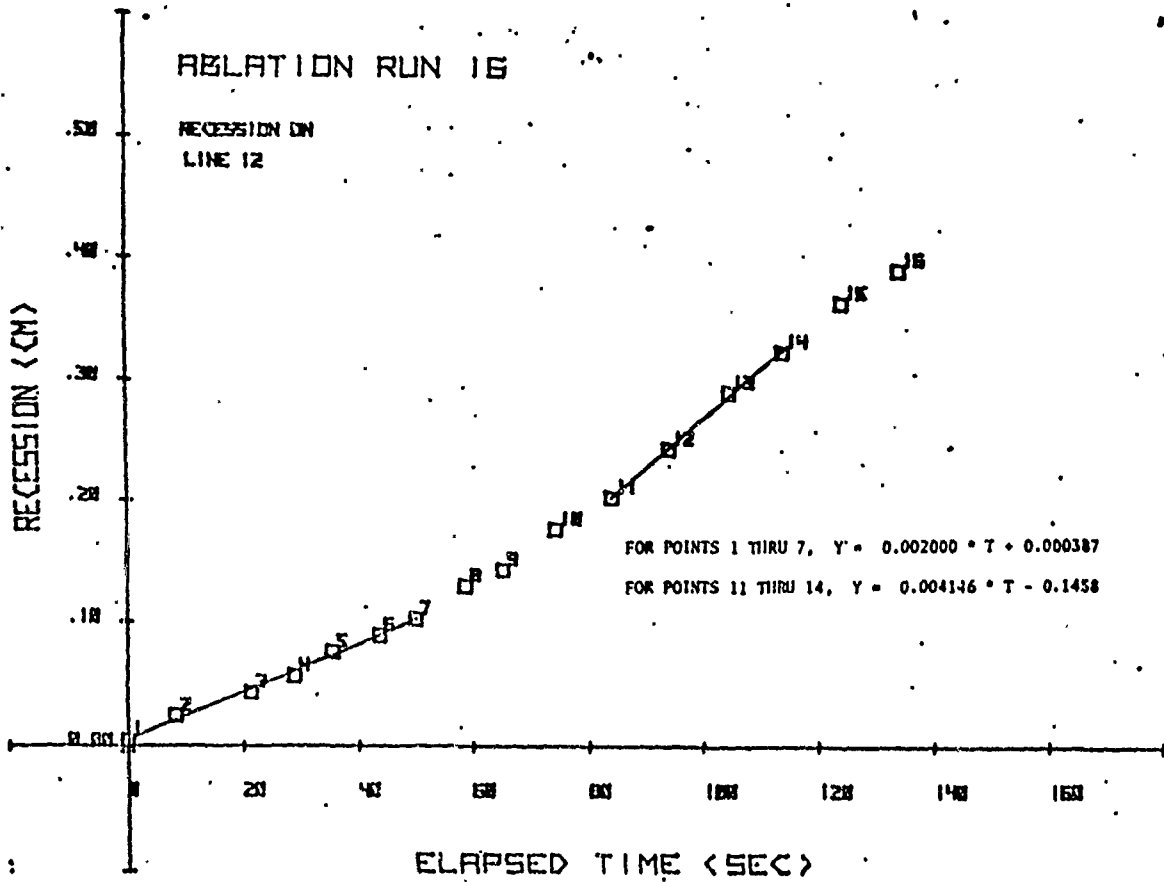
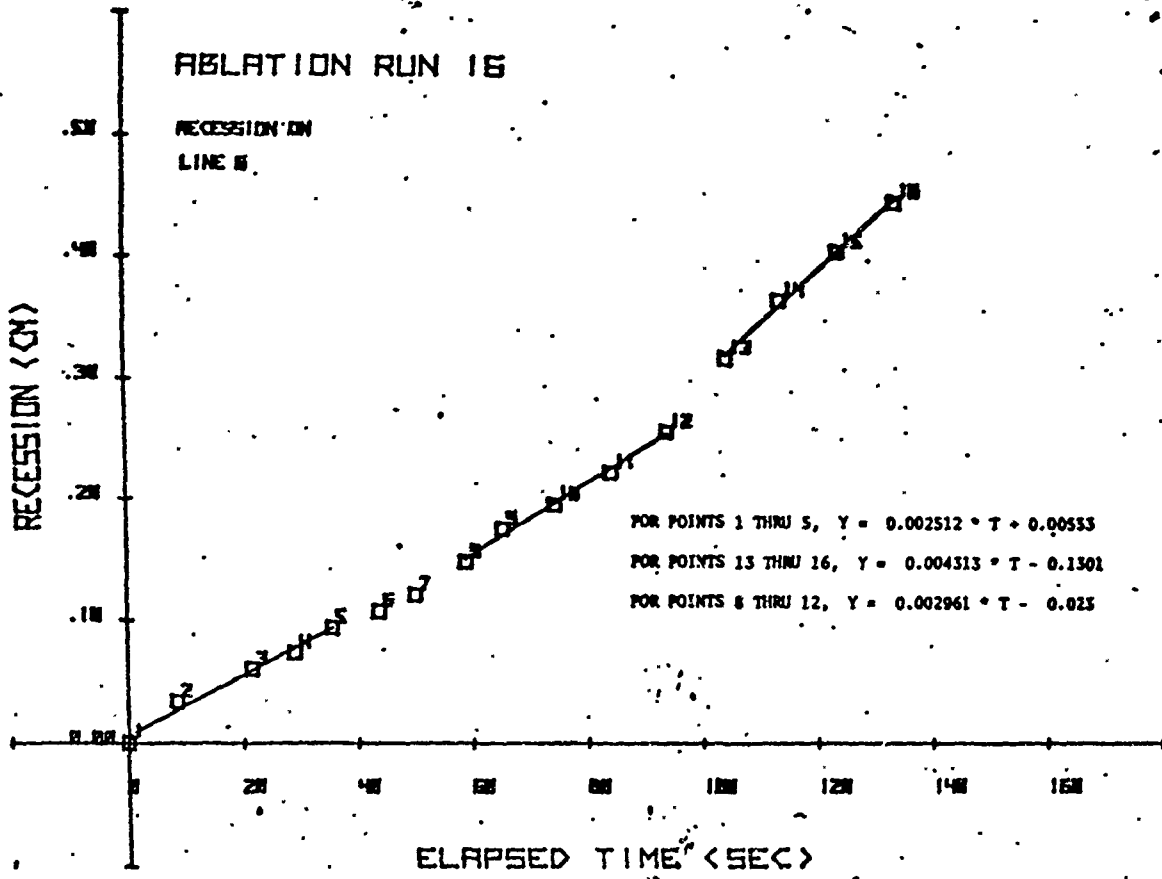








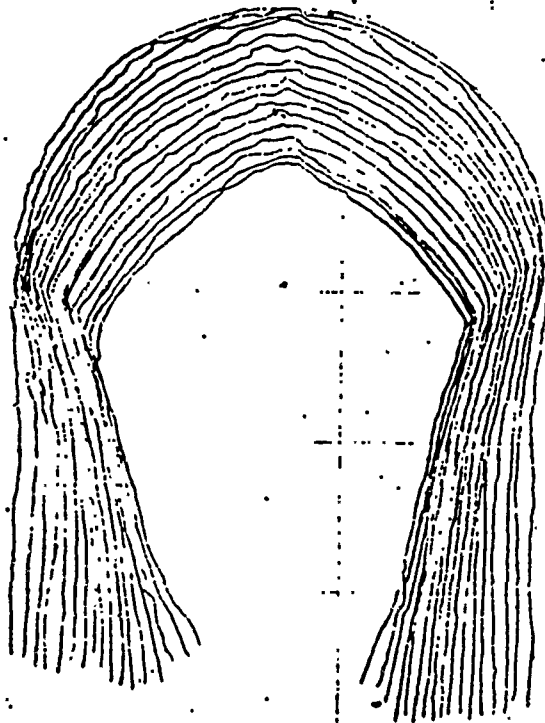


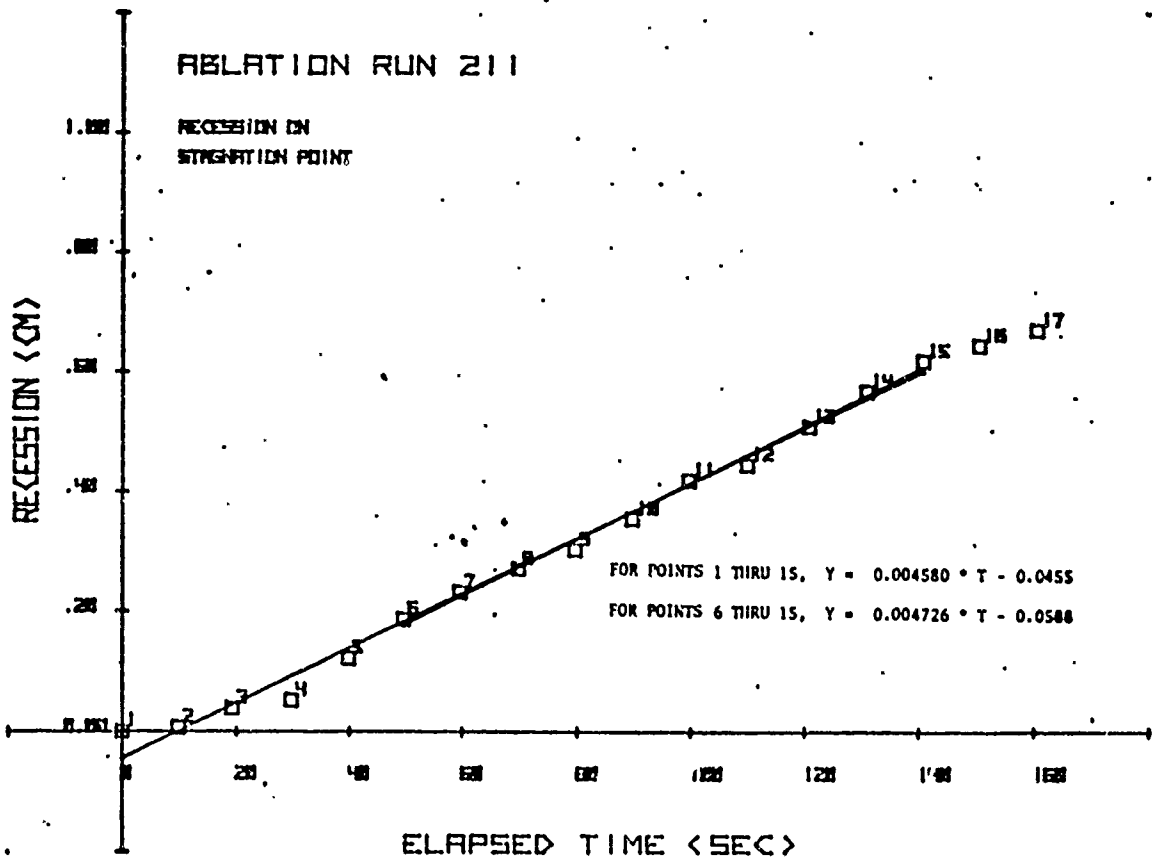


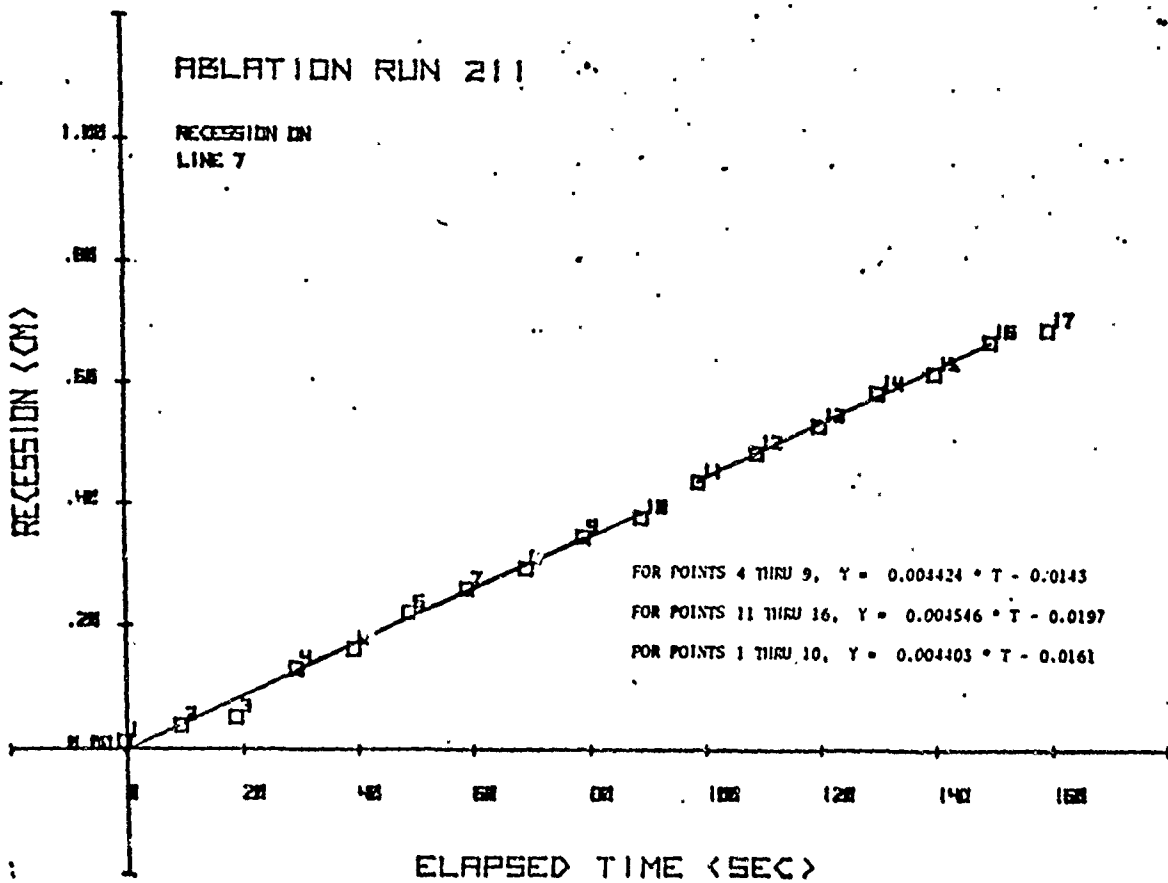
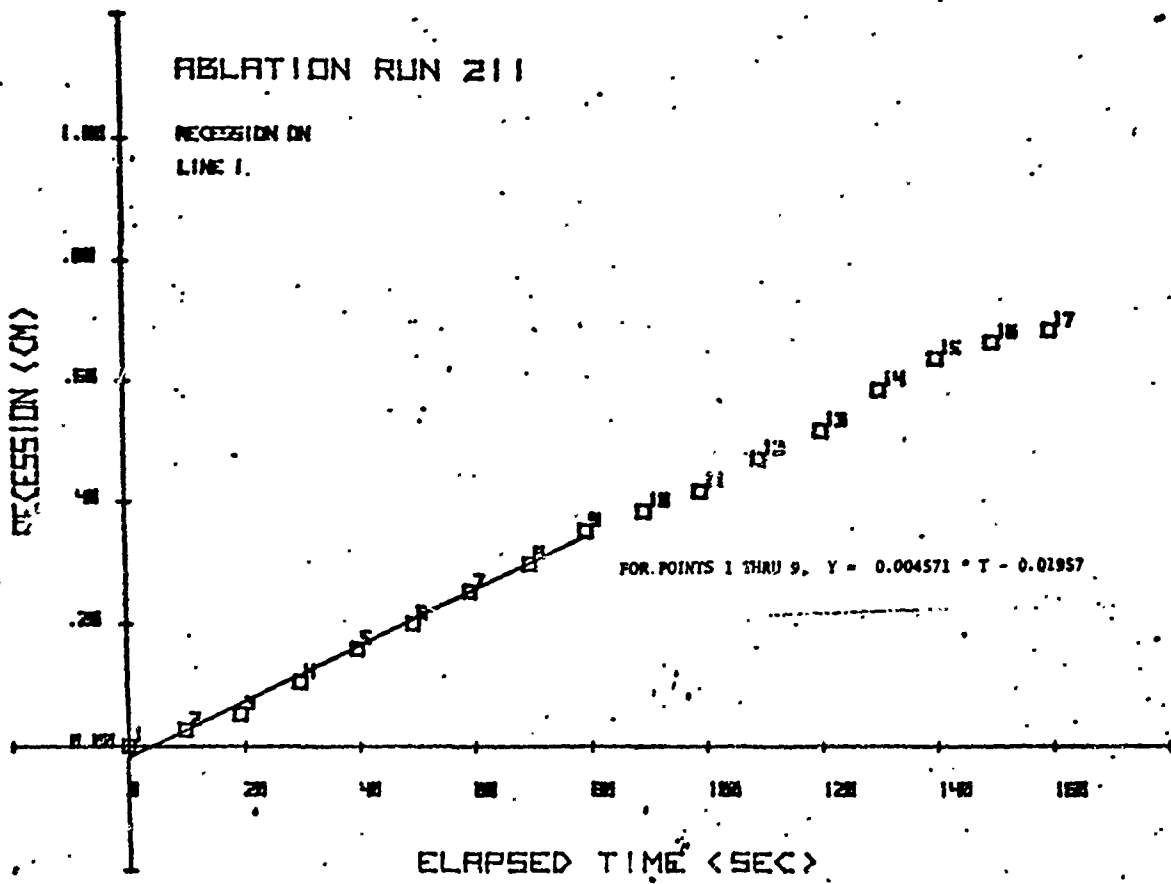
Run 7 (Also Identified as Run 21-1)

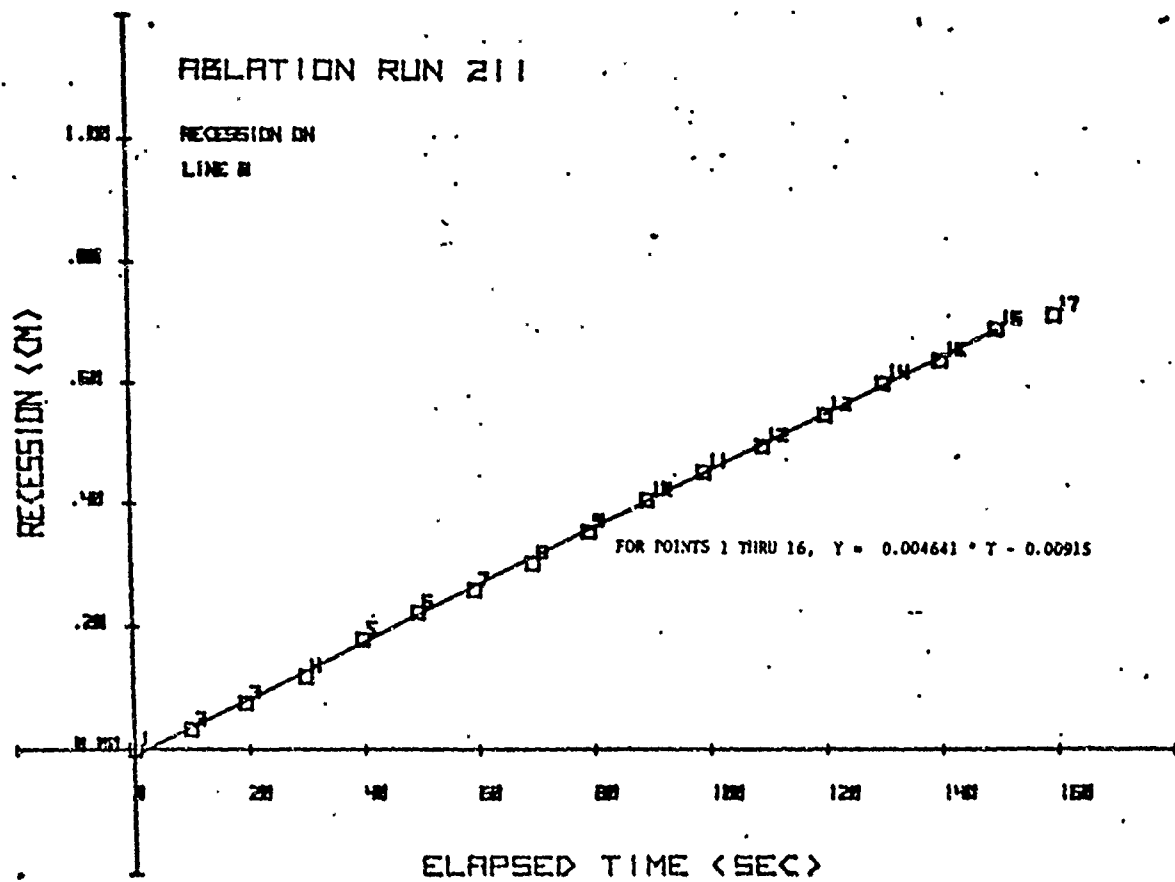
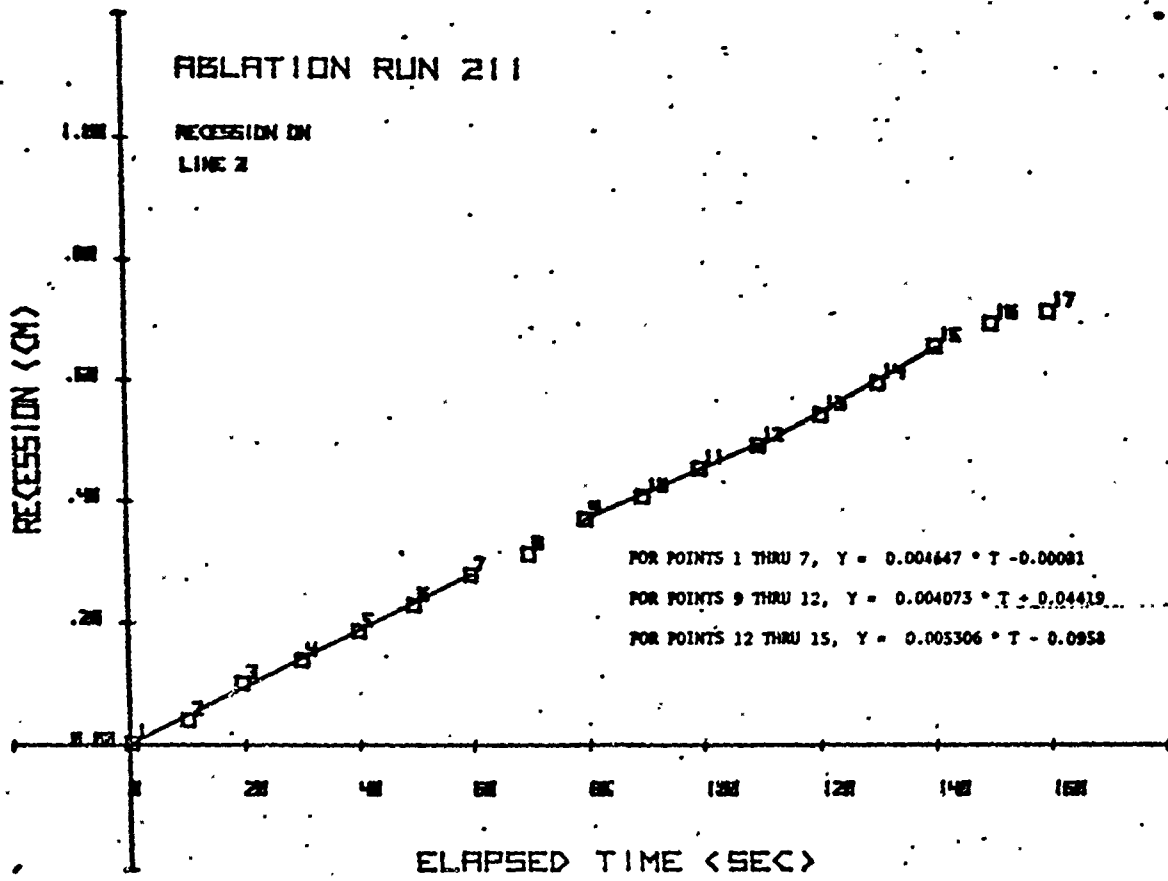
Simple Theory Stagnation Point Mass Flux: $0.00392 \text{ g/cm}^2 \cdot \text{s}$

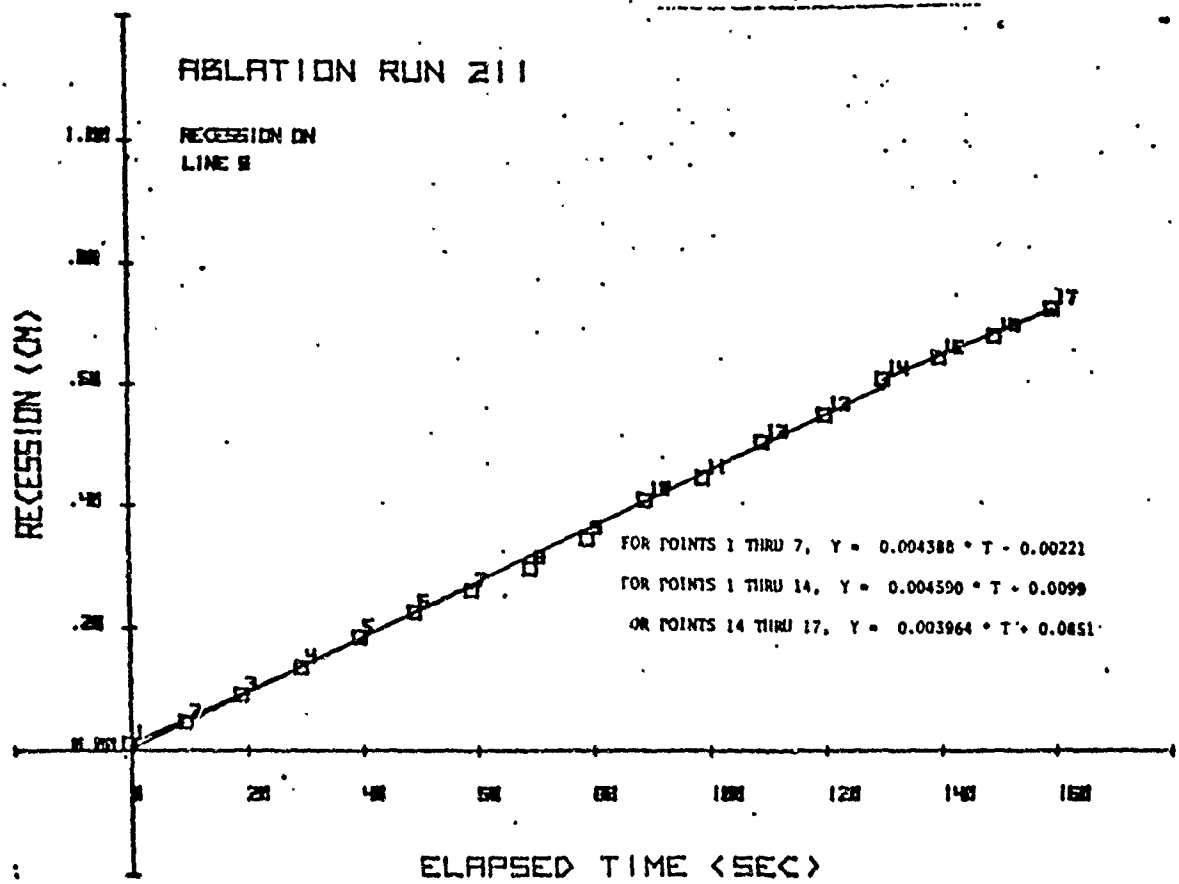
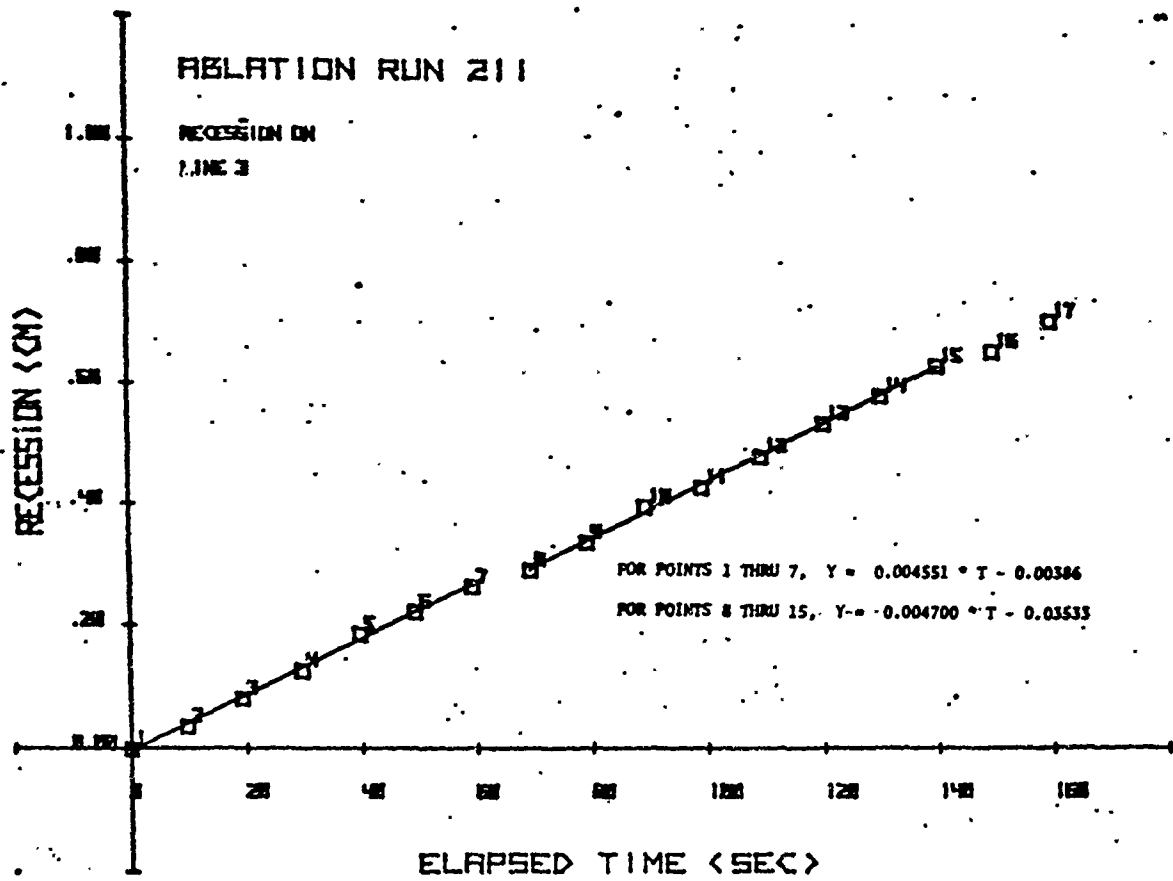
Position	Recession Rate $\text{cm/s} (\times 10^3)$	Mass Flux $\text{g/cm}^2 \cdot \text{s} (\times 10^3)$	Normalized
Stag Pt	4.58	2.84	0.724
15 right	4.57	2.83	0.722
15 left	4.42	2.74	0.699
30 right	4.65	2.88	0.735
30 left	4.64	2.88	0.735
45 right	4.55	2.82	0.719
45 left	4.39	2.72	0.694
60 right	4.10	2.54	0.648
60 left	4.47	2.77	0.707
75 right	2.90	1.80	0.459
75 left	2.93	1.82	0.464
90 right	----	----	----
90 left	----	----	----

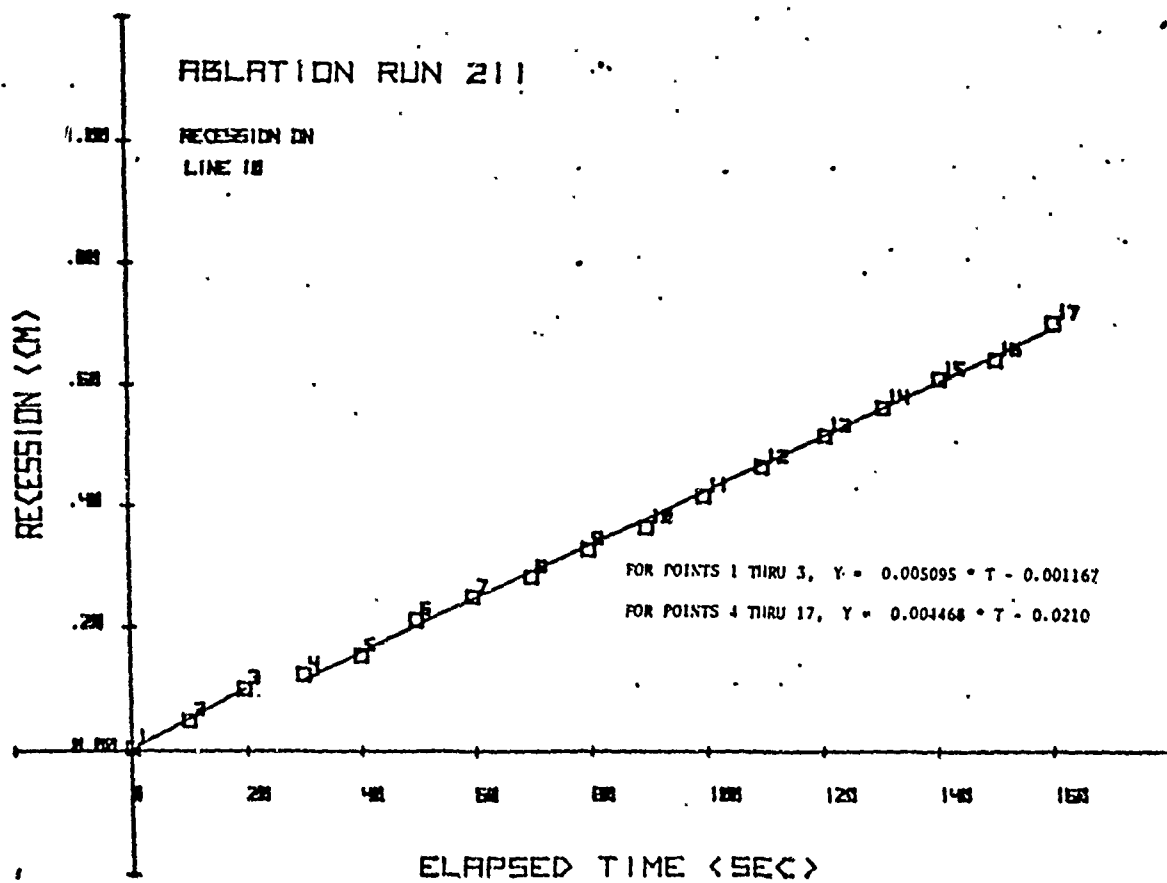
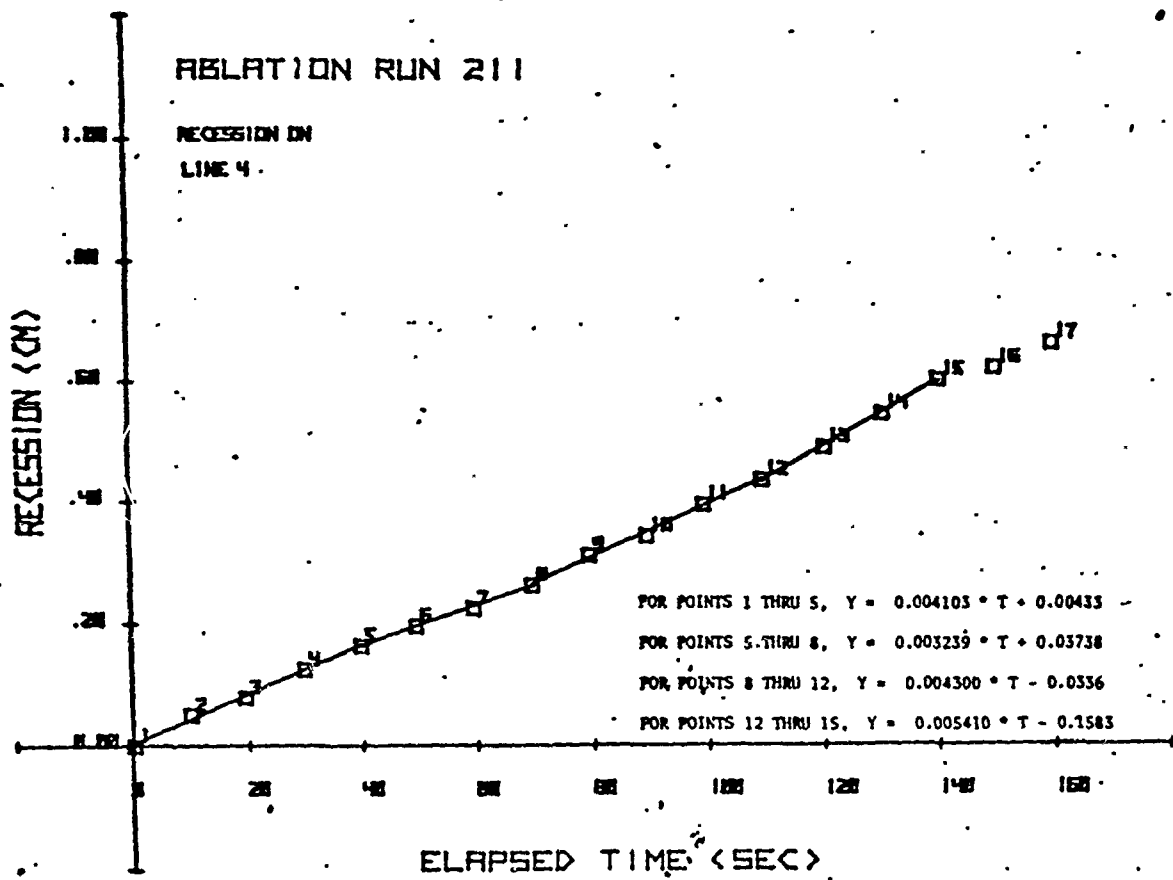


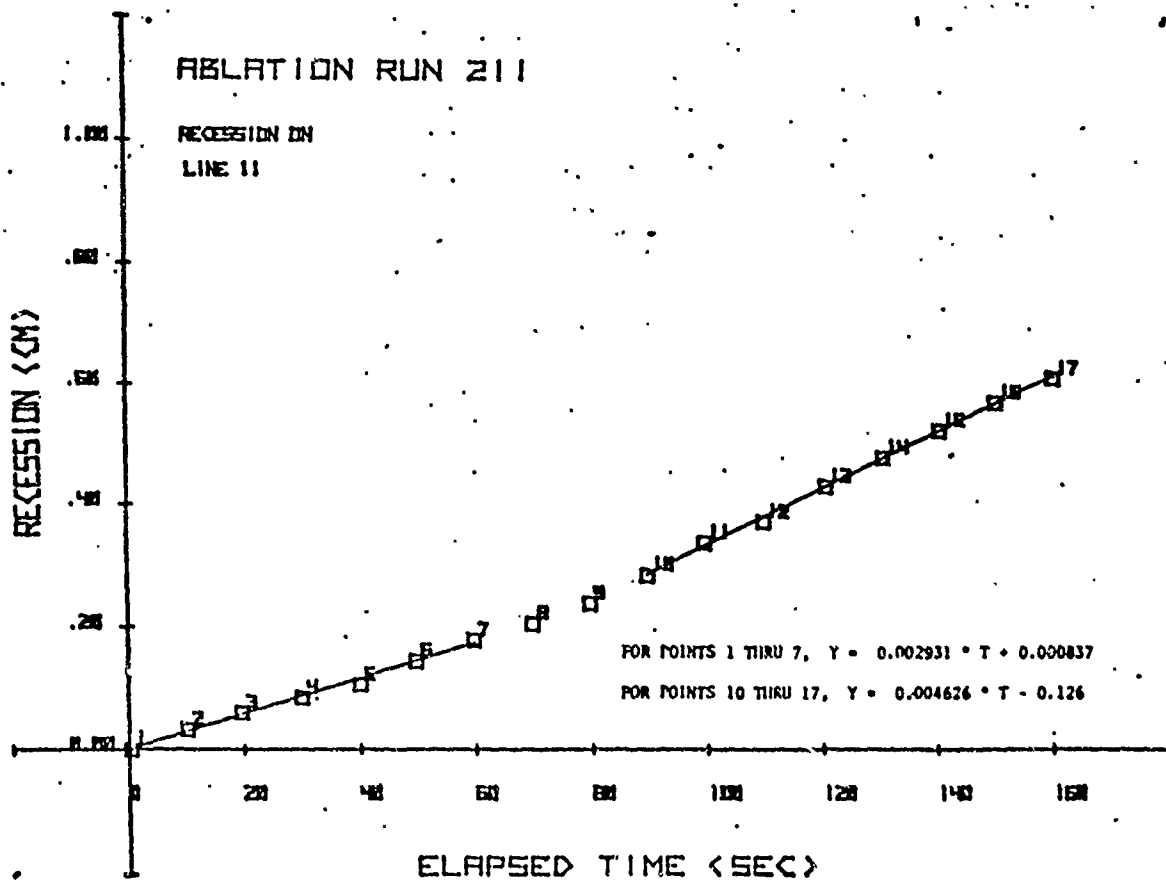
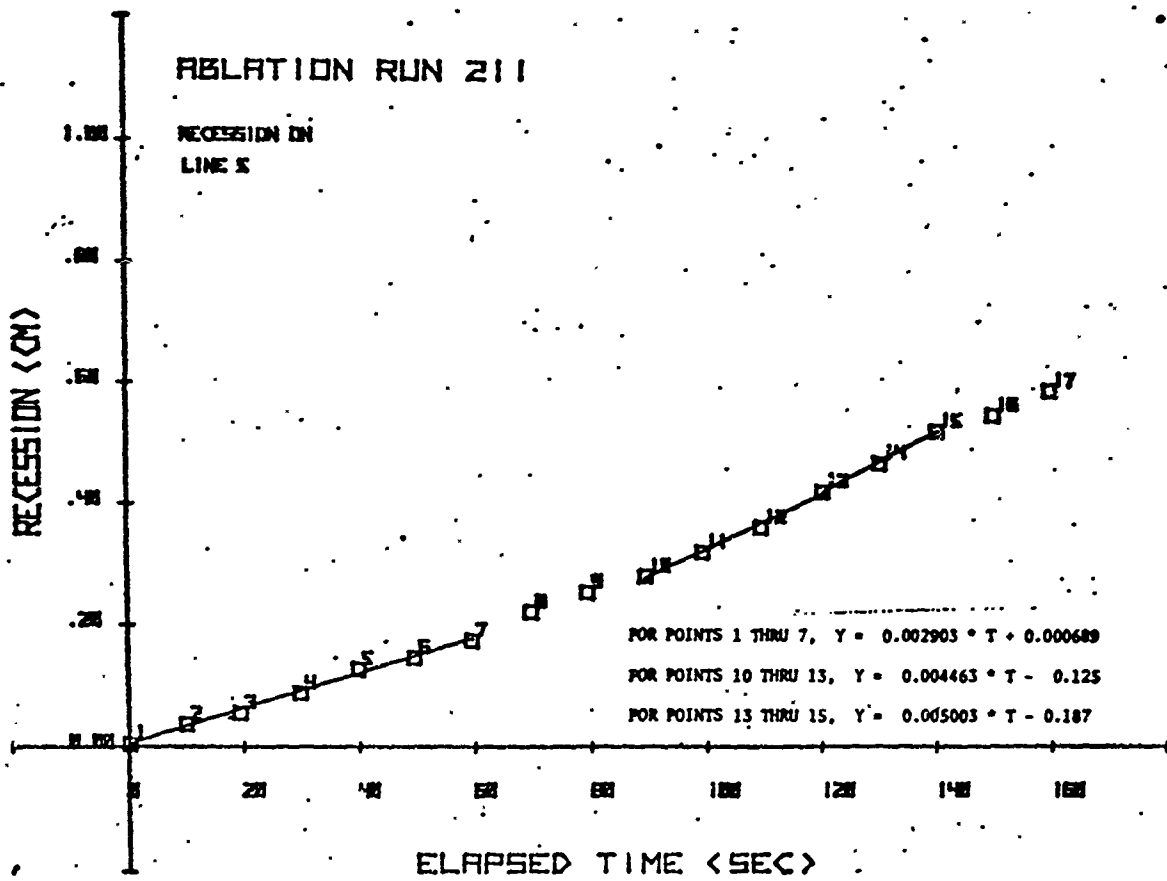








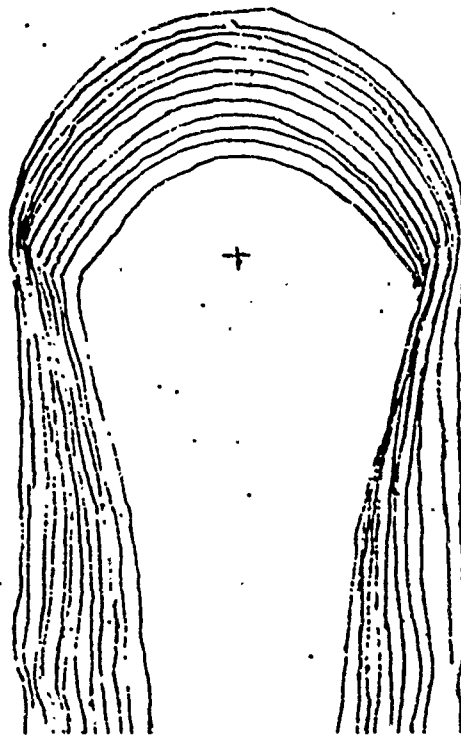


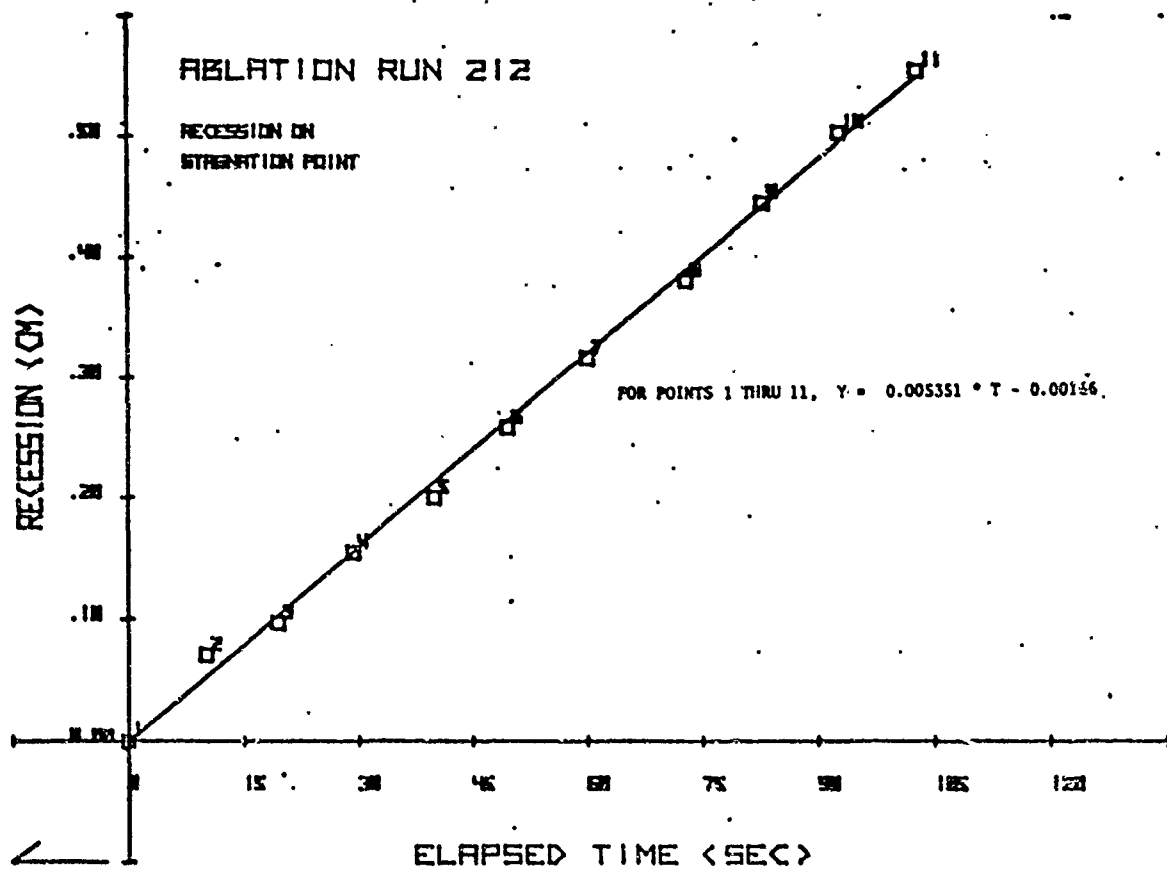


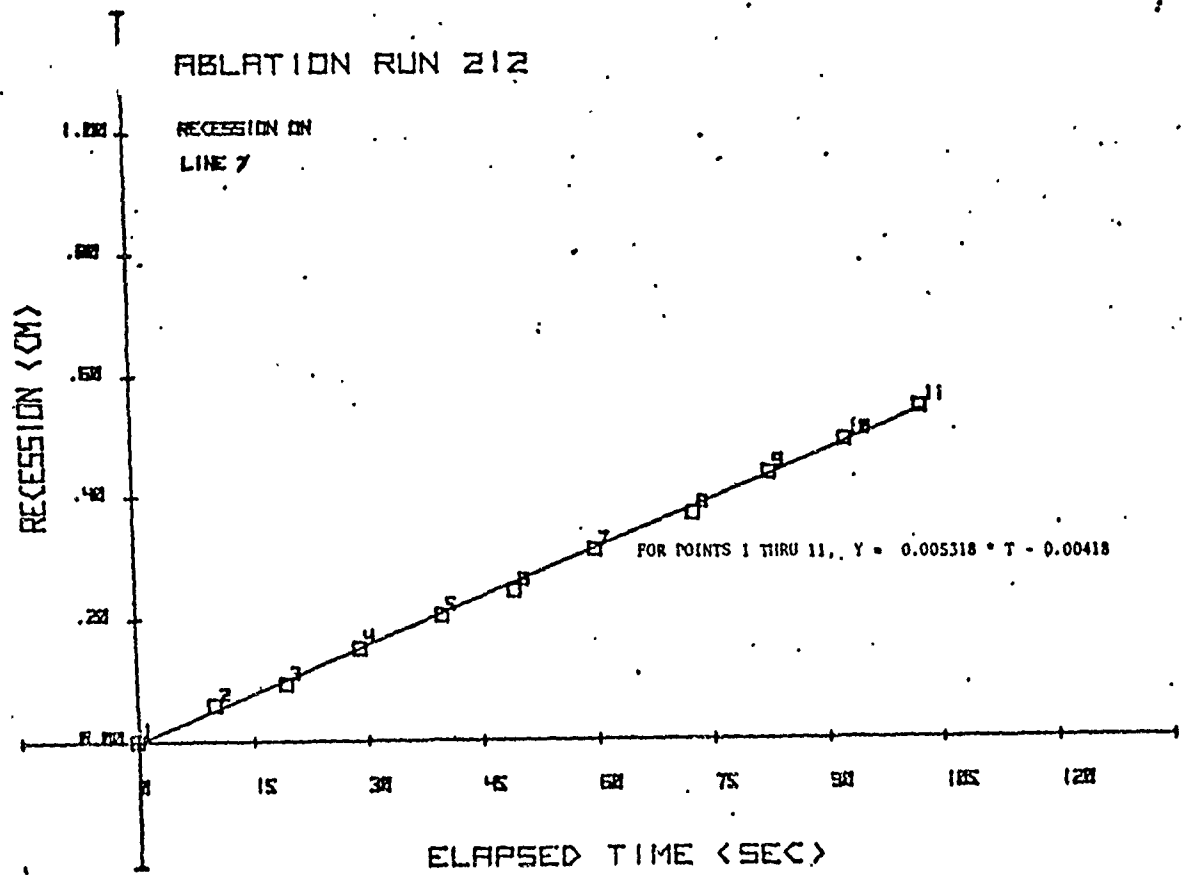
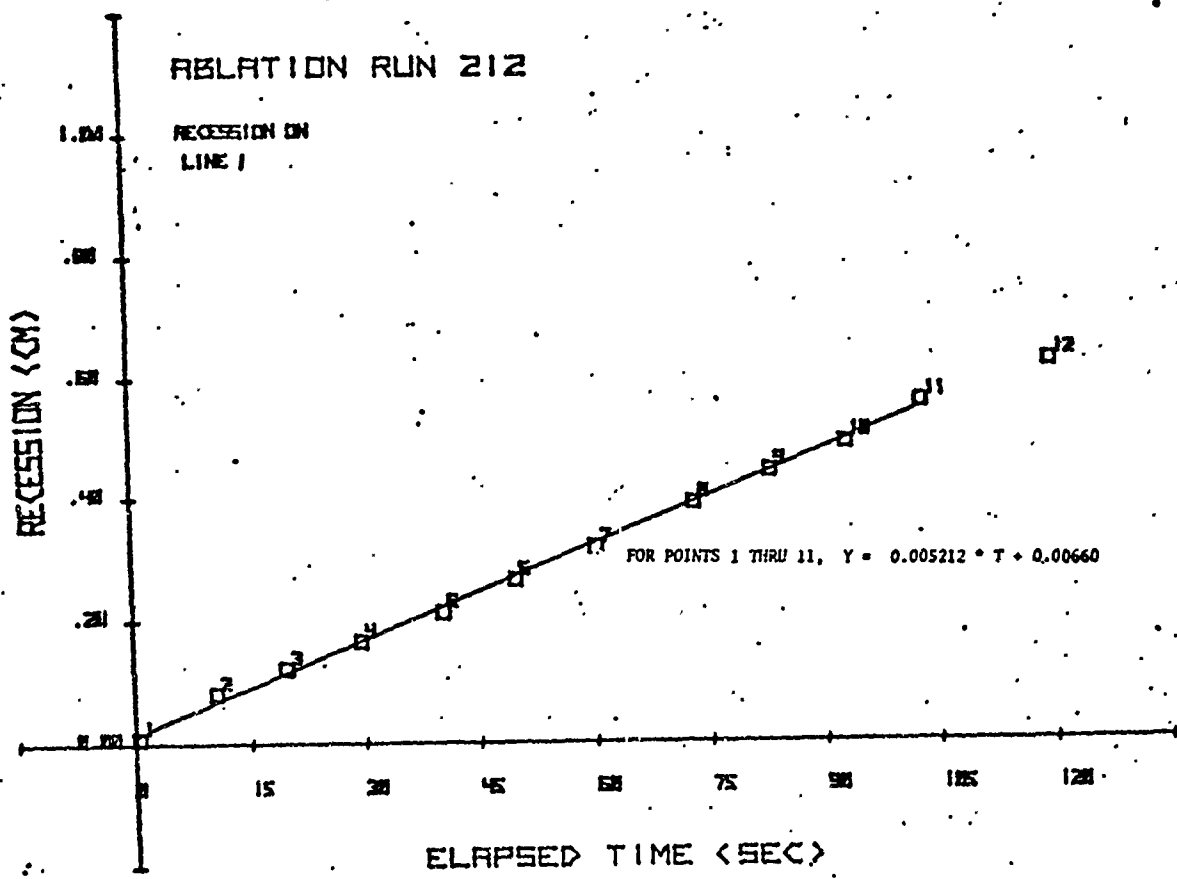
Run 8 (Also Identified as Run 21-2)

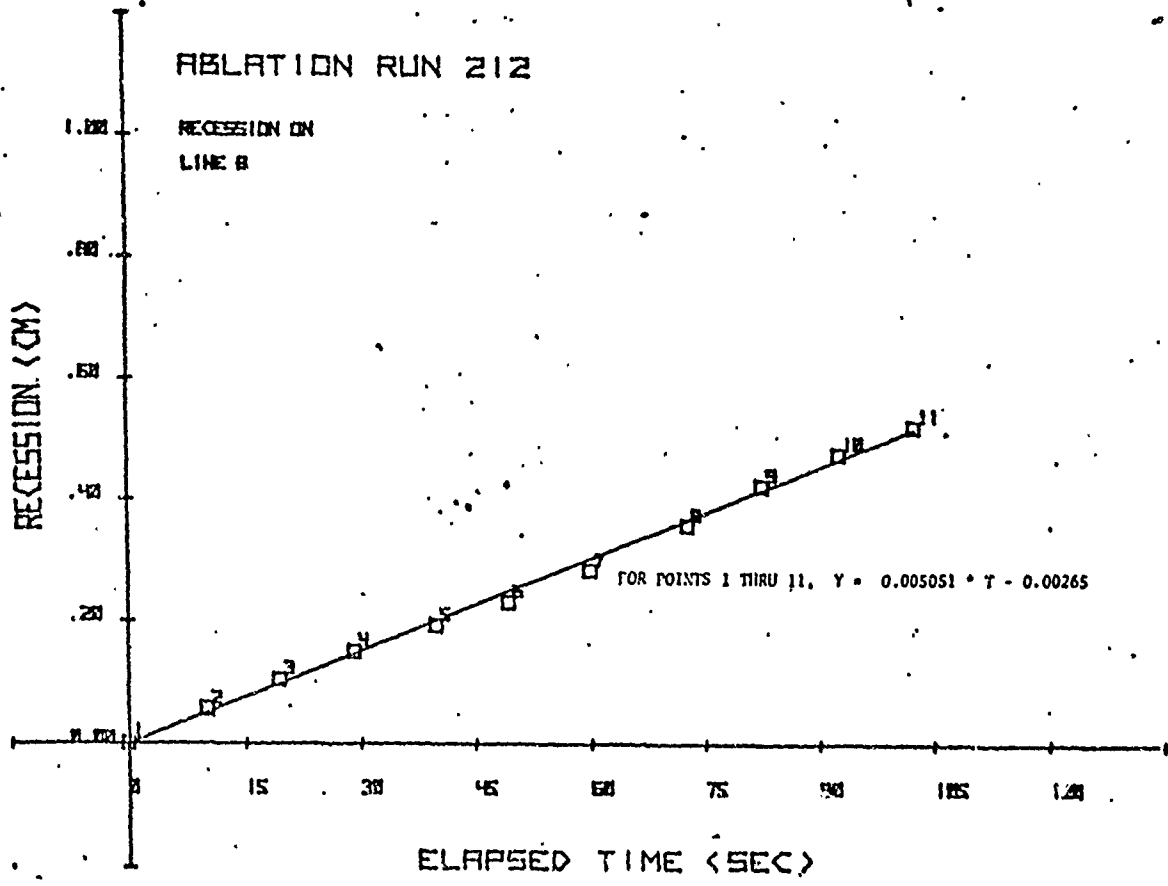
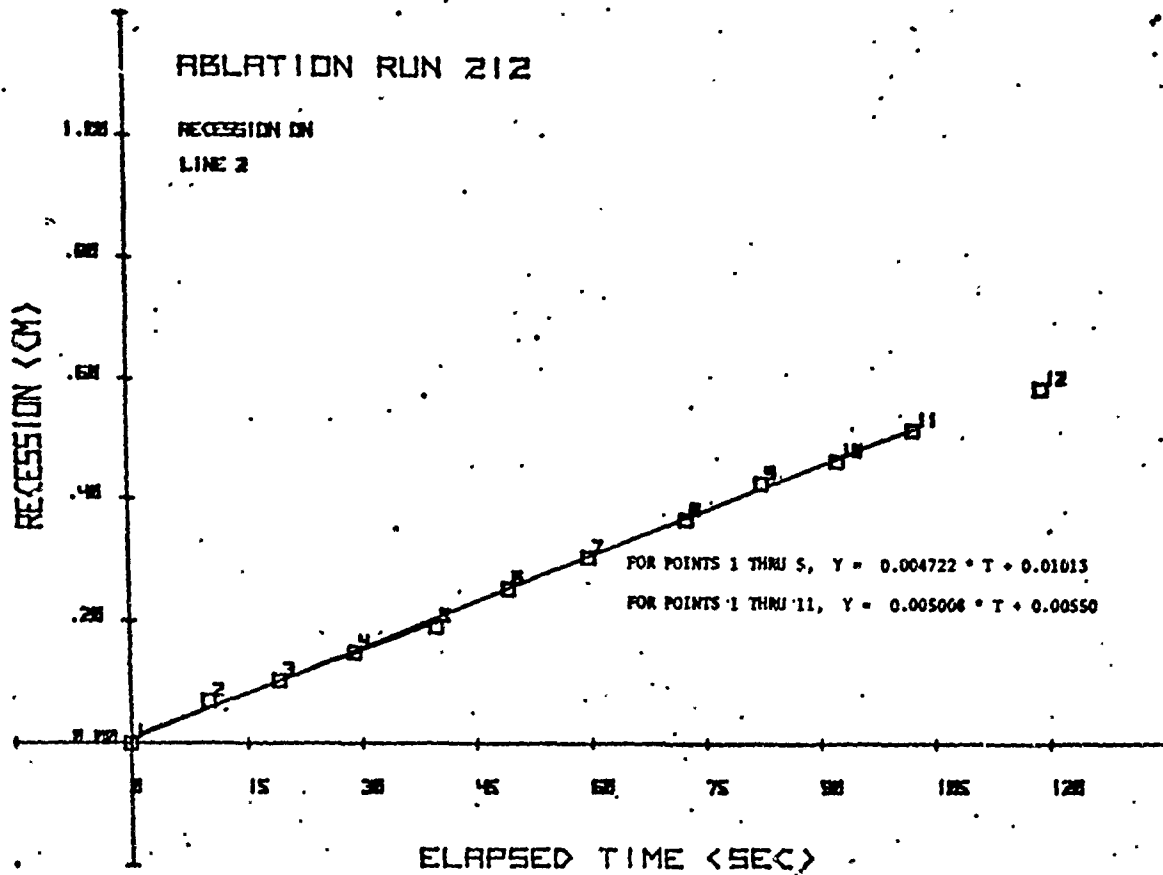
Simple Theory Stagnation Point Mass Flux: $0.00421 \text{ g/cm}^2\cdot\text{s}$

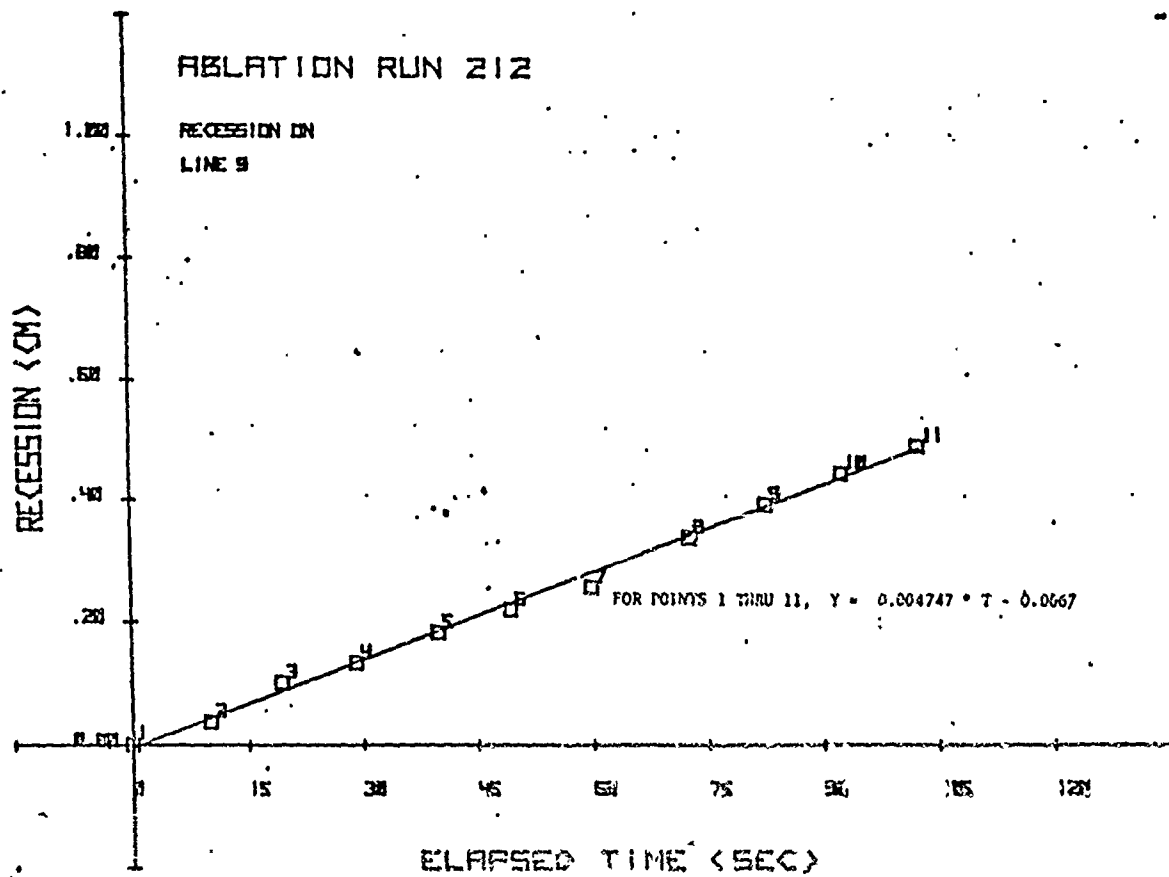
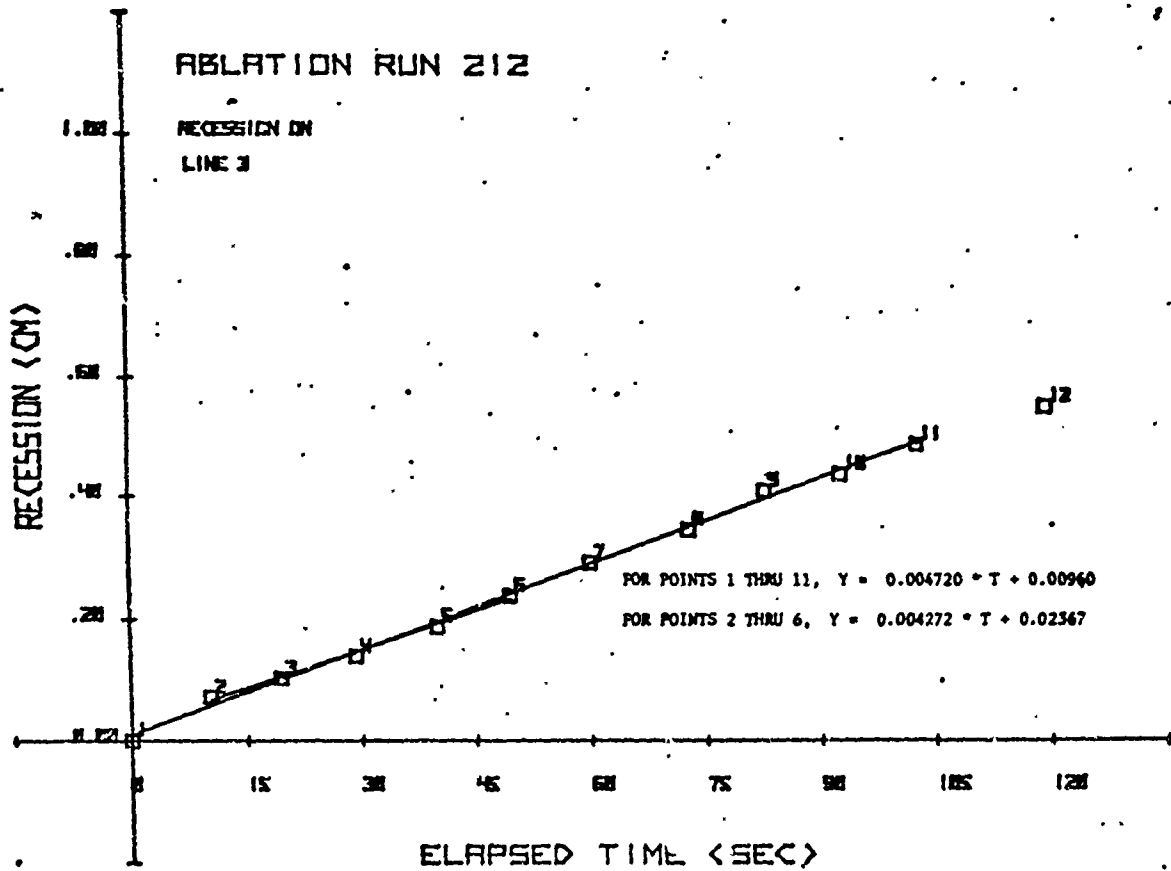
Position	Recession Rate $\text{cm/s} (\times 10^3)$	Mass Flux $\text{g/cm}^2\cdot\text{s} (\times 10^3)$	Normalized
Stag Pt	5.35	3.32	0.789
15 right	5.21	3.23	0.767
15 left	5.32	3.30	0.784
30 right	5.01	3.10	0.736
30 left	5.05	3.13	0.743
45 right	4.72	2.93	0.696
45 left	4.75	2.94	0.698
60 right	4.16	2.58	0.613
60 left	4.28	2.66	0.632
75 right	3.56	2.21	0.525
75 left	3.06	1.89	0.449
90 right	----	----	-----
90 left	----	----	-----

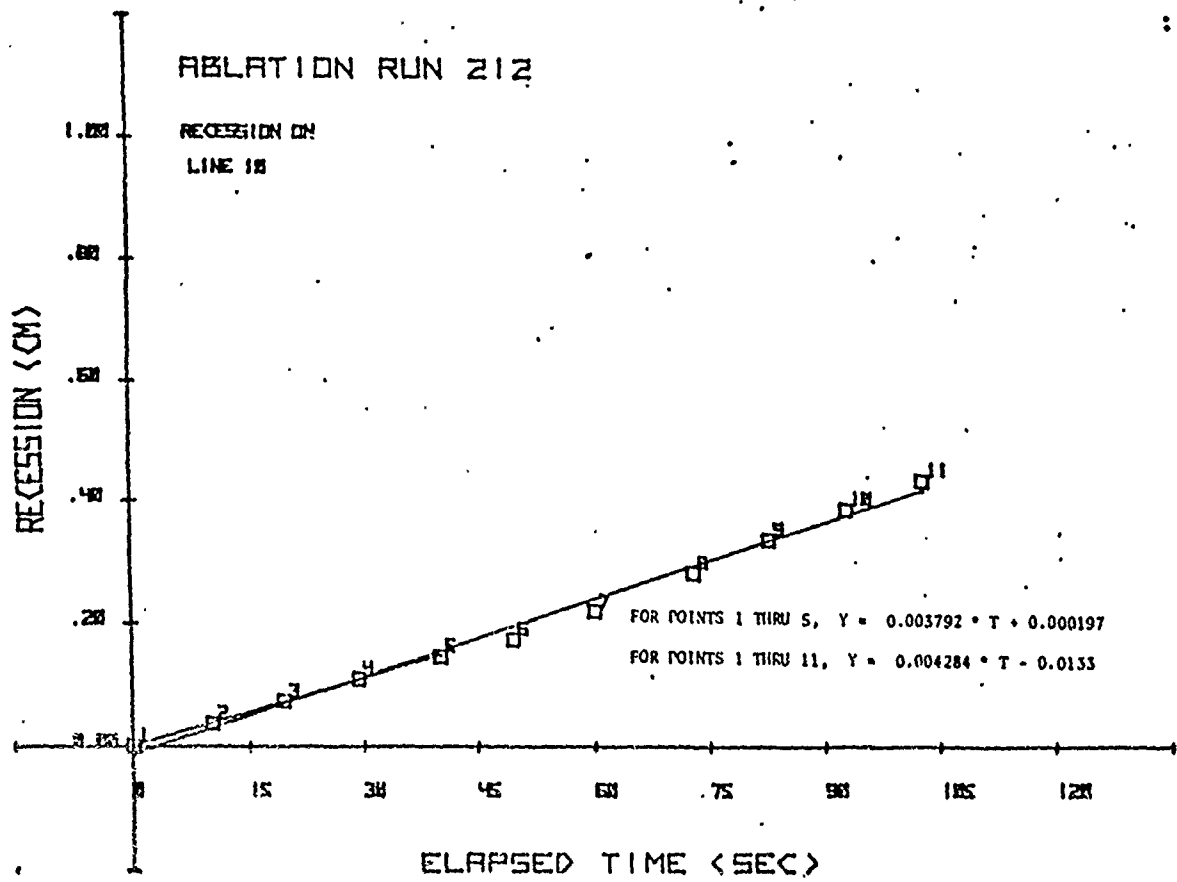
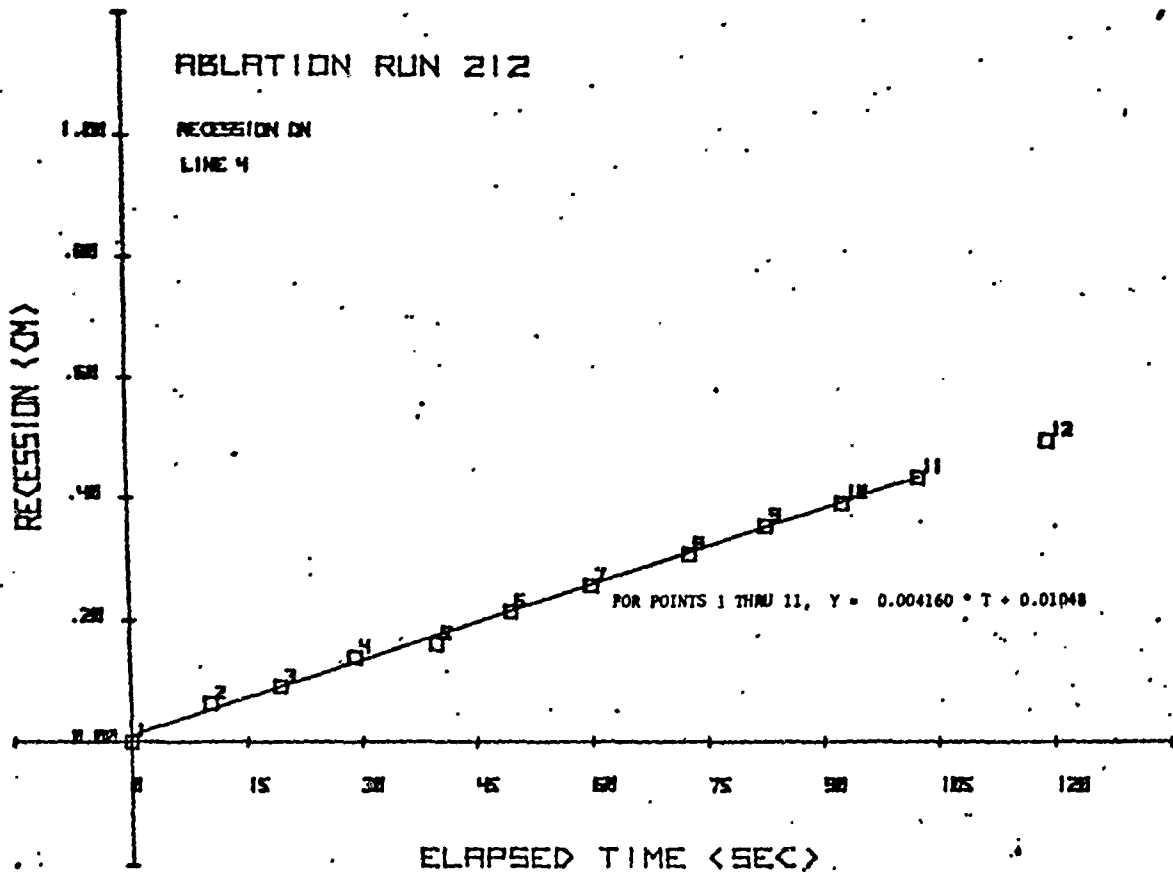






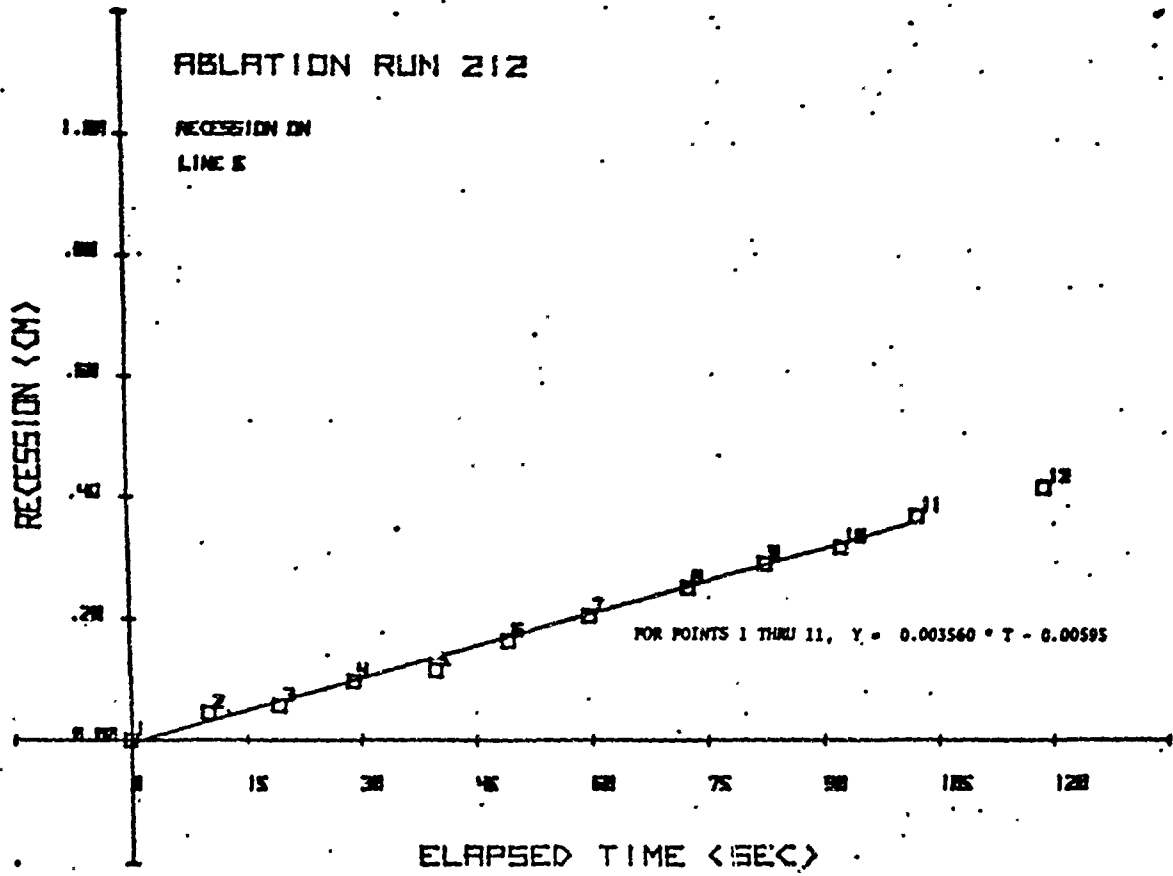






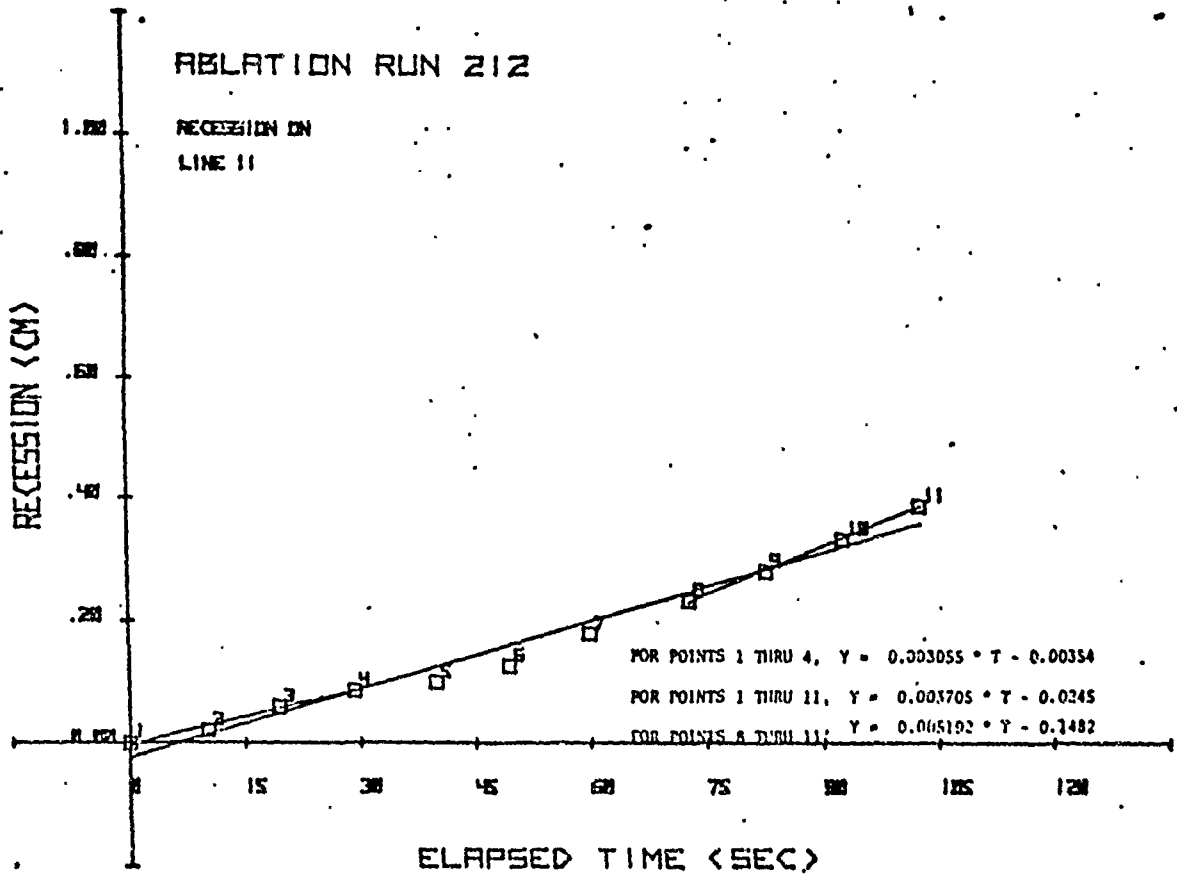
ABLATION RUN 212

RECESSION ON
LINE 8



ABLATION RUN 212

RECESSION ON
LINE 11

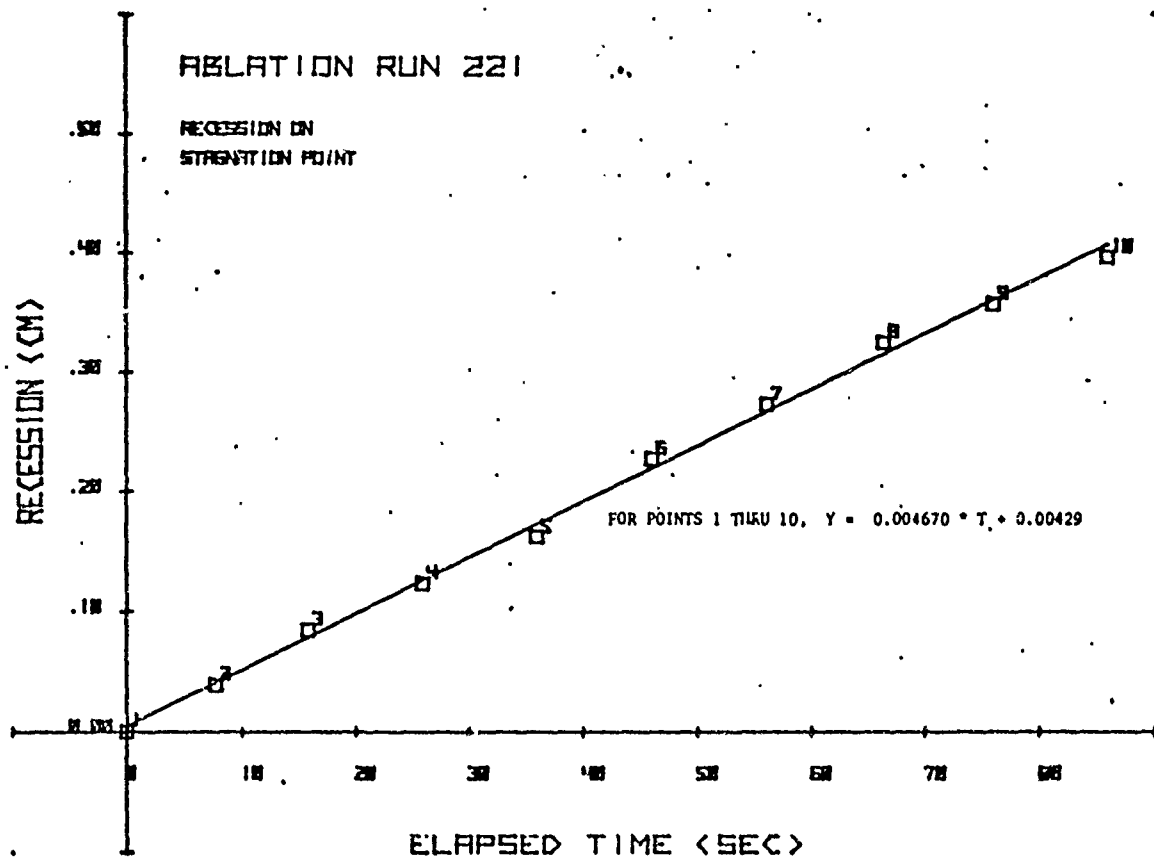


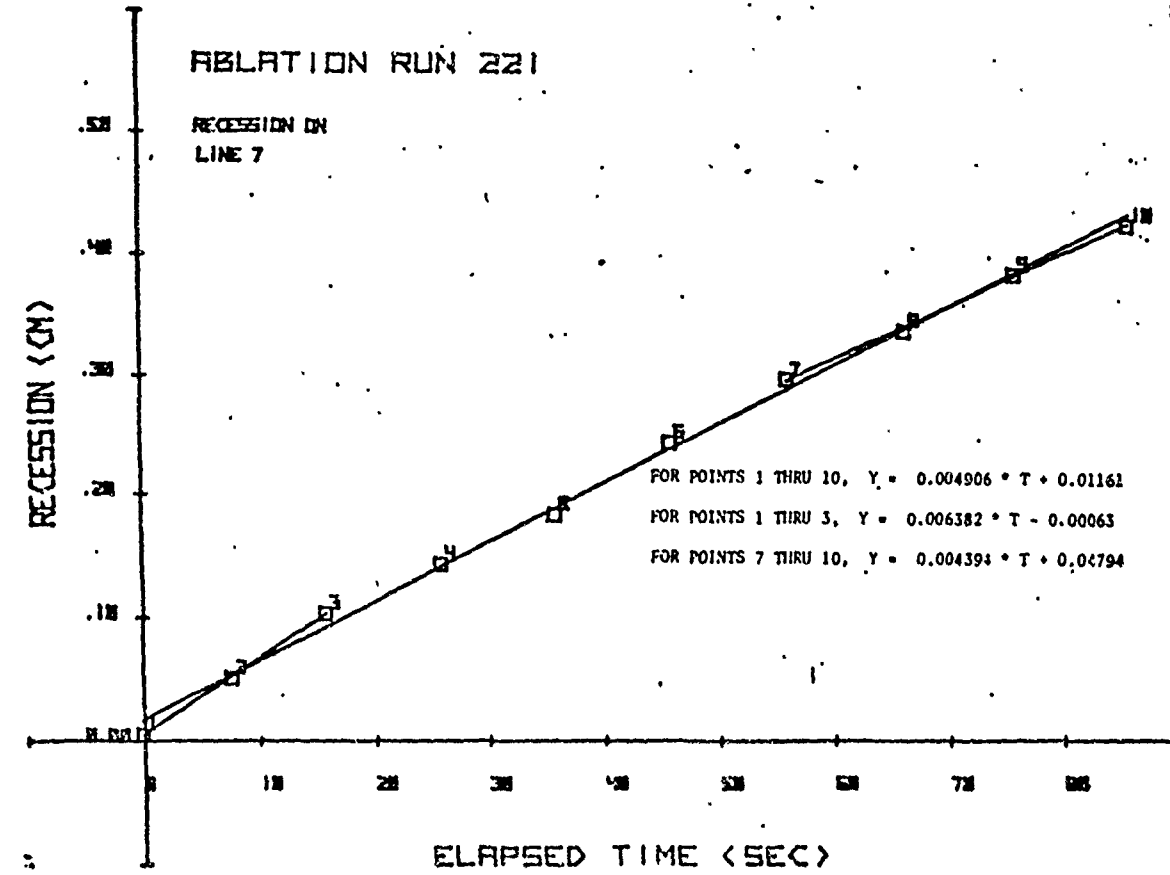
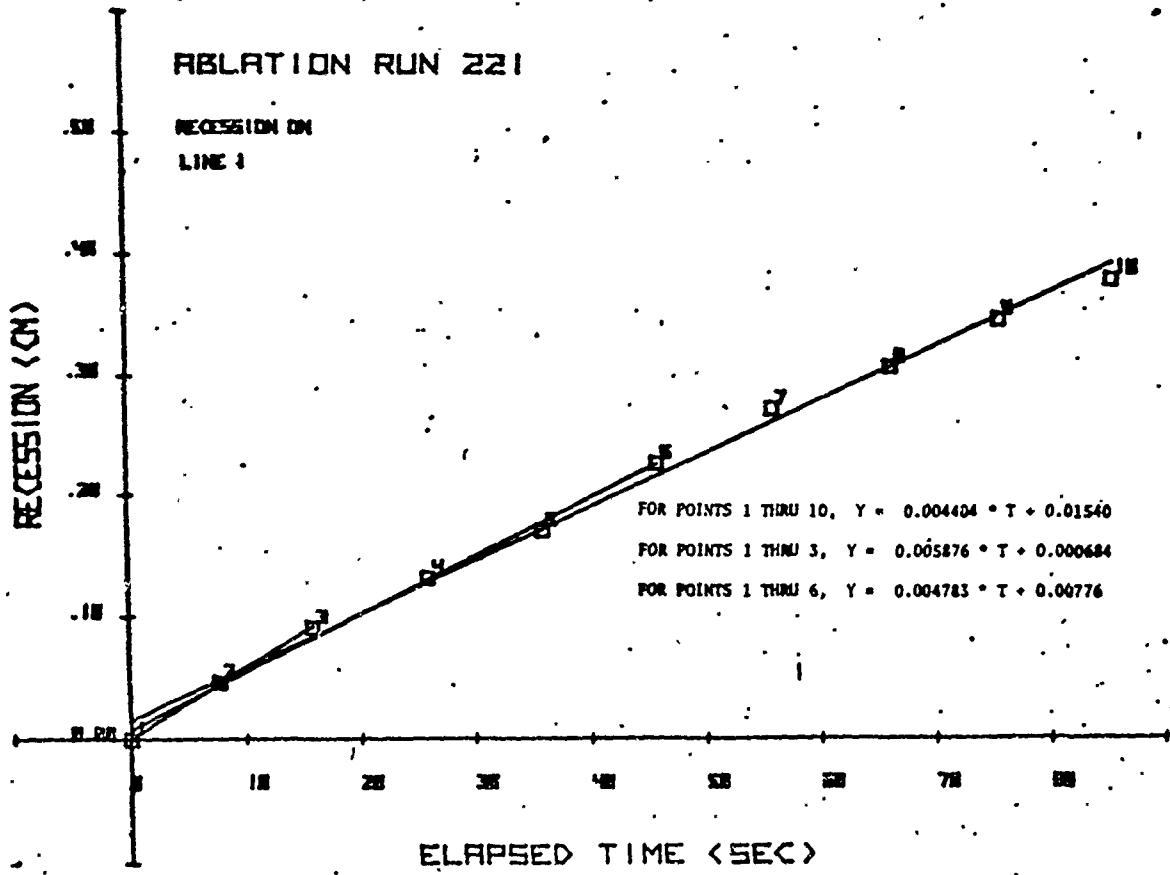
Run 9 (Also Identified as Run 22-1)

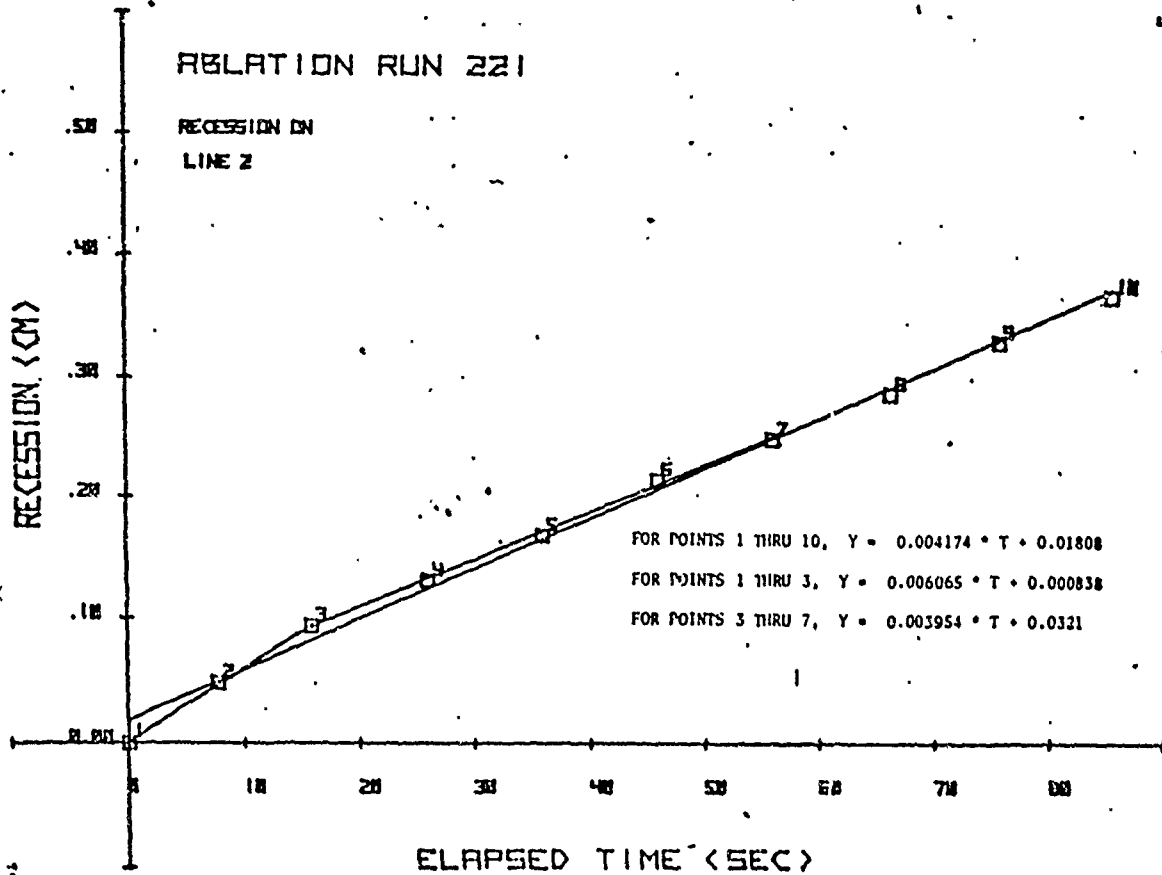
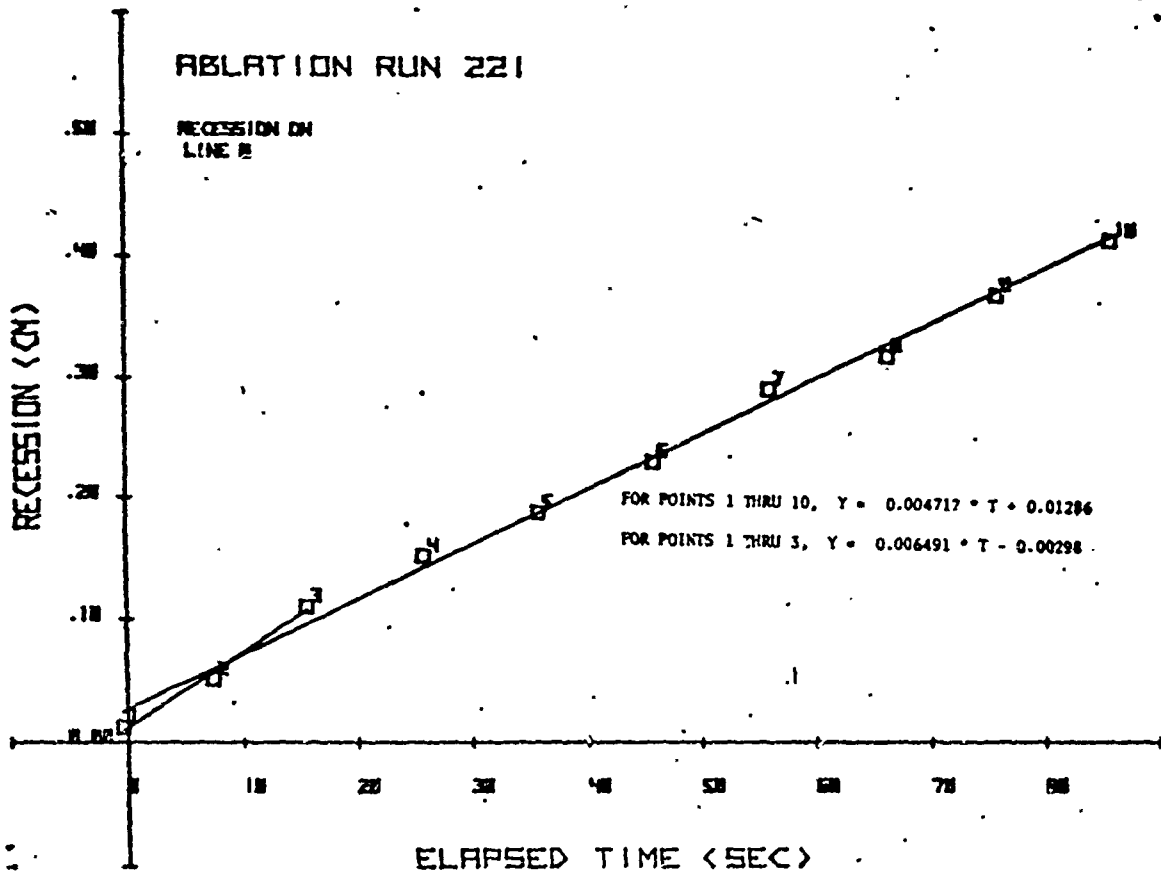
Simple Theory Stagnation Point Mass Flux: $0.00405 \text{ g/cm}^2 \cdot \text{s}$

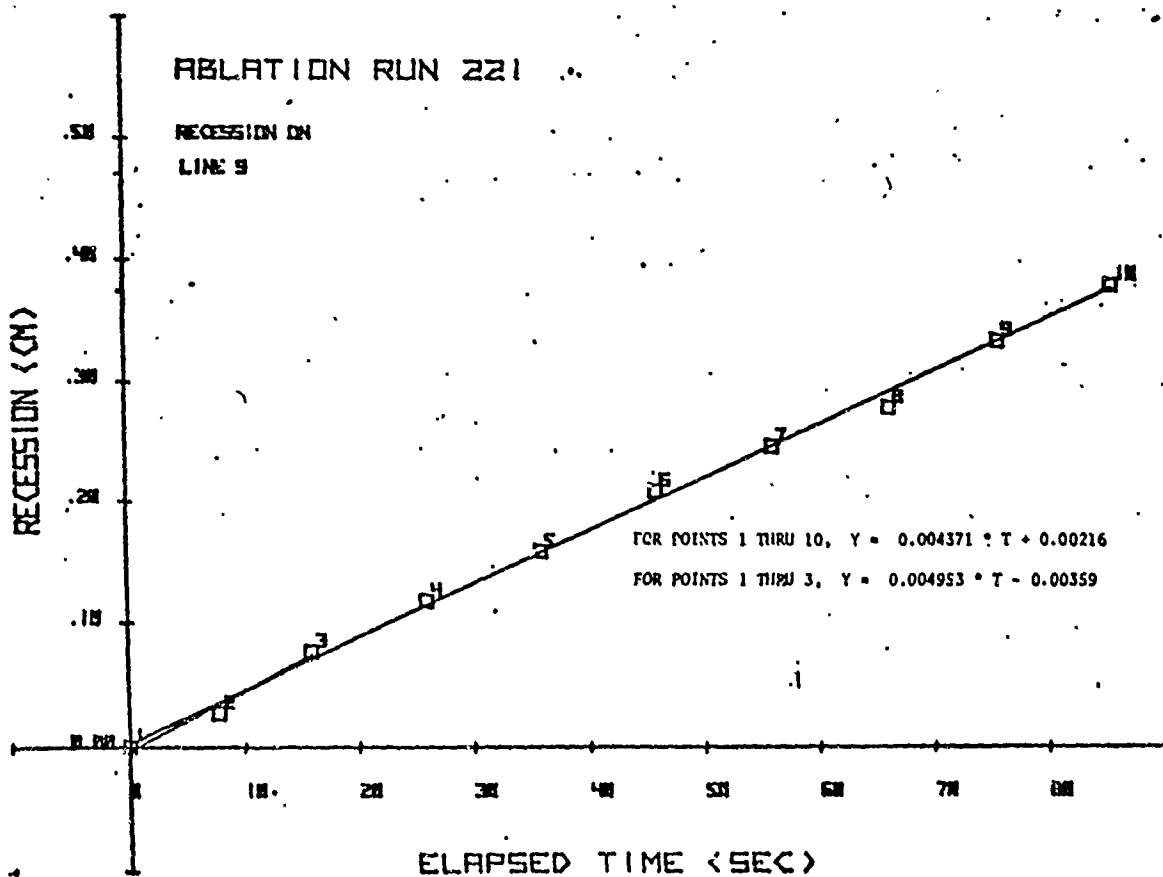
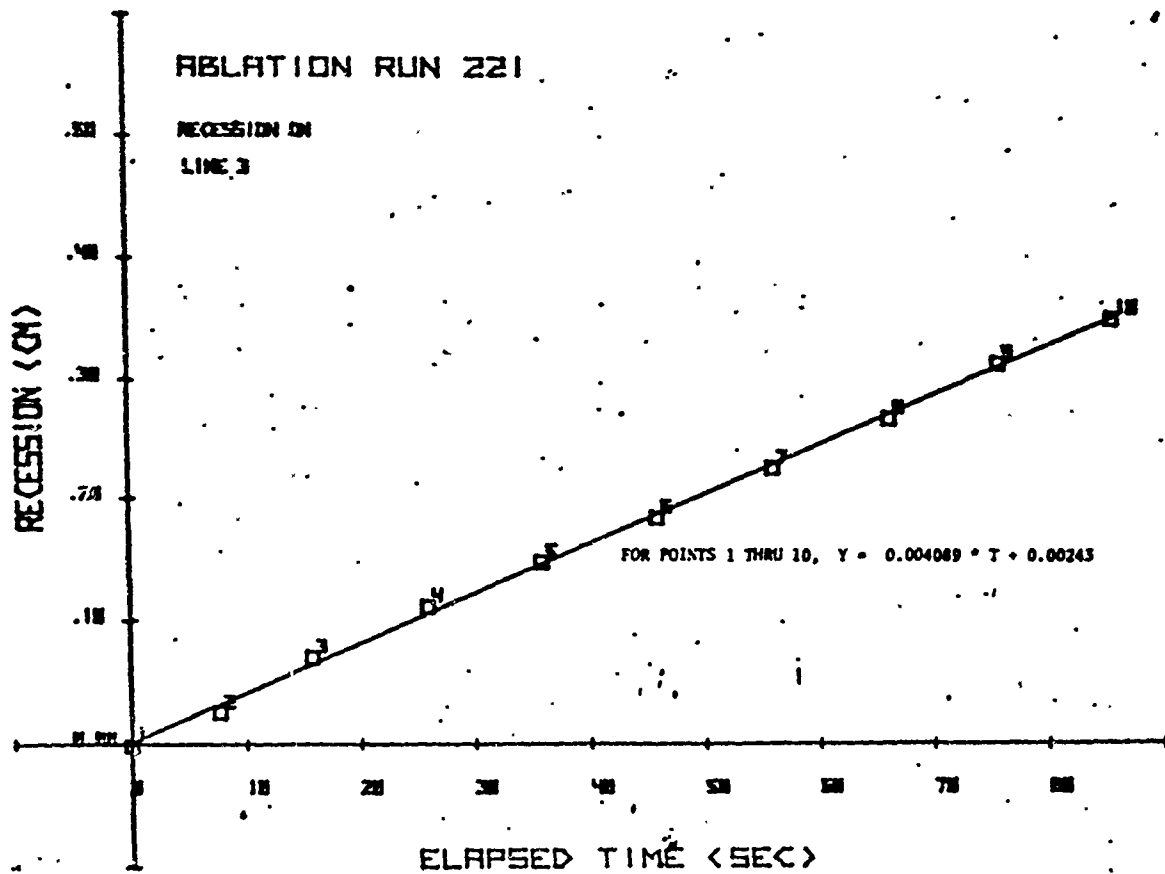
Position	Recession Rate $\text{cm/s} (\times 10^3)$	Mass Flux $\text{g/cm}^2 \cdot \text{s} (\times 10^3)$	Normalized
Stag Pt	4.85	2.96	0.731
15 right	4.75	2.90	0.716
15 left	4.98	3.04	0.751
30 right	4.25	2.59	0.640
30 left	4.80	2.93	0.723
45 right	4.16	2.54	0.627
45 left	4.44	2.71	0.669
60 right	3.62	2.21	0.546
60 left	4.31	2.63	0.649
75 right	2.87	1.75	0.432
75 left	3.23	1.97	0.486
90 right	2.21	1.35	0.333
90 left	2.69	1.64	0.405

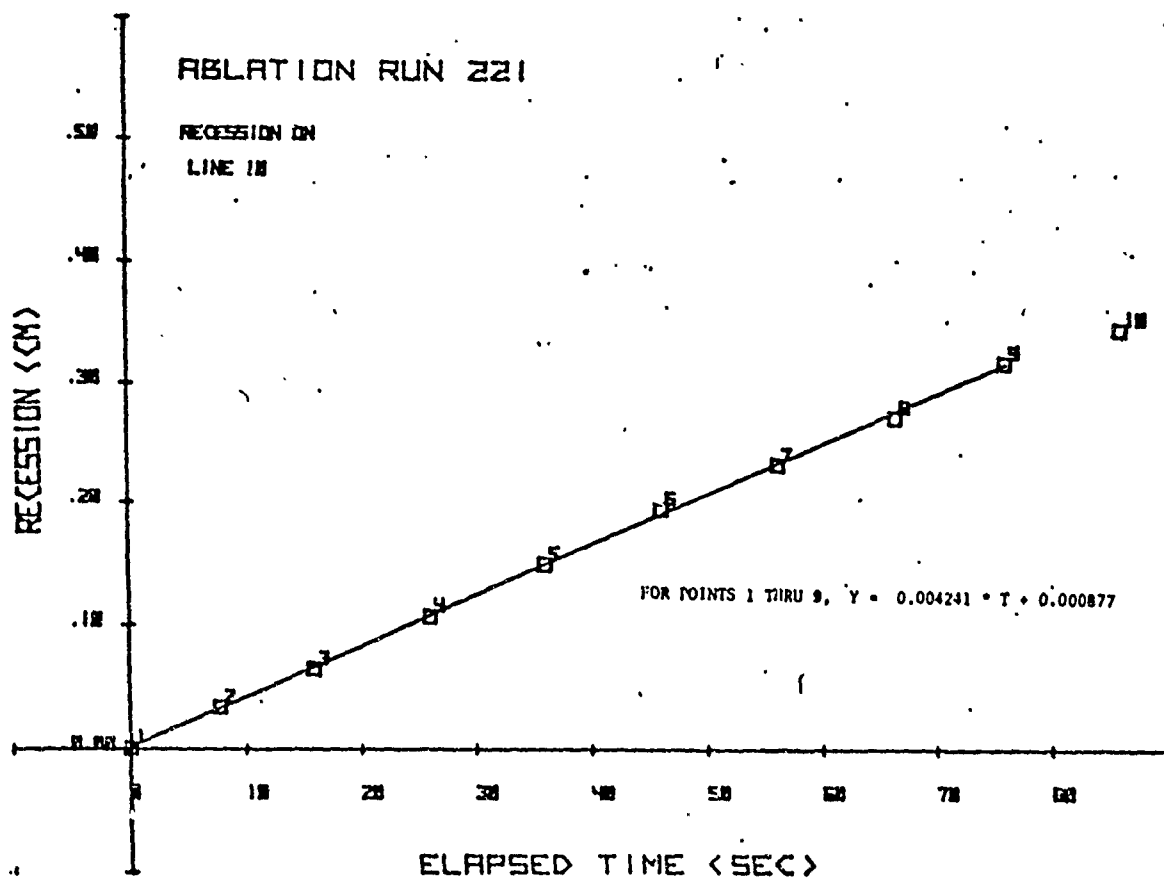
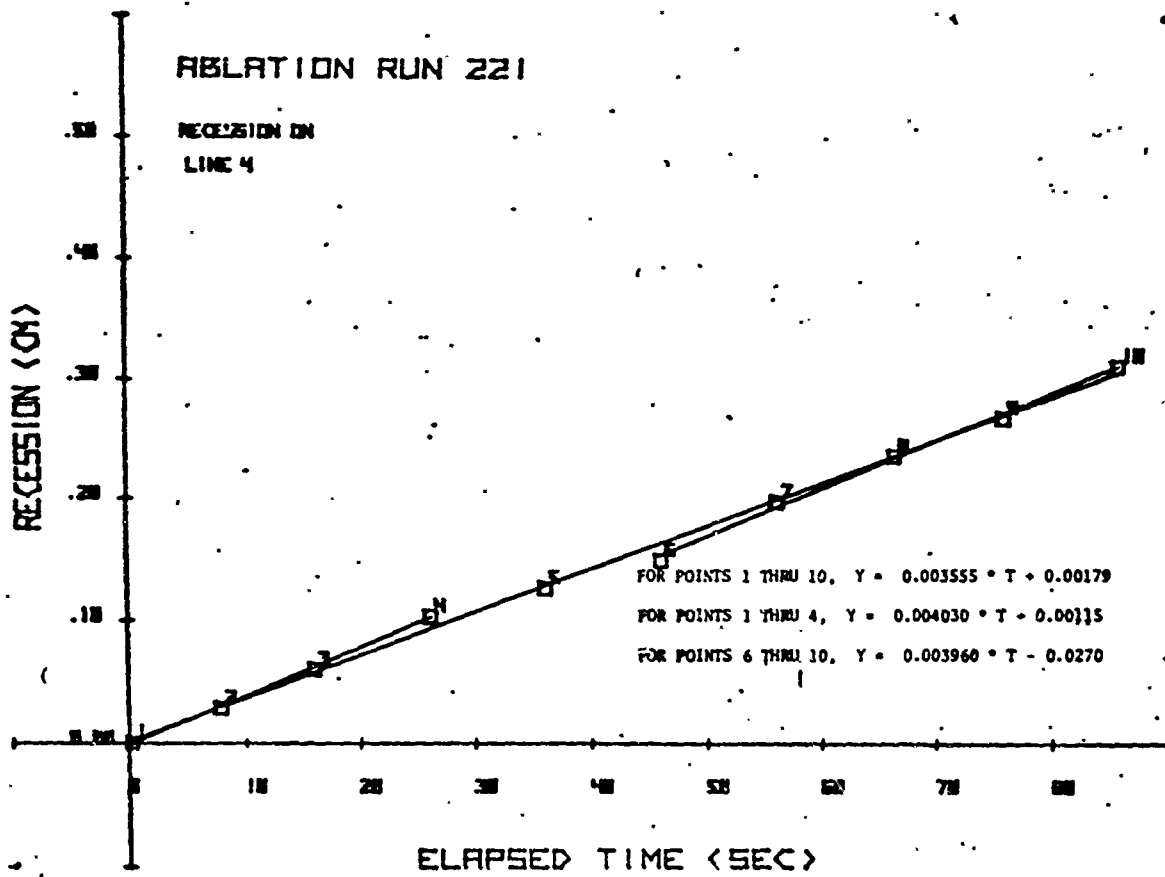


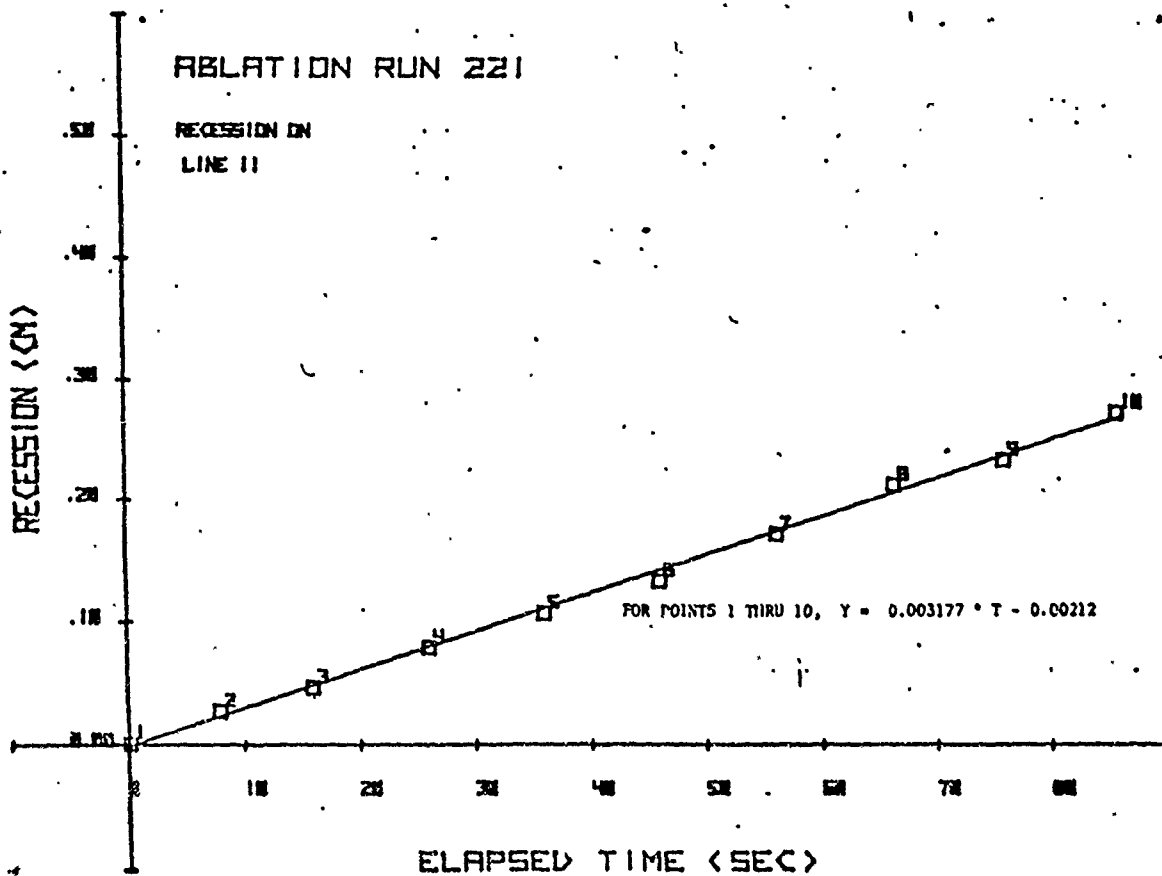
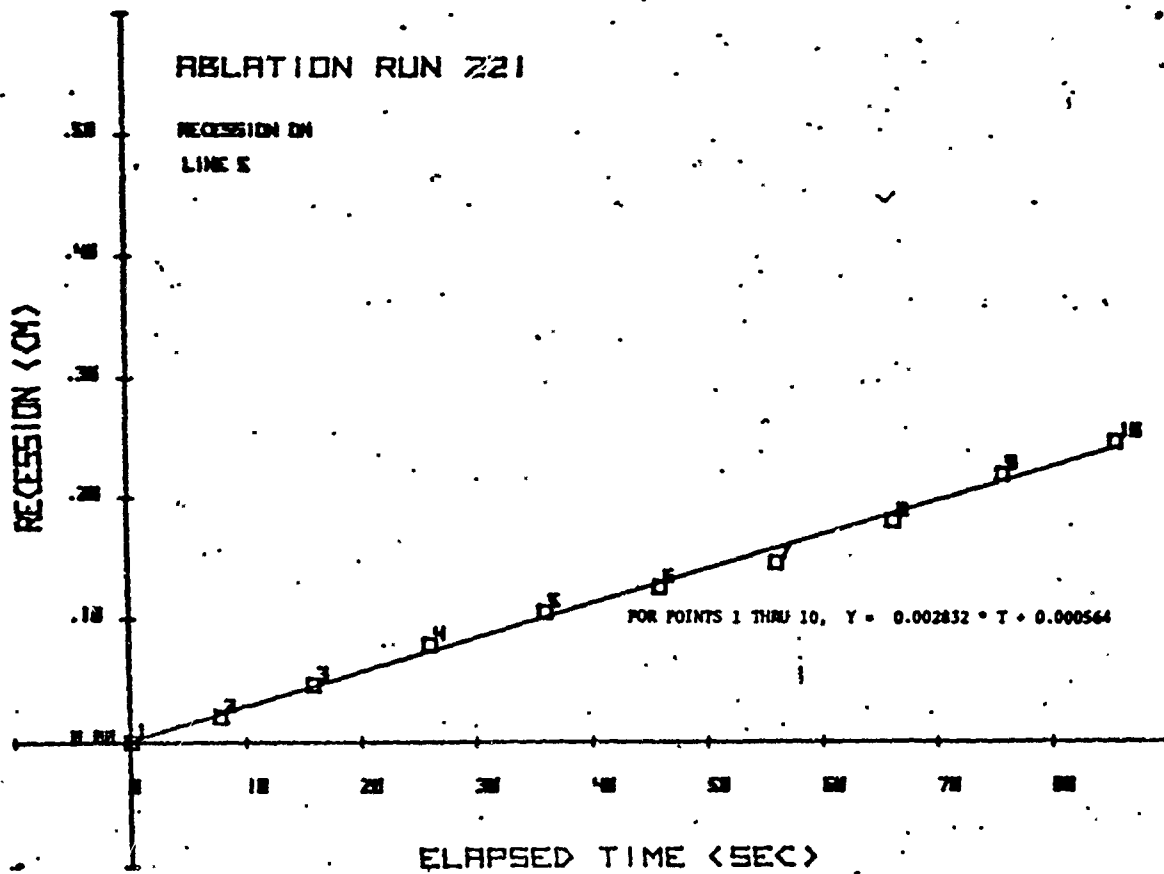


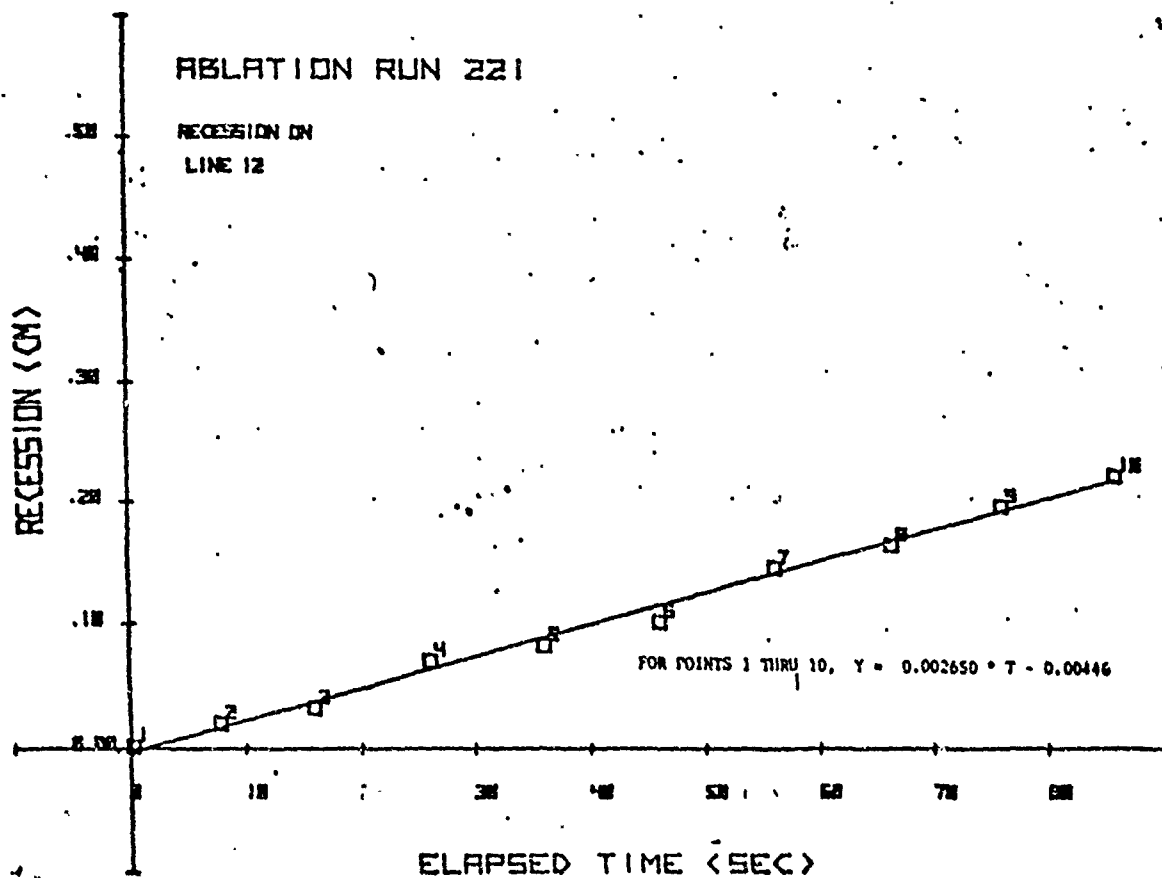
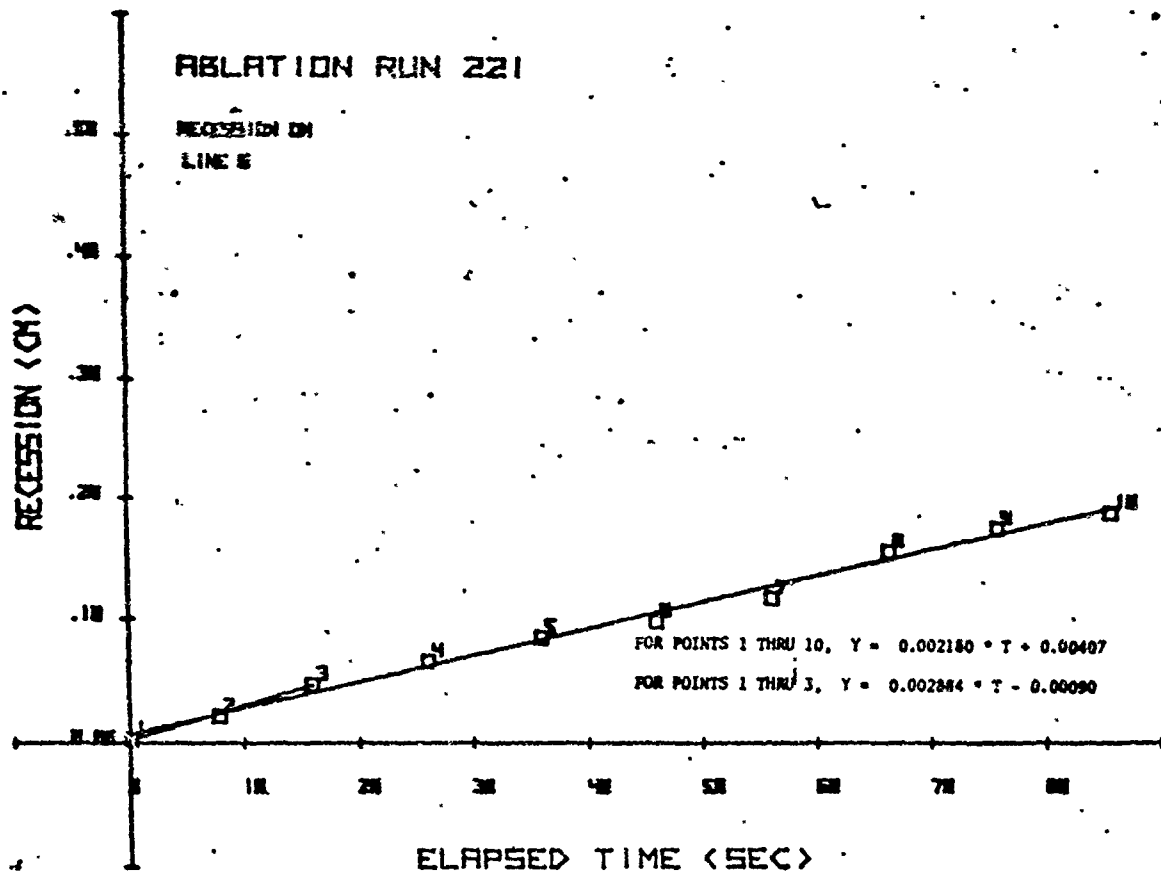












Vita

George Yount Jumper, Jr., was born on 21 May 1942 in Phoenix, Arizona, the son of George Y. Jumper, Colonel, USAF Retired, and Anita Speranza Jumper. He graduated from Sacred Heart High School, Salina, Kansas and entered The University of New Mexico, Albuquerque, New Mexico. He received a Bachelor of Science in Chemical Engineering and was commissioned as a Second Lieutenant in the USAF Reserve. He entered active duty in August 1964 to attend the Air Force Institute of Technology, Wright-Patterson AFB, Ohio, and received a commission in the Regular Air Force while there. He graduated with a Master of Science in Aerospace Mechanical Engineering in June 1966 and was assigned to the Service Engineering Division of the Sacramento Air Material Area, AFLC, McClellan AFB, California. He attended Squadron Officer School in 1969 and entered the Air Force Institute of Technology Resident PhD program. He was assigned to the Air Force Materials Laboratory in October 1971 where he accomplished his dissertation research.

Captain Jumper is married to the former Alexia Ann Shanley of the Bronx, New York and they have two children, Kevin and Geoffrey.

Permanent address: 3910 Simms Ave., S.E.
Albuquerque, New Mexico 87108

This dissertation was typed by Ms. Linda Moenter.